Optimisation topologique de structures lattices à base de surface minimale triplement périodique en Ti-6Al-4V pour implants osseux humains obtenus par fabrication additive

Chrysoula Chatzigeorgiou

▶ To cite this version:

Chrysoula Chatzigeorgiou. Optimisation topologique de structures lattices à base de surface minimale triplement périodique en Ti-6Al-4V pour implants osseux humains obtenus par fabrication additive. Mécanique des matériaux [physics.class-ph]. HESAM Université, 2022. Français. NNT : 2022HESAE011 . tel-03707088

HAL Id: tel-03707088
https://pastel.hal.science/tel-03707088

Submitted on 28 Jun 2022

HAL is a multi-disciplinary open access archive for the deposit and dissemination of scientific research documents, whether they are published or not. The documents may come from teaching and research institutions in France or abroad, or from public or private research centers.

L'archive ouverte pluridisciplinaire **HAL**, est destinée au dépôt et à la diffusion de documents scientifiques de niveau recherche, publiés ou non, émanant des établissements d'enseignement et de recherche français ou étrangers, des laboratoires publics ou privés.

ÉCOLE DOCTORALE SCIENCES DES MÉTIERS DE L'INGÉNIEUR
[LEM3 – Campus de Metz]

THÈSE

présentée par : **Chrysoula CHATZIGEORGIOU**

soutenance le : 31 **janvier 2022**

pour obtenir le grade de : **Docteur d'HESAM Université**

préparée à : **École Nationale Supérieure d'Arts et Métiers**

Spécialité : **Mécanique - Matériaux**

Topology optimization of Ti-6Al-4V Triply Periodic Minimal Surface-based lattices for human bone implants obtained by additive manufacturing

THÈSE dirigée par :
[Professor Fodil Meraghni],
[Professor Yves Chemisky]

et co-encadrée par :
[Dr. Boris Piotrowski]

Jury

M. Sébastien Laporte , Professor, IBHGC, Arts et Métiers-ENSAM Campus Paris	Président
Mme. Rachele Allena, Associate Professor, LJAD, Université Côte d'Azur	Rapporteur
M. Konstantinos Danas, Associate Professor, LMS, CNRS, Ecole Polytechnique	Rapporteur
M. Fodil Meraghni, Professor, LEM3, Arts et Métiers-ENSAM Campus Metz	Examinateur
M. Yves Chemisky, Professor, I2M, Université de Bordeaux	Examinateur
M. Boris Piotrowski, Doctor, LEM3, Arts et Métiers-ENSAM Campus Metz	Examinateur
M. Paul Lohmuller, Doctor, Université de Lorraine	Invité

T H È S E

Acknowledgements

I would like to express my sincere gratitude to my thesis director, Prof. Meraghni Fodil for his guidance and scientific support at all stages of the PhD project. Without his continuous encouragement and constructive remarks, I would have never completed this PhD thesis successfully. I also thank Prof. Chemisky Yves, my co-director, for his valuable advices and help along the PhD. I would like to extend my gratitude to Dr. Piotrowski Boris, my advisor, for all the useful advices, his patience, and the technical support as well. Thank you all my supervisors once more for providing me with various scientific opportunities and helping me start a career in science. I also thank LEM3 and I2M laboratories for hosting me these past three years.

I pay my deep sense of gratitude to all the committee members for kindly accepting the invitation, taking the time to read the final thesis manuscript, and asking their interesting questions; Prof. Laporte Sébastien, the president, associate professor Allena Rachele and associate professor Danas Konstantinos, the reporters, and the invited member Dr. Lohmuller Paul, with whom I was also having interesting discussions during my PhD studies.

Moreover, I am very thankful to Dr. Chatzigeorgiou Georges for his help and contribution to all the numerical aspects of my PhD as well as Gross Théophile for the continuous IT support. Special thanks to Peltier Laurent, Didier Paul, Moll Patrick for their friendly manners and help regarding the experimental part of my project. I also thank Prof. Laheurte Pascal for his contribution to the manufacturing of the specimens.

I also thank warmly all the members of LEM3 laboratory and especially SMART team for their kindness and help, Dr. Haddad Fares, Dr. Miqoi Nada, Chekkour Rabii, El Fallaki Idrissi Mohammed, Dr. Benaarbia Adil, Dr. Praud Francis, Dr. El-Hadi Tikarrouchine, Dr. Pomarede Pascal, Dr. Chen Qiang, Dr. Nachtane Mourad, Dr. Thiercelin Leo, Dr. El Hachi Younes, Sekkal Saif Eddine, Dr. Gaël Lecoz. Special thanks to Satouri Soheil, my office colleague, with whom I had scientific and funny discussions as well.

Finally, I would like to thank my mother, my sister and all my friends for their help and support throughout the PhD journey. A special thank you to Nikiforos for being so supportive and encouraging.

Abstract in French

Les structures lattice offrent des solutions performantes pour remplacer des structures tout en contrôlant leurs propriétés mécaniques. Ceci est particulièrement le cas pour réduire le phénomène de stress-shielding qui peut survenir dans l'os péri-implantaire suite à la pose d'implants. Outre les structures lattices à base de poutre largement étudiées, le concept de surfaces minimales triplement périodiques (TPMS) a été introduit pour créer des structures présentant des propriétés originales. Huit topologies de cellules unitaires basées sur TPMS et deux basées sur des poutres ont été étudiées numériquement pour calculer leurs propriétés élastiques effectives et la distribution des contraintes locales, en utilisant une méthode d'homogénéisation périodique. La dépendance de la topologie sur la distribution des contraintes locales est mise en évidence par une analyse statistique des cellules unitaires. La validation des résultats numériques a été effectuée par des résultats obtenus expérimentalement suite à la fabrication par une machine SLM de plusieurs structures et à des tests de compression. Deux types de sollicitation ont été étudiés : un cas standard mettant l'accent sur le module d'Young effectif des structures, et un cas destructif se concentrant sur la rupture de ces dernières. Sur la base de ces résultats, une étude numérique considérant le remplacement partiel d'un os par une structure lattice à base de TPMS, soumis à des conditions aux limites réelles, est développée. Un critère permettant de choisir une structure optimisée sur la base de contraintes mécaniques est proposé.

Mots clefs: structures lattices à base TPMS, déviation des contraintes, homogénéisation périodique, MEF, fabrication additive, prothèse de hanche

Abstract in English

Lattice structures offer the opportunity to control the mechanical properties of the structures they replace. The use of lattices in orthopedic implants is then a promising solution to the stress shielding problem that may occur postoperatively. Apart from the widely known strut-based lattices, the Triply Periodic Minimal Surfaces (TPMS) concept has been introduced to create surface-based lattices with tailored mechanical properties. Eight TPMS-based and two strut-based unit cell topologies have been numerically investigated to compute their apparent elastic properties and local stress distribution, considering a periodic homogenization method. The topology-dependence of the local stress distribution is highlighted by a statistical analysis of the unit cells. The validation of the numerical results has been performed by experimentally-obtained results following the fabrication of several lattices by an SLM machine and compression testing. Two solicitation types were investigated: a functional case emphasizes on the apparent Young modulus of lattices, and a destructive case focusing on fracture mechanism. According to all previous results, a numerical partial replacement of a real bone subjected to real boundary conditions by a TPMS-based unit cell is proposed according to various mechanical requirements.

Keywords: TPMS-based lattices, stress shielding, periodic homogenization method, FEA, additive manufacturing, SLM, hip implant

Table of contents

Acknowledgements i

Abstract in French iii

Abstract in English iv

Table of contents v

List of Tables ix

List of Figures x

First Part : Thesis in English 2

Introduction 3

1. The framework of stress shielding-related problems and surface-based lattices 7

  1.1. Introduction 7

  1.2. Bone: structure, self-healing ability, and treatment of fractures with orthopedic implants 8

    1.2.1. Bone structure and natural bone remodeling described by Wolff's law 8

    1.2.2. Orthopedic implants as a treatment for major injuries 10

  1.3. Postoperative biomechanical problems between the orthopedic implant and bone. 11

    1.3.1. Stress shielding effect 11

    1.3.2. Correlation between biomaterials for implants and stress shielding 12

    1.3.3. Two ways to reduce apparent elastic modulus: material- and geometry- based solutions 13

  1.4. Lattice structures; design and apparent elastic properties 13

    1.4.1. General introduction for architectured materials 13

    1.4.2. Strut-based and TPMS-based unit cells; the design concept 15

    1.4.3. From a unit cell to a lattice structure 19

    1.4.4. Apparent elastic properties for unit cells and lattices 20

    1.4.5. Design capabilities for TPMS-based lattices 21

  1.5. Additive manufacturing 23

    1.5.1. Brief introduction 23

    1.5.2. SLM technology 24

    1.5.3. Advantages and limitations of the SLM technology 26

    1.5.4. Medical applications of SLM technology 27

  1.6. Conclusions 29

2. Design, effective elastic properties and local stress distribution of TPMS-based lattices31

2.1. Introduction 31
2.2. Design of TPMS-based unit cells and lattices 32
2.2.1. Strut-based unit cell design process 32
2.2.2. TPMS-based unit cells design process 32
2.3. Numerical Periodic Homogenization 38
2.4. Effective mechanical properties of the unit cells 40
2.4.1. Brief introduction 40
2.4.2. Cubic stiffness symmetry and equations for the computation of the effective mechanical properties 41
2.4.3. Results, comparison, and analysis 43
2.4.3.1. Mechanical properties variation by topology and design parameter, t 43
2.4.3.2. Mechanical properties variation by topology and volume fraction 46
2.4.3.3. Comparison of the anisotropy of the unit cells 50
2.5. The meshing of the unit cells and mesh sensitivity analysis 52
2.6. Local stress distribution on unit cells 55
2.6.1. Introduction 55
2.6.2. Loading case and volume fraction sensitivity analysis 56
2.6.3. Local stress distribution in an iso-volume fraction case 58
2.6.4. Local stress distribution in an iso-elasticity case 62
2.7. Application: The most suitable topologies for a cortical bone replacement 63
2.8. Conclusions 67
3. Additive manufacturing of lattice structures: multiscale characterization and comparison with numerical predictions 70
3.1. Introduction 70
3.2. Experimental and numerical methods and results 72
3.2.1. Methodology 72
3.2.2. Experimental procedure; fabrication of lattices, mechanical testing, and characterization 73
3.2.2.1. Fabrication of the TPMS-based lattices by SLM technology and relative weighing 73
3.2.2.2. Acquisition of the experimental curves and apparent elastic modulus measurement for lattices under a compression load-unload 77

3.2.2.3. Interrupted tests, crack observation with x-ray micro-tomography, and final macroscopic facture 82
3.2.3. Numerical procedure using Finite Element Analysis; comparison of two different boundary conditions and calculation of the apparent elastic modulus of lattices 88
3.3. Comparison, presentation, analysis, and discussion of numerical and experimental results 90
3.3.1. Comparison of two boundary conditions and selection of the most representative 91
3.3.2. Fracture of the lattices; experimental results 96
3.3.3. Selection of safety factors for the biomechanical design of lattices and the most suitable topology 98
3.4. Conclusions 99
4. Partial replacement of femoral bone using TPMS-based lattices, modelling and stress analysis 101
4.1. Introduction 101
4.2. Methodology 104
4.2.1. Global model; femur bone with real elastic properties subjected to real boundary conditions 104
4.2.1.1. Creation of the 3D model 104
4.2.1.2. Applied real boundary conditions 108
4.2.2. Local model; unit cells with various topologies subjected to boundary conditions taken from the global model 111
4.3. Presentation and analysis of the results 113
4.4. Conclusions 121
General Conclusions and Perspectives 124
Appendices 128
A. Complete numerical chain for the design of TPMS-based unit cells 129
B. Design of TPMS-based unit cells according to the fundamental-patch design approach 132
C. Constitutive law of the Ti-6Al-4V alloys applied in Abaqus 135
D. Post-processing and data reduction steps for the as-acquired experimental curves... 137

E. Compressive Boundary Conditions (CBC) applied to single unit cell and lattices with multiple unit cell repetitions 140
Bibliography 143
Second Part : Extended summary in French 151
Résumé 175
Résumé en anglais 175

List of Tables

Table 2.1.Complete list of all the investigated unit cell types in this study. 37
Table 2.2. The table summarizes the weighted arithmetic mean and weighted standard deviation of the investigated normalized local stress distributions. 60
Table 2.3. The table summarizes the weighted arithmetic mean and weighted standard deviation of the investigated normalized local stress distributions. 63
Table 2.4. The table summarizes the weighted arithmetic mean and weighted standard deviation of the investigated normalized local stress distributions. 66
Table 3.1. The five investigated topologies at two stiffness levels with their corresponding volume fractions, the numerical and the experimental one, and the difference between them. 77
Table 3.2. The average experimental elastic modulus of 5 tested topologies is calculated by the elastic modulus of three tests per topology. 82
Table 3.3. The numerically computed apparent elastic modulus for five unit cell topologies after the application of PBC and CBC. 89
Table 3.4. Complete table with the numerically computed and experimentally measured elastic moduli and volume fractions for 5 investigated topologies. The relative differences are presented as well. 92
Table 4.1. The average stress values at the centroid of the elements for all the studied unit cells and the AoI. 117
Table 4.2. The table summarizes the weighted arithmetic mean, and weighted standard deviation of the investigated normalized local stress distributions and the volume fraction of the corresponding topologies. 118
Table 4.3. The results of the weight function, W, for the studied topologies. 121
Table Appendix.1. Tabular non-linear constitutive law of the Ti-6Al-4V material applied in Abaqus for numerical simulations. This law has been obtained by previously performed uniaxial compression loading tests in LEM3 laboratory. 136
Table Appendix.2. The numerical elastic moduli per topology after the application of both PBC and CBC boundary conditions, and the experimentally measured elastic modulus. 141

List of Figures

Figure 1.1. Cancellous and cortical bone structures of a femur bone [5]. 9
Figure 1.2. The three stages of bone remodeling according to the applied load, as described by Wolff's law [6]. 9
Figure 1.3. Example of hip and knee orthopedic implants [11]. 10
Figure 1.4. The effect of stress shielding on the peri-implant bone for a hip replacement after 1 month, 3 years, 5 years, and 11 years postoperatively. Densification of the bone is observed around the lower part of the implant while bone mass reduction occurs around the higher part of the stem [6]. 12
Figure 1.5. Two examples of a fabricated hip implant with a different internal structure. A compact hip implant (left) [33] and an architectured hip implant (right) [34]................ 14
Figure 1.6. A Diagonal unit cell (left) and an Octet-truss unit cell (right)............................. 15
Figure 1.7. a) Several TPMS unit cells in the domain [0-2*π] and their names [40], b) the wings of a butterfly with a Gyroid-like structure [48] 16
Figure 1.8 Four TPMS examples: a) Schoen's Gyroid (top left), b) Schwartz's Primitive (top right), c) Schoen's IWP (bottom left), and d) Neovius (bottom right)............................ 17
Figure 1.9. A cube partitioned by a) Gyroid and b) Primitive TPMS and the corresponding sheet (in grey colour) and skeletal (in blue and red colours) unit cells. 19
Figure 1.10. 3x3x3 lattice structures for Gyroid (left) and Schwartz Primitive (right) topologies. 20
Figure 1.11. a) Macro-porosity gradient for a sheet Gyroid lattice, b) unit cell size gradient for a sheet Gyroid lattice, and c) multi-morphology gradient for a sheet Schwartz Diamond - sheet Gyroid lattice [36]. 22
Figure 1.12. A schematic representation of an SLM configuration [65]. 25
Figure 1.13. The complete process from the CT scan images to the final 3D object obtained by SLM technology [71]. 28
Figure 1.14. Metallic SLM-fabricated implants and medical devices: a) craniofacial implant, b) dental implant, c) spinal implant, d) surgical guides, e) hip implant, and f) interbody fusion cages [70]. 29
Figure 2.1. Complete numerical chain for the design process followed in this study. 32
Figure 2.2. All four investigated TPMS in this study. 33
Figure 2.3. Gyroid surface as plotted in python for $t = 0.4476$ (left) and $t = -0.4476$ (right) in the domain $[0 - 2 * pi]$... 34

Figure 2.4. a) Two Gyroid unit cell surfaces with opposite offset, b) a cube partitioned by two opposite surfaces, c) two generated skeletal unit cells, d) a sheet unit cell (with two small parts on the corners to ensure periodicity), and e) a single skeletal unit cell in Salome Meca software. 36
Figure 2.5. All numerically investigated unit cell topologies. 37
Figure 2.6. Constraint driver connection with the nodes of the cubic unit cell [76]. 39
Figure 2.7. Constraints, in orange, and objectives, in blue color, or the problem to be addressed. 41
Figure 2.8. The design parameter, t, directly linked to the normalized effective values of the a) Young's modulus, b) Shear modulus, c) $C11*$, and d) $C12*$ elastic components. 45
Figure 2.9. The effective normalized a) Young's modulus, b) shear modulus, and c) Poisson's ratio versus the volume fraction of the unit cells are presented for the studied TPMS-based and strut-based unit topologies indicated in the legend. 48
Figure 2.10. An Ashby chart with the Young's modulus and density of the studied topologies by applying the mechanical properties of Ti-6Al-4V in Abaqus (pink bubble) and the target to be reached, the cortical bone (yellow bubble). 49
Figure 2.11. Evolution of the Zener ratio for all the investigated types of unit cells with several volume fractions. 50
Figure 2.12. IWP skeletal internal unit cell (left) and Diagonal unit cell (right). 51
Figure 2.13. Gyroid sheet and Octet-truss unit cells as meshed with tetrahedral elements in Abaqus software. 52
Figure 2.14. The FE mesh convergence for the normalized Young's modulus, E', of various unit cells has been reached. 53
Figure 2.15. Mesh sensitivity analysis for both local stress on the centroid and the average stress on the four integration points. 54
Figure 2.16. Distribution of the normalized local stresses over the range $0-1$ of a)-b) Gyroid skeletal, c)-d) Primitive sheet, e)-f) Neovius sheet, and g)-h) IWP skeletal internal unit cells for both loading cases, tensile and shear load. 57
Figure 2.17. Normalized local stress distribution of various unit cells at the same volume fraction of 0.30. The results are split into two separate graphs for easy comparison. 60
Figure 2.18. Normalized local stress distribution for the Diagonal, IWP skeletal internal, and Octet-truss unit cells over the range $0-1$ at the same effective Young's modulus, $E' = 7230\ MPa$. (Iso- effective elastic modulus comparison). 62

Figure 2.19. a) Mechanical requirements to be satisfied by the topologies to replace cortical bone successfully, and b) a chart explaining all the steps of the selection process. 65
Figure 2.20. Normalized local stress distributions of Gyroid sheet, Gyroid skeletal, Primitive skeletal, Primitive skeletal external, and IWP sheet unit cells over the range $0-1$ at the same apparent Young's modulus, $E' = 18500\ MPa$. (Iso- effective elastic modulus comparison) 66
Figure 3.1. SLM Solution 280 HL machine for the fabrication of the lattice structures. 75
Figure 3.2. A building plate with several as-built lattices with supports on top, directly after an SLM job is finished. 75
Figure 3.3. a) Two detached lattices from the plate with parts of the support structures still on the down-facing surface, and b) a Gyroid skeletal lattice with a polished bottom surface after the removal of the supports. 76
Figure 3.4. The Zwick-Roell 1476 machine with the extensometer used for the experiments and the lattice specimen positioned before a test. 79
Figure 3.5. As-obtained results for the first tested specimen per topology directly from the computer (dark blue), and post-processed results (light blue). 80
Figure 3.6. Two planes with multiple length measurements between two peaks of the Gyroid skeletal topology at a compressive load of $90\% * Fmax \approx 20500\ N$. 83
Figure 3.7. Three planes of a Gyroid skeletal lattice with small cracks detected with the aid of the x-ray microtomography. 84
Figure 3.8. An already compressed Gyroid skeletal lattice up to $65\% * Fmax$ is once more loaded-unloaded up to $75\% * Fmax$ and $90\% * Fmax$. The slopes of the regions are similar. 85
Figure 3.9. Gyroid skeletal unit cells compressed until the final macroscopic fracture at $45o$ with different volume fractions. $VF = 0.29$ (left) and $VF = 0.452$ (right). 86
Figure 3.10. Macroscopic fracture at $45o$ for three lattice topologies, i.e. a) Gyroid sheet, b) Gyroid skeletal, and c) Diagonal topology. 86
Figure 3.11. Drop of force when a specimen is fractured under a compressive load for a Gyroid sheet (left) and a Diagonal (right) topology. 87
Figure 3.12. Drop of force when a specimen is fractured under a compressive load for three lattice topologies with the same apparent elastic modulus. Diagonal (top left), IWP skeletal internal (top right), and Gyroid skeletal (bottom) topologies. 88

Figure 3.13. Compressive Boundary Conditions (CBC) in a graphical way applied in the second set of numerical tests in Abaqus. 89
Figure 3.14. Graphical presentation of the linear and non-linear response of the topologies after the application of both boundary conditions. 90
Figure 3.15. Graphical presentation of the linear and non-linear response of the topologies after the experimental and both the numerical tests. 93
Figure 3.16. μ-CT scan of a Diagonal topology where the extra material at the strut connection is obvious.. 94
Figure 4.1. The complete process starts from the acquisition of the CT-scan images up to the creation of the final implant and the application in the human body following the reverse engineering method [106]. 103
Figure 4.2. Three views of DICOM images of a patient's pelvis and femoral bone in Materialise Mimics software: a) coronal, b) axial, and c) sagittal views, d) the reconstructed 3D model of a femur bone and e) the anatomical planes [110]. 105
Figure 4.3. The 3D model of the femur with a) the uniform triangulation after the correction of the surface mesh and b) the FE volume mesh generated in 3-matic software with 654380 elements in total. 106
Figure 4.4. Ten subdivisions of the material type that corresponds to the elastic modulus of the cortical bone and the femur bone after the assignment of the material properties in Materialise Mimics software. 108
Figure 4.5. The coordinate system of a femur bone for the application of the component forces of the $FRES$ for a FEA [6], [114]. 109
Figure 4.6. The complete numerical model of the femoral bone in Abaqus and the values of the muscular forces applied to the reference points RP2 and RP3. 110
Figure 4.7. Highlighted element set that corresponds to the area of interest in the femoral bone. 111
Figure 4.8. Four investigated topologies with the same elastic modulus as the AoI and the corresponding volume fractions. 112
Figure 4.9. Von Mises stress contour of the whole femur and the AoI and the relevant contour legends. 114
Figure 4.10. Von Mises stress contours for a) Gyroid sheet, b) IWP sheet, c) Gyroid skeletal, and d) Primitive sheet unit cells in the stress range $0 - 350\ MPa$ indicated in the contour legend. 115

Figure 4.11. A neglected singularity in a relevant element for the IWP sheet topology caused by errors that arise either from the interpolation of the PBC or by the edges. 116
Figure 4.12. Local stress distributions of Gyroid skeletal, Gyroid sheet, IWP sheet, and Primitive sheet unit cells at the same apparent Elastic modulus, $EAoI = 13798\ MPa$. 118
Figure 4.13. a) volume fraction-weighted average stress, b) weighted SD-volume fraction, and c) weighted average stress-weighted SD graphs for all the studied unit cells. 120
Figure Appendix.1. Complete numerical chain regarding the design of Gyroid unit cells.... 130
Figure Appendix.2. a) Gyroid fundamental patch and TPMS unit cell, and b) Schwartz Primitive fundamental patch and TPMS unit cell. 132
Figure Appendix.3. a) Fundamental patch of Gyroid topology, b) assembly of 4 patches, c) assembly of all 8 patches which create the complete TPMS-based unit cell, d) unit cell after the application of a suitable thickness and d) the final smoothed unit cell. 133
Figure Appendix.4. Stress-Strain curve obtained after post-processing of experimental results. Particularly, SLM-fabricated specimens with Ti-6Al-4V alloy have been tested under uniaxial compression load. 135
Figure Appendix.5. The steps of the post-processing of the experimental force-displacement curves after the compression (loading-unloading) of the lattice structures in a graphical way. 139
Figure Appendix.6. Gyroid sheet lattices with $2 * 2 * 2$ (left) and $3 * 3 * 3$ (right) unit cells repetitions. 140
Figure Appendix.7. Graphical presentation of the linear and non-linear response of the topologies after the experimental and both the numerical tests for single unit cells and lattices with multiple unit cell repetitions. 142

First Part :

Thesis in English

Introduction

Orthopedic implants constitute a successful treatment for serious bone diseases, such as osteoarthritis and bone fractures. For instance, hip replacement is one of the most common operations considering orthopedic implants. Although the latter allow patients to retrieve their everyday activities, several postoperative biomechanical complications may occur a couple of years after surgery and induce pain feelings and necessitate revision surgery. From a mechanical point of view, a usual problem that occurs is called stress shielding due to the high stiffness mismatch between an implant and the bone. A negative result of the stress shieling is the density reduction of the bone surrounding an orthopedic implant. A solution to address the stress shielding problem is to reduce the stiffness of an implant to mimic the mechanical response of the bone. To achieve this objective, two ways are generally investigated. The first one is the use of materials with an elastic modulus close to the level of the bone, such as Beta-type titanium alloys. The latter present a very low elastic modulus that can reach up to $55\ GPa$ which is approximately two times lower compared to the commonly used for implants Ti-6Al-4V alloy with $E = 110\ GPa$. The second one is utilizing implants with an adapted geometry of their microstructure, i.e. architectured materials for tailoring the elastic modulus and to reduce it more than $55\ GPa$. This study is material-independent and the investigated way to material stiffness reduction is based on the generation of lattices structures and their topology optimization towards biomechanical applications.

The lattices which are a subclass of the architectured materials present a defined geometry that helps the control and optimization of the elastic and overall mechanical properties of the implants. Moreover, they could be useful to other tissue engineering applications. Lattices consist of several unit cell repetitions in all directions and the unit cells are periodic and contain all the necessary geometric details. The mechanical response of the lattices is topology-dependent and even though the lattices can have the same volume fraction, the mechanical properties may differ significantly. Therefore, the selection of an appropriate topology for the generation of implants is crucial.

The lattice structures are divided into two categories; strut-based and surface-based lattices. The mechanical behavior of strut-based lattices has been widely investigated over the past few years. However, the sharp connections between struts are considered as a drawback of the strut-based lattices because they may become high stress concentrations areas. In order to overcome this limitation, surface-based lattices have been recently investigated and only a few studies can be found in the literature. Particularly to ensure periodicity of the cells in the 3D space, the surface-based lattices are generated from the Triply Periodic Minimal Surfaces (TPMS) and they are referred to as TPMS-based lattices. Regarding the TPMS-based lattices, the lack of sharp edges may lead to better results regarding the stress concentration compared to the strut-based topologies. The TPMS-based lattices have got lately the attention of many researchers not only because of the opportunity they offer to optimize the overall mechanical properties but also because similar structures can be found in nature. Therefore, the TPMS-based lattices are considered as nature-inspired materials and promising structures for use in biomechanical applications.

The fabrication of lattices has been a challenge for researchers due to their complex geometry. However, thanks to the improvements in additive manufacturing (AM) technologies, the fabrication of complex geometries and shapes is achievable. There are various AM technologies among which the most suitable can be selected according to the application of the lattices and the corresponding utilized material. Selective Laser Melting (SLM) technology can be utilized for the fabrication of metallic lattice structures and implants with a great variety of alloys. The as-built structures present high accuracy because the SLM technique follows the near-net-shape concept and only limited post-processing is required. Therefore, tailor-made lattices and implants to the real elastic requirements can be fabricated successfully.

The main challenge of this study is the selection of the most suitable topology that meets the required criteria for a specific biomechanical application that is implants for bone replacement. The design of the TPMS-based lattices is based on a complex mathematical approach that consists of several steps. The developed design process permits the design of all possible TPMS and the creation of the relevant unit cells and lattices that are appropriate for both FEA and fabrication with AM technologies.

The understanding of the local stress state of the lattices is important in order to study their durability. Since the lattice structures are periodic, a numerical periodic homogenization method is implemented to single unit cells and the prediction of the stress state and apparent mechanical properties follows. When it comes to the comparison of different topologies concerning the above-mentioned predicted values, the finite element analysis method is a useful tool. The relation of the mechanical properties to a design parameter of the lattices is proposed to understand in depth the topology- and volume fraction-dependent results.

Before applying the aforementioned results to a case study, one must fabricate and test experimentally a couple of lattices to obtain the overall response. The first target of the experimental campaign is the validation of the numerical results concerning the elastic modulus of the lattices in a standard case. The second target is the comparison of the deformation mechanisms and final fracture of the tested lattices in a destructive case. Both targets allow the selection of an appropriate topology in the best- and worst-case study.

This work deals primarily with the design of complex TPMS-based and strut-based lattices, the numerical investigation of their mechanical properties considering a periodic homogenization method, and the presentation of statistical tools for the selection of an appropriate topology according to specific requirements. Experimental tests have been carried out to ensure validation of the results. The classification of the topologies is based on the numerically predicted and experimentally measured mechanical properties, emphasizing mostly on the apparent elastic modulus which allows stress shielding reduction. Particularly, this document is structured as follows:

The first chapter presents a comprehensive framework of the stress shielding problem that occurs for orthopedic implants and proposes the lattice structures as a promising solution. Then, the fundamental aspects of the strut-based and TPMS-based lattices, their complex design, and their mechanical properties are described. Finally, the additive manufacturing technology is detailed and it is proposed as the appropriate fabrication process for the lattice structures.

The second chapter focuses on the numerical analysis of the unit cells, namely eight TPMS-based and two strut-based unit cells topologies are investigated. The steps for the design of the lattices are given in detail and the mechanical properties of all the unit cells are computed and compared after the implementation of a periodic homogenization method. The local stress distribution of the unit cells is also examined and an application is presented taking into account all the aforementioned results.

The third chapter proposes a second set of numerical boundary conditions which is compared with the periodic boundary conditions in terms of elastic modulus computation. The numerical results are compared with the experimental results to assess the modeling approach and select the most representative boundary conditions. The macroscopic fracture under compressive loading and the apparent yield stress of the lattices are also investigated experimentally.

The fourth chapter proposes a biomechanical application in which a small part of a real femoral bone is replaced by a suitable TPMS-based unit cell which is referred to as a digital-implant. The applied load on the femur corresponds to a real loading case, i.e. walking. Four different unit cells are compared in terms of stress state and volume fraction when the elasticity requirement is satisfied.

1. The framework of stress shielding-related problems and surface-based lattices

1.1. Introduction

Medical implants are a common treatment for serious injuries and the need for orthopedic implants has been increased in the last few years. Patients' demands are higher as they expect to retrieve their daily activities after an implant operation. [1], [2]. Therefore, it is crucial to solving any postoperative biomechanical problems that occur, such as stress shielding-related problems. The latter leads bone density to decrease which results in instability of the implant and pain feelings.

A possible way to solve the aforementioned problem is the use of architectured implants whose internal part consists of a lattice structure. The lattices and particularly, the surface-based lattices offer an interesting way to control the mechanical properties of the implants and thus, to solve the related problems. The design and the fabrication of the complex surface-based lattices is a challenge but thanks to additive manufacturing technologies, the fabrication of the lattices is possible and highly accurate. This chapter focuses on the presentation of the advanced lattice-design methodology, the capabilities offered by additive manufacturing regarding fabrication, and the importance of the use of lattices in biomechanical applications. All the details about the design, the fabrication, and lattices in implants according to the literature are given in detail in the following sections.

This chapter is structured as follows: the 2nd section describes the bone remodeling for minor injuries and the use of orthopedic implants for major injuries. The 3rd section presents in detail the stress shielding phenomenon and the possible ways to solve the problems based on it. The 4th section introduces the lattice structures, their use for biomechanical applications, and their design. Section 5th presents additive manufacturing technology and how complex geometries such as lattice structures are fabricated. To finish, section 6th summarizes the most important concluding remarks

1.2. Bone: structure, self-healing ability, and treatment of fractures with orthopedic implants

1.2.1. Bone structure and natural bone remodeling described by Wolff's law

As people move and perform everyday physical activities, all human tissues are subject to forces. However, sometimes accidents such as falls may occur. These forces, according to their range and frequency, can often cause various minor or major injuries to the tissues. Some of these tissues, such as the bone, have the ability to heal themselves. This natural healing of any injured bone tissue is called bone biological remodeling. It involves a complicated phenomenon and continues throughout the whole life of a human. Bone structure is well-known to exhibit structural heterogeneity; it consists of two different structures; the cortical and the trabecular bone. The external part of the bone is the cortical bone, whereas the inner part is the trabecular bone, as illustrated in Figure 1.1. Both bone structures are able to remodel biologically [3].

From a morphological point of view, the cortical bone is always denser than the trabecular bone and thus, more rigid. Cortical bone is more efficient to bear compressive loading due to its morphology compared to trabecular bone. On the contrary, trabecular bone exhibits a higher rate of structural heterogeneity but a less brittle behavior compared to the cortical bone. The trabecular bone is also referred to as cancellous bone. Indeed, the particular mechanical properties of each bone structure depend on the exact position of the bone in the human body, the age of the human, the gender, etc [4]. The bone remodeling process occurs in both bone structures, as has already been mentioned. In Figure 1.1., the cancellous and cortical bone structures of a femur bone are presented. It is obvious that the two structures are utterly unlike.

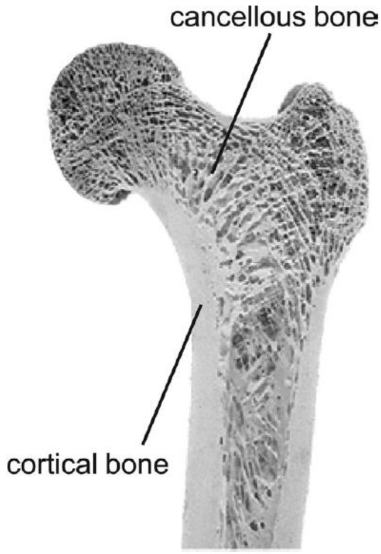

Figure 1.1. Cancellous and cortical bone structures of a femur bone [5].

The bone remodeling process is described by Wolff's law and takes place as a response to an applied stimulus [6], [7]. As shown in Figure 1.2., the density of the bone adapts to the applied stress; bone density tends to decrease when the load is less than the natural load (first threshold-phase 1) whereas the bone density tends to increase, until a physiological limit when the load exceeds an allowable value (second threshold-phase 3). The stage between the two thresholds (phase 2) is considered as the equilibrium zone where the applied load is standard, the density of bone remains constant, and the bone is healthy [8].

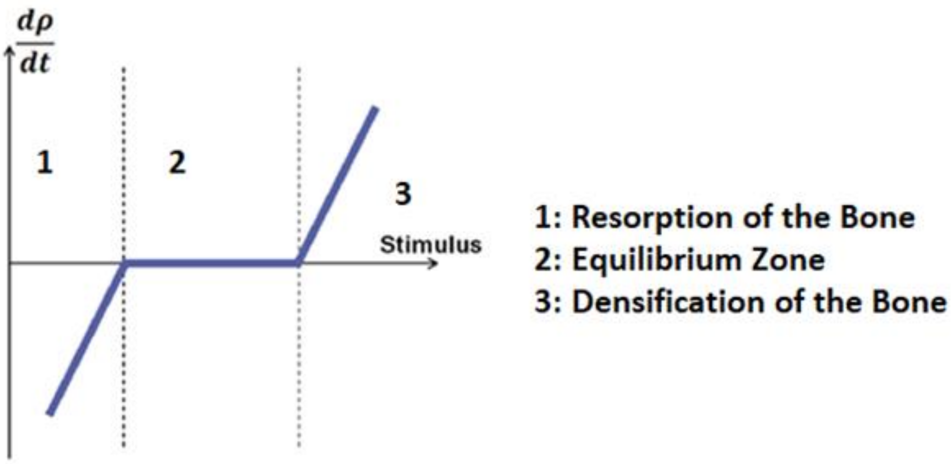

Figure 1.2. The three stages of bone remodeling according to the applied load, as described by Wolff's law [6].

1.2.2. Orthopedic implants as a treatment for major injuries

Bone remodeling helps the treatment of minor traumas on the bones. Nevertheless, there is a critical size of an injury from which the self-healing ability of the bone cannot succeed anymore. Then, human intervention is necessary for the complete healing of the injuries employing orthopedic implants and medical devices [9]. Orthopedic implants are specific medical devices that replace a whole or a part of the damaged bone while mimics their structure, density, mechanical properties, and function as much as possible. For a successful implant operation, both biological and mechanical requirements should be satisfied [10]. Orthopedic implant surgeries are a very common treatment for various severe orthopedic injuries and arthritis. After a successful operation, patients' pain is relieved and they can retrieve their physical activities and improve their quality of life [3]. In Figure 1.3., examples of a hip and a knee implant are presented.

Figure 1.3. Example of hip and knee orthopedic implants [11].

Over the past decades, the amount of patients in need of implant surgery is increasing due to the improvement of technology and thus the quality of medical examinations. The increased quality of the examinations allows physicians to detect any symptoms of severe diseases that necessitate the use of implants as a treatment in an earlier stage of a patient's life than before. Therefore, the mean age of the patients in need of an implant is decreasing and there is a high demand for orthopedic implants that allow them to continue their physical activities and normal living conditions to a high degree [12]. Therefore, any possible postoperative biomechanical problems that occur between an implant and a natural bone should be solved by enhancing the mechanical biocompatibility and durability of the implant. Therefore, patients' postoperative life conditions can be highly improved.

1.3. Postoperative biomechanical problems between the orthopedic implant and bone

1.3.1. Stress shielding effect

A commonly observed undesirable problem after orthopedic implant surgeries is the bone mass reduction of the peri-implant bone (see Figure 1.2.; phase 1). This problem is stress shielding-related [8], [13], [14]. Particularly, bone mass reduction is mainly induced by the significant stiffness mismatch between the implant and the neighboring bone [7]. In more detail, the bone is known to exhibit stiffness that varies in the range from $0.02\ GPa$ (trabecular bone) to $30\ GPa$ (cortical bone) and it is subject to a complex dynamic load [15]. On the contrary, the presence of a more rigid implant than the natural bone perturbates the load distribution; the implant bears a significant part of the load, whereas the peri-implant bone is relieved. In this case, stress shielding occurs, impacting bone density and the implant-bone interface durability [16]. Bone resorption and mass reduction affect hence the long-term performance and stability of the implants, induce pain feelings to the patients, and makes necessary a complex revision surgery [13]. Figure 1.4. shows the peri-implant bone density changes 1 month, 3 years, 5 years and 11 years after the operation as a result of the stress shielding.

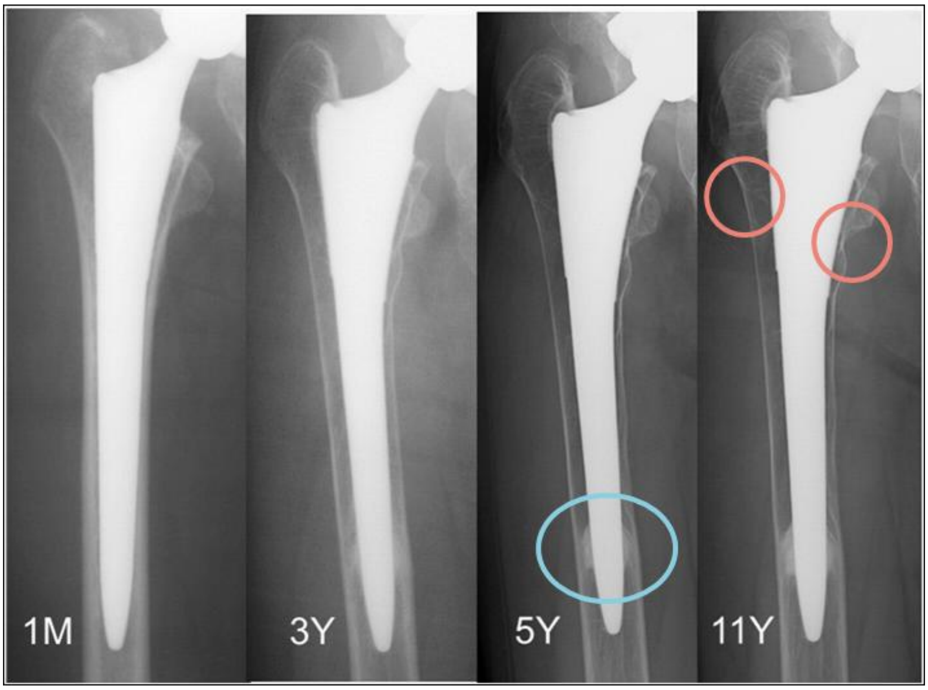

Figure 1.4. The effect of stress shielding on the peri-implant bone for a hip replacement after 1 month, 3 years, 5 years, and 11 years postoperatively. Densification of the bone is observed around the lower part of the implant while bone mass reduction occurs around the higher part of the stem [6].

1.3.2. Correlation between biomaterials for implants and stress shielding

The orthopedic implants are generally stiffer than the natural human bone because of the high-stiffness of their constitutive metals and alloys. Generally, they are made of various biocompatible metals and alloys; such as titanium alloys, stainless steel, and cobalt alloys. Among all these materials, titanium and its alloys are the most utilized because they combine great biocompatibility, high corrosion, fatigue resistance, and a relatively lower Young's modulus compared to the other biocompatible materials [9], [16]–[18].

Ti-6Al-4V is the most utilized titanium alloy in the biomechanical field with various applications in medical implants, in aerospace industry etc. However, it exhibits an approximate maximum apparent elastic modulus of $110\ GPa$, much lower and relatively closer to the levels of the bone than the elastic modulus of stainless steel, which is around $200\ GPa$ [6], [9], [19]–[21]. Even though Ti-6Al-4V-based implants present a relatively low apparent elastic modulus, they are still significantly stiffer than the surrounding host bone, which has a maximum elastic modulus of $30\ GPa$. Consequently, the stress shielding effect is unavoidable and its reduction is of high importance [9], [13]. The reduction of stress shielding can be achieved in two ways [22], [23]. These are described in the following sub-section.

1.3.3. Two ways to reduce apparent elastic modulus: material- and geometry-based solutions

The two ways adopted for reducing stress shielding are the following: the first one focuses on the selection of a titanium alloy based implant, with a low apparent elastic modulus that is as close as possible to the Young's modulus of the natural bone making use of solid-solid reversible phase transformations [17], [19], [24]. This results in the introduction of the second-generation or Beta-type titanium alloys [6], [25], [26]. However, there is still a limitation regarding the mechanical properties of these low elastic modulus alloys. Although these are subject to thermomechanical treatment and reduce their stiffness significantly, their apparent Young's modulus can reach a low value of $55\ GPa$ but it cannot be less than it. This value is still higher than the elastic modulus of the natural bone, which is a maximum of around $30\ GPa$ and after the application of these alloys, the stress shielding phenomenon could still occur [19], [27].

There comes the second solution to reduce the stress shielding effect which is the design of an architectured implant instead of a compact one which allows the control over the macro-porosity of the whole structure and thus its apparent mechanical properties. By designing a architectured implant, its apparent stiffness could be lower compared to the stiffness of a compact implant and thus closer to the levels of the human bone [28]. Architectured structures provide an opportunity to overcome the aforementioned material-dependent limitation by adapting their geometry, i.e. macro-porosity, to the elastic requirements of each application [26].

1.4. Lattice structures; design and apparent elastic properties

1.4.1. General introduction for architectured materials

Cellular materials are divided into two families, foams and lattices. The foams are stochastic cellular materials whose material arrangement in the 3D space is totally random. They present pores with arbitrary size and shape at arbitrary places inside the material itself [29]. On the contrary, lattice structures exhibit a strictly constructed and defined topology and they can also be referred to as architectured materials. Their topology is periodic and it involves several repeating unit cells at a row throughout all three directions. For the lattice structures, the notion of a unit cell is highly important. Thus, it is useful to introduce it first. A unit cell is the smallest part of a lattice that represents all the morphological details, as well as the overall behaviour. It can be repeated periodically to create a complete lattice [30], [31].

As has already been mentioned above, architectured materials can offer an opportunity to overcome any material-dependent limitations and to adjust their apparent elastic properties by adapting their topology. Architectured materials can be employed in various mechanical and biomechanical applications such as scaffolds for tissue engineering [32]. For instance, in Figure 1.5., two different hip implants are presented, a compact hip implant and an architectured one to help the reader visualize and compare the structural difference between the two.

Figure 1.5. Two examples of a fabricated hip implant with a different internal structure. A compact hip implant (left) [33] and an architectured hip implant (right) [34].

The first step in designing a lattice structure is the particular emphasis on the topological aspect of its architecture. It draws our attention that the particular topology of a lattice impacts in a high degree its apparent mechanical properties. This can be viewed as a great opportunity to tune locally these mechanical properties in order to mimic the mechanical response of a bone to be replaced [9], [35]. Moreover, the relative density of the lattices, or the so-called volume fraction, plays an important role in the control of their apparent mechanical properties [36].

It is noteworthy that the topology itself of the lattices induces local stress concentrations in various areas compared to compact structures, in which stress distribution is uniform [37]. Hence, the solution to this new problem, which is the minimization of the local stress concentrations is of great importance in order to improve the fatigue response of the lattice structures and to avoid unpredicted local failure due to plasticity and/or damage accumulation [38]. The local stress concentrations observed in several topologies should be avoided to maximize the apparent mechanical properties of the whole implant [36], [39].

Details about the categories of lattice structures, the design process, the computation of the apparent mechanical properties are given in the following section.

1.4.2. Strut-based and TPMS-based unit cells; the design concept

There are two distinct families of lattices with important morphological differences, the strut-based and the surface-based lattices [40]. The classical lattices are periodic and they consist of various-diameter cylindrical beams/struts at various orientations, such as the Octet-truss [41], body-centered cubic Bravais lattice (BCC) [42], and many more lattices with complex combinations of beams [37], [43]. The BCC lattice is also referred to as a Diagonal lattice. The design of the strut-based lattices is relatively simple; the necessary input for the design and generation of strut-based lattices is the number, orientation, length, and radius of the cylinders. In Figure 1.6., two examples of strut-based unit cells are presented, a Diagonal and an Octet-truss, respectively.

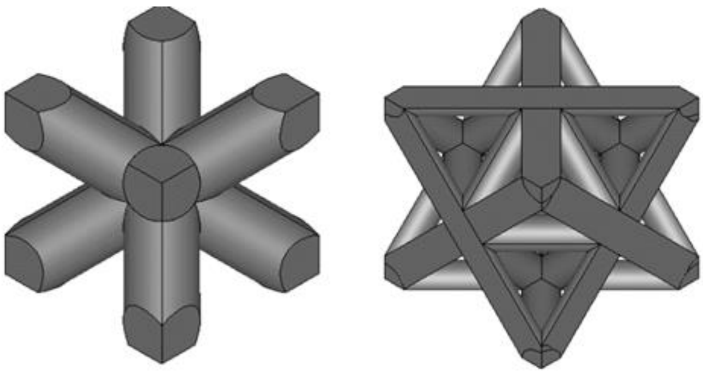

Figure 1.6. A Diagonal unit cell (left) and an Octet-truss unit cell (right).

To further broaden the lattice spectrum, surface-based lattices have been added to it lately. These lattices are based on Triply Periodic Minimal Surfaces (TPMS) and the generated topologies exhibit smooth connections instead of the sharp edges that the strut-based lattices present. They are also more biomimetic compared to strut-based lattices because they can be found in nature. For instance, some TPMS topologies are Schoen's Gyroid, Schwartz's Primitive, Neovius, and Schoen's IWP [44]–[47]. Several TPMS unit cells in the domain $[0 - 2 * \pi]$ are presented in Figure 1.7. Also, in Figure 1.7. the wings of a butterfly with a Gyroid-like structure are presented.

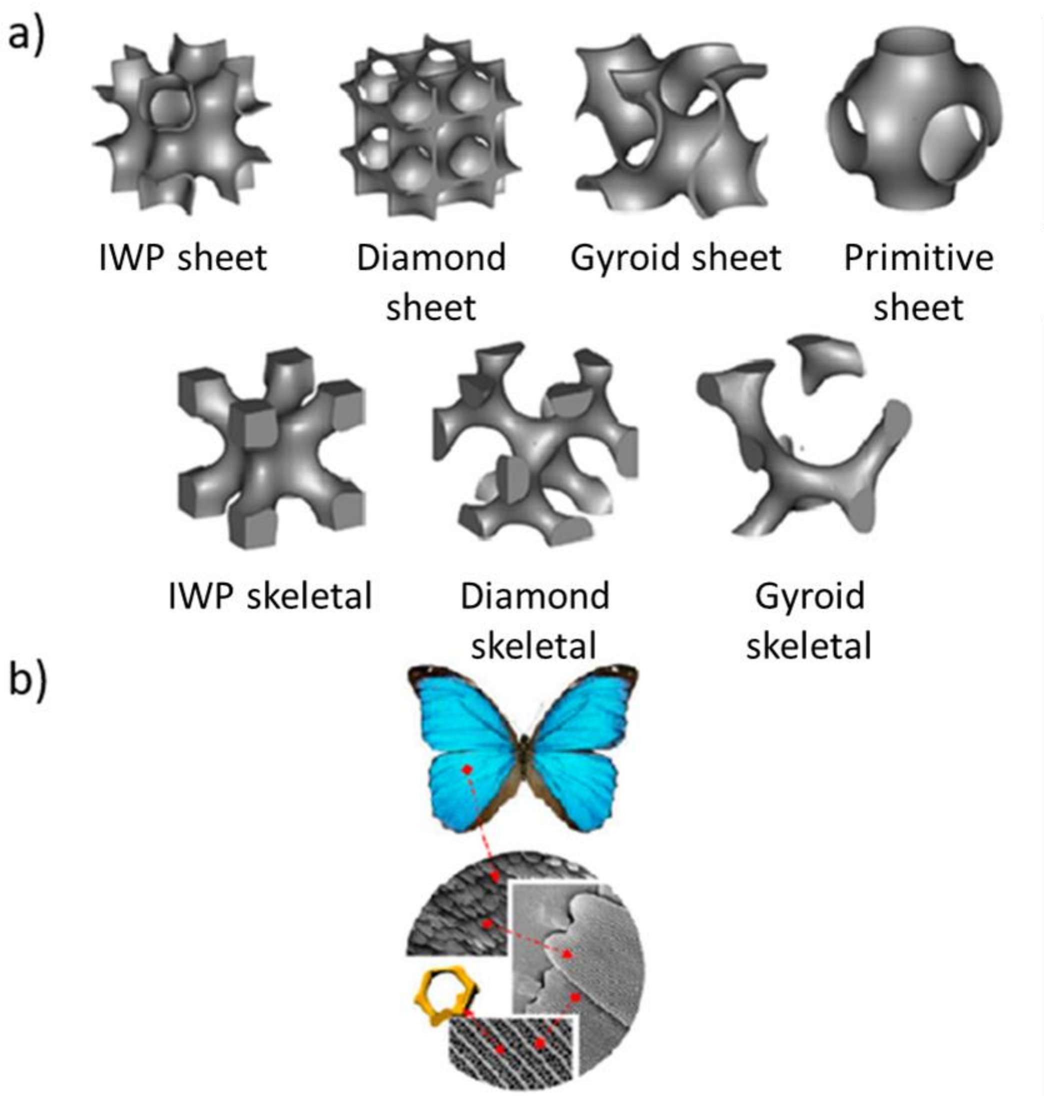

Figure 1.7. a) Several TPMS unit cells in the domain [0-2*π] and their names [40], b) the wings of a butterfly with a Gyroid-like structure [48]

As has been mentioned above, surface-based-lattice generation is based on TPMS. Particularly, TPMS are periodic surfaces in all three directions, as their name indicates. They have a zero mean curvature at every point and each surface divides the 3D Euclidean space into two non-interconnected sub-spaces. They can be defined and designed by mathematical equations which offer a pretty accurate approximation. The sinusoid level-set equations have the general form of:

$$f\ (x, y, z) = t \tag{1}$$

where t is a constant isovalue [49].

In Figure 1.8. four TPMS examples are presented and their corresponding equations are following, with some additional equations as well. The isovalue t controls the offset of the minimal surfaces and thus the volume ratio between the two partitioned sub-spaces, each one of these is related to one colour, either green or orange in Figure 1.8. In the case of $t = 0$, each sub-space has a volume fraction of 50%. When the isovalue is $t \neq 0$, with either a positive or a negative value, the volume ratio between the sub-spaces changes accordingly.

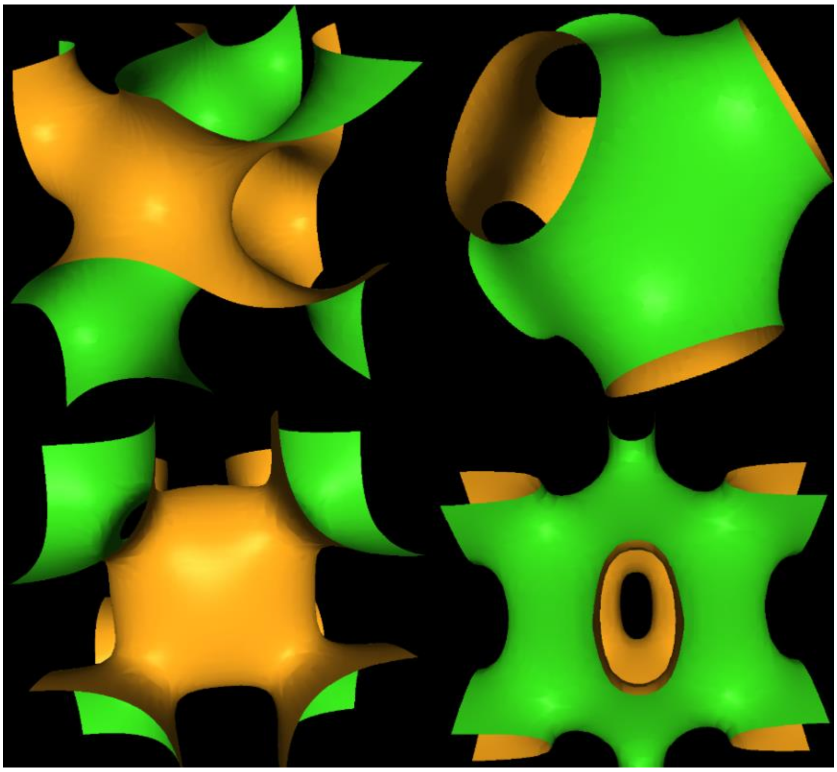

Figure 1.8 Four TPMS examples: a) Schoen's Gyroid (top left), b) Schwartz's Primitive (top right), c) Schoen's IWP (bottom left), and d) Neovius (bottom right).

Schoen's Gyroid:

$$cos(x) * sin(y) + cos(y) * sin(z) + cos(z) * sin(x) = t \quad (2)$$

Schwartz's Primitive:

$$cos(x) + cos(y) + cos(z) = t \quad (3)$$

Schoen's IWP:

$$cos(x) * cos(y) + cos(y) * cos(z) + cos(z) * cos(x) = t \quad (4)$$

Neovius:

$$3 * (cos(x) + cos(z) + cos(y)) + 4 * cos(x) * cos(z) * cos(y) = t \quad (5)$$

Schwartz's Diamond:

$$\cos(x) * \cos(y) * \cos(z) - \sin(x) * \sin(y) * \sin(z) = t \quad (6)$$

By filling with material a sub-space partitioned by a TPMS, a surface-based lattice 3D model is obtained, the volume fraction of which depends on the isovalue t. This is the general way to generate TPMS-based lattices. The design process adapts to the way the sinusoid equations are used and thus, two distinct types of lattices can be generated, the sheet and the skeletal. In particular, the skeletal parts can be generated when one of the two sub-spaces is the solid part, while the other sub-space is the void. In mathematical terms, this can be obtained when one of the two inequalities is satisfied; either the $f\,(x, y, z) \geq t$ or the $f(x, y, z) < t$. On the other hand, the sheet part can be generated when the space between two surfaces is the solid part or in other words, a prescribed thickness is given to the surface generated by the equation (1), when $t = 0$. In mathematical terms, a sheet lattice-type can be obtained when the double inequality is satisfied:

$-t \leq f(x, y, z) < t$ [36]. (7)

The difference between sheet and skeletal unit cells for two TPMS topologies can be observed in Figure 1.9.

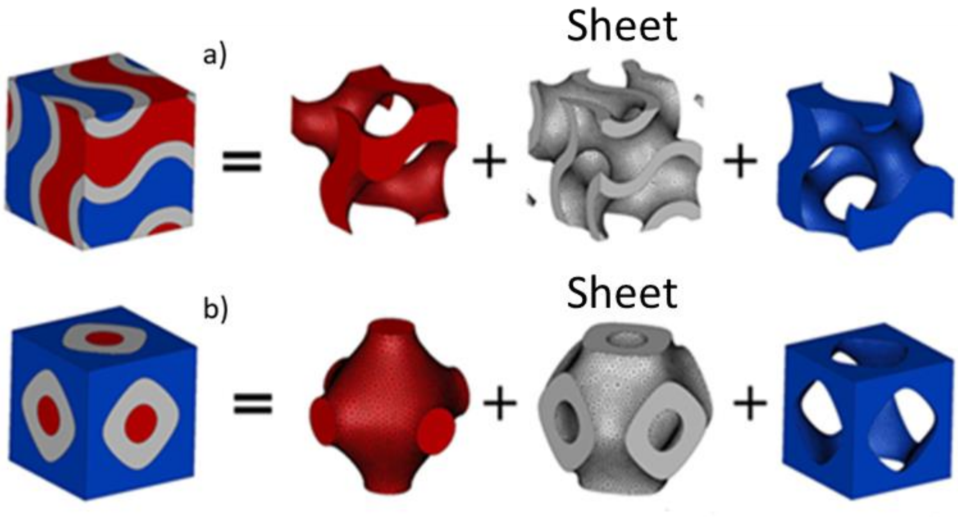

Figure 1.9. A cube partitioned by a) Gyroid and b) Primitive TPMS and the corresponding sheet (in grey colour) and skeletal (in blue and red colours) unit cells.

The cases presented in Figure 1.9. are Gyroid and Primitive topologies; the grey unit cells are the sheet unit cells whereas the red and the blue corresponds to the skeletal unit cells. It is obvious that the two skeletal parts for Gyroid topology are identical and have the same volume fraction. However, it is not the same for the Primitive. The two skeletal parts present totally different shapes. The similar-skeletal-shape property depends on the TPMS topology. For instance, IWP and Neovius topologies exhibit two non-identical skeletal parts too as the Primitive topology does. It is also important to note that the summation of the three volume fractions (2 skeletal parts and 1 sheet) is equal to the volume of a compact cube, because their volumes are complementary.

1.4.3. From a unit cell to a lattice structure

Once a surface is designed and a unit cell is generated by the methods described above, a network of unit cells is then generated, which is called lattice structure. A lattice structure is the periodic repetition of the unit cells throughout one, two, or all three axes. The lattice can be generated either by placing each unit cell next to the other, as described above or by designing a surface that represents a lattice structure with a particular number of unit-cell repetitions and then filling in a sub-space. In Figure 1.10. two $3x3x3$ lattice structures are presented, for the Gyroid sheet and Schwartz Primitive sheet topologies, respectively.

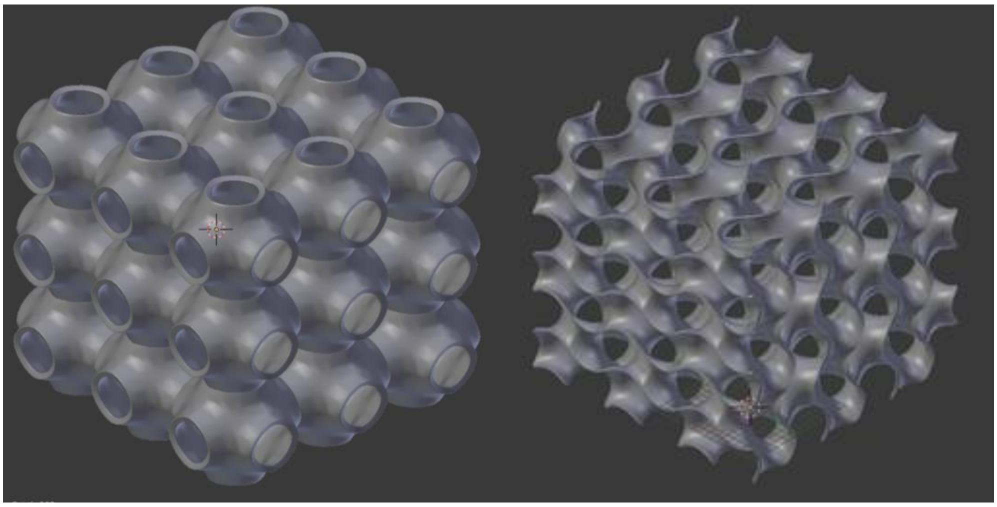

Figure 1.10. 3x3x3 lattice structures for Gyroid (left) and Schwartz Primitive (right) topologies.

It is obvious then that the unit cell is the representation of the complete lattice and it is periodically repeated. Therefore, the periodic homogenization method could be an interesting tool to compute the macroscopic mechanical response of the lattice. Periodic homogenization method is suited in finite elements analysis after the application of particular boundary conditions. More details about this method are given in section 2.3.

All the unit cells of the above-shown lattice structures exhibit a constant volume fraction and thus, the global volume fraction of the lattices is the same as the unit cells. The lattices are called constant volume fraction lattices or constant macro-porosity lattices. In the following sub-section, more complicated lattices are discussed in detail which do not present a constant macro-porosity.

1.4.4. Apparent elastic properties for unit cells and lattices

Once the design of the unit cells and lattices is complete, the numerical computation of the apparent mechanical properties follows. The computation method is based on both the applied numerical boundary conditions and the structure itself, namely a studied unit cell or a complete lattice. For instance, Maskery et al. [49] compute the elastic modulus for both unit cells and lattices which are subjected to compressive displacement by using a relation among the reaction force, displacement, cross-sectional area and height of the 3D model. Moreover, in the studies [50], [51] single unit cells are investigated which are subjected to periodic boundary conditions.

The well-known Gibson-Ashby equations are used in [51], [52]. On the contrary, the apparent elastic modulus of the unit cells in [50] is computed by utilizing the constants of the stiffness matrix.

1.4.5. Design capabilities for TPMS-based lattices

By definition, lattices are periodic structures with repetitive unit cells in all three or fewer directions [53]. In the previous figure, Figure 1.10., two sheet TPMS-based lattices with few unit cell repetitions are presented. The volume fraction is constant for both of these lattices. However, recently some researchers have started to work with architectured structures that do not present a constant volume fraction throughout one or more directions. Indeed, the lattices may present either a macro-porosity gradient or a structural gradient in one or more directions. Moreover, lattices may present a radial macro-porosity gradient. This kind of lattices provides a great opportunity to researchers for tailoring the mechanical response of various architectured materials [36], [54], [55].

Some interesting examples taken from the literature are presented in Figure. 1.11. Figure 1.11 a) shows the macroporosity gradient for a Gyroid sheet lattice structure, b) shows the unit cell size gradient for a Gyroid sheet lattice, and c) presents a multi-morphology lattice structure that includes the Schwartz Diamond, Gyroid sheet topologies, and a smooth transition from one topology to another [10].

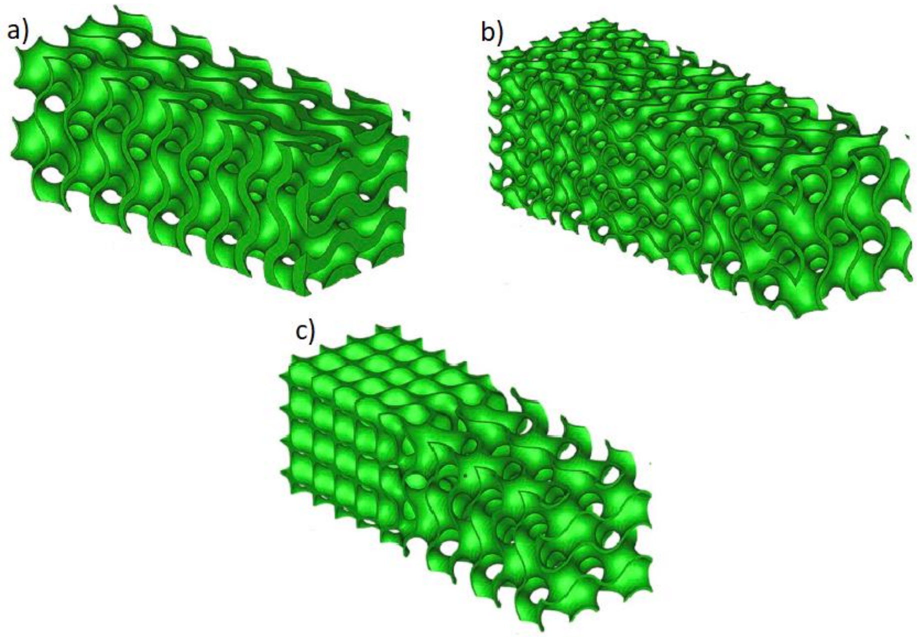

Figure 1.11. a) Macro-porosity gradient for a sheet Gyroid lattice, b) unit cell size gradient for a sheet Gyroid lattice, and c) multi-morphology gradient for a sheet Schwartz Diamond - sheet Gyroid lattice [36].

In terms of mathematical formulations, extra terms are added in the aforementioned sinusoid equations for the design of the lattice structures with a macroporosity gradient (see Figure 1.11. a)). The form of the sinusoid equation becomes

$$f(x, y, z) = t + a * x + b * y + c * z \tag{8}$$

where t is a constant value, x, y, z terms indicate the direction(s) of the gradient and the constant values of a, b, c define the amplitude of the gradient. When a macroporosity gradient is required only in one direction, then $b = c = 0$, and the obtained lattice has a similar gradient like the one presented in Figure 1.11. a) [36].

Regarding the multi-morphology lattices, the design is based on the combination of both the sinusoid TPMS equations and a sigmoid function that controls the smoothness of the transition [56]. A sigmoid equation has the form:

$$\gamma(x, y, z) = \frac{1}{1+e^{kG(x,y,z)}} \tag{9}$$

where k defines the amplitude of the transition area and $G(x, y, z)$ is the function that defines the shape of the transition area. The final form of the complete equation for the design becomes

$$f\ (x, y, z) = \gamma(x, y, z) * g\ (x, y, z) \tag{10}$$

where $\gamma(x, y, z)$ is the sigmoid equation while $f(x, y, z)$ and $g(x, y, z)$ are the sinusoid functions for the corresponding TPMS [36].

All the above presented equations and methodology show that the lattice design is powerful. Any possible topology, volume fraction and combination of topologies can be designed. The way to fabricate such complex geometries is the additive manufacturing technologies which is described in detail in the following section.

1.5. Additive manufacturing

1.5.1. Brief introduction

It is obvious that lattice structures present quite a complex geometry. An architectured material, for example, an implant, that consists of lattice structure exhibits also a considerable complex geometry. This two-scale advanced topology cannot be fabricated by using the conventional subtractive manufacturing processes, such as machining, due to their limited capabilities [38], [57]. However, thanks to the advent and recent improvements in additive manufacturing (AM) technologies, the fabrication of complex shapes, such as lattice structures is nowadays easily achievable [20], [58].

AM started to develop around 1980 and since then significant improvements have been made. AM is a technology that builds layer-by-layer a desirable object. As the name indicates, one layer is added on top of another layer. It is a powerful manufacturing technology and it has already entered the industrial field as a main or complementary manufacturing tool; it is used for automotive, aerospace, agriculture, and medical high-value applications [6], [59], [60].

There are various AM technologies and they are classified as follows: a) binder jetting, b) material extrusion, c) sheet lamination, d) vat photopolymerization, e) material jetting, f) direct energy deposition and g) powder bed fusion. Moreover, various materials are utilized for the fabrication of 3D objects, such as metals, polymers, photopolymers, composites, ceramic according to a particular AM technology [61]. Selective Laser Melting (SLM) is a process that belongs in the powder bed fusion category. It is considered as the very commonly utilized process in both the industrial and scientific fields. More details about this process are given in the following sub-section.

1.5.2. SLM technology

Powder bed fusion is an AM technology that includes two particular processes, the Selective Laser Melting (SLM) and Electron Beam Melting (EBM). In both processes, the use of a high-energy source is involved, laser beam or electron beam, respectively. The beam melts the metallic powder that is placed on the top of a plate and thus the 3D object is built layer-by-layer [61], [62].

Regarding the SLM technology, it has already entered production cycles in the industry to produce high-quality and precise metallic objects and components. The manufacturing time and cost vary per object. Complicated geometries, such as lattices can be easily fabricated via the SLM process, which offers great freedom of 3D design [54]. Apart from the lattice structure, the shape of the implant itself presents a complex shape, especially when it is a custom-made and a patient-specific implant. Therefore, the manufacturing capabilities of an SLM make possible and easy the fabrication of geometrically complex medical devices and implants [62], [63].

There are four steps to obtain a completely fabricated object ready to use. The first step is the Computer-Aided Design (CAD). A great number of design software are available for the generation of the proper 3D model. For an accurate 3D model design and analysis, several tools such as Finite Element Analysis (FEA) and numerical optimization tools may also offer an important advantage. In the end, a 3D model is saved with an .STL extension [62]–[64]. The latter is a neutral and commonly utilized format for AM technologies. It describes the surface of the object to be printed with small triangles. The size of the triangles is considered as the spatial resolution and it impacts the accuracy of the 3D object representation; the smaller the size of the triangles the closer is the 3D model to the real shape [59].

The second step is the pre-processing of the 3D model regarding the fabrication. The careful selection of suitable supports for the down-facing surface of the object to be printed is essential for a successful and precise fabrication without any problems and also the minimization of the required post-processing of the as-built object that follows [61], [64]. Then, a file with mathematically generated 2D ‘’slices’’ based on the 3D model is created virtually by a proper AM slicing software and is sent to the manufacturing machine. According to this file, which includes the printer commands in a g-code format, the fabrication takes place [62].

The third step is the fabrication of the object which includes several parts; the set-up of the machine parameters, the layer-by-layer (or slice-by-slice) fabrication of the object, and the cleaning of the machine. Particularly, the set-up of the machine parameters, such as the laser power, hatching distance, layer thickness, and scanning speed is crucial for the optimization and increasing efficiency of the fabrication process. Once the set-up of the parameters is ready, the fabrication can start. A thin layer of metallic powder is evenly spread on a plate and the laser beam melts the powder according to the input ‘’2D slices’’ file. Then the building platform is slightly lowered and another powder layer is spread on top of the first layer via a powder re-coater and the laser beam once more melts the defined areas of it. This procedure is repeated several times until the end of the fabrication. In the end, the removal of the plate with the fabricated objects is carried out. The complete cleaning of the machine is also a step that has not to be neglected [61], [64].

The last step is the post-processing of the as-built 3D objects. The detachment of the objects from the plate and the careful removal of the supports follow. Then, possible surface treatments can be performed to achieve an object-surface improvement [64].

In Figure 1.12. a schematic representation of an SLM configuration is shown.

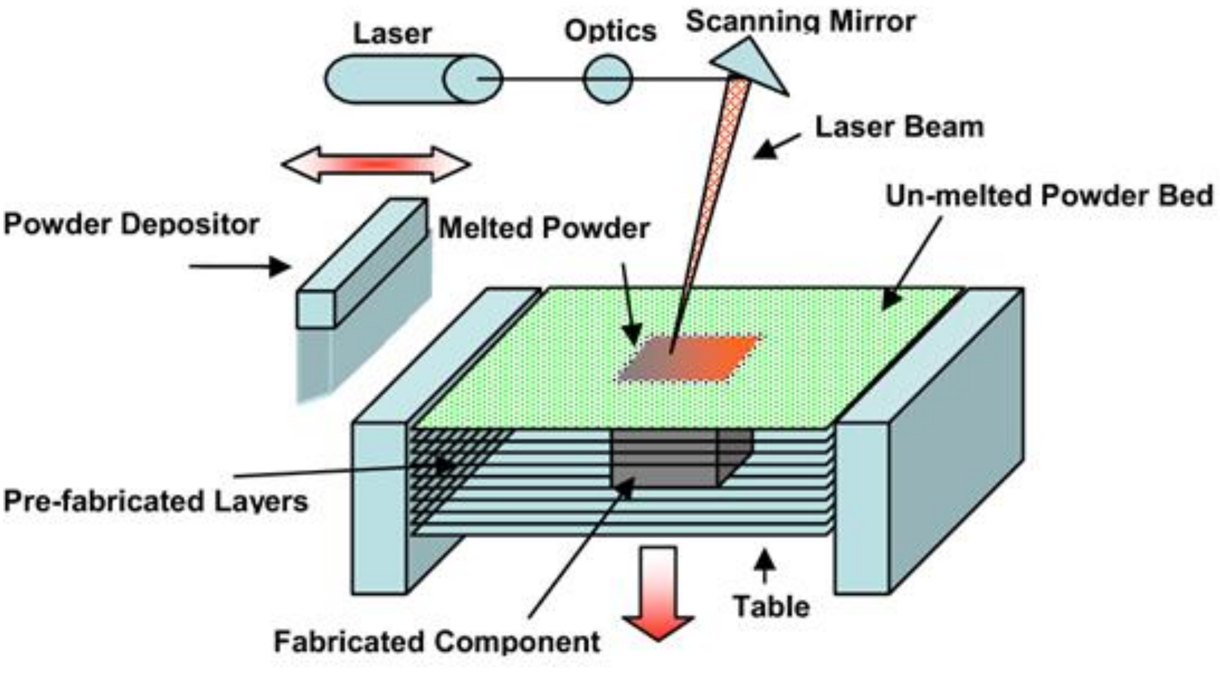

Figure 1.12. A schematic representation of an SLM configuration [65].

It is important to mention that the fabrication process takes place within a closed chamber. Inside the chamber, an inert gas, such as argon (Ar) or nitrogen (N2), flows regularly to lower the oxygen levels and reduces the possibility of metal oxidation during the fabrication process, which can affect the mechanical properties of the as-built part [62], [63].

1.5.3. Advantages and limitations of the SLM technology

The most important advantage of the SLM technology is the capability to fabricate geometrically complex shapes without any important design limitations compared to the traditional fabrication methods. This advantage offers the possibility to design complex-shaped objects. Particularly in the biomedical field, it is possible to fabricate patient-specific medical devices with complex geometries that can fit and help the patients more than the standard-shape medical devices. Absence of stiffness mismatch between the bone and the implant, enhanced biocompatibility and osseointegration are the potential results. Similarly, advantages from the precise fabrication of complex 3D object via SLM technology in other industrial fields such as the fabrication of more lightweight structures is a reality [62], [66].

A second advantage of the SLM technology is the fact that it is an environmentally friendly technology compared to the conventional subtractive manufacturing methods. Apart from the amount of material that is necessary for the fabrication, the remaining powder that has not been melted can be cleaned, recycled, and used again. Therefore, the cost of the supply of raw materials could be reduced. Moreover, machining is necessary on a few areas of the as-built object. Limited machining requirements reduce the material waste and thus the cost concerning the raw material supplies [63], [66], [67].

Apart from all the advantages of the SLM technology, there are a couple of limitations to take necessarily into account when this manufacturing technology is selected. The set-up of the machine parameters is really important to optimize the manufacturing process and to minimize possible defects. However, process parameters still play an important role in the mechanical properties of the specimen. For instance, porosity in the specimen may be caused by a high scanning speed and/or a low energy density during the fabrication process. The existence of pores in the as-built object may result in mechanical properties degradation [64], [68].

Furthermore, the anisotropy of the mechanical properties is a defect that cannot be totally eliminated. The mechanical properties of the 3D object throughout the fabrication direction are slightly different from the other two directions. Residual stresses and the partially melted previous layer by the beam affect also the mechanical properties. The residual stresses may be the cause of small-crack creation, even though the problem is addressed by heating the fabrication plate or performing thermal treatment to the as-built parts. Moreover, the state of the surfaces of the object affects the mechanical properties too. Partially melted powder grains increase the roughness and impact the fatigue behavior of the as-built specimen. The size of the powder grains and the flow of the inert gas (for example argon) affect the state of the surface of the as-built objects too [64], [69].

Despite all the aforementioned possible defects and process limitations, AM and particularly SLM technology still remains a promising manufacturing process that offers potential design freedom of 3D objects.

1.5.4. Medical applications of SLM technology

SLM-fabricated objects are utilized in various industrial and technological applications, such as automotive, aerospace, and medical applications. A great variety of materials are nowadays available in powder format targeted for the fabrication of 3D objects with SLM technology according to the requirements of each application. Particularly, medical applications require the involvement of titanium whose alloys exhibit exceptional mechanical properties and biocompatibility. Apparently, the high cost of the biocompatible materials increases also the cost of implant fabrication [70].

The design of the implants includes two steps. The first step focuses on the external shape of the implants that can be modeled geometrically by using anatomical data; i.e. DICOM images from patients' CT scans that stand for the shape of the human bone [71]. Then, the internal part of the implant can be designed by using CAD-based lattice structures according to particular mechanical properties requirements in order to create custom-made and patient-specific implants. In Figure 1.13. the complete process from the CT scan images to the finally fabricated 3D object is shown.

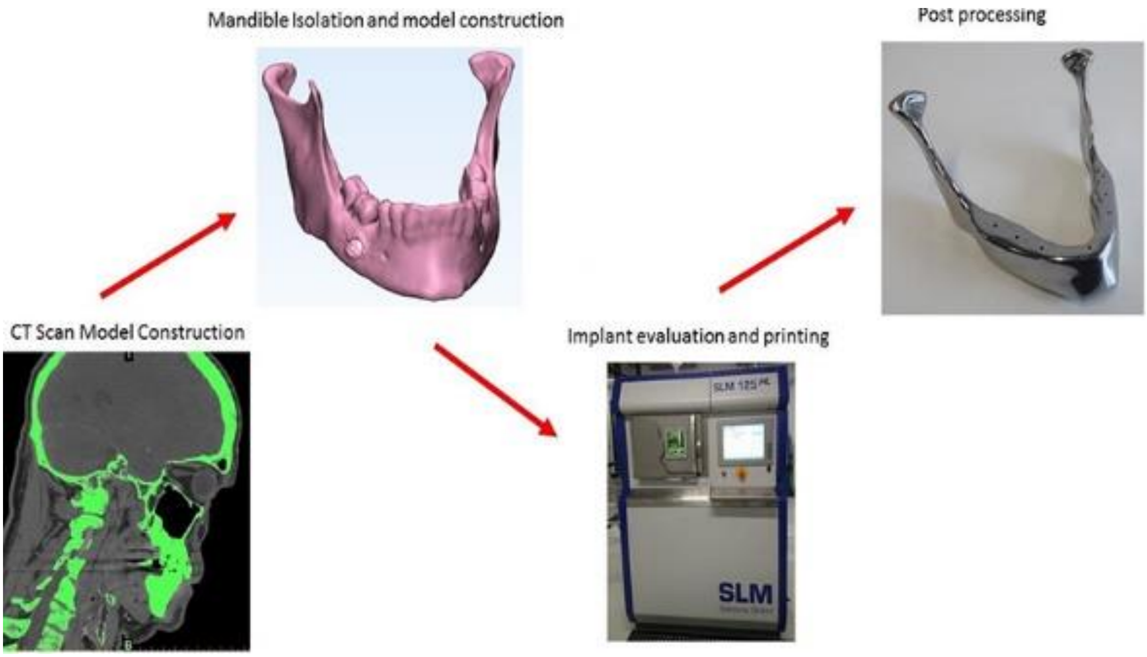

Figure 1.13. The complete process from the CT scan images to the final 3D object obtained by SLM technology [71].

Medical applications of metallic SLM-fabricated objects include surgical guides, dental implants, and a vast range of orthopedic implants, such as hip, spinal, craniofacial implants [70]. Metallic implants can be permanently or temporarily fixed in the human body depending on a particular treatment plan. Metallic implants can also be used for cosmetic applications [63]. Moreover, it should be noted that customized and patient-specific implants are easily fabricated by the combination of CT scan data and SLM technology for a higher rate of geometric precision and treatment success [2].

Following the process of the medical data, 3D implants and medical devices are fabricated by an SLM machine. In Figure 1.14. some examples of metallic SLM-fabricated implants and medical devices are presented.

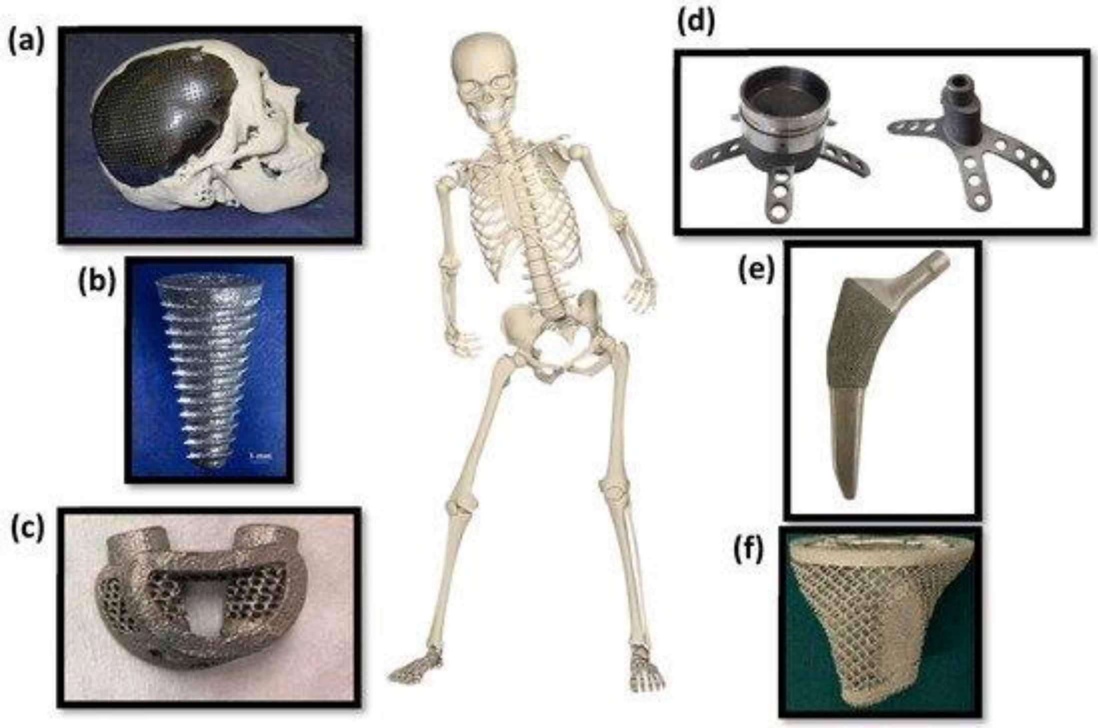

Figure 1.14. Metallic SLM-fabricated implants and medical devices: a) craniofacial implant, b) dental implant, c) spinal implant, d) surgical guides, e) hip implant, and f) interbody fusion cages [70].

1.6. Conclusions

In the present chapter, details about the stress shielding and the related biomechanical problems are given. The design of the lattice structures and the possible solution they offer as part of orthopaedic implants to biomechanical problems are discussed as well. The lattices are divided into two categories: the strut-based and the TPMS-based (surface-based) lattices. The TPMS-based lattices are then divided into two categories as well, i.e. the sheet and the skeletal ones according to the design process. All the above-mentioned are described in detail in the current chapter. To summarize everything in few words, the following conclusions have been reached.

- ✓ The stress-shielding-related problems can be solved by using lattices as the internal parts of orthopaedic implants and thus, the apparent elastic modulus of the implant can be lowered and the mechanical properties can be controlled.

- ✓ As the lattices are periodic structures, and the unit cell is the representative medium, the periodic homogenization method can be applied to solve the mechanical problem.
- ✓ Complex geometries, such as lattices can be fabricated by additive manufacturing technologies and particularly, SLM technology is suitable for biomechanical applications.
- ✓ The design capabilities for TPMS-based lattices are significant. Macro-porosity and/or unit cell gradient can be applied to the lattices. Also, multi-morphology lattices exhibit an interesting global topology.

2. Design, effective elastic properties and local stress distribution of TPMS-based lattices

2.1. Introduction

As previously mentioned, the lattices may be used in the biomechanical field. They can offer the opportunity to overcome any material-dependent limitations and solve any stress-shielding-related problems that occur by adapting their topology. The lattice geometries are quite complex but they can be fabricated with the aid of the advanced additive manufacturing technologies.

The numerical design of the lattices is the initial and very important step. The lattices are strictly defined structures that consist of multiple repetitions of a periodic unit cell. A unit cell contains all the morphological details and can be either strut-based or TPMS-based while the design process is adapted accordingly [30], [31]. In this study, two strut-based unit cells and eight TPMS-based unit cells have been designed. This is carried out to numerically investigate the elastic properties and response of the unit cells and to select those that match the elastic properties of a human bone.

Furthermore, among those that satisfy the elastic requirements a further investigation of the local stress distribution is performed. It is important to note that the complex lattice structures themselves induce local stress concentration on various areas of each lattice. The avoidance of unpredicted local failure due to damage accumulation is the reason why it is important to study the stress distribution.

All the above-mentioned are discussed in detail in the following sections. Particularly, this chapter is structured as follows: the 2nd section describes the design of the strut-based and TPMS-based unit cells, the 3rd section presents the numerical periodic homogenization method that is followed and the applied periodic boundary conditions. The computation of the mechanical properties of the unit cells and the mesh sensitivity analysis are presented in the 4th and 5th section, respectively. The next section includes the local stress distribution analysis. An application and the conclusions follow to complete this chapter.

2.2. Design of TPMS-based unit cells and lattices

2.2.1. Strut-based unit cell design process

The design and the generation of the strut-based lattices are performed using the computational environment of the software Abaqus/CAE 2018. A Python script is developed to enable and automate the design procedure of the strut-based lattices. The strut-based lattices consist of symmetric and periodic struts. The imported data to the script are the parametric shape and the number of the basic solids that constitute the unit cell, their orientation, and their geometric characteristics, such as the length and the radius. The two designed strut-based unit cells are the Diagonal and Octet-truss topologies presented in Figure 1.6.

2.2.2. TPMS-based unit cells design process

This section presents the complete numerical methodology regarding the design of the unit cells. It consists of various steps until the 3D models and the final files are ready either for FEA or for the fabrication. The complete numerical chain for the design process is presented in Figure 2.1.

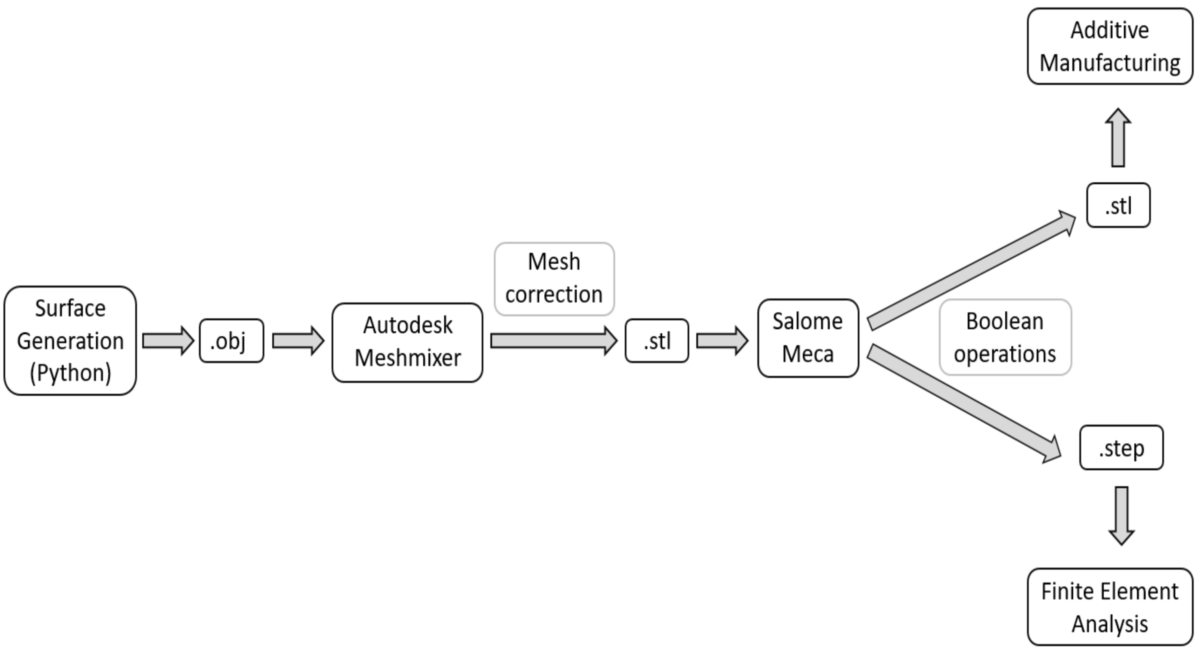

Figure 2.1. Complete numerical chain for the design process followed in this study.

Particularly, regarding the design of the TPMS-based unit cells, it follows the general rules and the mathematical approach discussed in section 1.4.2. First, two opposite surfaces are designed by using a custom-made Python script. The isosurfaces are designed according to the following level-set equations $f(x, y, z) = t$ and $f(x, y, z) = -t$, where t is a constant isovalue that controls the offset of the surfaces and thus, the volume of the sub-spaces that are being created. The absolute value of the two constants isovalues has been chosen to be the same, i.e. $|-t| = |t|$, so the two opposite surfaces have the same offset from the surface without any offset (the central surface for which it is $t = 0$). The investigated TPMS in this study are Schoen's Gyroid, Schoen's IWP, Schwartz' Primitive, and Neovius. The surfaces are inscribed in a bounding box with dimensions $1 * 1 * 1\ units$^3 and they are presented in Figure 2.2.

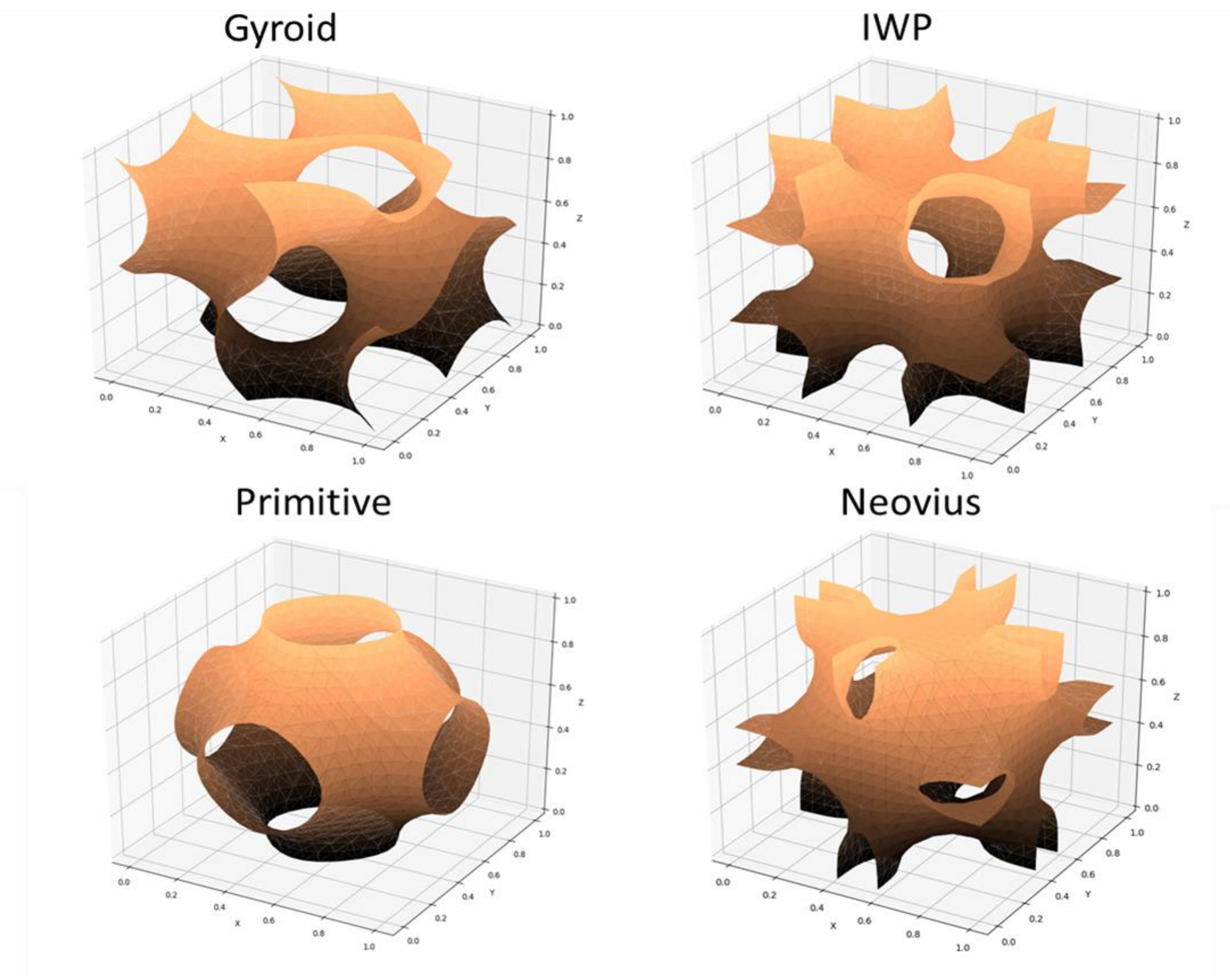

Figure 2.2. All four investigated TPMS in this study.

Each isosurface is saved separately in a file with an .OBJ extension. .OBJ extension files are text-based files and they contain 3D models. In an .OBJ file a surface of a 3D model is defined by numerous triangles and so there is a great number of lines in an .OBJ file which describes the geometric characteristics of a 3D model, such as the number and the coordinates of the nodes and the faces (i.e. the triangles). The reason why each .OBJ file contains only one surface and not the two opposite surfaces, is to facilitate the post-processing that follows [72]. Figure 2.3. presents two Gyroid surfaces with $t = 0.4476$ and $t = -0.4476$, respectively. They are plotted in python before any post-processing is applied.

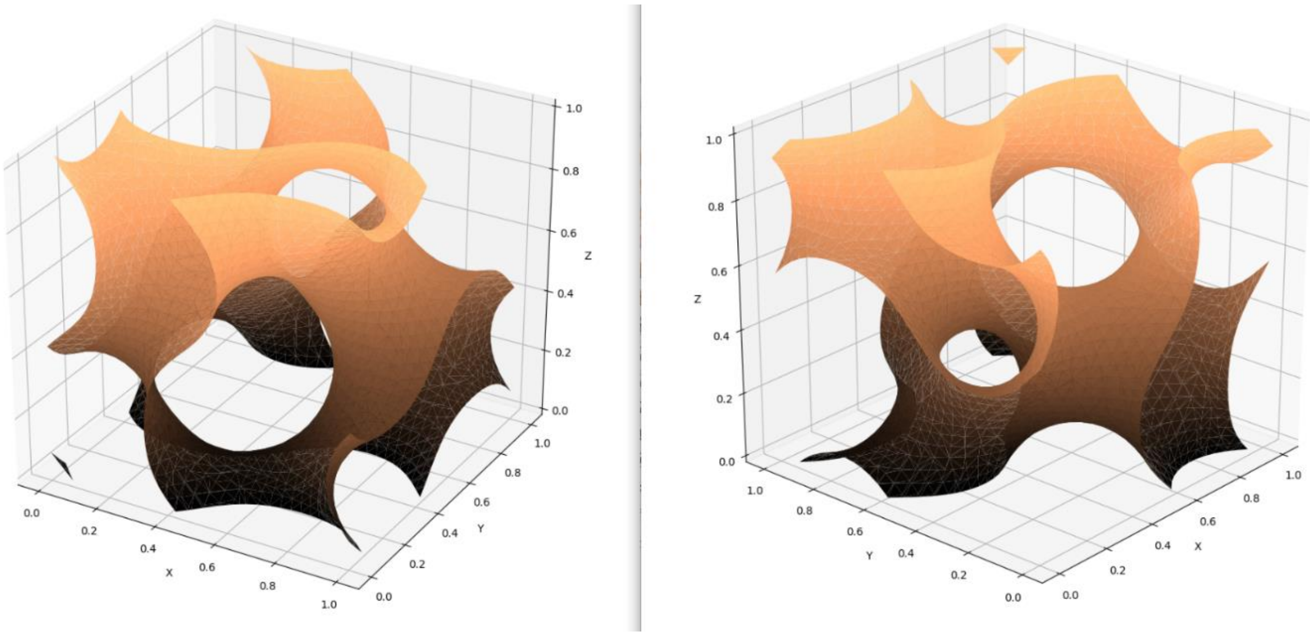

Figure 2.3. Gyroid surface as plotted in python for $t = 0.4476$ (left) and $t = -0.4476$ (right) in the domain $[0 - 2 * pi]$.

Once the .OBJ file is saved, it is imported in Autodesk Meshmixer software for some post-processing. The first step is to remesh the surface in order to improve and make more uniform the shape and the size of the triangles. There were some very small triangles and some elongated ones that could cause problems to the next steps of the numerical procedure. The second step is to export the file to .STL extension, which is the suitable file format to use for the upcoming steps.

By definition, in .STL (stereolithography) extension files the surfaces of the 3D models are represented by triangular facets, as they are in .OBJ files as well. The size and the geometry of the triangles affect the 3D model-surface accuracy, i.e. the smaller the facets, the higher the spatial resolution. Each facet is defined by a normal vector and the coordinates of the three nodes. .STL files are ‘’neutral’’ files and they can be exchanged among various CAD software [73].

Following the mesh correction, the .STL files that contain the two opposite TPMS are imported in the CAD environment of Salome Meca, version 9.3.0. for the conversion of the surfaces into solid unit cells. A 3D model of a cube is partitioned by the two surfaces by performing Boolean operations and thus, different-type unit cells are generated, i.e. a sheet and two skeletal unit cells. Figure 2.4. shows the two opposite surfaces in green and gold colors, the partition of the cube and the generated sheet (bronze color) and skeletal (blue color) unit cells as generated in Salome Meca software. It is noteworthy that in Figure 2.4.d) two small parts of the initial cube (on two corners) are added to the sheet unit cell to ensure the periodicity of the cell.

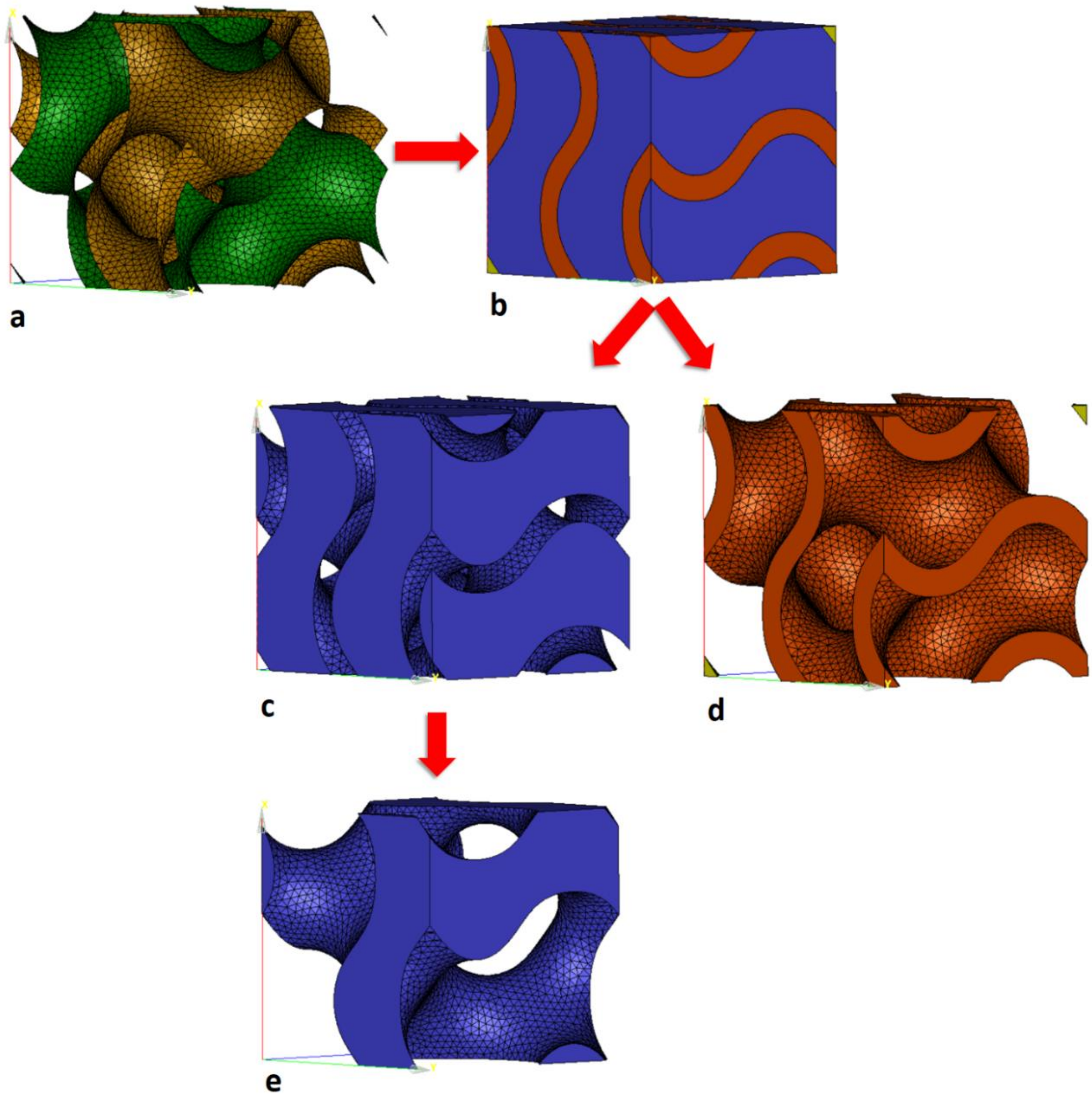

Figure 2.4. a) Two Gyroid unit cell surfaces with opposite offset, b) a cube partitioned by two opposite surfaces, c) two generated skeletal unit cells, d) a sheet unit cell (with two small parts on the corners to ensure periodicity), and e) a single skeletal unit cell in Salome Meca software.

Once the skeletal and sheet parts are generated, they are exported to both .STEP and .STL extensions from Salome Meca. Both file extensions are necessary for different purposes. The .STEP format is compatible for the finite element analysis software Abaqus and the numerical investigation while .STL is a compatible extension for the software used for the additive manufacturing process. Here, it is important to notice that the volume fraction of the unit cells varies according to the mathematical design of the initial surfaces. Specifically, the definition of the volume fraction of the unit cells is defined as:

$$Volume\ fraction = \frac{V_{solid}}{V_{total}} \tag{11}$$

where V_{solid} is the volume of the solid part and V_{total} is the volume of the bounding box. The complete list of all the investigated unit cell types in this study is presented in Table 2.1. and they are illustrated in Figure 2.5.

Strut-based unit cells	**TPMS-based unit cells**
Octet-truss	Gyroid sheet
Diagonal	Gyroid skeletal
	IWP sheet
	IWP skeletal internal
	Neovius
	Schoen's Primitive sheet
	Schoen's Primitive skeletal external
	Schoen's Primitive skeletal internal

Table 2.1.Complete list of all the investigated unit cell types in this study.

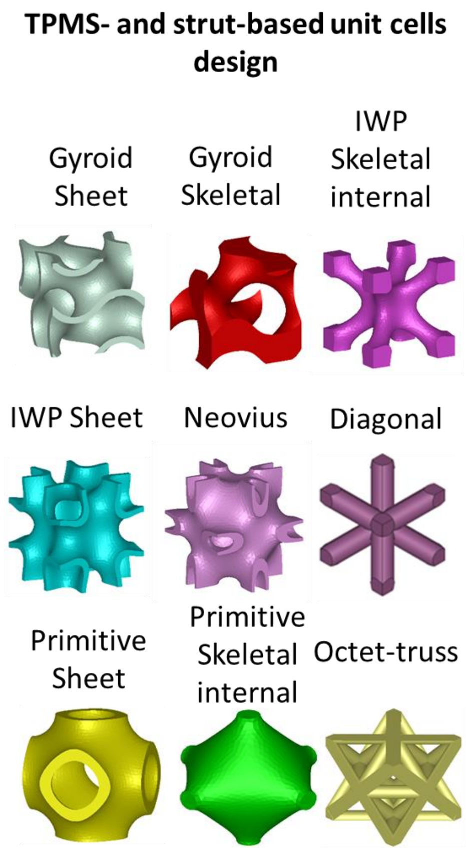

Figure 2.5. All numerically investigated unit cell topologies.

Once the design of all the lattice is complete, the numerical investigation follows. A .STEP file is imported in FEA software Abaqus for further pre-processing, and particularly for the generation of a FE-adapted mesh. A python script is developed for the import and the meshing of each unit cell in Abaqus and an .INP file is generated. This .INP file is further processed. A numerical periodic homogenization method is used and the first step is the application of the periodic boundary conditions on the unit cell. The complete methodology is described in detail in the following section.

2.3. Numerical Periodic Homogenization

A FE-compatible periodic homogenization method [74] is implemented on the lattice structures for accurately estimating their effective mechanical properties. The scale separation ($\bar{x} \gg x$) is necessary for the consideration of the unit cell as a representative part of the macroscopic homogenized material. In particular, the unit cell is the periodic part and with dimensions much smaller (x) compared to the macroscopic lattice ($\bar{x}$), it is henceforth referred to as Representative Volume Element (RVE). It represents then the microscopic scale of the problem. On the other hand, the lattices are periodic structures and they can comprise a great number of unit cell repetitions. They represent the macroscopic scale of the problem [75].

For the correct application of the periodic boundary conditions (PBC) the mesh of the RVE should be periodic. That means that for every node i on a boundary face of the RVE, another node j exists on the opposite face with the same relative position. The constraint driver method is used for the application of a displacement gradient to every pair of opposite nodes, i.e. node i and node j. This displacement gradient is connected to the macroscopic infinitesimal strain tensor, which is related to the constraint driver. The kinematic equation (12) is the complete expression of all the above described which are illustrated in Figure 2.6. More details about this method and application are available in [75].

$$u_i' = u_j' \iff u_i - u_j = \bar{\varepsilon} * \left(x_i - x_j\right) \quad \forall x \in \tag{12}$$

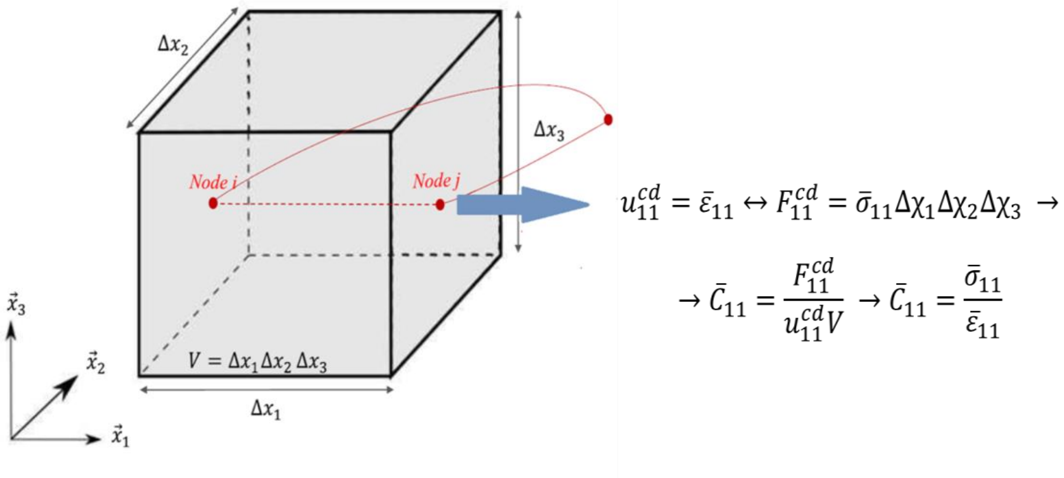

Figure 2.6. Constraint driver connection with the nodes of the cubic unit cell [76].

Moreover, considering the elastic regime, Hooke's law for the macroscopic material is $\bar{\sigma}_{kl} = \bar{C}_{klmn} * \bar{\varepsilon}_{mn}$, where $\bar{C}_{klmn}$ is the homogenized effective stiffness matrix, $\bar{\sigma}_{kl}$ the macroscopic effective stress tensor, and $\bar{\varepsilon}_{mn}$ the macroscopic effective strain tensor. The stress and strain tensors, as well as the elastic stiffness matrix, are symmetric tensors. Therefore, by using the Voigt notation to reduce their order, one could write the finally obtained relation $\bar{\sigma}_K = C_{KL} * \bar{\varepsilon}_L$. A linear perturbation method and six strain-controlled loading cases are implemented for every RVE. For each loading case, a component of the strain vector had the value 1, while the five remaining components are set equal to 0, according to equation (13).

$$\begin{bmatrix} \bar{\varepsilon}_{11} \\ \bar{\varepsilon}_{22} \\ \bar{\varepsilon}_{33} \\ \overline{2\varepsilon}_{12} \\ \overline{2\varepsilon}_{13} \\ \overline{2\varepsilon}_{23} \end{bmatrix} = \begin{bmatrix} 1 \\ 0 \\ 0 \\ 0 \\ 0 \\ 0 \end{bmatrix} \rightarrow \begin{bmatrix} \bar{\sigma}_{11} \\ \bar{\sigma}_{22} \\ \bar{\sigma}_{33} \\ \bar{\sigma}_{12} \\ \bar{\sigma}_{13} \\ \bar{\sigma}_{23} \end{bmatrix} \equiv \begin{bmatrix} C_{11} \\ C_{21} \\ C_{31} \\ C_{41} \\ C_{51} \\ C_{61} \end{bmatrix} \tag{13}$$

The values of the stress vector are calculated from the summation of the reaction forces (RF) on each face of the RVE divided by the effective surface of the corresponding surface in Abaqus. Therefore, the connection between the stiffness matrix and the stress tensor is obtained as indicated by equation (13). The result of each loading case is one column of the macroscopic stiffness tensor C_{KL}. By adding the columns of the remaining five loading cases, one obtains the complete macroscopic stiffness matrix, which is the assembly of the six computed columns.

Particularly, all the structures are triply periodic and thus, the stiffness matrix is cubic for all the investigated unit cells and volume fraction, no matter the topology. Therefore, only three independent parameters, C_{11}, C_{12}, C_{44} describe the elastic constitutive law for all the topologies, which can be obtained by only two loading cases, i.e. tension and shear. Equation (14) shows these two loading cases, respectively.

$$\begin{bmatrix}\bar{\varepsilon}_1\\\bar{\varepsilon}_2\\\bar{\varepsilon}_3\\\bar{\varepsilon}_4\\\bar{\varepsilon}_5\\\bar{\varepsilon}_6\end{bmatrix}=\begin{bmatrix}1\\0\\0\\0\\0\\0\end{bmatrix}\rightarrow\begin{bmatrix}\bar{\sigma}_1\\\bar{\sigma}_2\\\bar{\sigma}_3\\\bar{\sigma}_4\\\bar{\sigma}_5\\\bar{\sigma}_6\end{bmatrix}\equiv\begin{bmatrix}C_{11}\\C_{21}\\C_{12}\\0\\0\\0\end{bmatrix}, \qquad \begin{bmatrix}\bar{\varepsilon}_1\\\bar{\varepsilon}_2\\\bar{\varepsilon}_3\\\bar{\varepsilon}_4\\\bar{\varepsilon}_5\\\bar{\varepsilon}_6\end{bmatrix}=\begin{bmatrix}0\\0\\0\\1\\0\\0\end{bmatrix}\rightarrow\begin{bmatrix}\bar{\sigma}_1\\\bar{\sigma}_2\\\bar{\sigma}_3\\\bar{\sigma}_4\\\bar{\sigma}_5\\\bar{\sigma}_6\end{bmatrix}\equiv\begin{bmatrix}0\\0\\0\\C_{44}\\0\\0\end{bmatrix} \tag{14}$$

After the application of the periodic boundary conditions, the computation of the stiffness matrix and the overall apparent elastic properties of the unit cells are computed. The exact methodology is described in detail in the following section.

2.4. Effective mechanical properties of the unit cells

2.4.1. Brief introduction

A unit cell specific to medical applications should be generated by taking into consideration several parameters, namely the topology type, the volume fraction, and the bulk material properties. The problem is governed by all the aforementioned parameters that can be optimized. These parameters induce various effective mechanical properties, anisotropic response, and local stress distribution for every unit cell topology and consequently for the implants in which they are about to replace the internal compact part. The chart presented in Figure 2.7. shows the collected constraints and objectives of the present problem. The parameters taken into consideration are those in the boxes with the bold outline. The investigation is carried out in the elastic regime.

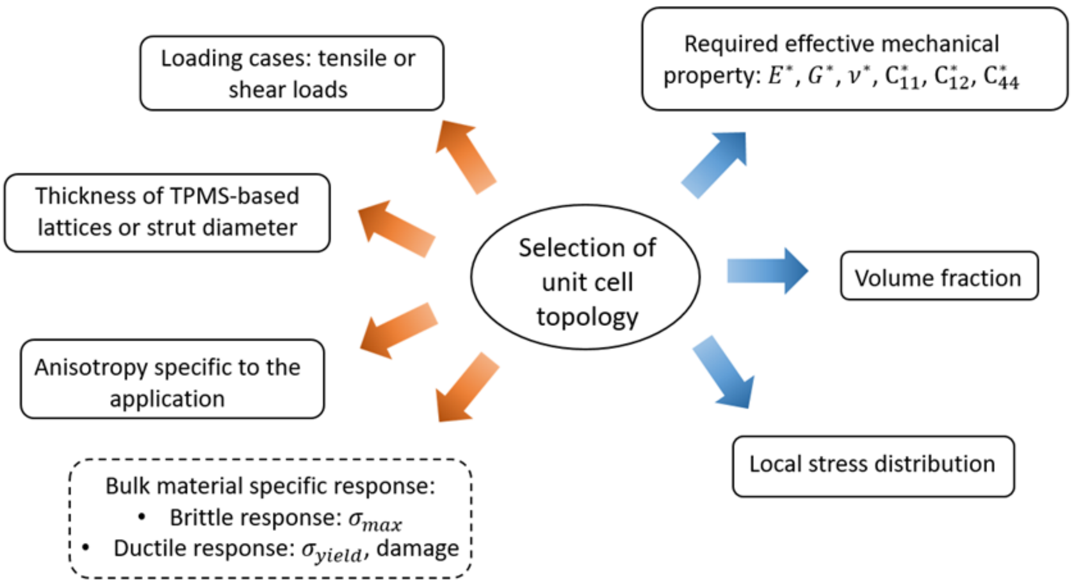

Figure 2.7. Constraints, in orange, and objectives, in blue color, or the problem to be addressed.

2.4.2. Cubic stiffness symmetry and equations for the computation of the effective mechanical properties

The computed macroscopic stiffness matrix for all the investigated unit cell topologies, both strut-based and TPMS-based ones, and with various volume fractions, presents a cubic symmetry. Therefore, the elastic constitutive law can be described by three independent parameters, C_{11}, C_{12}, and C_{44}. The general cubic stiffness matrix form for all the unit cells is indicated in equation (15).

$$C_{ij} = \begin{bmatrix} C_{11} & C_{12} & C_{12} & 0 & 0 & 0 \\ C_{12} & C_{11} & C_{12} & 0 & 0 & 0 \\ C_{12} & C_{12} & C_{11} & 0 & 0 & 0 \\ 0 & 0 & 0 & C_{44} & 0 & 0 \\ 0 & 0 & 0 & 0 & C_{44} & 0 \\ 0 & 0 & 0 & 0 & 0 & C_{44} \end{bmatrix} \tag{15}$$

The C_{11} and C_{12} components of the stiffness matrix are related to the tensile/compressive behavior of the unit cells, while the C_{44} component is related to the shear behavior. All the components of the macroscopic stiffness matrix are directly linked to the effective mechanical properties of the unit cells, such as the effective Young's modulus, E', effective Shear modulus, G', and effective Poisson's ration, ν'. The computation of the effective properties for all the cubic materials with various volume fractions is carried out according to the following equations [50]:

$$E' = \frac{C_{11}^2 + C_{11}C_{12} - 2C_{12}^2}{C_{11} + C_{12}} \tag{16}$$

$$G' = C_{44} \tag{17}$$

$$v' = \frac{C_{12}}{C_{11} + C_{12}} \tag{18}$$

Considering cubic symmetry, the degree of anisotropy of all the unit cells can be evaluated using an anisotropic ratio, the Zener's ratio, Z [48], [50], which is related to the components of the stiffness matrix, C_{11}, C_{12}, and C_{44} with the following relation:

$$Z = \frac{2 * C_{44}}{C_{11} - C_{12}} \tag{19}$$

When $Z = 1$, one can easily notice that $C_{44} = (C_{11} - C_{12})/2$. This is the case of an isotropic media. In our case of TPMS-based unit cells, it means that a unit cell exhibits an isotropic behaviour. $Z > 1$ means that the $2 * C_{44}$ is the predominant part of the equation, whereas $Z < 1$ means that the $C_{11} - C_{12}$ is the predominant part [50], [51].

The charts with the comparison of all the aforementioned effective properties and the Zener ratio for all the investigated topologies and volume fractions are presented and discussed in the following section. It is important to note that the mesh is generated by employing three-dimensional tetrahedral quadratic elements C3D10 in Abaqus. More details about the meshing of the structures are given in section 2.5. Moreover, the material properties used for the numerical analysis in Abaqus correspond to the material properties of the Ti-6Al-4V alloy, i.e. $E = 110\ GPa$ and $v = 0.3$. In the end, all the effective properties are normalized by the elastic modulus of the Ti-6Al-4V alloy and then, they are presented in the charts. This is performed to generate versatile and structure-dependent charts that can be a useful tool to a lattice designer, no matter the material properties.

2.4.3. Results, comparison, and analysis

In this section, all the numerical results regarding the computed effective mechanical properties of the investigated unit cells are presented. It is important to remind that the computation of the elastic properties is carried out according to the independent components of the stiffness matrices after the application of 6 loading cases. The later can be reduced to 2 loading cases, i.e. tension and shear, as have been explained previously. The section presents the effective mechanical properties variation by topology and isovalue t, the effective mechanical properties variation by topology and then the volume fraction followed by the study of the anisotropic behavior of the unit cells.

2.4.3.1. Mechanical properties variation by topology and design parameter, t

As the TPMS-based unit cells are designed by using initially the equation (1), the isovalue, t, or the so-called TPMS design parameter has a direct effect on the volume fraction and all the effective mechanical properties of the unit cells. Figure 2.8. illustrates the influence of t, on various computed effective properties of the unit cells, namely Young's modulus, Shear modulus, C_{11}^*, and C_{12}^* elastic components, without being necessary to compute the volume fraction of the unit cells. The Shear modulus is equal to the C_{44}^* elastic component as determined by equation (17) and thus, there is no reason to present the corresponding chart for the C_{44}^* component. All the properties have been normalized by dividing them by the elastic modulus of the bulk material, i.e. $E' = 110\ GPa$. This is performed to focus only on the influence of the topology, regardless of the material properties.

a)

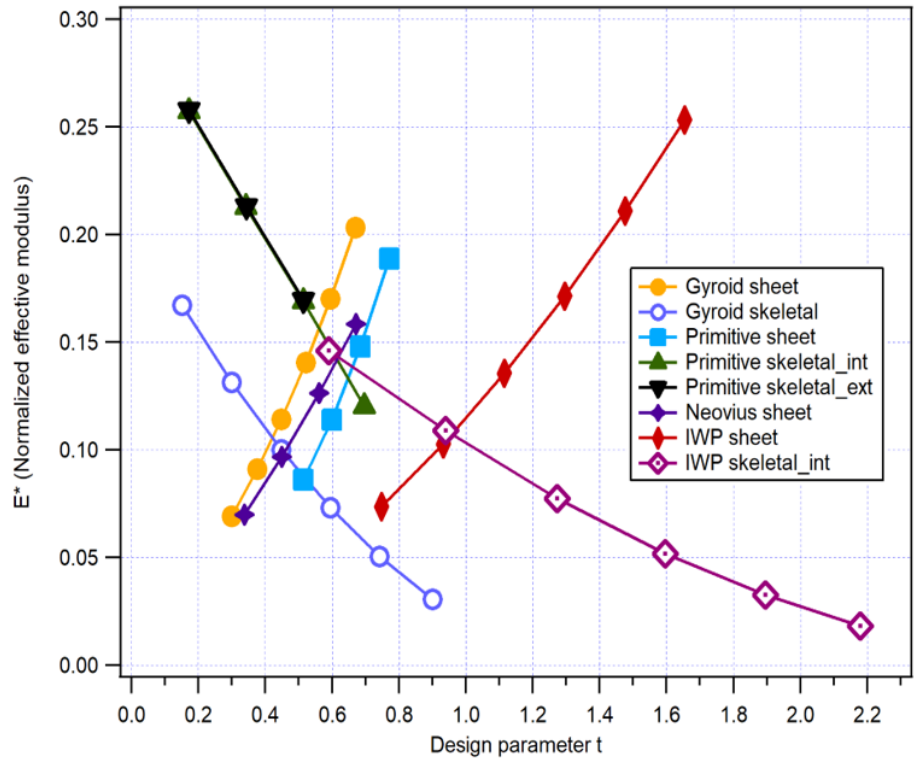

E* (Normalized effective modulus)
Design parameter t
Gyroid sheet
Gyroid skeletal
Primitive sheet
Primitive skeletal_int
Primitive skeletal_ext
Neovius sheet
IWP sheet
IWP skeletal_int
0.00
0.05
0.10
0.15
0.20
0.25
0.30
0.0
0.2
0.4
0.6
0.8
1.0
1.2
1.4
1.6
1.8
2.0
2.2

b)

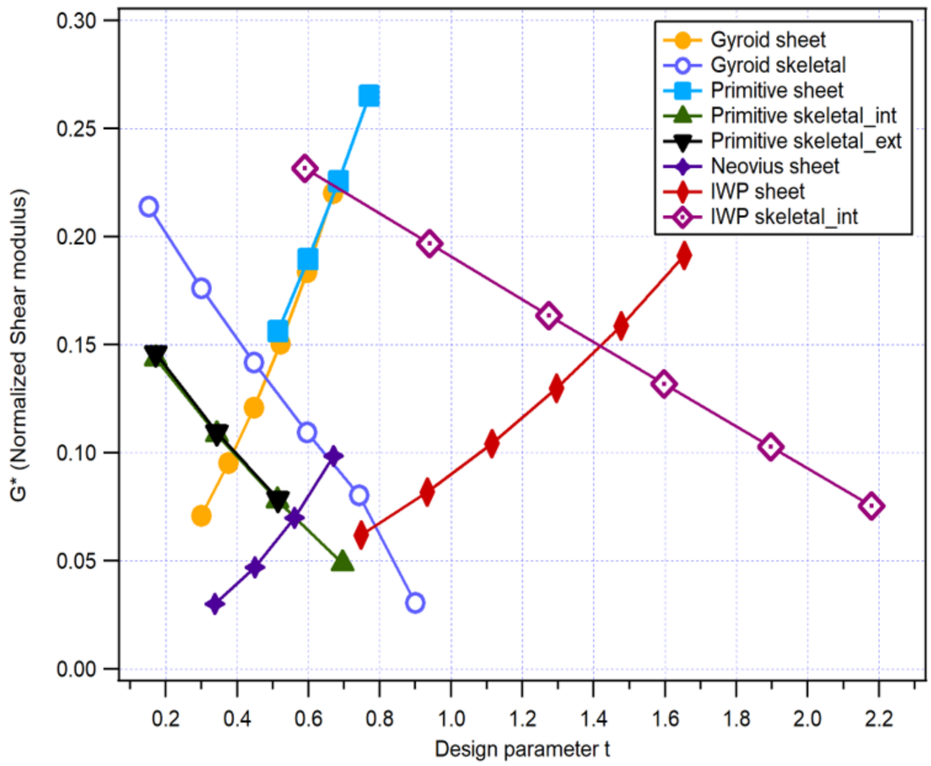

G* (Normalized Shear modulus)
Design parameter t
Gyroid sheet
Gyroid skeletal
Primitive sheet
Primitive skeletal_int
Primitive skeletal_ext
Neovius sheet
IWP sheet
IWP skeletal_int
0.00
0.05
0.10
0.15
0.20
0.25
0.30
0.2
0.4
0.6
0.8
1.0
1.2
1.4
1.6
1.8
2.0
2.2

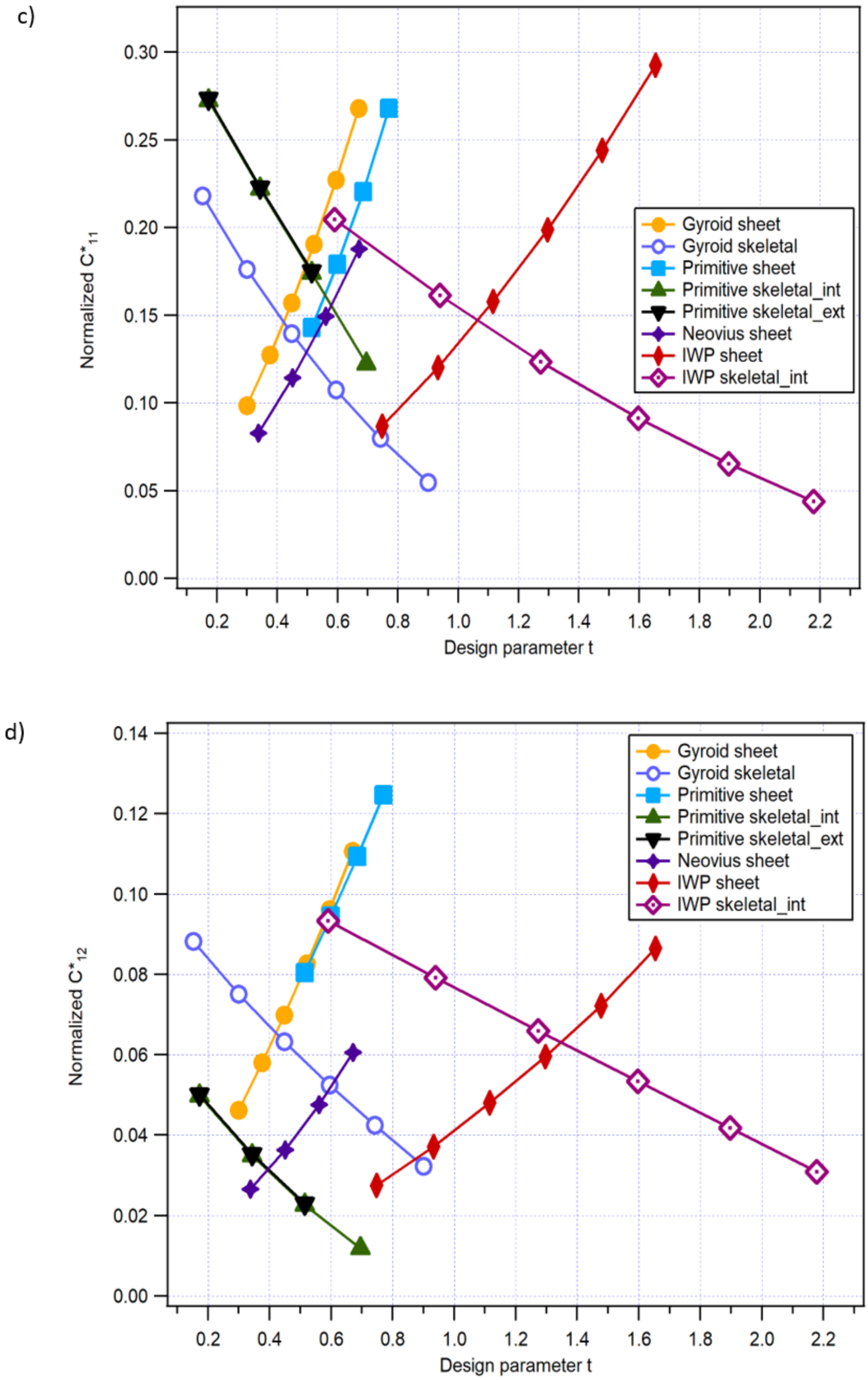

Figure 2.8. The design parameter, t, directly linked to the normalized effective values of the a) Young’s modulus, b) Shear modulus, c) C_{11}^{*}, and d) C_{12}^{*} elastic components.

The trend and the slope of the curves vary according to the topology. However, the trend of the curves for each topology is the same for all the investigated properties. In some cases, such as for Gyroid skeletal topology, the curve tends to evolve downward as the isovalue is getting larger and thus, the corresponding effective mechanical property is getting lower. In some other cases, such as for the IWP sheet topology, the curve tends to evolve upward as the isovalue is getting lower and thus, the corresponding effective mechanical property is getting larger.

The latter fact indicates that the isovalue magnitude affects in a different way the mechanical properties of the various unit cells topologies. Particularly, the curves for all the sheet topologies evolve upward and for all the skeletal ones downward. This is explained by the fact that the sheet and skeletal unit cells are complementary (see Figure 2.4.) and their mechanical properties evolve exactly in the opposite way. The isovalue t corresponds to the distance between the two initial surfaces, between of which the sheet unit cell is generated. The higher the t the larger is the volume fraction of the sheet unit cell and thus, the corresponding mechanical property. On the contrary, the higher the t, the lower is the volume fraction of the skeletal unit cells and thus, the corresponding mechanical properties. The charts presented in Figure 2.8. are very useful for a lattice designer because they lead to the acceleration of the design process according to specific mechanical requirements.

2.4.3.2. Mechanical properties variation by topology and volume fraction

The apparent mechanical properties and anisotropic behaviour at various volume fraction levels are investigated to identify the range and evolution of the mechanical properties per topology and to analyze them. The volume fraction is computed according to equation (11). The Figure 2.9. illustrates the relationship between the normalized mechanical properties and the volume fractions of the studied unit cells. All the mechanical properties of the unit cells have been normalized to focus only on the influence of the topology, regardless of the material properties. Moreover, some numerical results for a couple of topologies are taken from the literature regarding their apparent elastic modulus and they are added to Figure 2.9.) a) for comparison and validation of our results.

a)

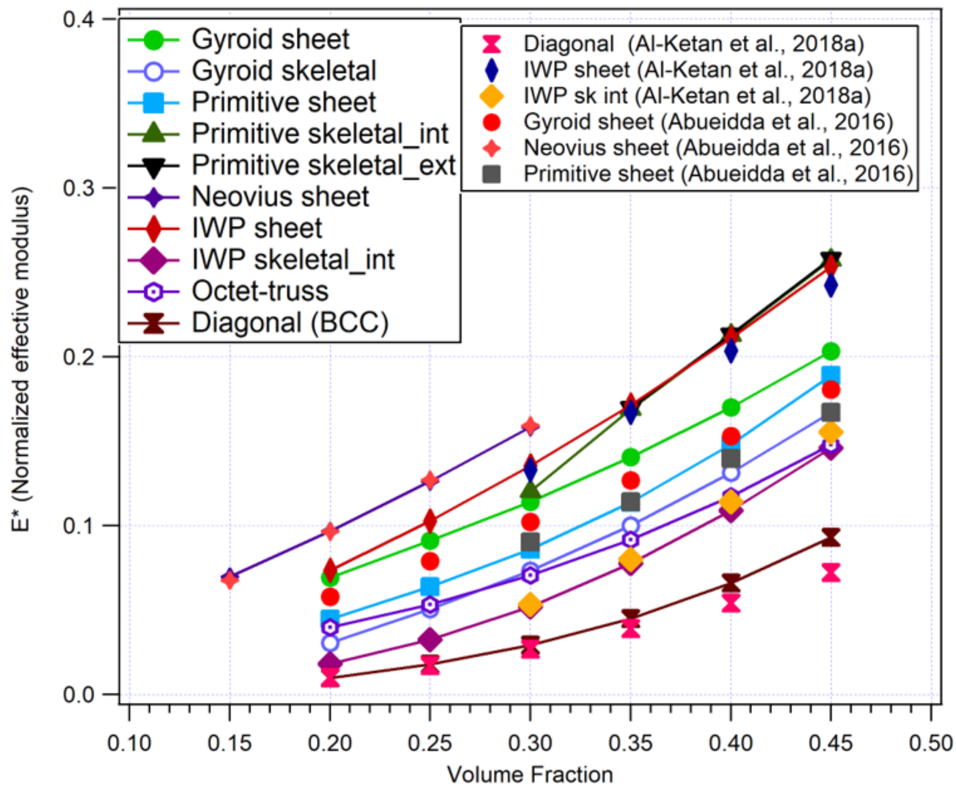

Gyroid sheet
Gyroid skeletal
Primitive sheet
Primitive skeletal_int
Primitive skeletal_ext
Neovius sheet
IWP sheet
IWP skeletal_int
Octet-truss
Diagonal (BCC)
Diagonal (Al-Ketan et al., 2018a)
IWP sheet (Al-Ketan et al., 2018a)
IWP sk int (Al-Ketan et al., 2018a)
Gyroid sheet (Abueidda et al., 2016)
Neovius sheet (Abueidda et al., 2016)
Primitive sheet (Abueidda et al., 2016)
E* (Normalized effective modulus)
Volume Fraction

b)

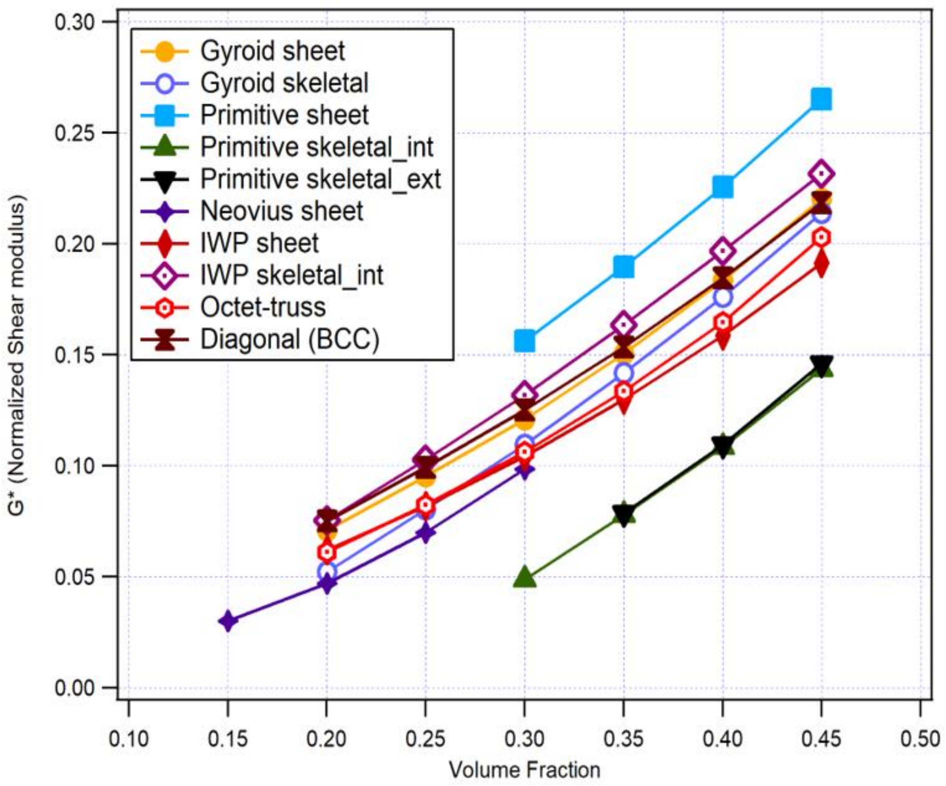

Gyroid sheet
Gyroid skeletal
Primitive sheet
Primitive skeletal_int
Primitive skeletal_ext
Neovius sheet
IWP sheet
IWP skeletal_int
Octet-truss
Diagonal (BCC)
G* (Normalized Shear modulus)
Volume Fraction

c)

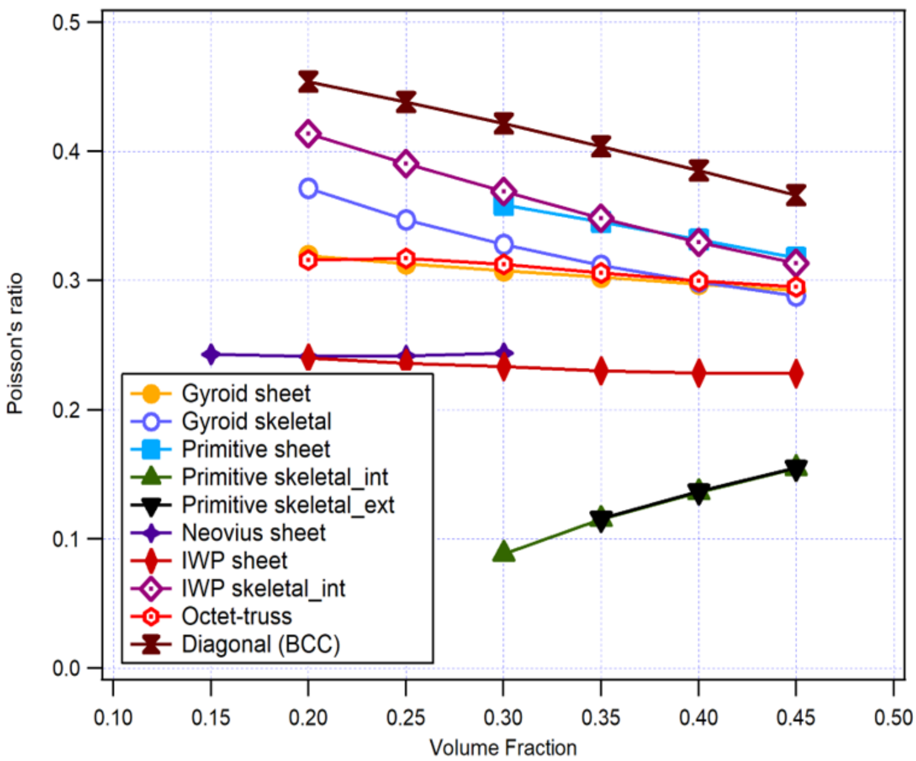

Figure 2.9. The effective normalized a) Young's modulus, b) shear modulus, and c) Poisson's ratio versus the volume fraction of the unit cells are presented for the studied TPMS-based and strut-based unit topologies indicated in the legend.

One can observe the evolution of the effective Young's modulus in Figure 2.9 a) and shear modulus in Figure 2.9. b) which is different for each type of topology. The slopes of the curves for all the topologies for both the E^* and G^* do not however exhibit large differences. Particularly, the slopes of the curves for the E^* exhibit a higher heterogeneity than those for the G^*; for example, Gyroid skeletal curve exhibits a steeper slope for the E^* compared to the Octet-truss curve. This means that for the same volume fraction increase, the E^* increase is higher for the Gyroid skeletal than for the Octet-truss topology. Therefore, the volume fraction increase does not have the same impact on the apparent elastic modulus increase. Moreover, the G^*-values gap is narrower compared to the E^*-values gap, namely, the G^*-values gap is 0.12 units approximately, while the maximum the E^*-values gap is 0.17. This means that a larger range of elastic modulus can be satisfied by a particular volume fraction of various topologies compared to the range of the shear modulus.

Figure 2.9. c) shows the computed Poisson's ratio of the unit cells and how is it affected by the topology and the volume fraction. Some topologies, such as Gyroid skeletal and Primitive

sheet, are highly sensitive to the changes of the volume fraction. On the contrary, Neovius sheet and IWP sheet topologies exhibit a quasi-constant Poisson's ratio.

By using the results above and by applying the mechanical properties of a commonly used titanium alloy for biomechanical applications, i.e. Ti-6Al-4V, to the normalized values, the apparent elastic modulus, and the density of the unit cells are being computed numerically in Abaqus [43]. Then, the computed values are placed on an Ashby chart (pink bubble) with other materials as references. In Figure 2.10. the Ashby chart with the TPMS-based lattices with Ti-6Al-4V properties and the cortical bone values range is presented. By performing this, one could get a visual comparison of the Young's modulus and density of the TPMS-based unit cells to other materials' properties. Moreover, the target to be reached, i.e. to mimic the cortical bone values by using lattices, is presented in bright yellow color on the chart.

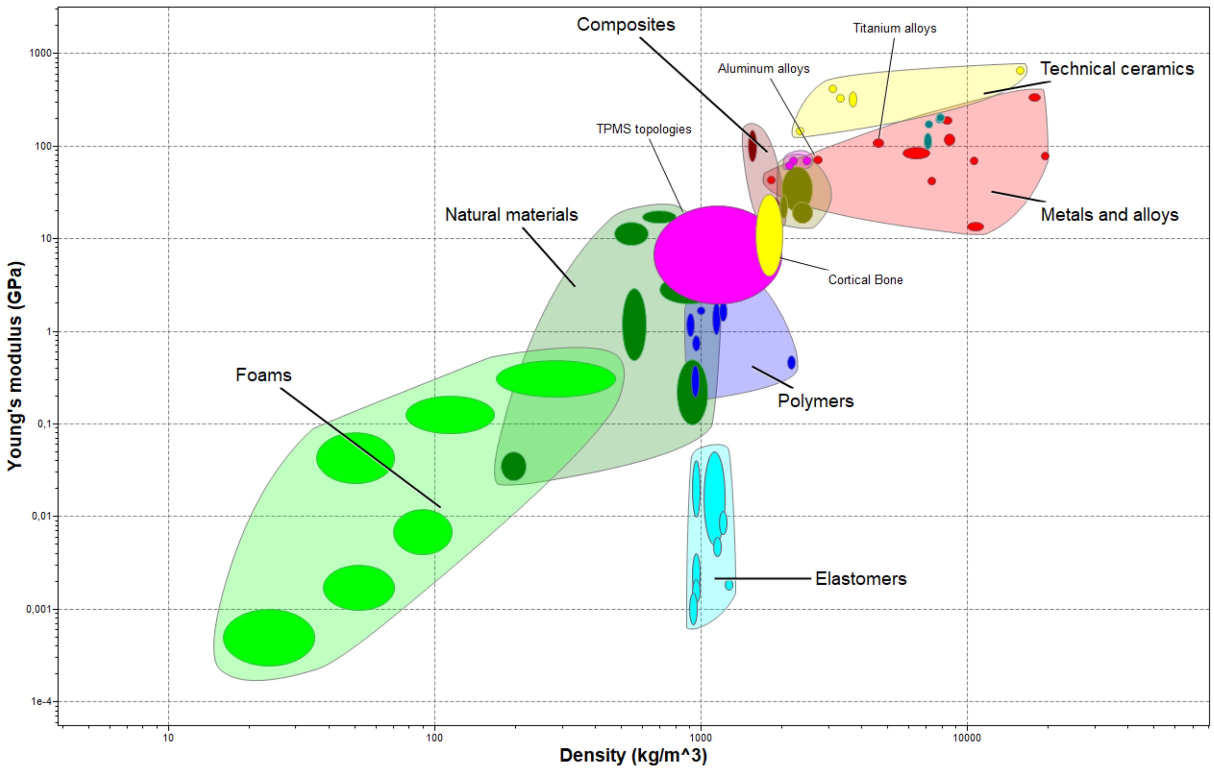

Figure 2.10. An Ashby chart with the Young's modulus and density of the studied topologies by applying the mechanical properties of Ti-6Al-4V in Abaqus (pink bubble) and the target to be reached, the cortical bone (yellow bubble).

2.4.3.3. Comparison of the anisotropy of the unit cells

Topology-induced anisotropy is also an important feature in the effort of designing mechanically compatible implants. Lattice structures present anisotropic behavior unlike the structures with a continuous distribution of material [14]. From the evaluation of the stiffness matrix, the cubic symmetry of all the mesostructures numerically simulated is verified and the three independent elastic components extracted. The cubic anisotropy is further investigated using the Zener ratio (see equation (19)). The Zener ratio for all the investigated structures is computed and compared to highlight the impact of one topology selection on the anisotropic response. Figure 2.11. shows the Zener ratio evolution for all the investigated types of unit cells with various volume fractions.

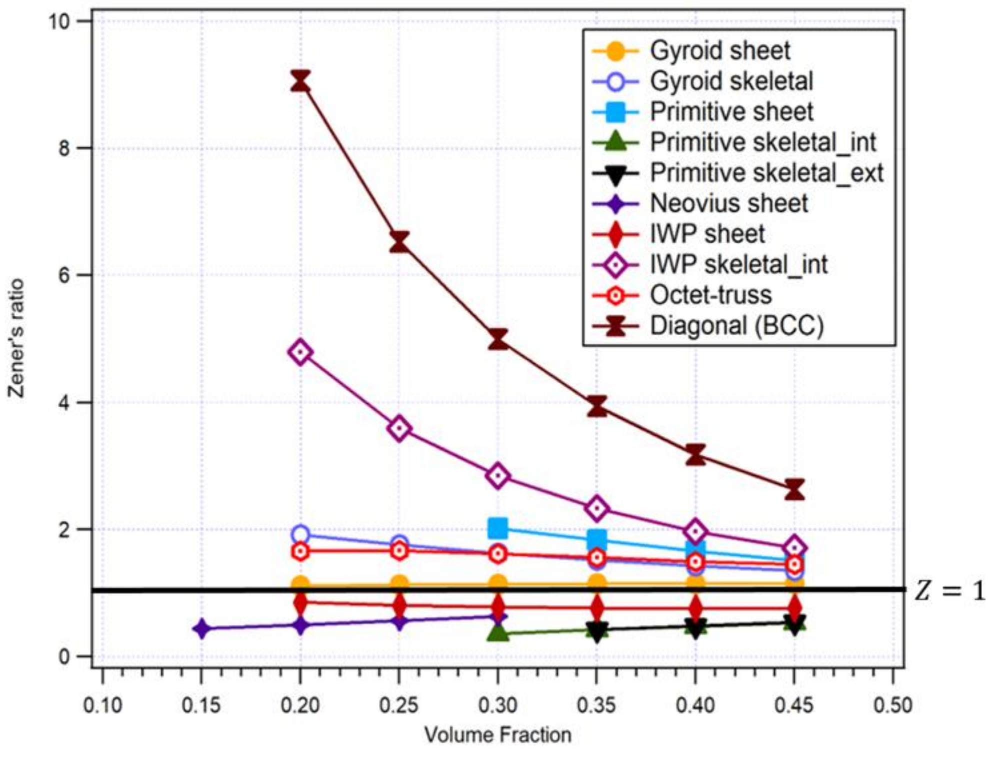

Figure 2.11. Evolution of the Zener ratio for all the investigated types of unit cells with several volume fractions.

Firstly, the Zener ratio for the majority of the topologies tends to unity with the increase in the volume fraction of the unit cells. As mentioned before, $Z = 1$ corresponds to an isotropic response of a unit cell. Indeed, the unit cells tend to be bulk cubes when their volume fraction increases, and thus, their behavior is getting closer to isotropy. Secondly, the Gyroid sheet and IWP sheet structures do not present any anisotropic behavior. Their Zener ratios are almost constant and close to one. Therefore, these two structures can be used in an application that requires isotropic behavior.

A third observation has to do with the most anisotropic unit cell type, which is the Diagonal topology. Figure 2.11. also demonstrates that the anisotropy of the Diagonal unit cell is highly dependent on its volume fraction. At low volume fractions, the anisotropy of the unit cell is considerably larger than at high volume fractions. The lattice tends to exhibit an isotropic response only at very high volume fractions. This means that the advantages of the pores and an isotropic response of the Diagonal structure cannot occur at the same time [77]. Then, a fourth observation is a high difference between the levels of anisotropy for the Diagonal and IWP skeletal internal structures, even though these two structures possess the same BCC configuration. Their topologies are similar; the only geometric difference is the smoother connections of the IWP skeletal internal unit cell compared to the abrupt connections of the Diagonal topology. These two topologies are illustrated in Figure 2.12. to remind of the geometric difference between them. A fifth observation is that some topologies exhibit $Z > 1$ and some other $Z < 1$. When the target is an isotropic response either a lattice with $Z = 1$ can be employed or a combination of two structures with $Z > 1$ and $Z < 1$ each one [77], [78].

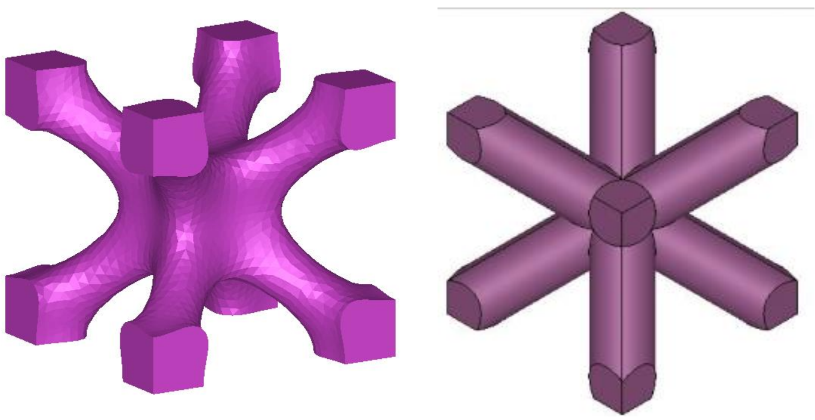

Figure 2.12. IWP skeletal internal unit cell (left) and Diagonal unit cell (right).

The next section presents the meshing process and all the results concerning the mesh sensitivity analyses conducted.

2.5. The meshing of the unit cells and mesh sensitivity analysis

In both cases of the strut-based and the TPMS-based lattices, the mesh of the unit cells is generated in Abaqus. Three-dimensional tetrahedral quadratic elements C3D10 are systematically adopted for the sake of comparing the final numerical results for the different types of studied unit cells. Figure 2.13. exhibits a TPMS-based and a strut-based unit cell as meshed in Abaqus, namely Gyroid sheet and Octet-truss topologies.

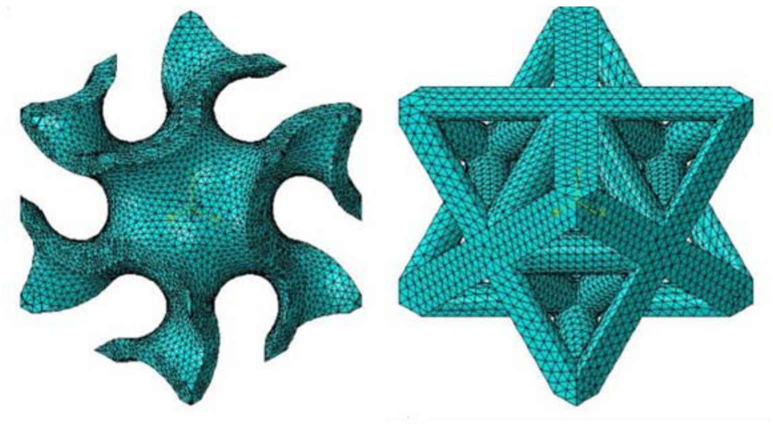

Figure 2.13. Gyroid sheet and Octet-truss unit cells as meshed with tetrahedral elements in Abaqus software.

A mesh size investigation is carried out for all the lattice types to ensure the numerical convergence results, their reliability, and mesh independence. Particularly, a mesh size convergence of all the effective elastic constants of the stiffness matrix and the above computed mechanical properties of the unit cells is reached, i.e. C_{11}, C_{12}, C_{44}, E', G', and ν'. For the sake of brevity and as the convergence has been reached for all the topologies and their mechanical properties, in Figure 2.14. only the mesh sensitivity analysis for the normalized Young's modulus of various unit cells is presented. It is obvious that the global size of the seeds for the generation of the mesh, and consequently the mesh size, does not affect the computed Young's modulus of the unit cells, which remains constant for all the investigated topologies.

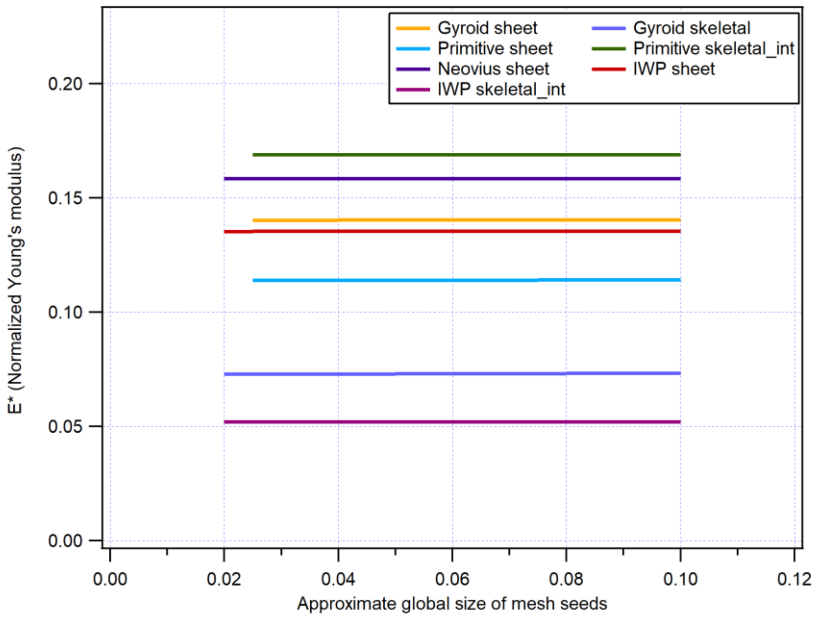

Figure 2.14. The FE mesh convergence for the normalized Young's modulus, E', of various unit cells has been reached.

Moreover, a mesh sensitivity analysis is carried out for the local stress distribution of the studied topologies. The first step is the comparison of the local stress on the centroid and the average stress on the four integration points. The results are presented in Figure 2.15.

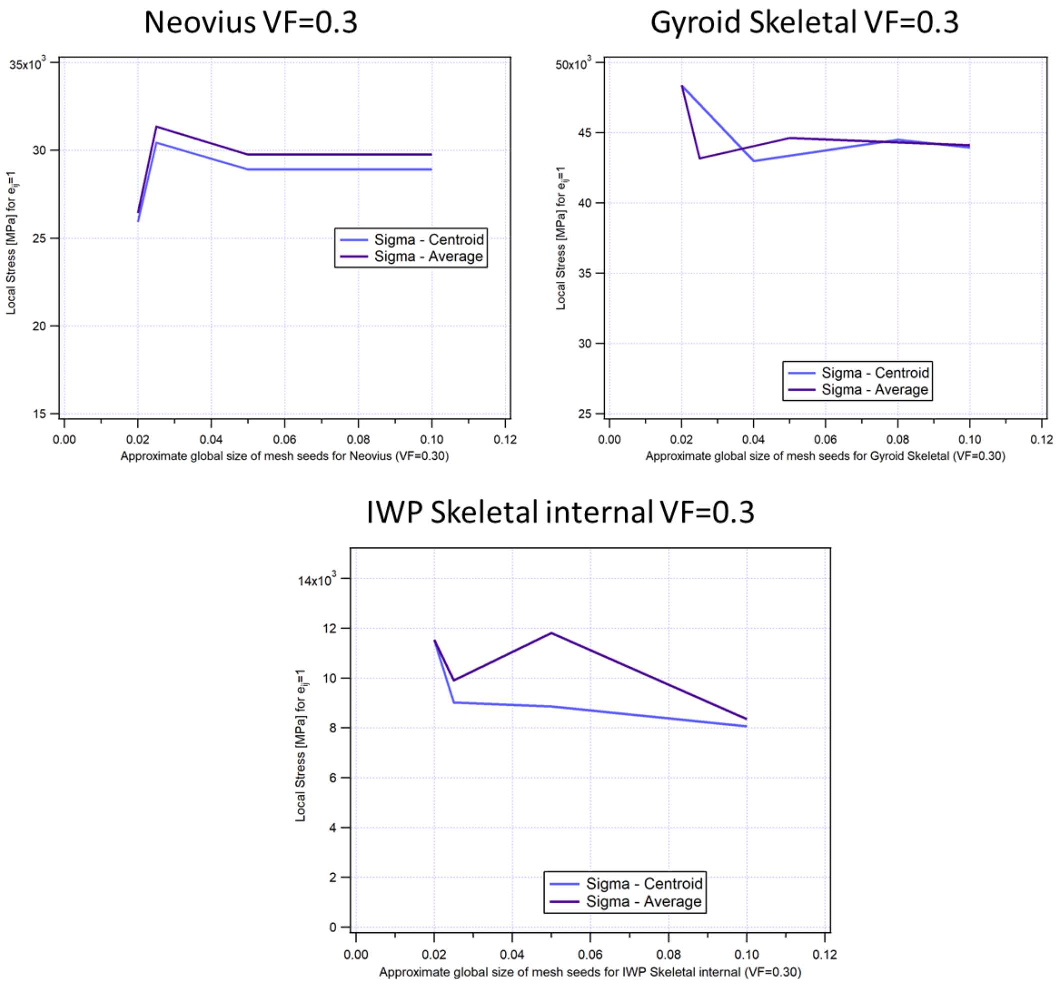

Figure 2.15. Mesh sensitivity analysis for both local stress on the centroid and the average stress on the four integration points.

As can be observed in Figure 2.15., the local stress on the centroid and the average stress on the four integration points trends are not always identical. Even though both local stress values vary slightly, the mesh size does not have any influence on the elastic constants of the unit cells (see Figure 2.14), and this is the most important result. Therefore, the local stress on the centroid is chosen to investigate the stress distribution of various topologies. The methodology and the results are presented in the next section.

2.6. Local stress distribution on unit cells

2.6.1. Introduction

The local stress distribution is another important feature to take into consideration when designing architectured implants, which are required to present good high cycle fatigue. Fatigue resistance and related durability are necessary for medical implants to avoid a postoperative failure, especially for young patients and thus the impact of stress concentrations is investigated in the lattices [14].

The first step is the design of the TPMS-based and strut-based unit cells. The second step is the investigation of their effective elastic properties and constants. Once all those steps are over, the investigation and analysis of the local stress distribution in the lattices follows. The local stress distribution in the elastic region of all the investigated unit cells is computed and quantitative analysis is carried out. The statistical results are presented and discussed in detail in this section in order to identify the most homogenized and suitable stress distribution, which is the target. A homogenized stress distribution indicates that no areas of the unit cell are subjected to extremely low or high stresses; two undesirable cases, especially when it comes to unit cells and lattices for biomechanical applications. High stresses can lead the lattice structure to exhibit a low or poor fatigue resistance. Otherwise, the parts of the unit cell that are subjected to very low stresses consist of a useless amount of material from a mechanical point of view, which increases the weight of the implant with no real benefits.

In the next three sub-sections, the following results are presented and discussed: first, the stress distribution in various unit cell topologies for two loading cases and various volume fractions, second, the local stress distributions in various unit cells in an ‘’iso-volume fraction’’ case, and third, the local stress distributions in various unit cells in an ‘’iso-elasticity’’ case. The first part of the study provides stress distribution results that determine any loading case and volume fraction dependency. The second and third parts of the study present actually the same method but for two different initial requirements, either volume fraction or elasticity. More details are given in the relevant sub-sections.

2.6.2. Loading case and volume fraction sensitivity analysis

Since the unit cells as parts of the lattices and implants are subjected locally to complex loads, the response of the unit cells in many loading cases should be investigated and analyzed. The local stress distribution is computed for both loading cases, i.e. tension and shear loads. The unit cell topologies under these two loads have been studied numerically in a quantitative way in this study. Figure 2.16. shows the local stress distribution results in these two loading cases over the population of finite elements for several studied unit cell topologies. The population of finite elements is expressed by:

$$N_{stress}/N_{total} \tag{20}$$

where N_{stress} is the number of finite elements that are subjected to a specific stress, and N_{total} is the total number of finite elements for each 3D model. Particularly, the charts that correspond to a specific topology in the two loading cases are illustrated in each horizontal level of Figure 2.16; the results for the tensile load at the left and the shear load at the right. Moreover, unit cells at various volume fraction levels have been studied to compare the results for the same topology and loading case but with different relative densities. The local stresses at every material point are normalized and distributed over the range $0-1$ for an easier comparison of the curves. The investigated unit cell topologies are the Gyroid skeletal, Primitive sheet, Neovius sheet, and IWP skeletal internal.

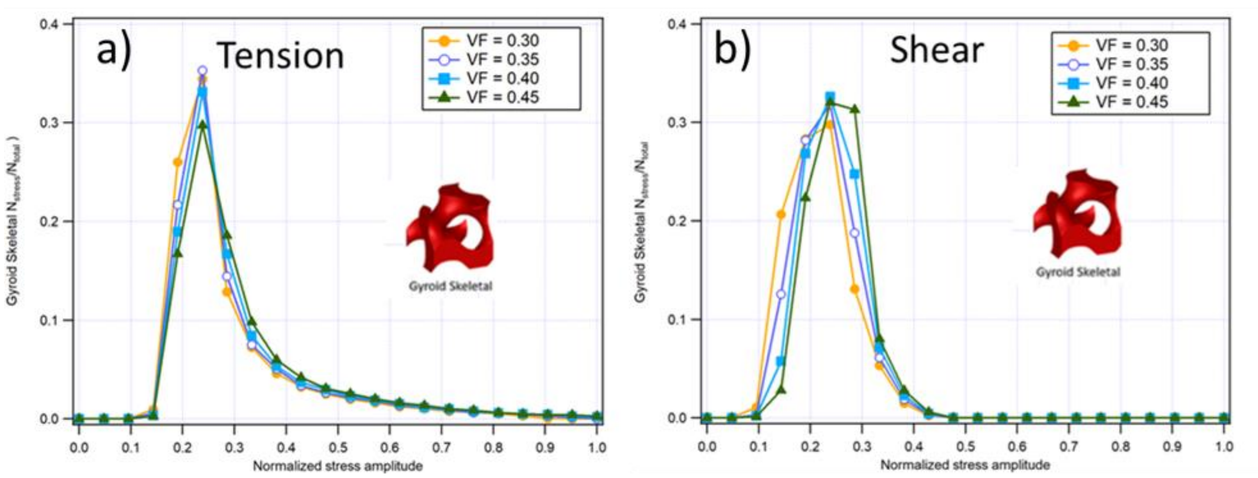

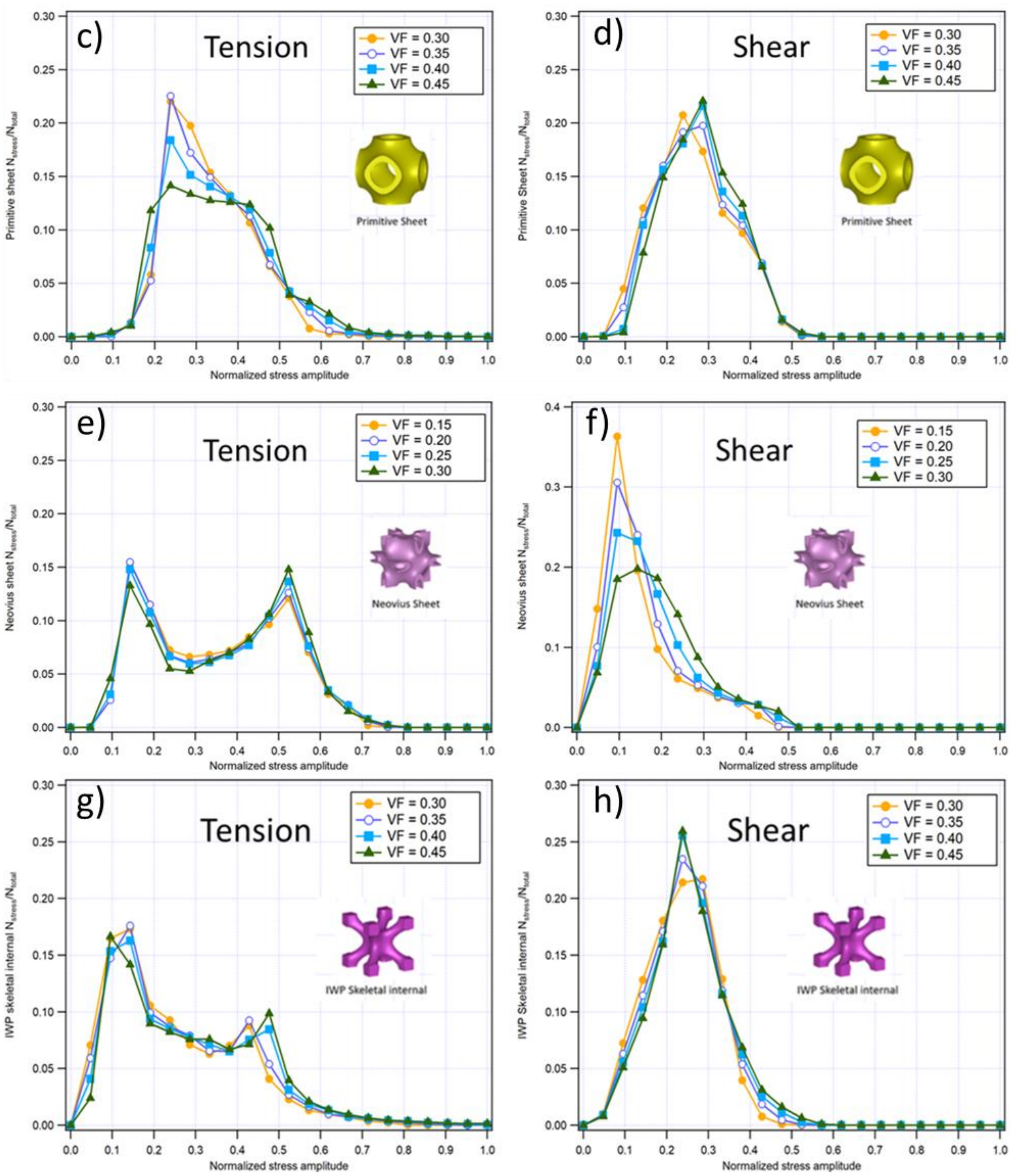

Figure 2.16. Distribution of the normalized local stresses over the range $0 - 1$ of a)-b) Gyroid skeletal, c)-d) Primitive sheet, e)-f) Neovius sheet, and g)-h) IWP skeletal internal unit cells for both loading cases, tensile and shear load.

Figure 2.16 a), c), e), g) exhibit the local stress distributions for a tensile load per topology and b), d), f), and h) exhibit the distributions for a shear load. The most suitable topology would be the one that exhibits a homogenized local stress distribution on all the elements for both loading cases. This means that if all the elements of a unit cell were subjected to a uniform stress value in both loading cases, this would be the most suitable topology to select. Each topology presents a different stress distribution for every loading case and the majority of the distributions are not sensitive to the changes in the volume fraction. Only the Primitive sheet is slightly sensitive to volume fraction changes for a tensile load and Neovius sheet topology for a shear load as shown in Figure 2.16. c), and f), respectively. Moreover, the majority of the local stress distributions exhibit approximately a normal distribution, apart from Neovius topology for a tensile load in e), and IWP skeletal internal topology for a tensile load in g). This means that a large group of finite elements is subjected to two different stress ranges.

2.6.3. Local stress distribution in an iso-volume fraction case

Since the volume fraction independence has been validated and the difference of the local stress distributions between the tensile and shear loads has been shown in the previous section, the tensile loading case is selected and only one volume fraction as well. The selected volume fraction is arbitrary and it is set as 0.30 for the study in this section. The target is to compare the local stress distributions of various unit cell topologies at the same volume fraction level, which is determined just before. By performing this study and the analysis of the results, we could select the most suitable topology among all the investigated ones, according to the most homogenized stress distribution, while a requirement of a particular relative density level is satisfied.

Figure 2.17. shows the local stress distribution of various unit cell topologies at the same volume fraction of 0.30 for a tensile loading case. The stress at every material point is computed for the unit cells and the stress values are distributed over the range $0 - 1$. Axis y denotes the number of the elements that are subjected to specific stress values over the population of elements for each model (see Equation (20)). For the sake of clarity, the results are split and presented in two separated graphs, i.e. Figure 2.17 a) and b). The Gyroid skeletal structure is set as the reference lattice type and it is presented on both graphs to compare all the unit cells results. Then, a statistical analysis of the results is carried out to highlight the suitable topologies by using the weighted arithmetic mean and weighted standard deviation of the sample.

In addition, Table 2.2. presents the weighted arithmetic mean and weighted standard deviation SD of the investigated normalized local stress distributions to identify the optimal structure with the most homogenized distribution. The weighted arithmetic mean is an indicator of the apparent elastic modulus of the unit cells; the higher the arithmetic mean value the higher the elastic modulus of the unit cell. Moreover, the standard deviation is an indicator of the apparent σ_{max} of the unit cells; taking into account that the bulk material properties are the same for all the topologies, some elements of the unit cells with a high standard deviation are subjected to higher stresses compared to those of the unit cells with a low standard deviation. This means that the apparent σ_{max} is closer to their apparent σ_{yield} and thus, closer to plastic deformation of the unit cell.

a)

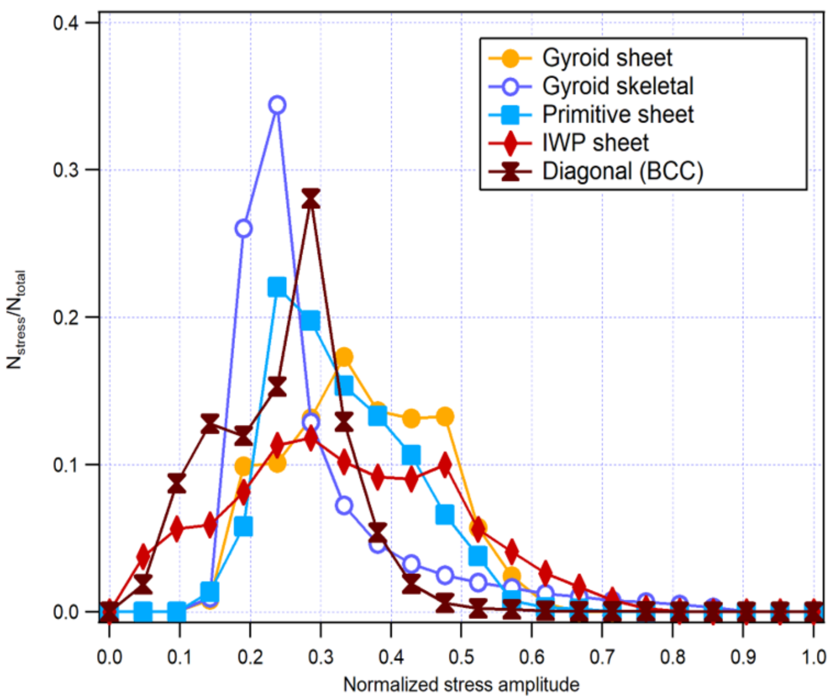

b)

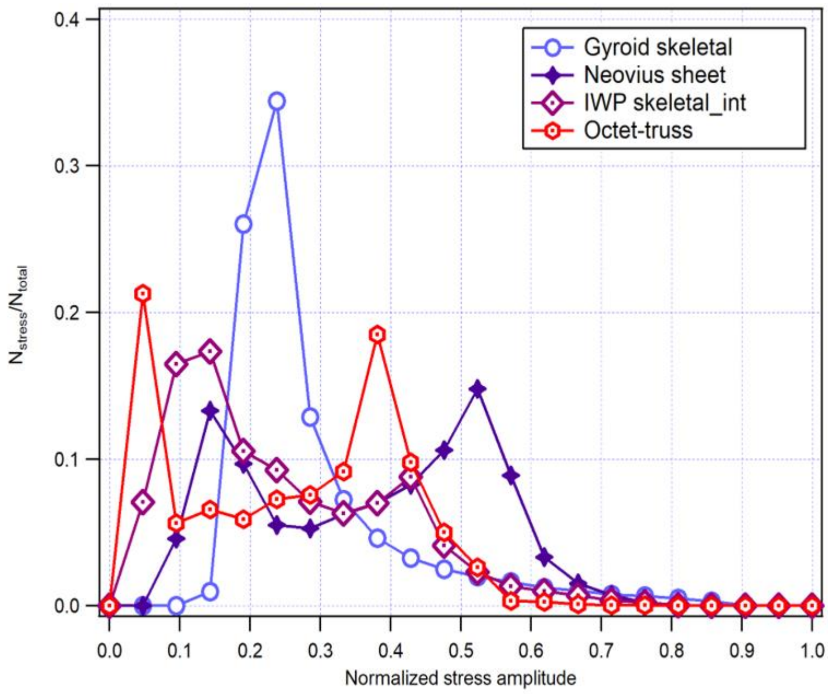

Figure 2.17. Normalized local stress distribution of various unit cells at the same volume fraction of 0.30. The results are split into two separate graphs for easy comparison.

	Weighted arithmetic mean	Weighted SD
Gyroid sheet	0.358	0.105
Gyroid skeletal	0.289	0.127
Primitive sheet	0.329	0.095
IWP sheet	0.335	0.157
Diagonal	0.245	0.093
Neovius sheet	0.370	0.209
IWP skeletal Int	0.246	0.152
Octet-truss	0.260	0.154

Table 2.2. The table summarizes the weighted arithmetic mean and weighted standard deviation of the investigated normalized local stress distributions.

In Figure 2.17. b), one can observe that the Octet-truss curve exhibits a peak at very low-stress values, which means that a great number of elements are subjected to very low stresses, with values close to zero. Therefore, a large amount of material in this unit cell could be removed by performing topology optimization without modifying significantly its apparent mechanical properties, and particularly without achieving a lower apparent elastic modulus.

Neovius sheet and IWP skeletal internal unit cells exhibit a similar distribution. However, the low stresses that a group of elements is subjected to are slightly higher stresses than for the Octet-truss topology. Diagonal topology exhibits two peaks as well, but the first peak is much lower than the second one. The previously described suggestion, i.e. a possible topology optimization, could contribute to the improvement of the local stress distribution without modifying significantly the apparent elastic modulus of the unit cell, but not that much as for the Neovius and IWP skeletal internal topologies. Gyroid skeletal and Primitive sheet present almost a normal distribution, while Gyroid sheet unit cell presents three low peaks.

Furthermore, the statistical analysis is carried out. The computed arithmetic mean and weighted standard deviation of the stresses are presented and compared in Table 2.2. The weighted arithmetic mean indicated the apparent elastic modulus of the unit cells. The highest weighted arithmetic mean belongs to Neovius sheet topology, which means that this unit cell presents the highest apparent elastic modulus at a volume fraction of 0.30. This can also be observed in Figure 2.9. a). The weighted mean stress of the Diagonal structure is the lowest and so dies its apparent elastic modulus. The sheet TPMS-based topologies present a higher mean stress than the skeletal TPMS-based and strut-based topologies which means that their apparent elastic modulus is also higher than the apparent elastic modulus of the skeletal TPMS-based and strut-based topologies.

Neovius sheet and Diagonal topologies present the highest and lowest weighted SD values, respectively. Neovius sheet exhibits the broadest local stress distribution, while the Diagonal structure exhibits the narrowest and the most homogenized one. This means that the density of the Neovius sheet could be optimized in terms of local stress distribution by suppressing the elements subjected to low-stress values. The majority of the elements of Diagonal topology are subjected to stresses that are closer to the weighted arithmetic mean compared to the other unit cells. The Primitive sheet presents a slightly higher standard deviation which means that the majority of its elements are subjected to stresses that are very close to the weighted arithmetic mean as well.

Taking into consideration these first results and the analysis with the statistical tools, Diagonal topology could be considered as the most suitable one when the objective of the application is both the minimization of the elastic modulus and mass. However, an important drawback, which is the highest anisotropic ratio of the Diagonal topology, should be taken into account. A deeper investigation on further criteria, such as damage criteria, is necessary for the selection of a topology that exhibits the best behavior in high cycle fatigue though.

2.6.4. Local stress distribution in an iso-elasticity case

While the topologies that have been analyzed in the previous sub-section have the same relative density but not the same apparent elastic modulus, a different comparison can be adapted among the topologies, which are illustrated in Figure 2.18. Figure 2.18. presents the local stress distributions for three unit cells topologies with the same apparent elastic modulus, set as $E' = 7230\ MPa$, but at different volume fraction levels. The numerically applied bulk material properties are the following: $E_{Bulk} = 110\ GPa$ and $\nu = 0.3$. The topology of the unit cells induces different local stress distributions which play an important role in the high cycle fatigue of the lattices and thus, the implants. Then, Table 2.3. summarizes the weighted arithmetic mean and weighted standard deviation of the investigated local stress distributions.

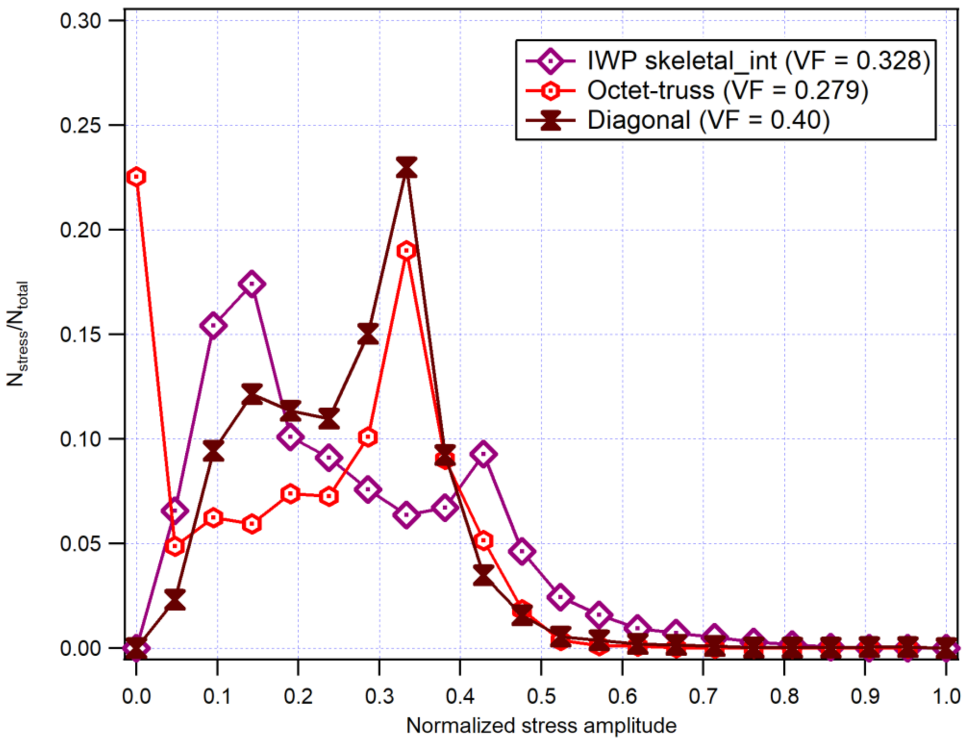

Figure 2.18. Normalized local stress distribution for the Diagonal, IWP skeletal internal, and Octet-truss unit cells over the range $0 - 1$ at the same effective Young's modulus, $E' = 7230\ MPa$. (Iso- effective elastic modulus comparison).

	Weighted arithmetic mean	Weighted SD
IWP skeletal internal	0.255	0.157
Octet-truss	0.212	0.160
Diagonal	0.262	0.111

Table 2.3. The table summarizes the weighted arithmetic mean and weighted standard deviation of the investigated normalized local stress distributions.

The Diagonal and IWP skeletal internal unit cells have the same BCC topology, but the Diagonal is a strut-based unit cell whereas IWP skeletal internal is a TPMS-based one with smooth surfaces, as illustrated in Figure 2.12. The local stress distributions of both unit cells exhibit two peaks and their majority of finite elements are subjected to two ranges of stresses. However, their volume fractions differ significantly, which are 0.328 for the IWP skeletal internal and 0.40 for the Diagonal topology. This is validated by the different weighted mean stress values as can be observed in Table 2.3.

Moreover, the Diagonal structure has the narrowest local stress distribution, according to the weighted SD, which is the lowest. Therefore, it could be considered as the most suitable topology when the objective is a homogenized distribution. On the contrary to the former advantages of the Diagonal topology, IWP skeletal internal unit cell presents a larger number of finite elements that are subjected to low stresses and thus, volume and mass optimization could take place and decrease even more the volume fraction of the unit cell. The final selection can be done according to specific requirements regarding not only the apparent mechanical properties and stress distribution but the amount of the material utilized, i.e. the relative density of the unit cells.

2.7. Application: The most suitable topologies for a cortical bone replacement

The combination of all the previously described methods generates the complete methodology that can be applied to every case study by adapting it to the specific requirements.

The application discussed in this section is the replacement of a cortical bone by using unit cells and thus, lattices for the internal part of an implant. The first step is the generation of a vast range of unit cells with various volume fractions. The next step is the selection of a group of unit cells that satisfies the first set of mechanical requirements, i.e. the relative density and the effective elastic modulus of the human bone. Cortical bone exhibits an elastic modulus in the range $4 - 30\ GPa$ and a density that varies between 1.6 and $2\ g * cm^{-3}$[79]. Using Figure 2.9. a) and the material properties of Ti-6Al-4V alloy, i.e. $E = 110\ GPa$ and $\nu = 0.3$, we define the range of the normalized targets as shown in Figure 2.19. Figure 2.19. a) presents the range of the normalized elastic modulus {1} and the relative density {2} of the cortical bone as they are reported in [79]. The number of unit cells that satisfy those two requirements is limited. Also, Figure 2.19 b) presents the chart that explains all the steps of the selection process.

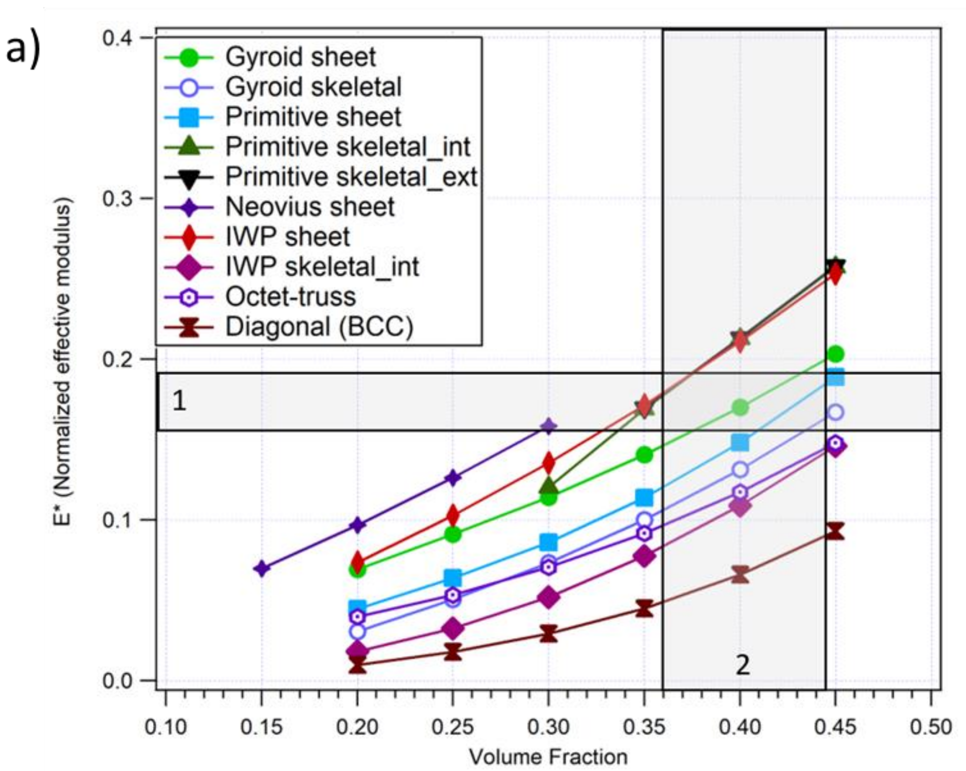

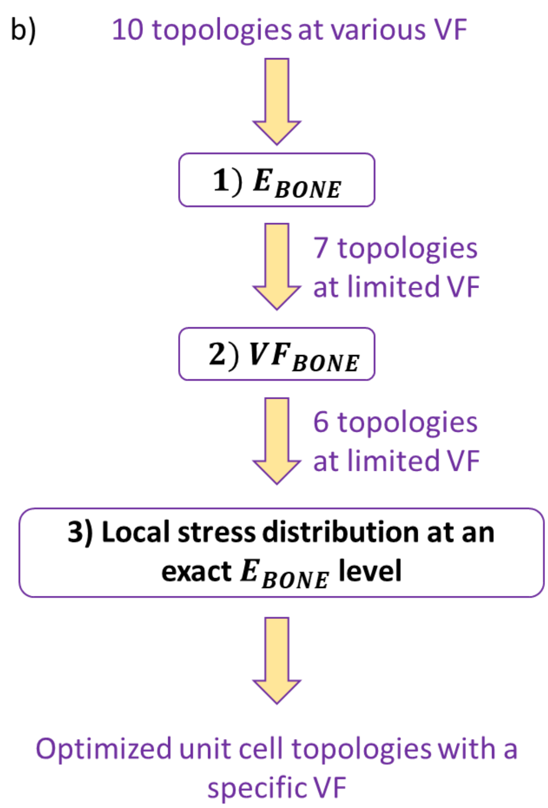

Figure 2.19. a) Mechanical requirements to be satisfied by the topologies to replace cortical bone successfully, and b) a chart explaining all the steps of the selection process.

The first objective is the architectured structure to exhibit the same apparent elastic modulus as the cortical bone, being portrayed by the horizontal highlighted area in Figure 2.19. The second objective is the density of the cortical bone to be reached, which is portrayed by the vertical highlighted area. Six topologies can satisfy these objectives which appear in the section of the requirements; the IWP sheet (in red), Primitive skeletal external (in black), Primitive skeletal internal (in dark green), Gyroid sheet (in light green), Primitive sheet (in light blue), and Gyroid skeletal (in dark blue).

The third step is the satisfaction of the third objective, which is the selection of a lattice structure that exhibits the most homogenized local stress distribution. By applying the above-mentioned material properties of the Ti-6Al-4V alloy to the selected topologies that satisfy the first two requirements and by setting the apparent elastic modulus target as $E' = 18500\ MPa$, we can study their local stress distribution and compare the curves. $E' = 18500\ MPa$ could be considered as an apparent elastic modulus that represents the elastic modulus of the cortical bone to be replaced. Indeed, the local stress distributions of several unit cells with the same apparent elastic modulus are presented in Figure 2.20. Then, Table 2.4. summarizes the weighted arithmetic mean and weighted standard deviation of the investigated local stress distributions for statistical analysis of the results.

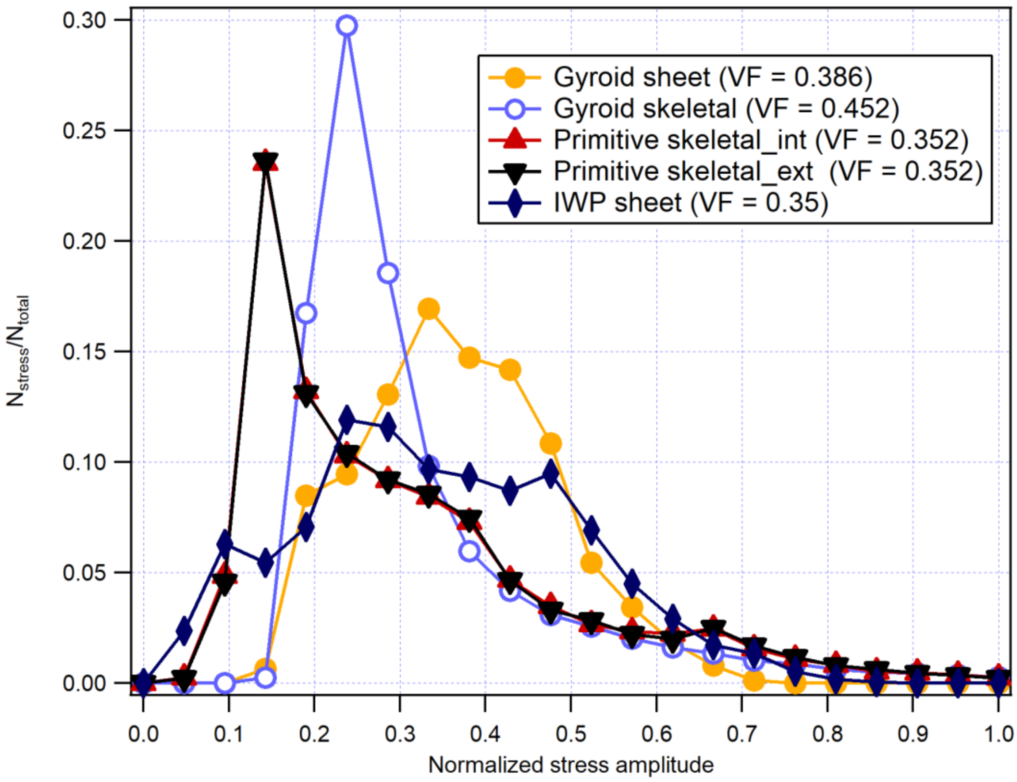

Figure 2.20. Normalized local stress distributions of Gyroid sheet, Gyroid skeletal, Primitive skeletal, Primitive skeletal external, and IWP sheet unit cells over the range $0 - 1$ at the same apparent Young's modulus, $E' = 18500\ MPa$. (Iso- effective elastic modulus comparison)

	Weighted arithmetic mean	**Weighted SD**
Gyroid sheet	0.368	0.111
Gyroid skeletal	0.322	0.150
Primitive skeletal Int	0.305	0.190
Primitive skeletal Ext	0.306	0.190
IWP sheet	0.347	0.160

Table 2.4. The table summarizes the weighted arithmetic mean and weighted standard deviation of the investigated normalized local stress distributions.

A first observation is the identical volume fractions and local stress distributions for the two types of Primitive skeletal unit cells, even though their shapes are not the same (see Figure 1.9. for the different shapes of the Primitive skeletal unit cells). Their volume fraction is the lowest among the volume fractions of all the studied structures. Second, the Gyroid sheet topology exhibits the lowest standard deviation which means that its normalized stress distribution is the most homogenized among all the others. There are no elements that are subjected to higher normalized stress values than 0.72 as shown in the chart. According to this first analysis, the Gyroid sheet topology could be considered as the most suitable one for the replacement of a cortical bone, because it satisfies all the three requirements described above.

2.8. Conclusions

In the present chapter, a complete numerical qualitative and quantitative approach is performed to design, analyze, and finally select a suitable unit cell as the representative topology for the creation of an architectured implant. Multiple repetitions of the unit cells lead to the design of lattice structures. A large database of TPMS-based and two strut-based unit cells with various volume fractions is designed for this investigation, which is carried out with the aid of finite element analysis and the application of a periodic homogenization method in the elastic region.

The following conclusions have been reached:

- ✓ The direct relation of various normalized apparent mechanical properties to the isovalue t of the TPMS equations makes straightforward the design process when there are no specific requirements regarding the volume fraction of the unit cells. As has been shown the increase of the isovalue t does not mean necessarily that the apparent elastic modulus of a unit cell is increased.

- ✓ Gyroid sheet and IWP sheet topologies present an almost isotropic response. Their computed Zener ratios are quasi-constant and close to $Z = 1$, a value that indicates an isotropic behavior. Moreover, only their Zener ratios are volume fraction independent, which means that they could be chosen as suitable topologies when an isotropic behavior is a requirement at any possible volume fraction.

- ✓ It is known that IWP skeletal internal and Diagonal unit cells present the same BCC topology; IWP skeletal internal as a TPMS-based unit cell presents a smooth surface, whereas Diagonal as a strut-based unit cell owns sharp strut-corrections. These are the most anisotropic topologies, especially at low volume fractions, and the evolution of their anisotropic response is similar. The only difference is that IWP topology is always less anisotropic than the Diagonal one as a result of a more evenly distribution of the material in the unit cell.

- ✓ As all the unit cells are triply periodic the local stress distributions for the tensile load in the three principal directions are the same. The same result applies to the three shear loading cases. For all the studied unit cells, the computed distributions of the normalized local stresses are not sensitive to volume fraction changes, in both tensile and shear loads.

- ✓ According to a statistical analysis conducted for the local stress distributions of the unit cells, a large number of finite elements of some topologies, such as Octet-truss, IWP skeletal internal and Neovius sheet, are subjected to very low stresses, with values close to zero, and thus, topology optimization could be performed in order to suppress the elements that are not useful and to reduce the volume fraction and the mass of the unit cells.

- ✓ According to a statistical analysis conducted for the local stress distributions of the unit cells, it is shown that the Diagonal structure exhibits a narrower stress distribution than the IWP skeletal internal topology at the same apparent elastic modulus. Further analysis should be done to select the finally suitable topology because IWP skeletal internal presents other advantages, such as the possibility to perform topology optimization and thus, mass reduction due to a large number of finite elements that are subjected to very low stresses and they could be suppressed.

- ✓ A Gyroid sheet topology with a $VF = 0.386$ is selected as the most suitable one for cortical bone replacement. It satisfies several objectives, such as the effective elastic property and the density of the cortical bone, and also it exhibits a homogenized local stress distribution, based on a statistical analysis carried out.

- ✓ The same methodology presented in an application can be employed by replacing the third criterion of homogenized local stress distribution with another criterion, such as one based on the anisotropy and the Zener ratio evolution.

Several structures have been further investigated to validate all the above results and conclusions. Lattices with multiple unit cell repetitions are fabricated and tested under a compressive load. All the details about the experimental part of the methodology are given in the following section.

3. Additive manufacturing of lattice structures: multiscale characterization and comparison with numerical predictions

3.1. Introduction

In the previous chapter, a deep investigation has been carried out regarding the apparent elastic properties and local stress distribution on various lattice topologies after the application of periodic boundary conditions (PBC). However, when it comes to the selection of the most suitable topology for a biomechanical application, further investigation is necessary. Particularly, two cases are considered in this chapter for the selection of an appropriate lattice structure, namely the standard and destructive cases. The standard case deals with the selection of the representative boundary conditions for a lattice whose elastic properties mimic the properties of the real bone. The destructive case deals with the selection of a lattice after the complete plastic deformation and fracture under a compressive load. Although the complete fracture of an implant is a non-desirable outcome, the investigation of this case is important in order to identify the worst-case limits per topology. To study the aforementioned cases, the numerical models developed in chapter 2 are used for further numerical tests. They are used as well for the design of the real specimens and experimental tests.

As this chapter analyses the comparison between experimental and numerical results, only a few lattice topologies have been selected for investigation due to some limitations. These limitations are the cost and the availability of the raw material for the fabrication of the lattices and the post-processing and testing time of the as-built structures. The selected lattices for both numerical and experimental investigation should satisfy specific elastic properties that correspond to the elasticity of the real bone. Two different apparent elasticity levels are selected arbitrarily and have been set as the target, namely $E' = 14300\ MPa$ and $E' = 5600\ MPa$. As the global elastic modulus of the cortical bone is in the range of $3 - 30\ GPa$, those two elasticity levels are chosen to represent two stiffness levels of a cortical bone. In total 5 unit cell topologies are selected to fabricate and numerically investigate, Gyroid sheet (VF=0.386), and

Gyroid skeletal (VF=0.452) for the first elasticity level and IWP internal (VF=0.328), Gyroid skeletal (VF=0.29), and Diagonal (VF=0.4) topologies for the second elasticity level.

Regarding the standard case, the application of two different boundary conditions, namely the compressive boundary conditions (CBC) and the PBC on the aforementioned topologies is carried out. Then, a comparison of the final elastic properties is important for the selection of the most representative numerical boundary conditions. The latter should mimic as much as possible the real-life boundary conditions. Second, experimental validation of the numerical results should follow, which represents actually the real-life applied load. After the comparison of two different numerical boundary conditions and the experimental tests, the selection of the suitable lattice is validated.

Regarding the destructive case, more numerical and experimental tests have been carried out to investigate the non-linear response of the unit cells subjected to a compressive load. Moreover, the experimental investigation of the as-built lattices continues up to the level of the fracture. Various lattices have been compressed until the final fracture which is presented and analyzed at a macroscopic level. Moreover, interrupted compression tests have been conducted to investigate the appearance and propagation of the possible cracks at a microscopic level. X-ray microtomography is used to help us identify the plastic deformation and the cracks at different compressive load levels.

Regarding the experimental tests, it should be mentioned that the architectured materials, such as TPMS-based and strut-based lattices present various macro-, micro-mechanical properties, and deformation behaviors. The deformation behaviors are topology-dependent and they are different from those of the compact bulk materials. Therefore, the mechanical characterization is performed via adapted experimental tests according to International Standard ISO 13314 [80].

International Standard ISO 13314 is used for the design of the metallic lattices and generally porous materials, the compression testing procedure, and the characterization of the lattices [80]–[82]. In particular, ISO Standard 13314 [80] provides requirements about the percentage of porosity in the lattices, the external geometry, the dimensions and the repetitions of the unit cells of the lattices, the number of the specimen to test, the room temperature, and the speed of the compression plates of the machine. All lattices have been fabricated by an SLM machine. More technical information is given in section 3.2.

In summary, there are two main objectives in this chapter: a) the comparison of the experimental and numerical apparent elastic modulus and non-linear response of the lattices after the application of two different numerical boundary conditions and the selection of the most representative one, and b) the experimental investigation of the fracture of the lattices in a macroscopic and a microscopic level under a quasi-static compressive load. The complete methodology and the results for each objective are presented and analyzed in the following sections of this chapter.

Particularly, this chapter is structured as follows, section 3.2 presents the methodology of both the numerical and experimental procedures and the corresponding results, section 3.3 focuses on the comparison of the numerical and experimental results and the complete analysis, and finally, all the conclusions are presented in section 3.4.

3.2. Experimental and numerical methods and results

3.2.1. Methodology

As mentioned above, two apparent elasticity levels have been set as targets in order to design, numerically investigate, and fabricate lattices. The elasticity levels are $E' = 14300\,MPa$ and $E' = 5600\,MPa$ which corresponds to two cortical bone elastic modulus levels. 5 unit cell topologies are then selected to design which are the following: Gyroid sheet (VF=0.386), and Gyroid skeletal (VF=0.452) for the first elasticity level and IWP internal (VF=0.328), Gyroid skeletal (VF=0.29), and Diagonal (VF=0.4) for the second one. They are all exhibited in Table 3.1. Particularly, Gyroid skeletal topology is designed, fabricated, and mechanically tested at both elasticity levels, to compare the results and identify accordance with the results at different volume fractions. Moreover, IWP internal and Diagonal topologies have been selected to investigate deformation and fracture on these particular lattices at the same apparent elasticity level. Those two present the same BCC topology. The difference between these two topologies is the fact that the IWP internal exhibits smoother strut connections than the Diagonal. They are both illustrated in Figure 2.12 in the previous chapter.

Regarding the material properties as input for all the numerical tests, they have been extracted by previously conducted experiments and it is assumed that the material exhibits a homogeneous and isotropic behavior. The bulk Ti-6Al-4V alloy produced by an SLM machine and experimentally tested in LEM3 laboratory by Dr. Boris Piotrowski has an elastic modulus $E = 85\ GPa$ and it is described by a non-linear constitutive law as presented in Appendix C. As all lattices have been fabricated with a Ti-6Al-4V alloy by an SLM machine, the experimentally acquired constitutive law should be applied to the numerical tests.

Numerical simulations have been performed for single unit cells for the aforementioned topologies with applied PBC and CBC to compare both the apparent elastic modulus and the macroscopic non-linear behavior. The most representative boundary conditions are then selected. Furthermore, numerical tests with applied CBC for lattices with multiple unit cell repetitions, such as 2x2x2, 3x3x3 lattices, have been carried out to address the problem of the number of unit cell repetitions. The latter investigation is conducted to identify the significance of a Representative Volume Element (RVE) with the same unit cell repetitions as the real lattice to its overall response when the CBC are applied.

Regarding the experiments, the lattices have been designed and compressed according to the International Standard ISO 13314 as previously described. The elastic modulus and the non-linear response are compared with the relevant numerical results to select the appropriate boundary conditions and the most suitable lattice. After the comparison between numerical and experimental results, an experimental investigation of the fracture occurred for all the topologies is conducted. Macroscopic observation and analysis of the deformation and final fracture of the lattices are carried out. Based on the extracted conclusions, safety factors are chosen by following an engineering approach for the selection of the most suitable topology for a biomechanical application. More details about the experimental procedure and the applied protocol are given in the following section.

3.2.2. Experimental procedure; fabrication of lattices, mechanical testing, and characterization

3.2.2.1. Fabrication of the TPMS-based lattices by SLM technology and relative weighing

According to the ISO Standard 13314, the cubic specimens are designed with 5 repetitive cubic unit cells in all directions. Each unit cell has dimensions $3 * 3 * 3\ mm^3$. The single unit cells are designed following the procedure described in section 2.2.2. and repeated in each direction. An additional step of the final .STL files check and repair are performed to ensure successful fabrication. For instance, overlapping, intersecting, and missing triangles, holes, noise shells, and flipped normals are only a few of the possible .STL errors that can occur [83], [84].

Once the preparation and repairing of the lattice files are done, the .STL files are imported into Materialise Magics software for the last steps of the pre-processing. First, the parts are positioned on the virtual build platform with the appropriate orientation. It is essential to position the parts on the platform in an efficient way in order to fabricate as many parts as possible under exactly the same conditions but at the same time to leave enough free space between them to ensure flawless detachment once the printing job is finished. Even though the set-up of the machine parameters in all jobs is the same, slight differences may occur caused by the experiment itself. Regarding the orientation of the parts on the platform, it is not taken into consideration in this case because the lattice specimens are cubic and triply periodic.

The generation of the support structures for the down-facing surface follows and it is quite a challenging step. Even though the TPMS-based lattices are defined as self-supported structures during the 3D printing process [85], they cannot be printed directly on the build platform. The correct detachment of the parts could be impossible. There are various default types of support structures in the software; ‘block' and 'contour' types with perforations are used for easier removal at the end. Once the complete pre-processing is over, the .SLM file is generated and transferred to the printing machine.

All the lattices in this study have been fabricated by an SLM Solution 280 HL machine, shown in Figure 3.1. to obtain near-net-shape structures [86]. The process of the fabrication is described in section 1.5.2. The machine parameters used for the fabrication are the following: laser power $200\,W$, hatching distance $0.08\,mm$, scanning speed $1650\ mm/s$, and layer thickness $0.03\ mm$. Moreover, the particle size of Ti-6Al-4V alloy powder is in the range $10-65\ \mu m$ [87].

Figure 3.1. SLM Solution 280 HL machine for the fabrication of the lattice structures.

Once the printing job is finished, the plate with the as-built lattices cools down in the chamber. Then, the plate is removed from the chamber and the latter is cleaned from the remaining powder according to a specific protocol. A plate with several as-built lattices is shown in Figure 3.2. Various topologies can be seen from left-to-right, i.e. IWP internal, Gyroid skeletal with a high volume fraction, Gyroid skeletal with a low volume fraction, and Gyroid sheet topologies.

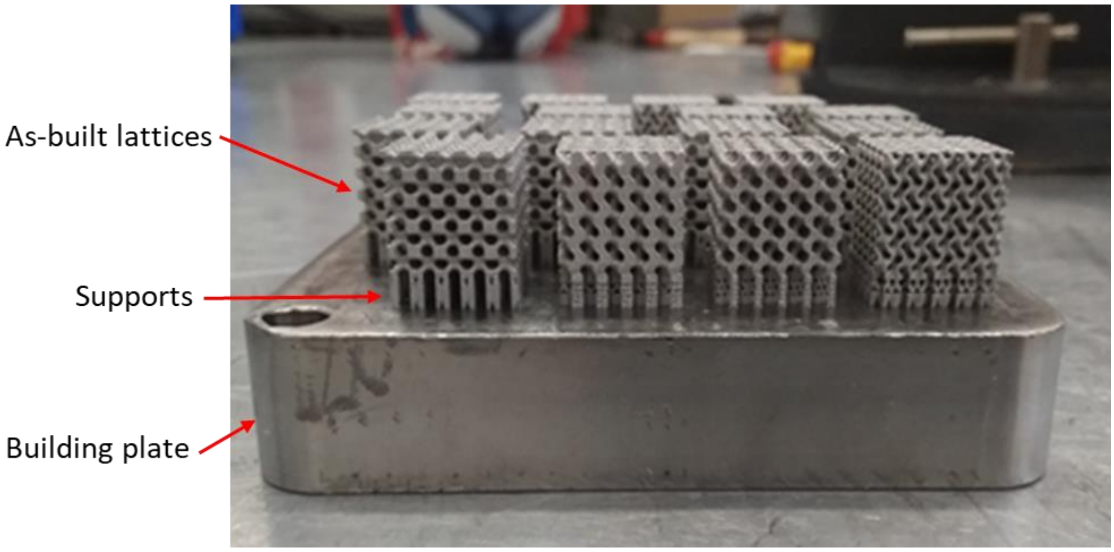

Figure 3.2. A building plate with several as-built lattices with supports on top, directly after an SLM job is finished.

Then, the post-processing of the lattices follows. The detachment of the parts is carried out by breaking carefully the support structures. This step ensures undamaged lattices. However, parts of the supports still remain on the down-facing surface that needs to be removed for high surface quality. The largest parts of the supports are removed manually with the aid of a pair of pliers and then, the lattices are transferred to a grinding-polishing machine for the final polishing. This step is important to avoid any unexpected and undesirable cracks during the mechanical testing caused by a non-smooth surface. It is also important to remove the excess material and to reach the targeted volume fraction of the CAD design. In Figure 3.3.a) two detached lattices with parts of the supports still on them and b) a lattice with a polished bottom surface are presented.

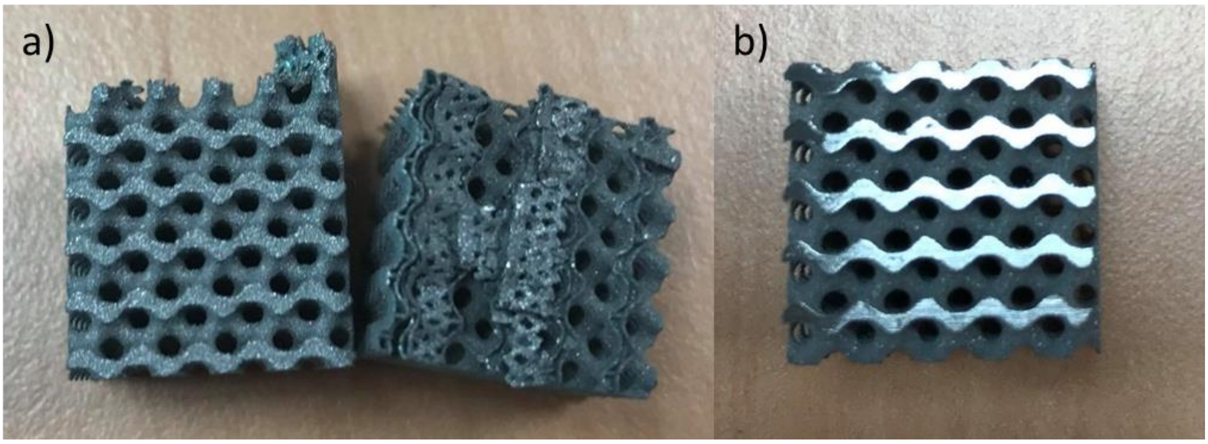

Figure 3.3. a) Two detached lattices from the plate with parts of the support structures still on the down-facing surface, and b) a Gyroid skeletal lattice with a polished bottom surface after the removal of the supports.

The manual polishing of the down-facing surface of all the lattices ensures maximum parallelism between the top and bottom surfaces. This is performed to avoid any undesirable and unpredicted cracks during the testing that follows, as have been mentioned previously. Then, the specimens are collected and a relative weighting is carried out in order to compute the volume fraction of the fabricated lattices and to compare it with the volume fraction of the CAD model. High precision for the testing is important and thus, the weight of the lattices is measured with a precision balance. By applying the Ti-6Al-4V density, $\rho = 4{,}42 * 10^{-3}\ g/mm^3$ to the equation $VF_{EXP} = \frac{m_{measured}}{\rho}$, the volume fraction of the specimens is computed. In Table 3.1. the topologies for a particular stiffness level and the corresponding volume fractions are presented. Moreover, the difference between the numerical and the experimental volume fractions is computed and presented as well.

Topology	Stiffness level target [MPa]	VF_{CAD}	VF_{EXP}	$Diff = \left\lvert \frac{VF_{CAD} - VF_{EXP}}{VF_{CAD}} \right\rvert$
Gyroid sheet	14300	0.38	0.39	1.27%
Gyroid skeletal	14300	0.45	0.46	2%
Gyroid skeletal	5600	0.29	0.29	0%
IWP internal skeletal	5600	0.32	0.34	3.35%
Diagonal	5600	0.40	0.41	1.25%

Table 3.1. The five investigated topologies at two stiffness levels with their corresponding volume fractions, the numerical and the experimental one, and the difference between them.

After the relative weighing, the lattices are ready for mechanical testing according to the ISO Standard 13314. More information about the compression testing and the characterization methods is given in the next sections.

3.2.2.2. Acquisition of the experimental curves and apparent elastic modulus measurement for lattices under a compression load-unload

As has been mentioned previously, the first objective of chapter 3 is the comparison between experimentally- and numerically-acquired elastic modulus and non-linear response of lattices. In this section, the experimental protocol is detailed and the raw/post-processed results are presented.

Five lattice topologies have been designed, fabricated by an SLM machine, and then tested under a uniaxial compressive load according to the ISO Standard 13314 in order to get the force-displacement curves. The latter helps us calculate the apparent elastic modulus of each lattice and identify the non-linear region. The details about the dimensions of the real specimens and the unit cell repetitions are given in section 3.2.1.1. According to the International Standard, a minimum of 3 specimens have to be tested for the calculation of the elastic modulus. Moreover, one specimen is required for the preliminary test and the estimation of the plateau stress. In total five lattices per topology are fabricated, four of which are tested and one is a spare if required.

The specimens are tested under a uniaxial compressive load at room temperature as there is no need for special thermal conditions. A Zwick-Roell 1476 machine equipped with a 100 kN load cell is used for the compression tests. The deformation is measured with the aid of an extensometer multiXtens which is positioned on the compression platen close to the tested specimen. The bottom and top surfaces of a lattice specimen are lubricated to avoid barrelling effect and the specimen is positioned on the bottom compression platen of the machine. It is important to note that the as-fabricated top surface and its parallel previously-polished surface are perpendicular to the compression platens. By positioning the lattices this way between the compression platens, the avoidance of any non-complete-parallelism problems caused by the manual polishing process is reinforced. Moreover, the compression strain rate for all the tests is constant and it is set at $10^{-3}\ s^{-1}$, the lowest allowed value according to the ISO Standard 13314, which is converted into compression velocity for the machine, i.e. $\dot{\delta} = l * \dot{\varepsilon} = 15 * 10^{-3}\ mm/s$. In Figure 3.4. the compression platens, the extensometer, and a placed lattice specimen ready for a test are presented.

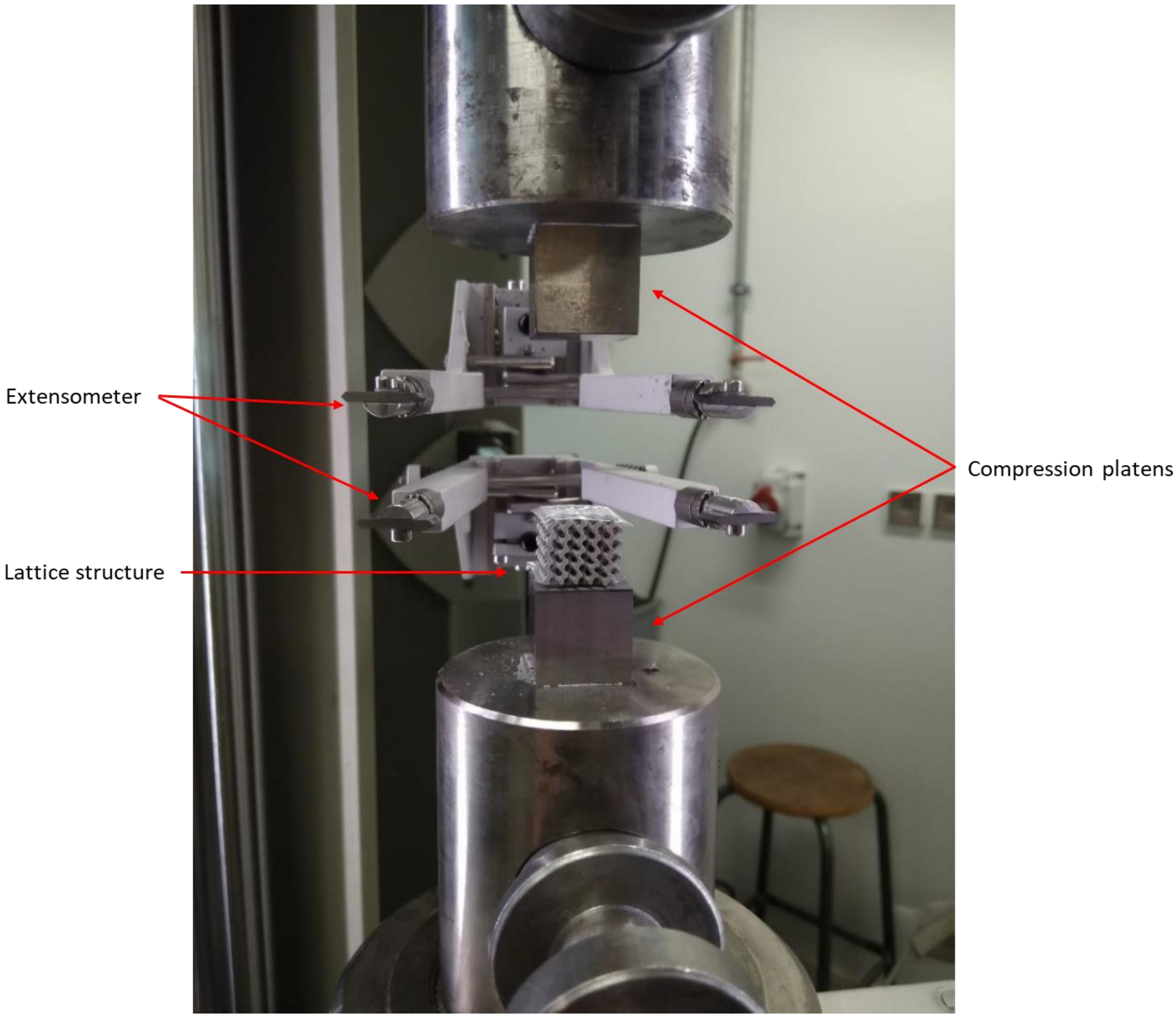

Figure 3.4. The Zwick-Roell 1476 machine with the extensometer used for the experiments and the lattice specimen positioned before a test.

In the first, preliminary test per topology, the lattices are subjected to a monotonic compression loading until the complete fracture of the specimen. The target is the determination of the plateau stress. Then the values at 70% and 20% of the plateau stress are computed according to the ISO standard. These values represent the starting and ending points of the unloading for the next compression tests, respectively [80]. Three specimens per topology are then tested for the measurement of the elastic modulus. They are compressed until the starting point of the unloading where the force is then gradually reduced. Once the ending point is reached, the lattices are compressed again until the final fracture. The as-obtained force-displacement curves for the first specimen per topology directly from the computer connected to the compression machine are presented in dark blue color in Figure 3.5.

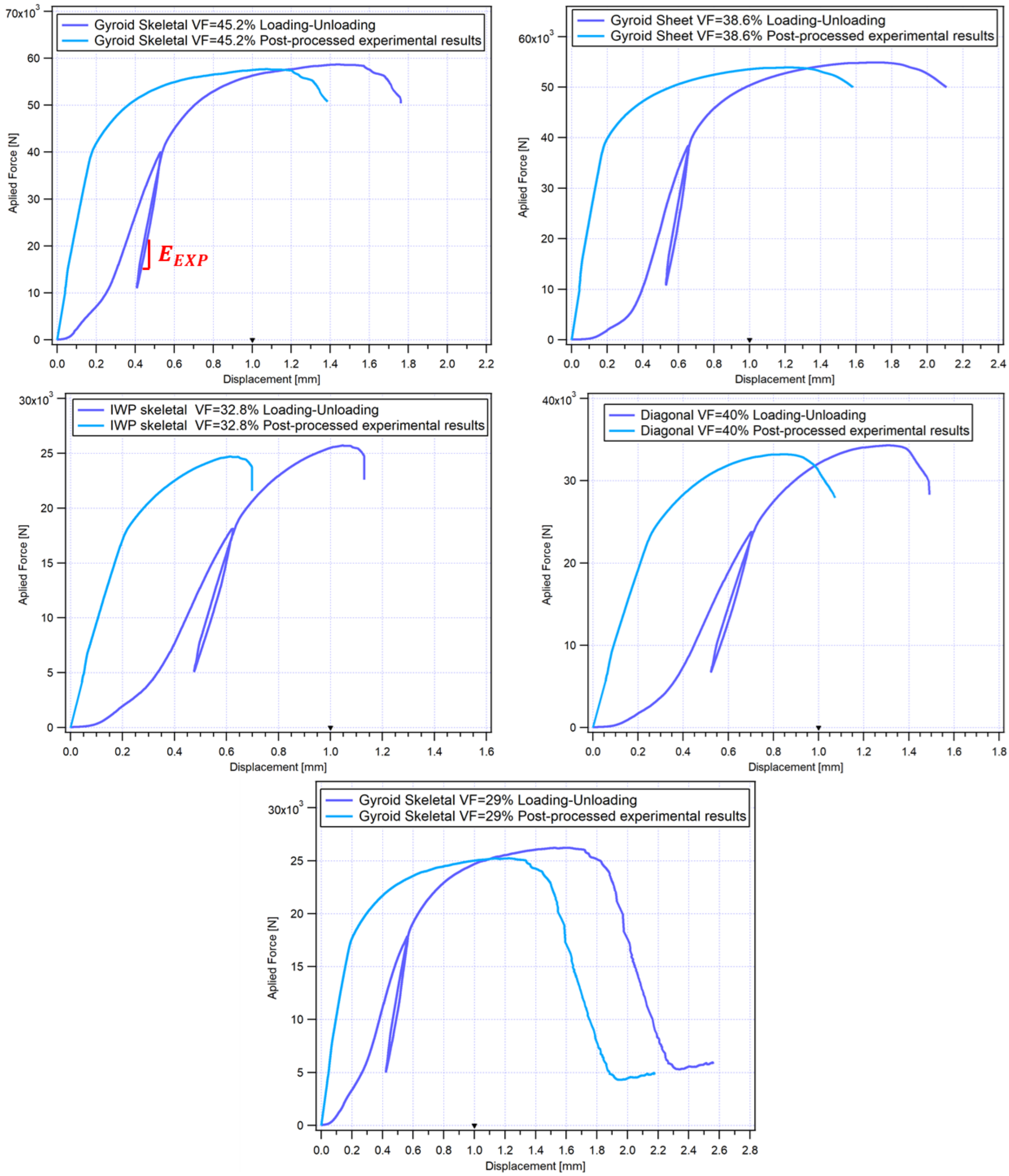

Figure 3.5. As-obtained results for the first tested specimen per topology directly from the computer (dark blue), and post-processed results (light blue).

The slope of the first part of the curves (dark blue curves in Figure 3.5) that corresponds to the first loading is not the real elastic modulus of the lattices. As explained in the ISO standard, the slope of the second loading represents the apparent elastic modulus of the lattices. Therefore, the post-processing of the force-displacement curves follows to allow the graphical comparison of the experimental linear and non-linear responses with the numerical ones which is performed later. This process is not included in the ISO standard.

The post-processing consists of 3 steps, which are presented graphically in Appendix D. First, a small part at the beginning of the curves (approximately up to 1000N) which is almost parallel to the displacement-axis has to be deleted. This clearance should be performed to correct small errors of the machine and to obtain setup compliance. Then, the starting point of the remaining curve is translated to the origin of the coordinate system.

Second, the part of the corrected curve that corresponds to the first loading consist of two parts, the ‘’initial’’ and the ‘’pseudo-elastic’’. The presence of the ‘’initial’’ part indicates various minor experimental processes errors before the real compression of the lattice starts. This could be for example the lack of the complete parallelization of the sample between the two platens as soon as the first low load is applied. This lack of parallelism of the top and bottom surfaces leads certain areas of the lattices to be more loaded at the beginning of the compression test and the result is to get the ‘’initial’’ part of the curve. The ‘’missing pseudo-elastic part’’ of the remaining curve is added by elastic prediction to reach a point with no stress. Then, the complete curve is translated along the x-axis up to the origin.

Third, the removal of the regions of the curve that correspond to the loading and unloading follows. The slope of the loading region is affected by various errors that occurred during the testing process, such as a slight sliding of the specimen at the beginning of the compression. The ‘’missing elastic part’’ of the remaining curve is added by elastic prediction and then, the complete curve is translated along the x-axis up to the origin. In Figure 3.5. the final curves for all the topologies following the post-processing are shown in light blue color.

The linear part of the final force-displacement curves represents the experimental apparent elastic modulus of the lattices [80]. The average value of three loading-unloading tests per topology is the experimental apparent elastic modulus of the specimens, E_{EXP}. The experimental elastic modulus of all the topologies is presented in Table 3.2.

Topology	E_{EXP} [MPa]
Gyroid sheet (VF = 0.386)	14565.85
Gyroid skeletal (VF = 0.452)	15687.44
Gyroid skeletal (VF =0.29)	5932.60
IWP skeletal internal (VF =0.328)	5658.90
Diagonal (VF = 0.40)	6243.20

Table 3.2. The average experimental elastic modulus of 5 tested topologies is calculated by the elastic modulus of three tests per topology.

Once the first group of the compression tests for the calculation of the apparent elastic modulus is complete, the second group of tests follows. The latter includes interrupted compression tests for the investigation and acquisition of preliminary qualitative results regarding the plastic deformation occurred and the crack initiation and propagation. X-ray micro-tomography is used to observe the cracks at a microscale. The complete methodology followed is described in detail in the next section.

3.2.2.3. Interrupted tests, crack observation with x-ray micro-tomography, and final macroscopic facture

The tests described in this section are: a) interrupted tests performed at different force levels to observe any plastic deformation and any cracks (functional damage), that occurred with the help of the X-ray micro-tomography, b) loading-unloading tests to identify the importance of the functional damage caused by comparing the slopes, and c) uniaxial compression until fracture to investigate the final macroscopic fracture. a) and b) sets of tests are performed only for a Gyroid skeletal topology at $VF = 0.29$ because the experimental process is raw material-consuming.

The previously-done preliminary test which is used for the estimation of the maximum force applied, F_{max}, is useful one more time for the new set of experiments. Three percentages of the maximum force are computed, namely $65\% * F_{max}$, $75\% * F_{max}$, and $90\% * F_{max}$. Each new specimen is compressed up to a specific percentage of the F_{max}. Then, the plastic deformation is identified by measuring the length between two points and by comparing it to the distance between two other similar points. In Figure 3.6. two planes with multiple length measurements between two points (at curve peaks) of a Gyroid skeletal lattice at a compressive load of $90\% * F_{max} \approx 20500\ N$ are presented.

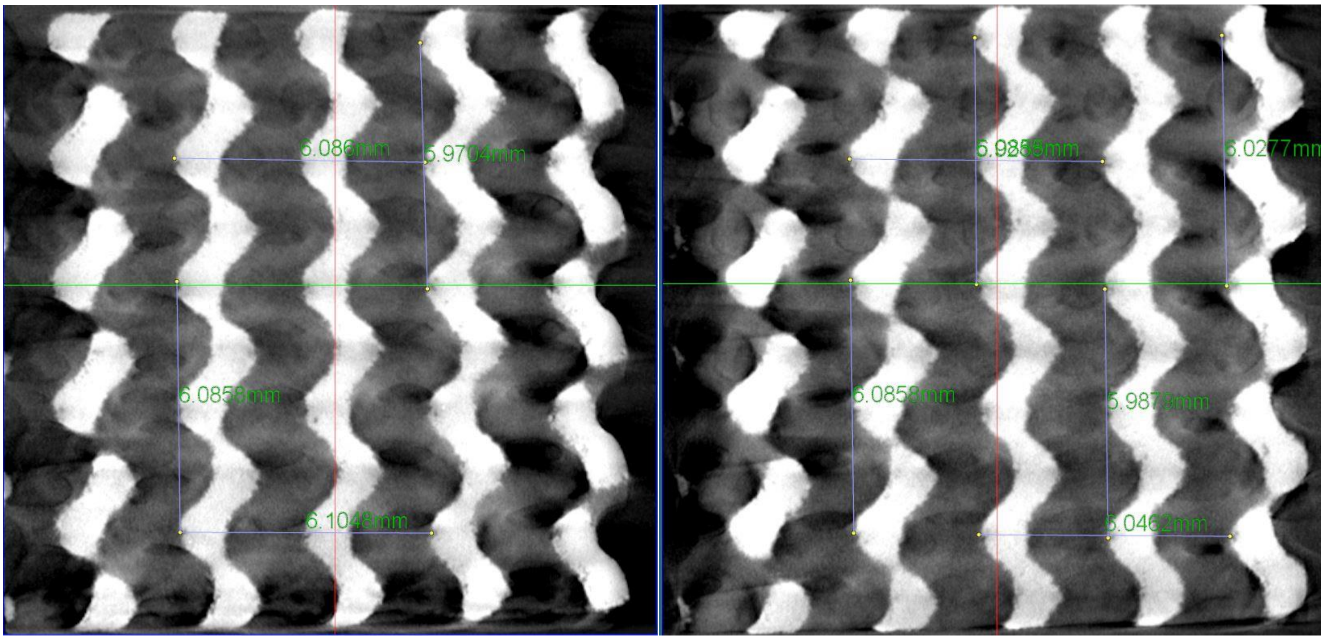

Figure 3.6. Two planes with multiple length measurements between two peaks of the Gyroid skeletal topology at a compressive load of $90\% * F_{max} \approx 20500\ N$.

Apart from the measurement of the plastic deformation, the appearance of some cracks can be detected at certain force levels with the aid of the x-ray micro-tomography on a Gyroid skeletal lattice that has been compressed until $90\% * F_{max} \approx 20500\ N$. Three planes with small cracks are shown in Figure 3.7.

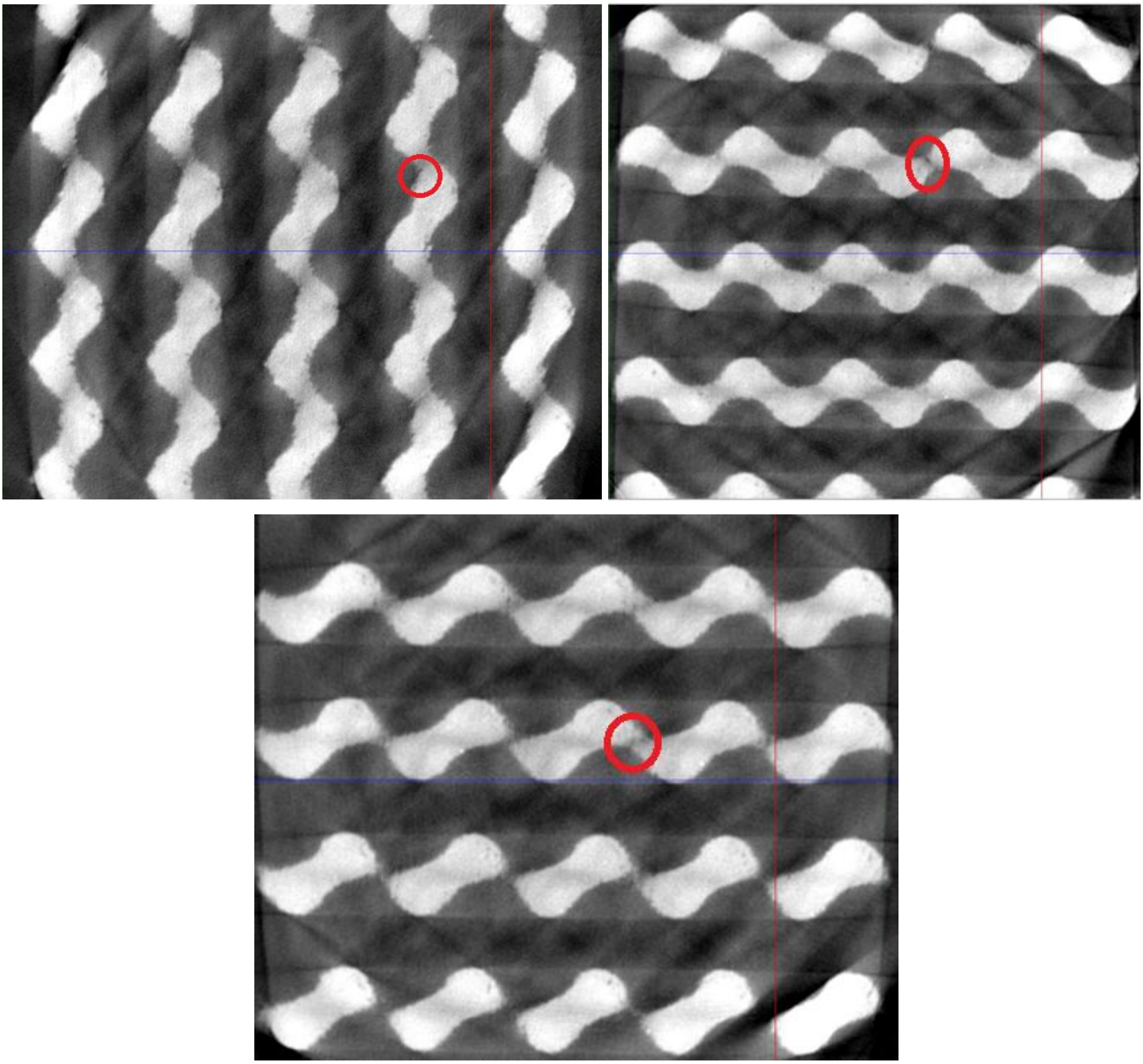

Figure 3.7. Three planes of a Gyroid skeletal lattice with small cracks detected with the aid of the x-ray microtomography.

The next step is the identification of the importance of the functional damage caused, i.e. appearance of permanent plastic deformation and cracks. This has been investigated by carrying out another test. A Gyroid skeletal lattice that has already been compressed until $65\% * F_{max}$ and has been left to relax is again compressed. It is important to note that the permanent plastic deformation and damage is negligible at this level of compression force ($65\% * F_{max}$) which will be discussed in the relevant section. This is the reason why the loading-unloading tests can be carried out without any problem. The lattice is then loaded up to $75\% * F_{max}$, unloaded, loaded again up to $90\% * F_{max}$ compression force levels unloaded and then loaded up to the final fracture. The acquired curve of the above-described compression test is shown in Figure 3.8.

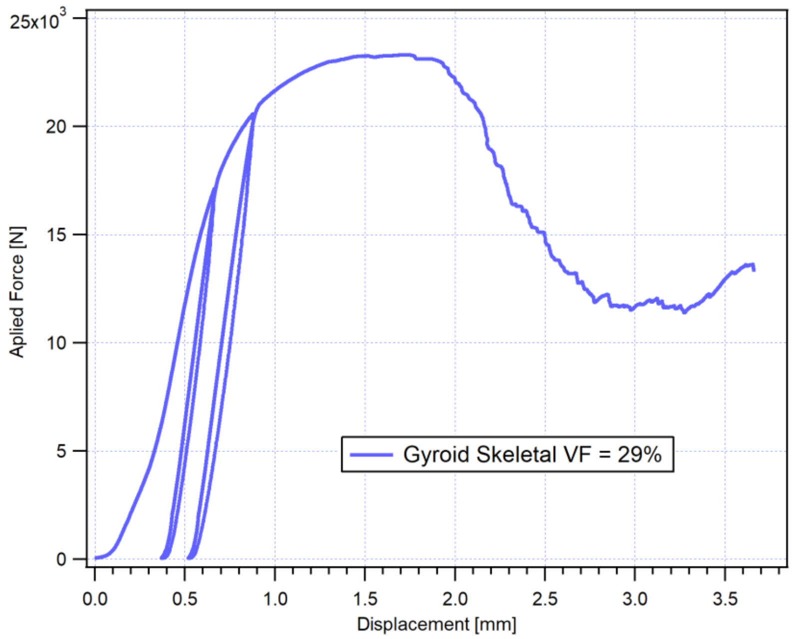

Figure 3.8. An already compressed Gyroid skeletal lattice up to $65\% * F_{max}$ is once more loaded-unloaded up to $75\% * F_{max}$ and $90\% * F_{max}$. The slopes of the regions are similar.

Once the microscopic analysis is complete, the macroscopic analysis of the fracture follows. All five fabricated lattices mentioned in Table 3.1. have been tested under a uniaxial monotonic compression load until the final fracture. These are actually the ‘’preliminary’’ tests performed previously. At first, the macroscopic fracture of lattices with the same topology but different volume fractions is investigated. In Figure 3.9 two compressed and fractured specimens with the same topology, i.e. Gyroid skeletal, with two different volume fractions, $VF = 0.29$ and $VF = 0.452$ are presented.

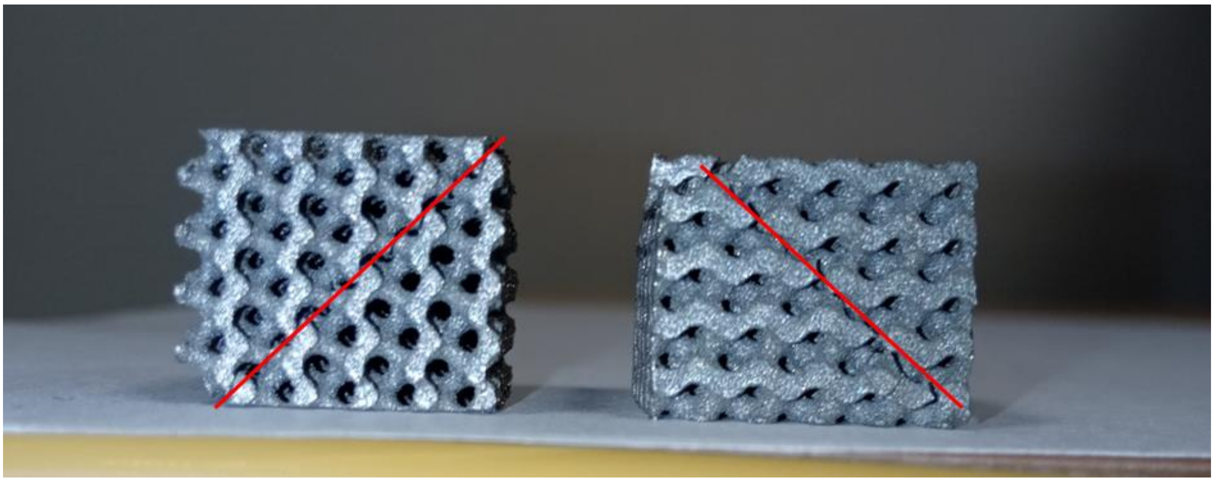

Figure 3.9. Gyroid skeletal lattices compressed until the final macroscopic fracture at 45^o with different volume fractions. $VF = 0.29$ (left) and $VF = 0.452$ (right).

The presentation of the fractured lattices based on various topologies follows. In Figure 3.10., the macroscopic fracture of three topologies is presented. These three lattices exhibit neither the same apparent elastic modulus nor the same relative density.

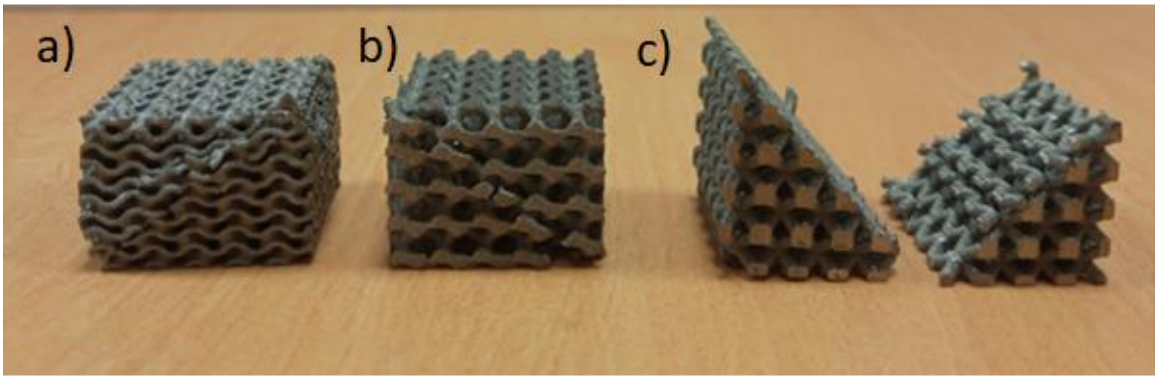

Figure 3.10. Macroscopic fracture at 45^o for three lattice topologies, i.e. a) Gyroid sheet, b) Gyroid skeletal, and c) Diagonal topology.

The way the force that causes the fracture drops is related to the macroscopic deformation of the lattices and the nature of the macroscopic fracture. The force-displacement curves for Gyroid sheet and Diagonal topologies are presented in Figure 3.11. The drop of force is indicated with a red circle.

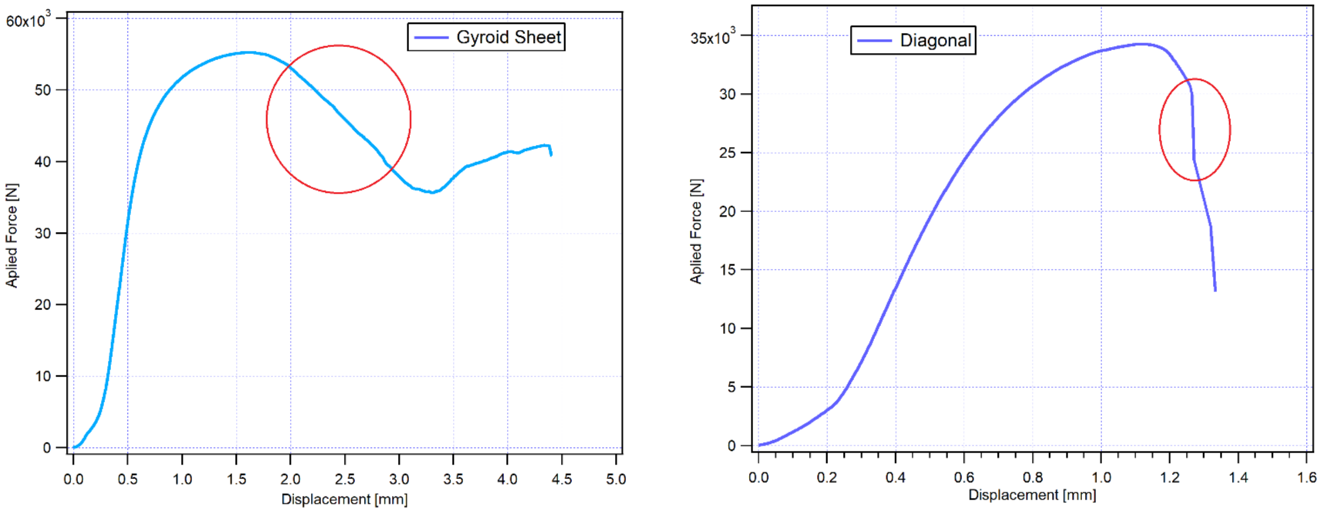

Figure 3.11. Drop of force when a specimen is fractured under a compressive load for a Gyroid sheet (left) and a Diagonal (right) topology.

Moreover, the force-displacement curves for three lattices with the same apparent elastic modulus are shown in Figure 3.12. The drop force is indicated with a red circle.

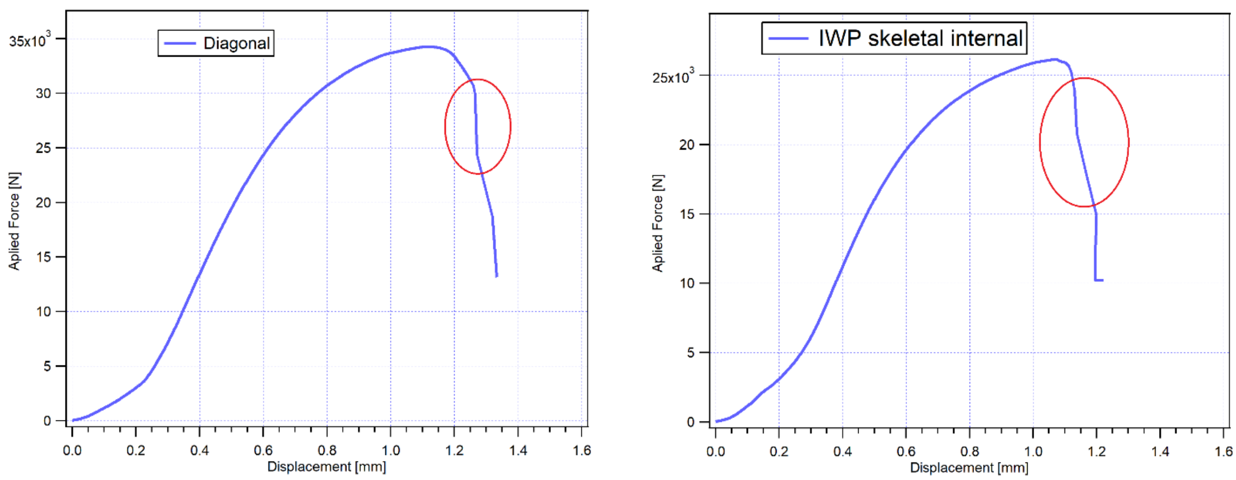

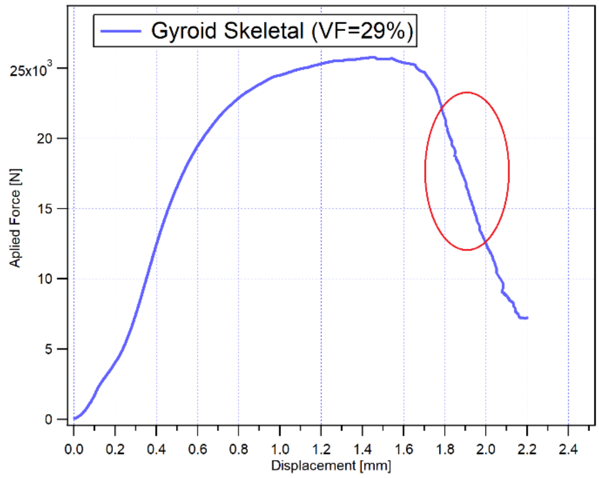

Figure 3.12. Drop of force when a specimen is fractured under a compressive load for three lattice topologies with the same apparent elastic modulus. Diagonal (top left), IWP skeletal internal (top right), and Gyroid skeletal (bottom) topologies.

Once the presentation of the experimental protocol, methodology, and the obtained results is finished, the presentation of the numerical procedure and results follows. Section 3.2.3. includes all the details about the numerical part of the investigation.

3.2.3. Numerical procedure using Finite Element Analysis; comparison of two different boundary conditions and calculation of the apparent elastic modulus of lattices

The five aforementioned topologies have been numerically investigated by using the Finite Element Analysis software Abaqus. Two sets of tests have been carried out for single unit cells with different boundary conditions, namely PBC and CBC. This has been performed to compare the results and select the representative of the real experimental boundary conditions based on the estimation of the apparent elastic modulus of the unit cells. The mesh and the applied non-linear constitutive law (Appendix C) are the same in both numerical models. In Figure 3.13., the CBC are presented in a graphical way.

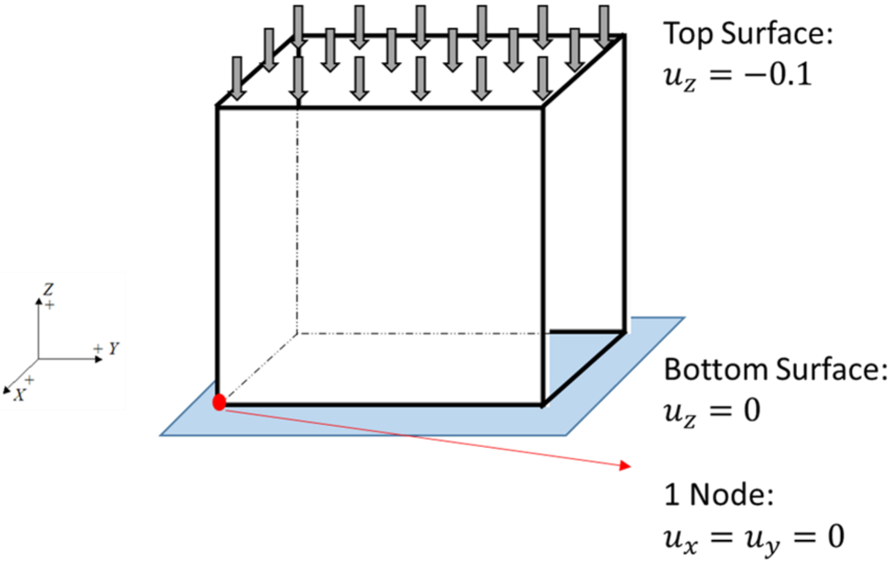

Figure 3.13. Compressive Boundary Conditions (CBC) in a graphical way applied in the second set of numerical tests in Abaqus.

Once the computations are over, the elastic modulus of the unit cells is calculated. The equation (16) given in chapter 2 is used for the calculation of the elastic modulus after the application of the PBC. The summation of the reaction forces (RF) divided by the area (A) and the applied displacement divided by the initial length of the unit cell gives the elastic modulus after the application of the CBC. In Table 3.3. the computed elastic modulus of all the unit cells after the application of both boundary conditions is presented.

Topology	**Stiffness level target**	**E_{PBC} [MPa]**	**E_{CBC} [MPa]**
Gyroid sheet	14300	14280.2	10533.0
Gyroid skeletal	14300	14310.8	14104.0
Gyroid skeletal	5600	5586.8	5133.7
IWP skeletal	5600	5602.5	4803.2
Diagonal	5600	5603.1	4462.0

Table 3.3. The numerically computed apparent elastic modulus for five unit cell topologies after the application of PBC and CBC.

The next step of the numerical investigation is the graphical comparison of both the linear and non-linear responses of the topologies. The responses of all unit cells after the application of both boundary conditions are plotted in Figure 3.14.

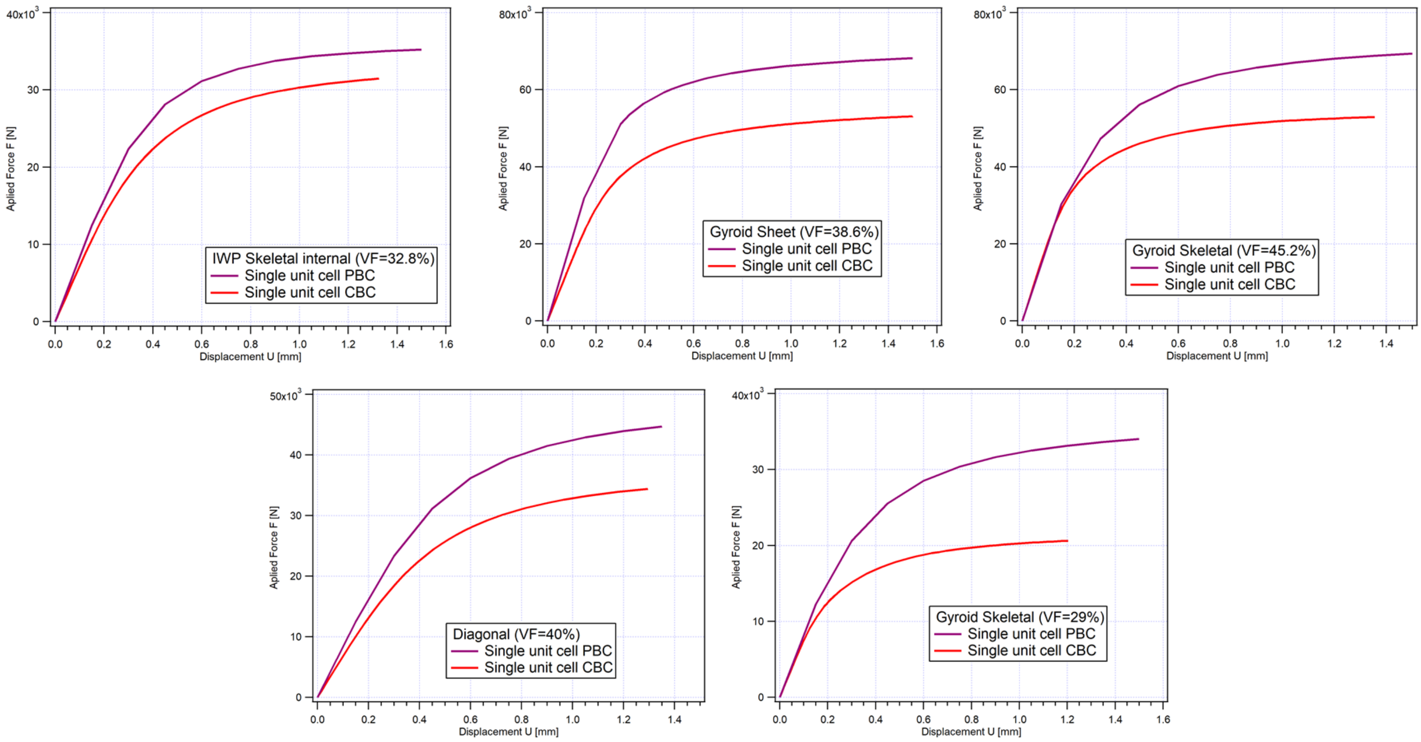

Figure 3.14. Graphical presentation of the linear and non-linear response of the topologies after the application of both boundary conditions.

All the numerical and experimental results are plotted on the same graphs, compared, and discussed in detail in the following section.

3.3. Comparison, presentation, analysis, and discussion of numerical and experimental results

In this section, all the numerical and experimental results for the investigated topologies are presented together and compared. In the standard case, the stiffness match between lattices and human bone is essential. Therefore, the selection of the numerical boundary conditions that allow the most accurate computation of the elastic modulus of the unit cells is important. In the destructive case, the investigation of the so-called functional damage, i.e. the plastic deformation and the occurrence of a few cracks, is carried out experimentally. This section is structured as follows: the first part is a discussion about the complete comparison of the numerically computed and the experimentally measured elastic moduli per topology and the selection of the most suitable numerical boundary conditions. The second part includes a discussion about the experimental results regarding the functional damage and the final fracture of the lattices. The last part presents the selection of safety factors for the design of lattices aimed at biomechanical applications in an engineering approach.

3.3.1. Comparison of two boundary conditions and selection of the most representative

A collection of all the previously described numerical and experimental results per topology for a global comparison is presented in Table 3.4. The numerically computed volume faction of the unit cell, $\boldsymbol{VF_{CAD}}$ is compared with the experimentally measured volume fraction of the lattices, $\boldsymbol{VF_{EXP}}$. $\boldsymbol{Diff\ (a)} = \left|\frac{VF_{CAD}-VF_{EXP}}{VF_{CAD}}\right|$ is the relative difference between those two values. $\boldsymbol{E_{EXP}}$ is the experimentally measured elastic modulus of the lattices, $\boldsymbol{E_{PBC}}$ and $\boldsymbol{E_{CBC}}$ are the computed elastic moduli of single unit cells after PBC and CBC application, respectively. $\boldsymbol{Diff\ (b)}$ and $\boldsymbol{Diff\ (c)}$ are the relative differences between $\boldsymbol{E_{EXP} - E_{PBC}}$ and $\boldsymbol{E_{EXP} - E_{CBC}}$, respectively. They are defined as $\boldsymbol{Diff\ (b)} = \frac{E_{EXP}-E_{PBC}}{E_{EXP}}$ and $\boldsymbol{Diff\ (c)} = \frac{E_{EXP}-E_{CBC}}{E_{EXP}}$.

Topology	$\boldsymbol{VF_{CAD}}$	$\boldsymbol{VF_{EXP}}$	$\boldsymbol{Diff\ (a)}$	$\boldsymbol{E_{EXP}}$ **[MPa]**	$\boldsymbol{E_{PBC}}$ **[MPa]**	$\boldsymbol{E_{CBC}}$ **[MPa]**	$\boldsymbol{Diff\ (b)}$	$\boldsymbol{Diff\ (c)}$
Gyroid sheet	0.386	0.39	1.3%	14565	14280	10533	1.96%	27.68%
Gyroid skeletal	0.452	0.46	2%	15687	14310	14104	8.77%	10.09%
Gyroid skeletal	0.29	0.29	0%	5932	5586	5133	5.82%	13.46%
IWP skeletal int	0.328	0.34	3.4%	5658	5602	4803	0.99%	15.12%
Diagonal	0.4	0.41	1.3%	6243	5603	4462	10.25%	28.53%

Table 3.4. Complete table with the numerically computed and experimentally measured elastic moduli and volume fractions for 5 investigated topologies. The relative differences are presented as well.

Moreover, the force-displacement curves for all the topologies obtained from the experimental and both the numerical tests are collected and plotted on the same graphs for an easy global graphical comparison. They are presented in Figure 3.15.

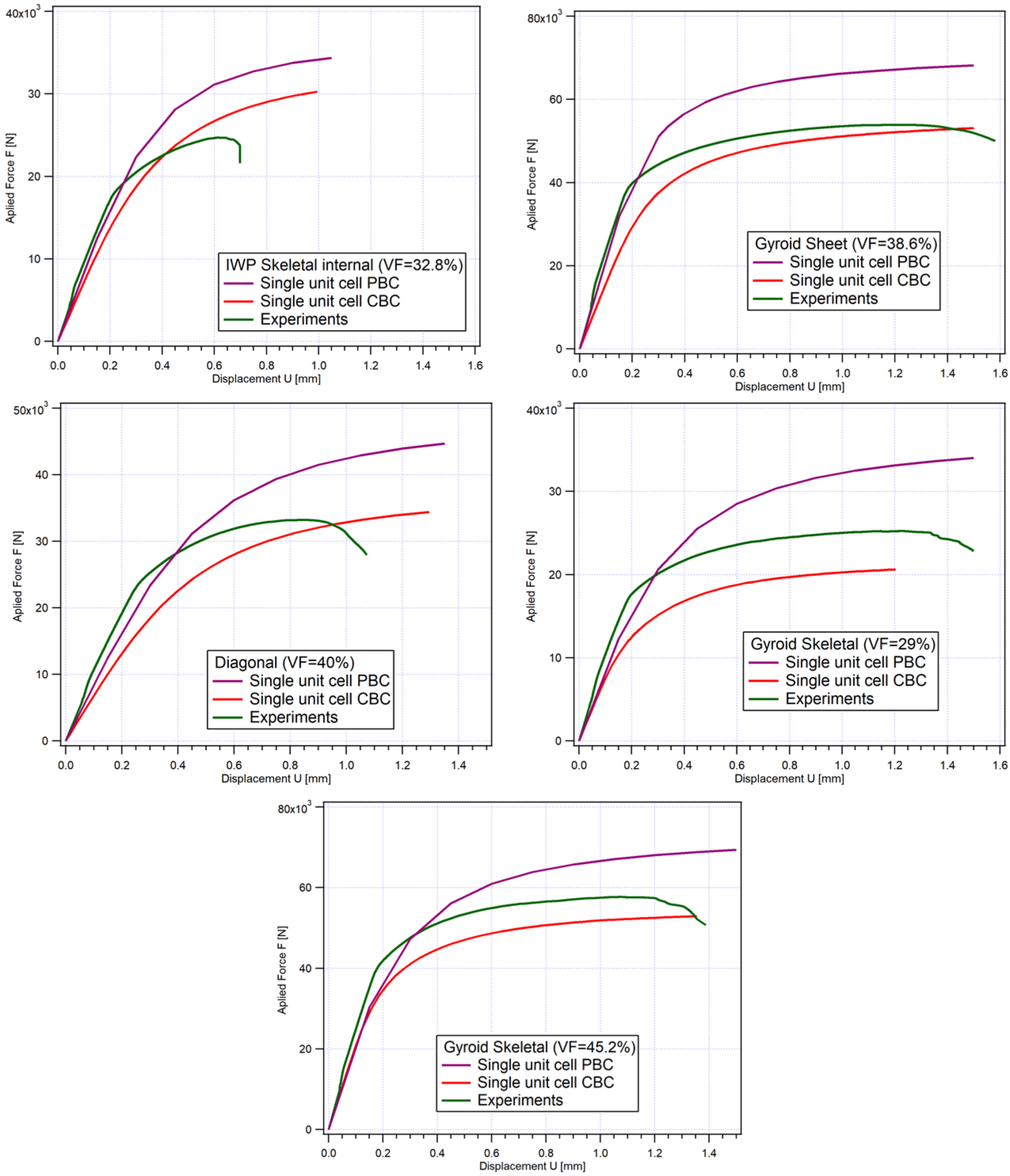

Figure 3.15. Graphical presentation of the linear and non-linear response of the topologies after the experimental and both the numerical tests.

As can be seen in Table 3.4., there is a slight volume fraction difference between the numerical 3D model and the experimental specimen for almost every topology, apart from the Gyroid skeletal topology at a low volume faction level (VF=0.29). This volume fraction difference may be caused by various experiment-dependent reasons. The 3D model is a perfect structure and it is sure that it cannot be exactly reproduced by any experimental method. Therefore, the fabrication procedure itself may cause a slight volume fraction variation. For instance, half-melted powder grains exist all over the surface of the lattices. Also, extra deposition of material at the bottom face of unsupported surfaces (orientation level = 0^o) occurs due to the temperature fluctuation. Extra material is also deposited at the corners (i.e. strut connections) of the strut-based lattices. The latter can be seen in Figure 3.16 for a Diagonal lattice. The red arrow indicates the area with the extra material. Furthermore, the process of the removal of the supports and polishing of the bottom surface is done manually, and thus, all the material that should have been removed, in the end, may not have been perfectly removed. The half-melted grains do not have an effect on the overall stiffness of the lattice, but the extra remaining material of the supports at the bottom surface after the polishing may increase slightly the stiffness of the lattice.

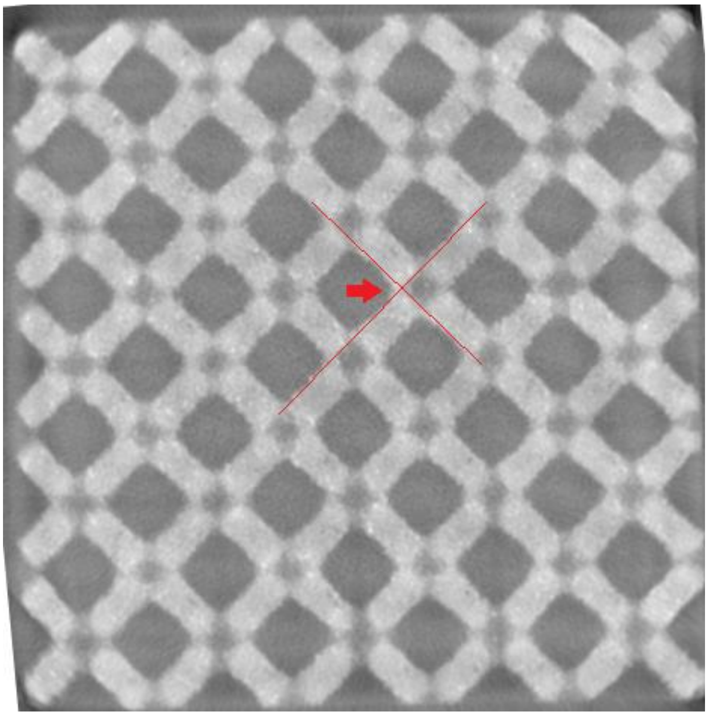

Figure 3.16. μ-CT scan of a Diagonal topology where the extra material at the strut connection is obvious.

Regarding the experimentally measured elastic modulus of the lattices as presented in Table 3.4. and Figure 3.15., it is always larger than the computed elastic modulus obtained from the numerical tests with both boundary conditions. In particular, the relative difference between the experimental and numerical results after the application of the PBC varies at an acceptable range for all the investigated topologies. The relative difference is topology-dependent and especially some topologies such as IWP skeletal internal and Gyroid sheet exhibit a very low difference between numerics and experiments. This difference is the result of various errors that occur. It should be taken into account that the periodic homogenization normally should be applied when the scale separation assumption, $\bar{x} \gg x$, is considered. In this particular case, this assumption is not completely respected. While the size of the unit cell is much lower than the size of the real specimen, the number of unit cell repetitions in the experimentally tested lattices is not large enough. The number of the unit cell repetitions is only 5 per direction. The violation of the scale separation assumption is one of the main sources of the non-zero relative difference.

The lowest difference between $\boldsymbol{E_{EXP}}$ and $\boldsymbol{E_{PBC}}$ is presented by the IWP skeletal internal (~1%) and the largest by the Diagonal topology (~10%). It is quite interesting that these two extreme cases are presented by these two topologies, which exhibit the same global BCC structure, as shown in Figure 2.12. Deposition of material at the corners of strut connections for a Diagonal lattice caused by both thermal fluctuation and the topology itself may be an explanation, as previously presented in Figure 3.16.

Regarding the relative difference between the experimental and numerical results after the application of the CBC, it is always larger than the difference between $\boldsymbol{E_{EXP}}$ and $\boldsymbol{E_{PBC}}$ and it varies at a non-acceptable range for the investigated topologies. Only the difference for the Gyroid skeletal with VF=0.452 could be considered as accepted. Some topologies can reach a difference up to almost 29%, which is very large. This difference may be caused by boundary effects in the numerical models.

The comparison of the computed elastic modulus of unit cells after the application of two types of numerical boundary conditions shows that the results after the application of the PBC are much closer to the results obtained from the experiments. Therefore, the PBC are selected as the most representative boundary conditions although the scale separation assumption is not rigorously respected.

Moreover, the maximum force and the apparent non-linear threshold σ_{yield} of the lattices after the application of the PBC are always larger than the corresponding experimental values. The fabrication and testing processes are governed by various experimental-process-dependent errors such as residual stresses during fabrication, the material metallurgy itself after the fabrication, and the local stresses during testing that can affect the global stress state of the lattice. Therefore, the experimental results differ from the numerical ones. Moreover, the accumulated damage as presented in Figures 3.6., 3.7., 3.8. and possible buckling caused by high local stresses in the experimentally tested specimens may lead the non-linear region of the curves and the apparent σ_{yield} to be lower than the corresponding numerical ones. For instance, this is the case for the Gyroid sheet topology; the maximum force at the non-linear part is much larger than the experimental force and this may be caused by the local buckling of the very thin ''sheets'' of the lattice itself.

3.3.2. Fracture of the lattices; experimental results

In order to investigate the functional damage and the final facture of the lattices in the destructive case, various experimental tests have been carried out. As previously described in section 3.2.2.3. the following tests have been conducted: a) interrupted tests at different force levels to observe any plastic deformation and any cracks (functional damage) that occurred with the help of the X-ray micro-tomography, b) loading-unloading tests to identify the importance of the functional damage by comparing the slopes of the elastic regions, and c) uniaxial compression tests until fracture to investigate the final macroscopic fracture. a) and b) sets of tests are performed only for a Gyroid skeletal topology at $VF = 0.29$ because the experimental process is highly raw-material-consuming whereas c) compression tests are performed for all topologies.

Compression tests have been carried out up to various force levels for a Gyroid skeletal lattice. These are refered to as interrupted tests. Figure 3.6. shows two planes of the Gyroid skeletal topology with multiple length measurements between two points, i.e. curve peaks, at a compressive load of $90\% * F_{max} \approx 20500\,N$. The difference among length measurements indicates plastic deformation. The variability of the length measurements is significant, especially in the vertical axis. The vertical measurements vary in the range from 6.9855 to $5.9878\,mm$ $(+/-\ 0.01156\,mm)$ which indicates permanent plastic deformation. On the contrary, the horizontal length measurements do not present important variations. At $65\% * F_{max}$ and $75\% * F_{max}$ levels, there is not any significant plastic deformation. However, it should be mentioned that the slight variability in the fabrication parameters due to the nature of the process, has an effect on the plastic deformation of all the lattices at all force levels.

Apart from the measured plastic deformation, a few cracks have been also observed. Specifically, Figure 3.7. shows three planes of a Gyroid skeletal lattice with small cracks detected with the help of the x-ray micro-tomography. The lattice has been compressed until the force level: $90\% * F_{max} \approx 20500\ N$. The number of the occurrence of the cracks is very low and cracks can be found only in a few planes of the lattice structure even though the percentage of the compression force is high. No cracks have been observed at $65\% * F_{max}$ and $75\% * F_{max}$ force levels.

To identify then the importance of the plastic deformation and cracks to the apparent elasticity of the lattice, a loading-unloading test has been carried out. An already compressed Gyroid skeletal lattice up to $65\% * F_{max}$ level which has been left to relax is again loaded up to $75\% * F_{max}$ and $90\% * F_{max}$ and unloaded successively. The plastic deformation is negligible at the level of compression force $65\% * F_{max}$ and thus, further loading is allowed. The final force-displacement curve is presented in Figure 3.8.

The difference in the slopes, i.e. the ''elastic modulus'', of the unloading regions of the curve can indicate the effect of the damage on the stiffness of the lattice. The slopes are the same, and thus the microscale functional damage (plastic deformation and the occurrence of few cracks) is considered insignificant and it does not affect the macroscale stiffness. Moreover, it seems that the local cracks do not affect the local stress concentrations. Therefore, this non-zero functional damage can be considered as a geometry-based phenomenon that is neither related to material nor rheology.

Regarding the macroscopic fracture of the lattices under a uniaxial compression load, the results presented in Figure 3.9. indicate that the volume fraction does not affect the macroscopic fracture which occurs at 45^o for two lattices with the same topology as mentioned also in [88]. Moreover, the fractured lattices presented in Figure 3.10. indicate that generally, the fracture occurs at 45^o for all the topologies. After a combination of the results presented in Figures 3.10. and 3.11., the Diagonal topology presents a ''brittle'' macroscopic fracture, as the two halves are totally separated and the drop of force in the force-displacement curve is abrupt. Actually, the smooth or abrupt drop of force is an indicator of the type of macroscopic fracture of the lattices, i.e. ''brittle'' or ''ductile'' fracture. The maximum shear force is applied on the fracture plane for the Diagonal lattice. On the contrary, the Gyroid sheet lattice exhibits a ''pseudo-ductile'' macroscopic fracture and the barrel effect is obvious. The force drops in the smoothest way among all lattices. This ''ductile'' fracture is caused by the instability of the lattice geometry and not by the material itself. The buckling of the ‘’sheets’’ of the Gyroid sheet lattice occurs due to their low thickness. The fracture of the Gyroid skeletal topology is characterized as neither ‘’brittle’’ nor ‘’ductile’’ because it is governed by all the previous fracture mechanisms. The drop of the force is neither very smooth nor very abrupt. The drop of force for the IWP skeletal internal topology is the same as the drop of force for the Diagonal topology.

3.3.3. Selection of safety factors for the biomechanical design of lattices and the most suitable topology

When it comes to the design of lattices for biomechanical applications by taking into consideration the fatigue life, the appearance of even small cracks is not accepted. The functional damage that occurs in the lattices, i.e. the plastic deformation and the occurrence of a few cracks, may lead to structural damage of the lattices after the application of a cyclic load. Therefore, the $F_{\max\_applied} < 90\% * F_{max} \rightarrow \sigma_{\max\_applied} < 90\% * \sigma_{max}$ level cannot be considered as an accepted force/stress limit for the design of lattices, where $F_{\max\_applied}$ and $\sigma_{\max\_applied}$ are the maximum force and stress that should be applied to lattices designed in the future and F_{max} and σ_{max} are the force and stress that have been applied to the lattices of this study.

However, in this study a deep local-fatigue analysis has not been carried out; only a brief experimental macroscopic-fracture analysis has been made. Therefore, in this case, the local damage in the lattices is not taken into consideration for the design of lattices to be used as parts of implants. Only the avoidance of an abrupt fracture is important. According to an engineering approach, , the $F_{\max\_applied} < 90\% * F_{max} \rightarrow \sigma_{\max\_applied} < 90\% * \sigma_{max}$ level is then considered as accepted in this case.

Regarding the investigated topologies, the Gyroid sheet exhibits a global failure which is ‘’pseudo-ductile’’ and not a ‘’pseudo-brittle’’ one. Moreover, the Gyroid sheet topology exhibits very good manufacturability and a low difference between numerical and experimental volume fraction and apparent elastic modulus. Therefore, it can be considered as a suitable topology for biomechanical applications.

3.4. Conclusions

In the present chapter, both the numerical and the experimental results regarding the linear, non-linear response of various lattices, the functional damage and the final fracture are presented. First, unit cells are numerically investigated with the application of both periodic (PBC) and compressive boundary conditions (CBC) regarding the elastic modulus measurement. Second, experimental compression tests are carried out to validate the numerical results by measuring the elastic modulus and getting the non-linear response of the lattices. Moreover, experimental investigation of the functional damage occurred and the macroscopic fracture of the lattices has been carried out. In the end, the most representative boundary conditions and the most suitable lattice topology are selected according to the complete numerical-experimental analysis.

The following conclusions have been reached:

- ✓ The lattices can be fabricated in a very accurate way by using additive manufacturing technology and an SLM machine. The volume fraction discrepancy between numerical models and fabricated lattices varies at an acceptable range for all the lattices.

- ✓ The application of the PBC allows a very accurate prediction of the apparent elastic modulus of the lattices. Therefore, they are selected as more representative boundary conditions compared to the CBC even though the scale separation assumption for the application of the periodic homogenization is not rigorously respected for the fabricated specimens.

- ✓ The maximum force and the apparent non-linear threshold σ_{yield} of the lattices are always larger than the corresponding experimental values. This is due to accumulated fabrication and testing process errors and the functional damage that occurs.

- ✓ Even though the functional damage that occurs affects the experimental results regarding the maximum force and the apparent non-linear threshold σ_{yield}, it does not affect the apparent stiffness of the lattices.

- ✓ All the lattices, no matter neither the topology nor the volume fraction present a final fracture at around 45^{o}. However, some topologies present a ‘’brittle’’ macroscopic fracture whereas others exhibit a ‘’ductile’’ fracture. The type of the macroscopic deformation and fracture is topology-dependent.

- ✓ Gyroid sheet topology can be considered a suitable topology for biomechanical applications because it exhibits very good manufacturability, a low difference between numerical and experimental results, and a macroscopic ’pseudo-ductile’’ failure.

A couple of topologies have been studied to replace parts of the real bone which is subjected to real load for the validation of the selection of the most suitable topology for biomechanical applications. All the details are given in the following chapter.

4. Partial replacement of femoral bone using TPMS-based lattices, modelling and stress analysis

4.1. Introduction

As have been detailed in chapters 2 and 3, the use of lattice structures offers the opportunity to control and tailor the apparent elastic modulus and overall mechanical properties of an implant. Therefore, lattices can replace certain parts or a whole biomedical device and allow the construction of custom-made and patient-specific implants. The latter can mimic the material properties of the real human bone successfully. By performing this process, any postoperative mechanical problems that occur, such as the stress shielding, are minimized as has been previously mentioned [15], [20], [63], [89].

Hip replacement is one of the most common operations regarding orthopedic implants. It is the treatment of various femoral health issues, such as rheumatoid arthritis, osteoarthritis, tumors, and fractures that can occur. Various medical imaging techniques, such as Magnetic Resonance Imaging (MRI) and Computed Tomography (CT scan) are used by physicians and surgeons for the diagnosis of hip diseases [90], [91]. Moreover, the aforementioned medical techniques are helpful diagnostic tools to monitor any problems that occur on implants after a hip replacement [92], [93].

Furthermore, medical imaging techniques are very helpful when it comes to the collection of personal medical data and orthopedic information from the patients in order to create patient-specific implants. The size and shape of the femoral bone and the hip joint differ among the people depending on age, sex, height, etc [94]. Moreover, the elastic modulus of a bone is not a constant value. It varies in the global range $0.02 - 30\ GPa$ according to the bone structure, i.e. cancellous or cortical, and according to the direction, i.e. longitudinal or transverse [15], [95]. Therefore, the patient-specific implants can be utilized when the commercial implants are not suitable for the patients due to anatomical geometry discrepancy. The custom-made and patient-specific implants offer a promising option to treat hip diseases in a more tailored way, minimize surgical time and overall procedural costs, and improve patients' outcomes [71], [96], [97]. Concerning the fabrication of the custom-made implants, thanks to additive manufacturing technology, the fabrication of complex, freeform geometries and shapes is easily achievable [98].

The storage of medical data has been a challenge due to the occurrence of several medical equipment manufacturers. A standard for the storage and exchange of the patients' images has been necessary and the DICOM (Digital Imaging and Communication in Medicine) international standard has been developed [99], [100]. The latter allows easy storage and transmission of patients' medical information obtained from medical devices with the aforementioned imaging techniques [99], [101], [102]. The images with the DICOM format present the scanned area of a human body at three planes, i.e. the sagittal, coronal, and axial planes, and all the morphological features of the hard and soft tissues are portrayed [96]. They are grayscale images according to the Hounsfield Units (HU) which allow the measurement of the radio-density in a quantitative way. Indeed, the density of the tissues in the human body is proportional to the absorption of the x-ray beams. Distilled water corresponds to 0 HU, while air is described with around -1000 HU. Dense tissues with high HU, such as the bone are portrayed with white color whereas tissues with lower HU, such as fat and muscles are portrayed in various grey levels. Air is presented with black color [103]–[105].

DICOM images are a very useful tool not only for radiologists and surgeons but for engineers as well. After the acquisition of the images and the appropriate post-processing, the 3D volume can be reconstructed for further investigation, such as FEA or fabrication with additive manufacturing techniques and experimental testing. This process is known as reverse engineering and it could help the improvement of the treatment by creating patient-specific implants and by optimizing topologically the final medical devices. An example of the complete process that starts from the acquisition of the CT-scan images up to the creation of the final implant and the application in the human body following the reverse engineering method is illustrated in Figure 4.1. The contribution of this chapter to the complete process focuses on the virtual design and the FEA testing of various TPMS-based lattice topologies. The selection of the most appropriate topology for an orthopaedic implant is based on the numerical results.

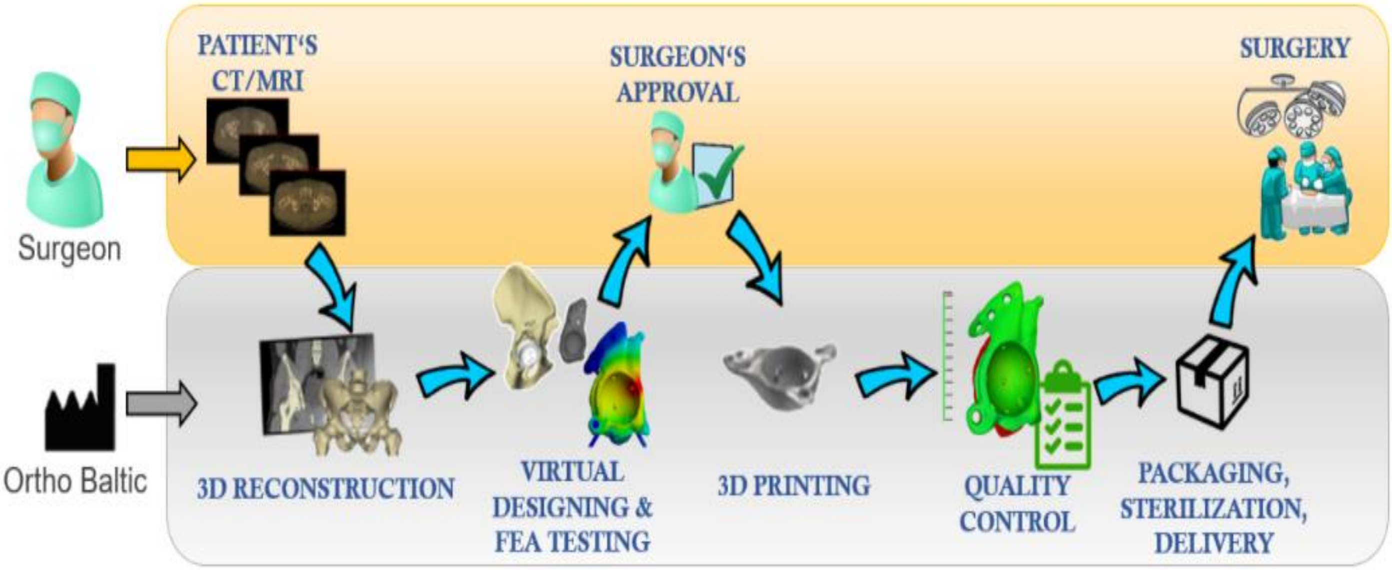

Figure 4.1. The complete process starts from the acquisition of the CT-scan images up to the creation of the final implant and the application in the human body following the reverse engineering method [106].

It is noteworthy that DICOM images give information about the radio- density of the human tissues and thus, about the local elastic modulus apart from their morphological features. Many researchers have investigated the correlation of the HU and the elastic modulus of various human tissues such as [105], [107]–[109].

The objective of this chapter is the replacement of a specific part of a femoral bone constructed by DICOM images by TPMS-based unit cells in a numerical way. The unit cells are generated to have the same elastic modulus as the femoral part and the boundary conditions that are subjected to simulate the physiological load. The comparison of the stress state among the femoral part and the unit cells leads to the selection of the most appropriate topology for the replacement in a particular case study.

All the above-mentioned are discussed in detail in the following sections. Particularly, this chapter is structured as follows: section 4.2. describes the complete methodology and all the steps followed regarding the generation of the global and local models and the FEA, section 4.3. presents all the numerical results and complete analysis, and finally, section 4.4. presents the conclusions that have been reached.

4.2. Methodology

This section describes the steps of the implemented numerical methodology in a real case study. The methodology is divided into two parts, the generation of the global and local models for FEA, respectively. The creation of the global model is based on DICOM images for the geometric model and the assignment of the material properties. The applied boundary conditions correspond to the physiological load on a femoral bone and they have been acquired from experimental testing on real patients given in a public database. The creation of the local model is based on the global model regarding the local elastic properties and the local boundary conditions. All the details about the steps of the methodology are given in the following sections.

4.2.1. Global model; femur bone with real elastic properties subjected to real boundary conditions

4.2.1.1. Creation of the 3D model

The first step involves the generation of a macroscopic 3D model which consists of a femur bone. In the framework of a scientific cooperation with Institut de Biomécanique Humaine Georges Charpak (IBHGC) laboratory, medical images in a DICOM format from an anonymous female patient have been used in this study. The stack of DICOM images is imported into Materialise Mimics software. The segmentation of the images starts with the creation of a mask representing a femur bone based on the HU of the real cortical bone, i.e. $HU \geq 700$ [108]. The internal cavity that corresponds to the trabecular bone has lower HU. The area is then selected manually in each image and finally, unified with the initial mask. A final mask of the complete femur bone, i.e. both cancellous and cortical structures is created. The 3D model is generated and is exported to .STL file format. In Figure 4.2., the DICOM images of a patient's pelvis and femoral bone in Materialise Mimics software are presented. The images are displayed in three views, namely a) the coronal, b) the axial, and c) the sagittal views. The axial view can be referred to as transverse view as well. The created mask after the segmentation portrayed in beige, d) the reconstructed 3D model, and e) the three anatomical planes are presented as well. The three views are in accordance with the anatomical planes in Mimics software.

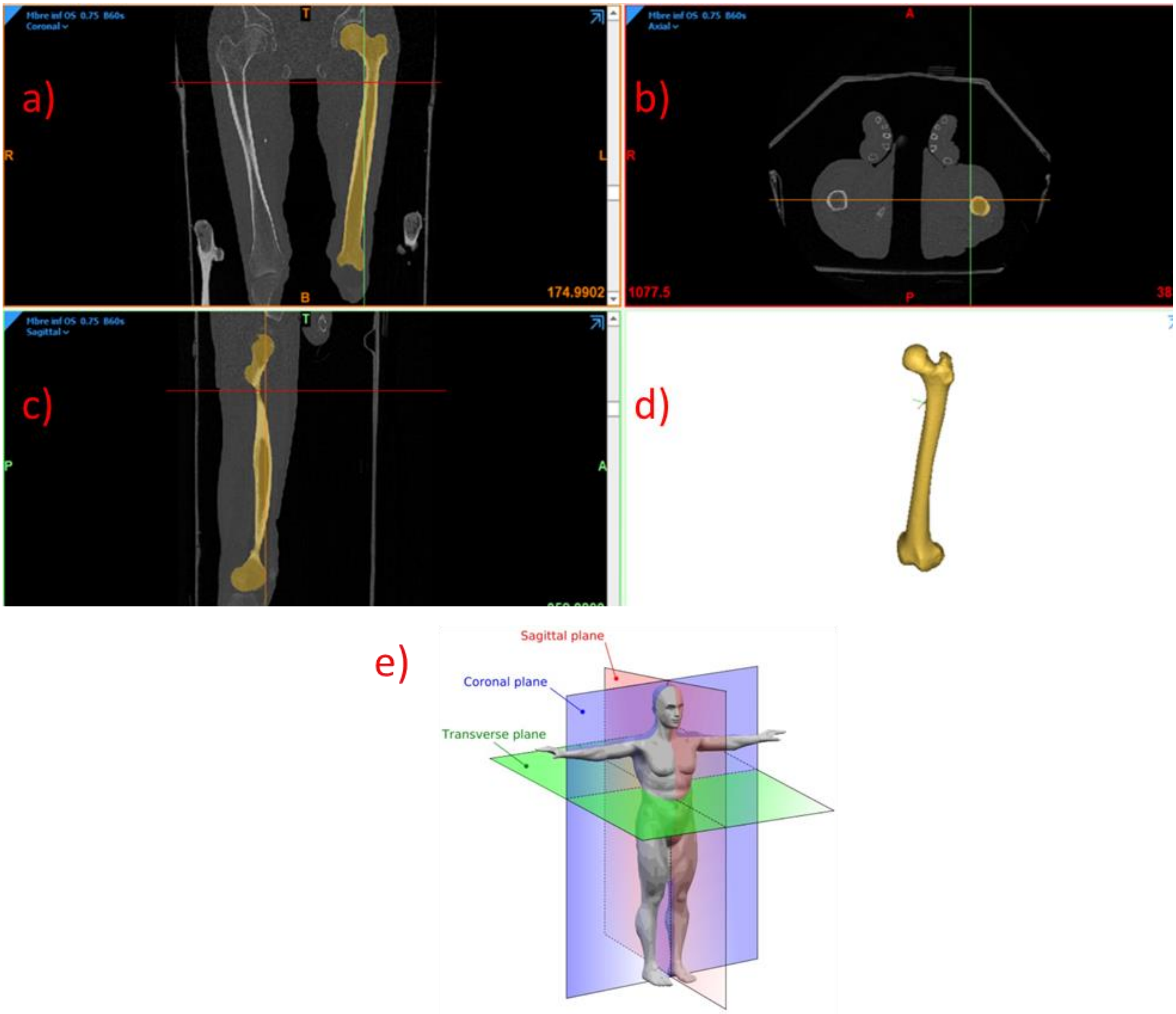

Figure 4.2. Three views of DICOM images of a patient's pelvis and femoral bone in Materialise Mimics software: a) coronal, b) axial, and c) sagittal views, d) the reconstructed 3D model of a femur bone and e) the anatomical planes [110].

Once the 3D model is ready, it is imported into Materialise 3-matic software. Since the two softwares are products of the same company, they are connected. Thus, a simple 'copy-paste' operation of the object is enough to transfer the 3D model. The latter is subjected to a 'smooth' operation in order to obtain a smoother surface than the initial model. The surface mesh is corrected, it gets more uniform and its quality is higher than before and more appropriate for FEA. Then, the FE volume mesh is generated with tetrahedral C3D4 elements based on the triangulation of the surface mesh. In Figure 4.3. a) the 3D model with the uniform triangulation after the correction of the surface mesh is presented. In Figure 4.3. b) the FE volume mesh (654380 elements) of the femur is presented as well.

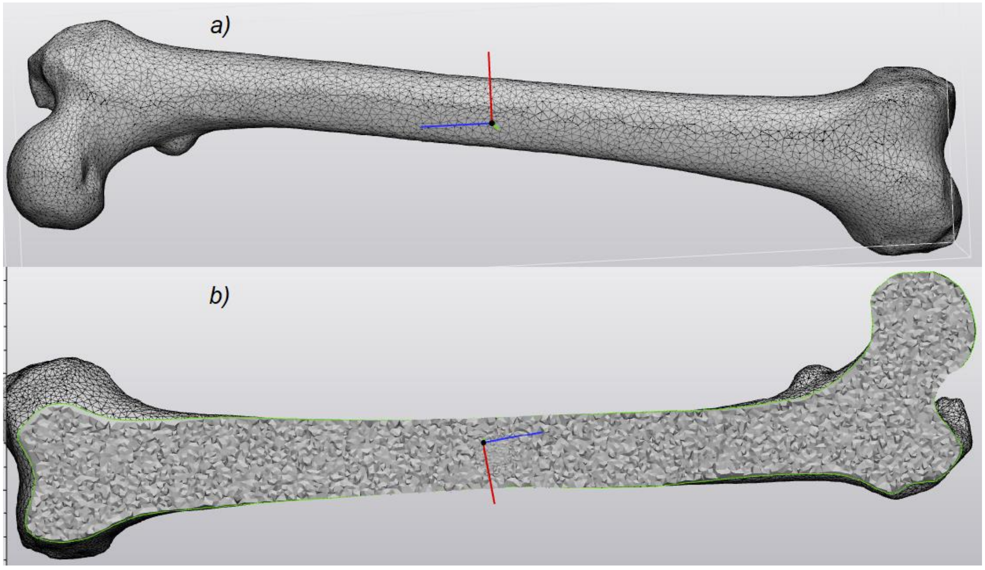

Figure 4.3. The 3D model of the femur with a) the uniform triangulation after the correction of the surface mesh and b) the FE volume mesh generated in 3-matic software with 654380 elements in total.

The new 3D model is copied to Mimics software again for an accurate assignment of the elastic material properties by combining the information of the DICOM images and the volume mesh. Particularly, in [108], a table is presented with the typical range of the HU for various human tissues for both adults and children. The HU values corresponding to compact and trabecular bones for adults have been selected and they have been rounded for an explicit representation of the HU bounds. In this case study, three different material types have been created according to the acquired different HU ranges. The first HU range corresponds to the cortical bone and it is defined as $HU_{cortical} > 700\ HU$. The second range corresponds to the trabecular bone and it is defined as $150\ HU \leq HU_{trabecular} \leq 700\ HU$. The third HU range corresponds to the soft tissues, such as muscles and fat and it includes the lowest positive HU values and the negative ones as well [108].

Regarding general case of the cortical bone, a linear relation between the elastic modulus and the density described by the HU gives accurate results according to [107]. Three different elastic modulus ranges describe the cortical bone in the longitudinal and two transverse directions. However, in this case study, the elastic properties of the bone are assumed linear and only one elastic modulus range for the cortical bone is applied which is set between $10000 - 18000\ MPa$ in order to take into consideration both the high and the low elastic modulus of the femoral cortical bone in all directions [111], [112]. Therefore, a different elastic modulus value is applied to each element according to the intensity of the grey level (HU) and to a linear law where $E_{min} = 10000\ MPa$ and $E_{max} = 18000\ MPa$.

Regarding the specific case of the femoral trabecular bone, a set of equations has been used to relate the HU that describes the density, and the applied elastic modulus according to [107] where several equations are proposed for a couple of different bones. The equations taken from [107] and used in this study considering one more time isotropic material properties are the following:

$$\rho = 131 + 1{,}067 * HU_{trabecular} \tag{21}$$

$$E = 0.25 * \rho^{1.3} \tag{22}$$

where ρ is the density described by the HU and E is the applied elastic modulus to each element. Particularly, equation 21 relates the density of the tissues to the HU values from the DICOM images. Then, equation 22 allow the assignment of the elastic properties to the elements according to the previously defined density of the tissues.

For the elements with $HU_{low} < 150\ HU$, if there are any, a very low elastic modulus has been given. Each material type is divided into several subdivisions. For instance, the material type that corresponds to the elastic modulus of the cortical bone is divided into ten subdivisions. Those ten subdivisions and the femur bone after the assignment of the material properties are presented in Figure 4.4.

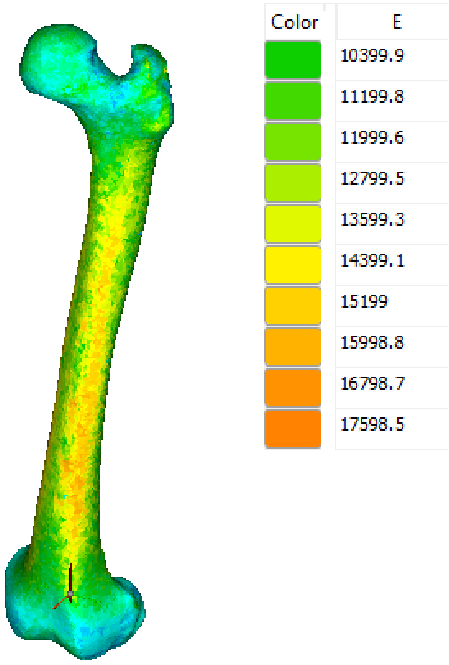

Figure 4.4. Ten subdivisions of the material type that corresponds to the elastic modulus of the cortical bone and the femur bone after the assignment of the material properties in Materialise Mimics software.

Once the assignment of the material is completed successfully, an .INP format file is exported from Mimics. This file is the input file to Abaqus for a FE analysis that follows. The kind of boundary conditions that represent the real load on the femur bone are detailed in the next section.

4.2.1.2. Applied real boundary conditions

A femoral bone is typically subjected to a complex load, which varies according to the activity performed by a person, such as walking, stair climbing, jumping, and jogging. A combination of skeletal and muscular forces leads to the final complex load as explained in [113]. In this case, the walking loading case has been selected. In order to define the boundary conditions to use for a FE analysis of a complete femur bone, the computation of the resultant hip contact force F_{RES} and its components F_x, F_y, and F_z is necessary. The database https://orthoload.com collects several data obtained from in-vivo tests on patients with hip implants performing several common everyday activities. The methodology for the computation of the F_{RES} described in [113], [114] is applied to ten patients, and the final F_{RES}

signals are averaged and adapted to a body mass of 75 kg which is the average weight of people in Europe. The aforementioned data and methodology have been combined in [6] where the maximum F_{RES} is computed. That F_{RES} is utilized in this study as well. The selected forces for the application to a FE model are the following: $F_{RES} = 1859\ N$, $F_x = 535\ N$, $F_y = -342\ N$ and $F_z = -1747\ N$. The coordinate system of a femur bone for the application of the component forces for FEA is shown in Figure 4.5. Moreover, all the displacements and rotations in all three directions at the lowest part of the femoral bone, i.e. the knee joint have been blocked for the mechanical equilibrium.

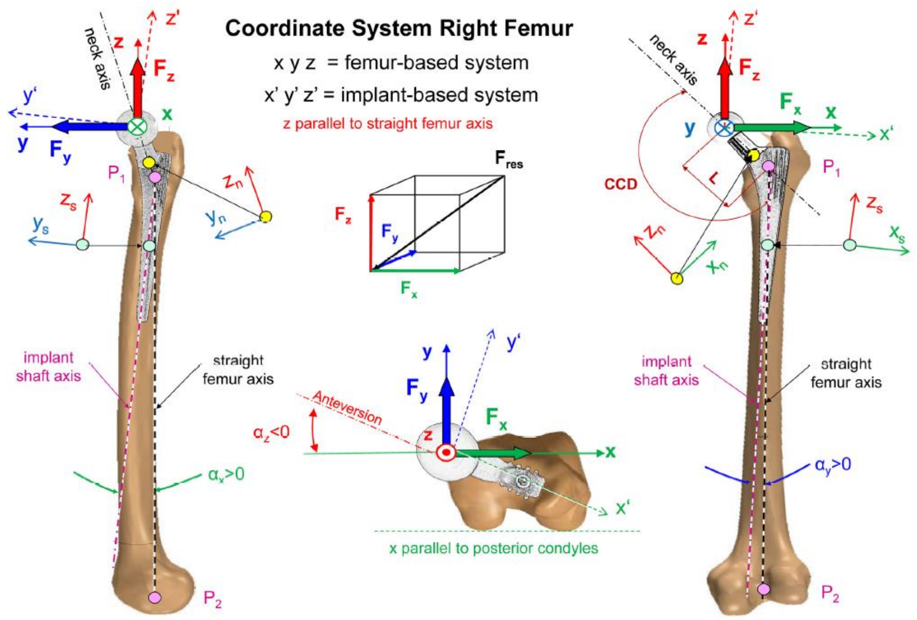

Figure 4.5. The coordinate system of a femur bone for the application of the component forces of the F_{RES} for a FEA [6], [114].

The next step is the definition of the muscular forces to which the femoral bone is subjected. The data taken from the database https://orthoload.com, the CT-scan data from Visible Human [115], and the methodology described in [113] are combined in [6] where the simplified muscular forces are computed. Those muscular forces are selected and used in this study. The complete numerical 3D model of the femoral bone in Abaqus and the values of forces are presented in Figure 4.6. The RP1 is the point where the F_{RES} is imposed and the RP2 and RP3 are the reference points where the muscular forces are imposed. All the degrees of freedom of those three reference points and the relevant nodes around them have been constrained to be connected. This is carried out to avoid any singularities and non-realistic final results caused by the application of the boundary conditions. The lower part of the femur is totally blocked, where $U_1 = U_2 = U_3 = UR_1 = UR_2 = UR_3 = 0$ are applied.

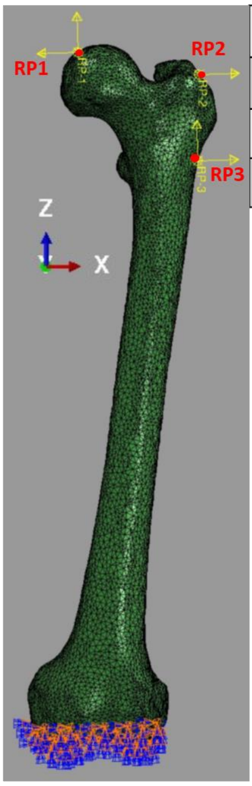

	F_x	F_y	F_z
RP1	535 N	-342 N	-1747 N
RP2	333 N	-103 N	-378 N
RP3	159 N	-150 N	470 N

Figure 4.6. The complete numerical model of the femoral bone in Abaqus and the values of the muscular forces applied to the reference points RP2 and RP3.

The following step is the creation of an element set which is actually the Area of Interest (AoI) in the bone. The AoI has been selected to correspond to a part of the cortical bone of a femur that needs to be replaced by a unit cell. The latter should satisfy the elastic requirements of the cortical bone to get a successful replacement without the occurrence of the stress shielding problem.

The element set is placed close to the perimeter of the femoral stem so as the AoI correspond to a part of the cortical bone. The elements of the AoI have different elastic moduli according to the HU and the assignment of the material as described above. The elastic moduli of all the elements of the AoI vary in the range of the elastic modulus of the cortical bone. An average value, E_{AoI}, is then computed and it is set as the target for the unit cell design. The elements have been selected manually so as the shape of the element set to be as much as possible close to a cubic shape. The area of interest is highlighted in Figure 4.7.

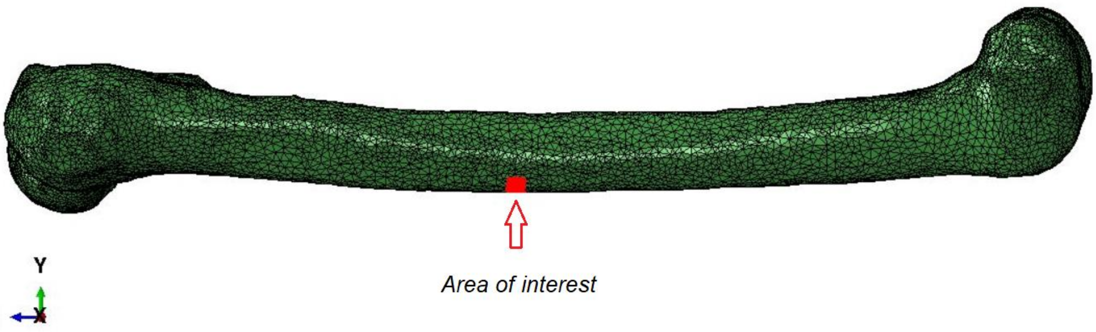

Figure 4.7. Highlighted element set that corresponds to the area of interest in the femoral bone.

Once the FEA of the femoral bone is complete, the average strain tensor of the AoI is computed following the equation (23) for all six cases:

$$[\bar{\varepsilon}_{ij}] = \frac{1}{V_{total}} \sum_{k=1}^{N} (\varepsilon_{ij})_k * v_k \qquad (23)$$

where $\bar{\varepsilon}_{ij}$ corresponds to the components of the average strain tensor, N is the total number of elements, $(\varepsilon_{ij})_k$ is the strain of each element, v_k is the volume of each element, and V_{total} is the total volume of the AoI. The complete average strain tensor is then applied to a single unit cell by using periodic boundary conditions in a mixed loading case. All the details about the creation of the local models and the FEA are given in the following section.

4.2.2. Local model; unit cells with various topologies subjected to boundary conditions taken from the global model

Once the computation of the global model is over and the E_{AoI} and the average strain tensor of the AoI have been computed, the design and the FEA of the local model, i.e. unit cells, follows. The objective is to design unit cells with the same elastic modulus as the corresponding of the AoI. This is performed to successfully replace the AoI by the unit cells taking into consideration the stress shielding minimization. First, the E_{AoI} has been normalized and then, by using the normalized value and the chart in Figure 2.8.a), the related design parameter t has been identified for several topologies. Four different topologies, namely Gyroid sheet, IWP sheet, Gyroid skeletal, and Primitive sheet, have been selected and the relevant cubic unit cells have been designed according to the methodology described in chapter 2. All four unit cell satisfy the elastic requirements of the AoI, namely they have the same elastic modulus as the E_{AoI}. The volume fraction of the unit cells varies according to the selected topology. The size of the unit cells is similar to the average size of the AoI, even though the size does not play any important role due to the application of the PBC described afterward. In Figure 4.8. all the investigated unit cells and their relevant volume fractions are presented.

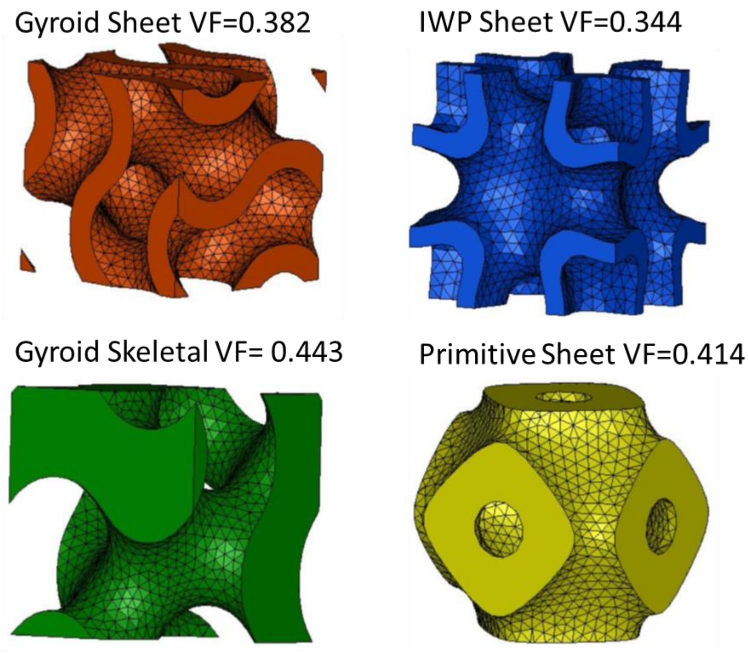

Figure 4.8. Four investigated topologies with the same elastic modulus as the AoI and the corresponding volume fractions.

Once the geometric models are ready, they are meshed properly with a periodic mesh in a similar way as the one described in chapter 2. The applied material properties are the following: $E = 85000\ MPa$ and $v = 0.3$ which have been determined experimentally by our team in LEM3 laboratory for SLM-fabricated specimens with Ti-6Al-4V alloy. The computed average strain tensor (equation 23) is imposed as input to all unit cells considering periodic boundary conditions in a single, mixed loading case. The average Von Mises stress σ_{avg} per topology is computed and the complete stress ranges are acquired by Abaqus as well. A comparison of the σ_{avg} with the σ_{yield} of the bulk material of the unit cells and the average stress of the AoI is carried out. The local stress distribution over the population of the finite elements is computed for all the investigated topologies for a global comparison of the stress state among the investigated unit cells and the AoI. In the following section all the results are presented, compared and a complete analysis is performed.

4.3. Presentation and analysis of the results

In this section, all the numerical results for the global and local models are presented and compared. The geometry of the global model is based on real morphological data from DICOM images, the elastic modulus distribution of the global model is in accordance with the real density described by the HU, and the applied boundary conditions correspond to a real, physiological loading case, i.e. the walking. An AoI is defined at a part of the femoral bone. In this case study, the average elastic modulus of the AoI is computed and the result is $E_{AoI} = 13798\ MPa$. Moreover, after the FEA, the average strain tensor of the AoI is computed as well which is:

$$\begin{bmatrix} \bar{\varepsilon}_{11} \\ \bar{\varepsilon}_{22} \\ \bar{\varepsilon}_{33} \\ \bar{\varepsilon}_{12} \\ \bar{\varepsilon}_{13} \\ \bar{\varepsilon}_{23} \end{bmatrix} = \begin{bmatrix} -5.47e-4 \\ -3.27e-4 \\ 12.98e-4 \\ -1.05e-4 \\ -11.53e-4 \\ -1.45e-4 \end{bmatrix}.$$

The global model has been set as the reference for the creation of the local models in terms of stiffness and boundary conditions requirements. FEA has been performed for all four topologies by applying the average strain tensor to the unit cells in a mixed loading case considering periodic boundary conditions and the constraint driver method described in chapter 2.

It is worth noticing that the periodic homogenization normally should be applied when the scale separation assumption, $\bar{x} \gg x$, is considered. In this particular case, this assumption is not rigorously respected in all implant directions. Indeed, even though the size of the unit cells is much lower than the size of the whole bone, the number of the unit cell repetitions of a lattice that could be utilized as an implant cannot be large enough in all three directions. The elastic modulus in the longitudinal direction is approximately the same, even though it evolves according to the position. Therefore, the number of unit cell repetitions in this single direction could be appropriate in terms of periodic homogenization. On the contrary, the elastic modulus in the radial directions presents high variation due to the bone structure changes, from cortical to trabecular. Therefore, the number of the periodic unit cells with the same apparent stiffness is very limited in the radial directions and the scale separation assumption is violated. However, the PBC have been selected as the boundary conditions that offer satisfying results concerning the computation of the apparent elastic modulus of the unit cells although the scale separation assumption is not rigorously respected, as has been proven in chapter 3. Furthermore, the combination of the application of both the PBC and the real boundary conditions, i.e. the average strain tensor acquired by the global model offers an accurate approximation of the physiological load on a part of the femoral bone.

When it comes to the numerical results, this study focuses on the Von Mises stress of the investigated models. In Figure 4.9. the Von Mises stress contours of the whole femur and the AoI are presented as well as the contour legends.

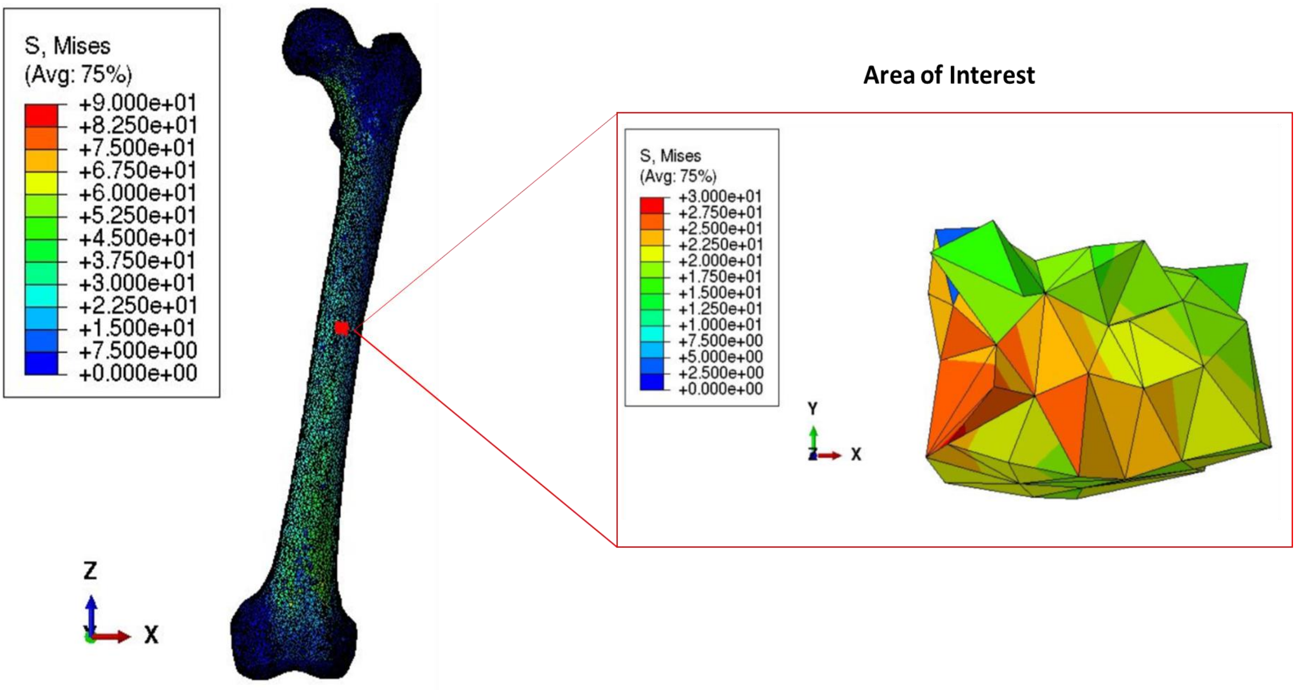

Figure 4.9. Von Mises stress contour of the whole femur and the AoI and the relevant contour legends.

This is considered as a common configuration that corresponds to the applied forces on a femur when a person is walking. The femoral stem is subjected to higher stresses compared to the upper and lower part of the bone as shown in Figure 4.9. The Von Mises stress for the complete femur in the range of $0 - 90\ MPa$ is presented in the contour legend. The AoI is a representative part of the cortical bone regarding both the elasticity and the stress state. The Von Mises stress for the AoI varies in the range of $0 - 30\ MPa$ and the average stress value computed at the centroid is $\sigma_{AoI\_AVG} = 21.662\ MPa$.The above presented average strain tensor of the AoI is imposed to the investigated unit cells for the computation of the Von Mises stress range and average stress value. The Von Mises stress contours for a) Gyroid sheet, b) IWP sheet, c) Gyroid skeletal, and d) Primitive sheet unit cells are illustrated in Figure 4.10.

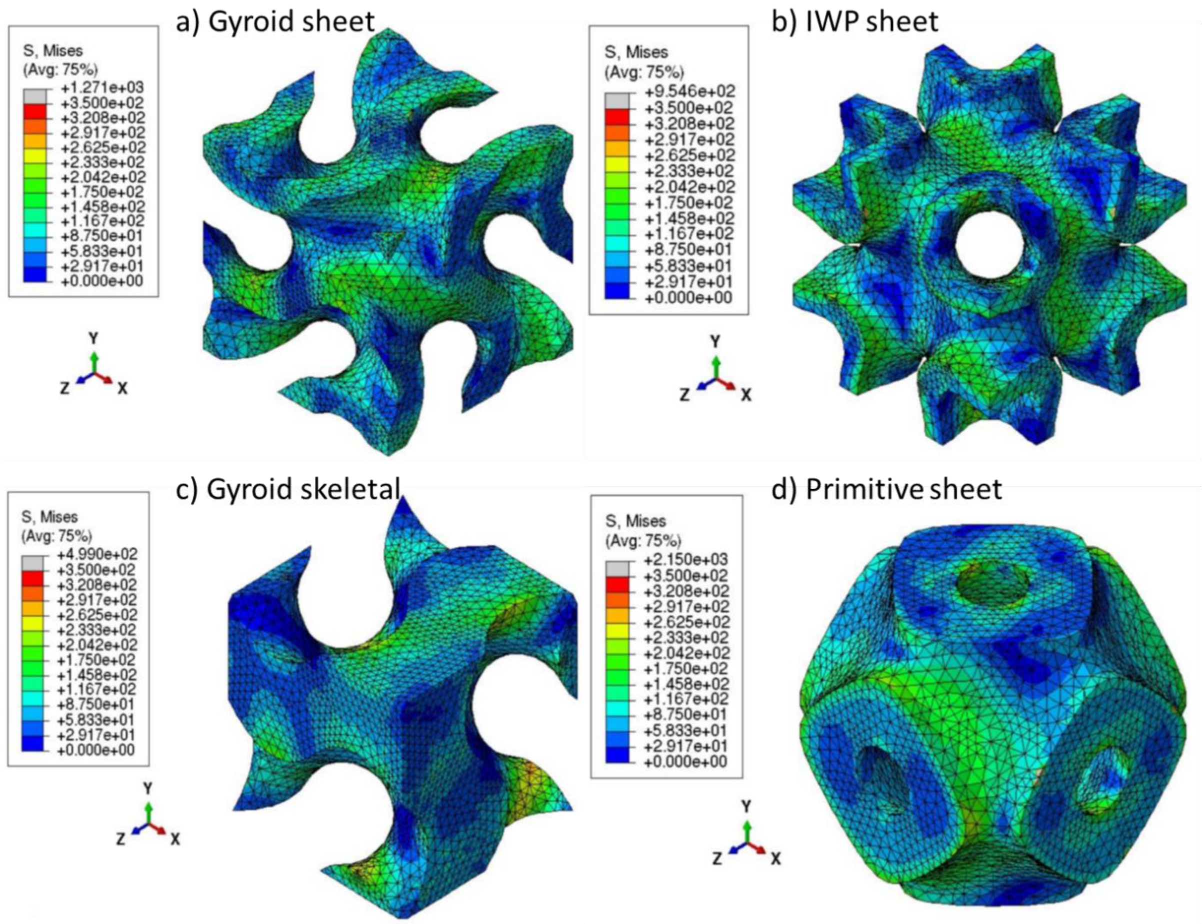

Figure 4.10. Von Mises stress contours for a) Gyroid sheet, b) IWP sheet, c) Gyroid skeletal, and d) Primitive sheet unit cells in the stress range $0 - 350\ MPa$ indicated in the contour legend.

In Figure 4.10. the stress distributions on the unit cells after the application of a physiological average strain combined with the PBC are compared in a qualitative way. The stress distribution is topology-dependent and the stress values vary in the range of $0 - 350\ MPa$. The maximum value which is the upper bound of the stress range, i.e. $\sigma_{max} = 350\ MPa$, is lower than the $\sigma_{yield\_Bulk} = 830\ MPa$ [116] which is the yield stress of the Ti-6Al-4V alloy. The latter is the material whose elastic properties have been utilized in Abaqus for the numerical analysis of the unit cells. Therefore, all the topologies have succeeded to mimic the local elastic modulus of the AoI without being subjected to local stresses that exceed the σ_{yield} and entering the non-linear regime of the constituent material.

It is noteworthy to mention that in the final results of all the numerical models some singularities may appear which extend the Von Mises stress range indicated in the legends. This is the reason why all the contour legends have been presented in Figure 4.10. Those singularities may be caused by errors that arise either from the interpolation of the PBC due to remaining minor imperfections in the periodic mesh or by the edges and finally, they are neglected. Particularly, in Figure 4.11. a neglected singularity in the relevant element for the IWP sheet topology is presented.

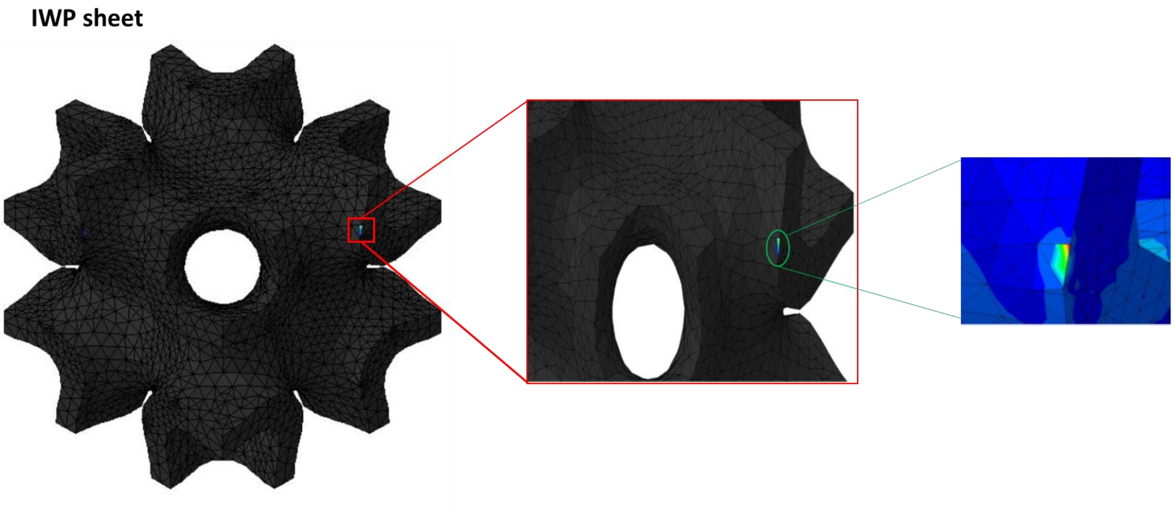

Figure 4.11. A neglected singularity in a relevant element for the IWP sheet topology caused by errors that arise either from the interpolation of the PBC or by the edges.

In order to quantify the above results the average stress values, σ_{AVG} at the centroid of the elements have been computed for all the studied unit cells. The average stress values for all the unit cells and the AoI are presented in Table 4.1.

Topology	Average Stress [MPa]
Gyroid sheet	79.12
Gyroid skeletal	74.28
IWP sheet	81.62
Primitive sheet	81.79
AoI	21.66

Table 4.1. The average stress values at the centroid of the elements for all the studied unit cells and the AoI.

The σ_{Bone} is the average stress that corresponds to the AoI and is shown to be the lowest among all the stress values. Although the Von Mises stress is distributed in the range of $0 - 350\ MPa$, the σ_{AVG} is presented to be much lower than the upper bound for all the topologies. This means that the majority of the elements are subjected to low stress. The minimum stress value which is closer to the σ_{Bone} is presented by the Gyroid skeletal topology whereas the maximum is presented by the Primitive sheet. Therefore, Gyroid skeletal could be selected as the best-fit geometry when the lowest average stress is the most important criterion.

Furthermore, the local stress distribution over the range $0 - 350$ is computed for all the unit cells considering periodic boundary conditions in a mixed loading case. Statistical analysis is then performed considering the normalized stress distribution over the range $0 - 1$ for all topologies in order to simplify the calculations. The weighted arithmetic mean and standard deviation, SD, are computed in order to complete the quantitative comparison of the topologies. In Figure 4.12. the stress distributions over the population of the finite elements for the unit cells at the same apparent Elastic modulus are exhibited. The statistically computed values are presented in Table 4.2.

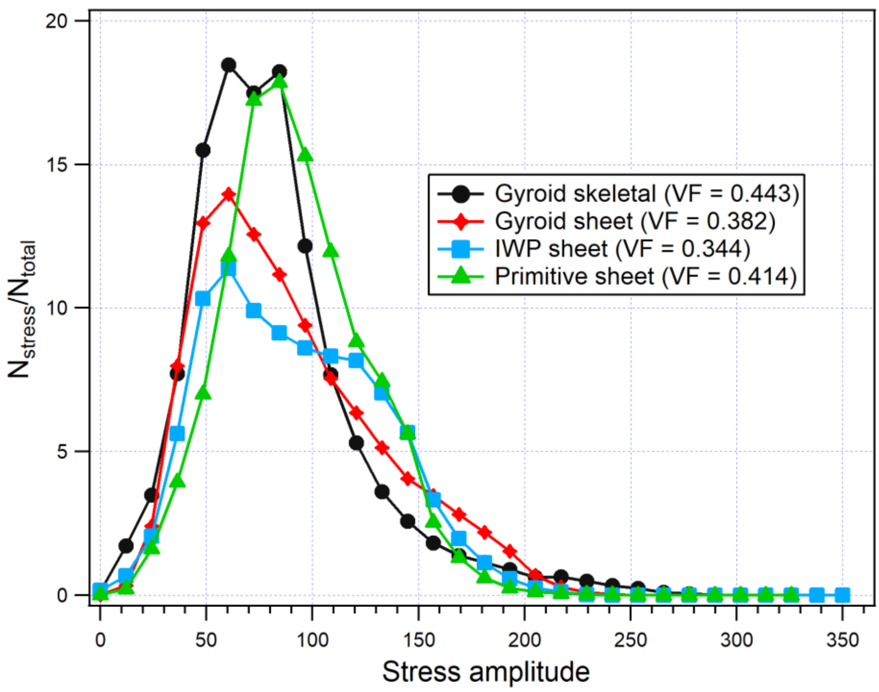

Figure 4.12. Local stress distributions of Gyroid skeletal, Gyroid sheet, IWP sheet, and Primitive sheet unit cells at the same apparent Elastic modulus, $E_{AoI} = 13798\ MPa$.

	Weighted arithmetic mean	**Weighted SD**	**VF**
Gyroid skeletal	0.235	0.115	0.443
Gyroid sheet	0.255	0.121	0.382
IWP sheet	0.262	0.114	0.344
Primitive sheet	0.263	0.093	0.414

Table 4.2. The table summarizes the weighted arithmetic mean, and weighted standard deviation of the investigated normalized local stress distributions and the volume fraction of the corresponding topologies.

As shown in Figure 4.12., the topology of the unit cells induces different local stress distributions which could play an important role in the high cycle fatigue of the lattices and thus, the fatigue of the implants. All stress distributions present a main peak between 0.235 and 0.263. The standard deviation shows how broad or narrow is a distribution. Therefore, it is an indicator of the apparent σ_{max} of the unit cells. As all the unit cells have been numerically studied with the same bulk material properties, some elements of the unit cells with a high standard deviation are subjected to higher stresses compared to those of the unit cells with a low SD. This means that among the studied structures, the apparent σ_{max} of the Gyroid sheet is closer to the apparent σ_{yield} and thus, closer to the plastic deformation. On the contrary, the Primitive sheet exhibits the lowest SD (narrowest and best distribution) but the highest average stress (the worst among all) This means that the distribution of the Gyroid sheet is broader and the apparent σ_{max} is higher and closer to the apparent σ_{yield}. In this particular case, the apparent σ_{max} of the unit cells is always lower than the $\sigma_{yield\_Bulk} = 830\ MPa$ because the stress range of the distributions is $0 - 350\ MPa$. On the contrary, the Gyroid sheet presents a lower weighted mean stress than the Primitive sheet. The volume fraction of the Gyroid sheet is also lower than the volume fraction of the Primitive sheet topology. Therefore, the selection of a TPMS-based lattice depends on the particular requirements to cope and there is not a unique solution. A solution is based on the application and a compromise among topology, volume fraction, stress state, etc. should be made. All the above-mentioned results are shown graphically in Figure 4.13. for an easy comparison of the topologies according to various requirements. Particularly the following graphs are presented: a) volume fraction-weighted average stress, b) weighted SD-volume fraction, and c) weighted average stress-weighted SD.

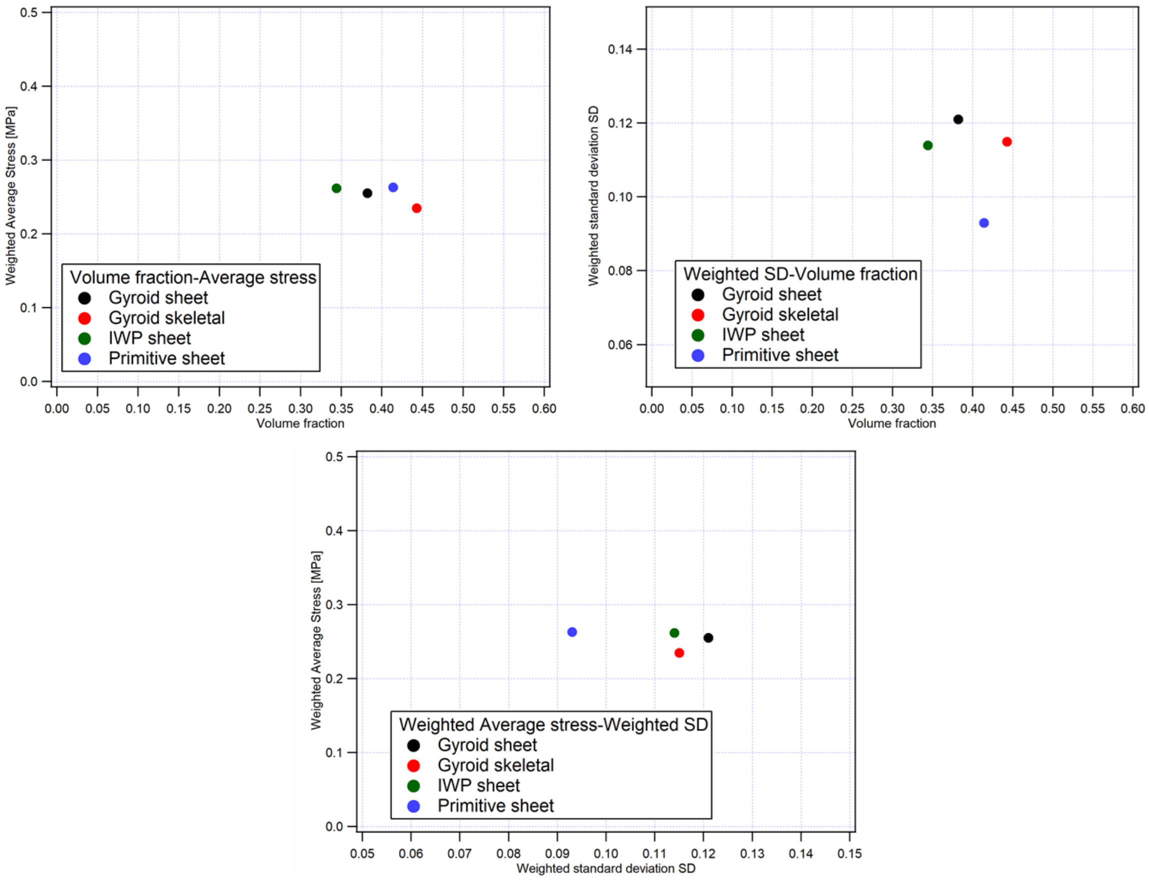

Figure 4.13. a) volume fraction-weighted average stress, b) weighted SD-volume fraction, and c) weighted average stress-weighted SD graphs for all the studied unit cells.

Figure 4.13. collects all the results for the studied topologies after the application of the real strain corresponding to an everyday activity, i.e. walking, considering periodic boundary conditions. The results refer to the following investigated parameters: the volume fraction of the unit cells, the weighted average stress, and the weighted SD. They consist a multi-parameter problem and thus, a single solution that complies with all the requirements cannot be found.

A researcher interested in replacing a part of a bone with TPMS-based lattices could use the above-presented statistical findings and graphs, and a weight function to select the most suitable topology in a particular case. For instance, a weight function:

$$W = VF^a * SD^b * WA^c \tag{24}$$

where W is the weight, VF is the volume fraction, SD is the weighted standard deviation, WA is the weighted mean stress, and a, b, c are the weights to the above parameters, gives the results presented in Table 4.3.

Topology	**W**
Gyroid sheet	0.01179
Gyroid skeletal	0.01187
IWP sheet	0.01017
Primitive sheet	0.01009

Table 4.3. The results of the weight function, W, for the studied topologies.

In this loading case, i.e. walking, the same weight is applied to all parameters and the results are generated with $a = b = c = 1$. The lowest W is presented by the Primitive sheet unit cell. Therefore, it could be selected as the most suitable topology to satisfy all the above-mentioned requirements. However, in another case study, the values of the weights may be different according to particular requirements. For instance, in another loading case, such as jumping, the σ_{max} of the unit cells will be larger. The importance of a low SD will be then higher and the weight b should be larger. The weights configuration in that case could be for example the following: $a = c = 1$ and $b = 3$ in order to highlight the importance of a low SD. A lattice topology with a low SD should finally be selected as the most suitable in this particular loading case.

Specific requirements determine the most suitable unit cell topology. The requirements are defined by the part of the bone to be replaced and thus, different topologies and volume fractions can be selected for different parts of the bone. The combination of the unit cell topologies may result in multi-morphology lattices or macro-porosity gradient lattices that satisfy the requirements in the most accurate way.

4.4. Conclusions

In the present chapter, a complete numerical quantitative approach is presented to replace an area of interest of a femoral bone (global model) with a TPMS-based unit cell (local model). The latter could be considered as a digital-implant. The elastic modulus distribution and the applied load on the 3D model correspond to a realistic stiffness distribution and loading case. The strain tensor has been extracted from the area of interest and applied to four unit cells for a complete investigation concerning various parameters. The objective is to define which topology is the most suitable for the replacement according to particular requirements.

It should be mentioned that the proposed methodology is general and can be applied in any case where it is necessary to replace a structure by TPMS-based lattices. The complete stress and statistical analysis can be performed after the application of various boundary conditions as well. The study case of a partial bone replacement by a TPMS-based unit cell aims at describing all the steps of the methodology and presenting the results that can lead to the selection of a suitable topology and the optimization of the structure.

The following conclusions have been reached:

- ✓ The assignment of the real elastic properties to a bone and the application of a real loading for FEA result in the actual stress-strain state in the bone. The actual strain state can be used for further investigation of potential implant topologies to select the most suitable according to particular requirements.

- ✓ The actual strain of the real bone can be combined with periodic boundary conditions for application to the potential implant topologies. The selection of the PBC in combination with the actual strain offers a satisfying approximation of the real loading on a specific area of a bone.

- ✓ Four unit cell topologies with the appropriate elastic modulus have been investigated to replace a part of a femoral bone. The examined parameters are the volume fraction of the unit cells, the average stress, and the standard deviation of the stress distribution. They create a multi-parameter problem. Due to the complexity of the problem, there is not a unique solution. Upon requirements based on patient's profile in terms of activities, age etc. a different topology could be selected as the most suitable.

- ✓ In this case study, the Gyroid skeletal is the most suitable topology when the lowest average stress is the most important criterion, the IWP sheet is the most suitable when the lowest volume fraction is necessary, and the Primitive sheet is defined as the best topology when the narrowest stress distribution is required. The Primitive sheet is selected as the most suitable unit cell because it exhibits the lowest weight obtained by a weight function. Different weights can be applied to particular requirements, in order to select an appropriate topology.

- ✓ As the requirements to satisfy are defined by the position of the part of the bone to be replaced, different topologies and volume fractions can be selected for each part bone part replacement. The combination of the unit cell topologies may result in multi-morphology lattices or macro-porosity gradient lattices that meet the local requirements in the most accurate way. Examples of multi-morphology and macro-porosity gradient lattices are presented in Figure 1.1.

General Conclusions and Perspectives

The work of this thesis contributed to the solution of a mechanical problem regarding orthopedic implants consisting of architectured material. The numerical results and experimental findings obtained from the proposed methodology aimed at the design and selection of an appropriate lattice topology that meets the required criteria, such as low elastic modulus and avoidance of high-stress concentrations. The proposed methodology combined both numerical simulation and experimental investigations.

The first challenge was the development of a complete numerical chain to design successfully TPMS-based unit cells and lattices appropriate for both FEA and additive manufacturing. Aiming at the prediction of the apparent mechanical properties and the study of the local stress distributions in the unit cells, a periodic homogenization method was implemented and applied. The latter was applicable to the TPMS-based lattices due to their periodic microstructure. In order to ensure the capability to fabricate the investigated structures with additive manufacturing, they were fabricated by the SLM technique. Then, uniaxial compression loading tests were performed and compared with the predicted numerical elastic properties as well as the overall response. The objective was to take into account all the results obtained from the above-described methodology to partially replace a real bone subjected to real loading by a TPMS-based unit cell.

Particularly, throughout this thesis, an experimental and extended numerical investigation was proposed to describe the mechanical properties of ten unit cell topologies emphasizing on the control of the apparent elastic modulus. A low elastic modulus was aimed at reducing the stress shielding phenomenon. The methodology proposed herein started with the numerical design of the unit cells using a mathematical formulation describing the surfaces. All the details for the complex design of eight TPMS-based and two strut-based topologies were explained. Two types of boundary conditions were applied numerically to the unit cells to compute the apparent mechanical properties. All the results were finally compared with the relevant experimental ones to determine which boundary conditions resulted in the prediction of the most representative elastic modulus. Furthermore, the local stress distribution analysis allowed the comparison of the stress state of the unit cells. It was also very interesting to compare the macroscopic deformation mechanisms and fracture of the lattices that lead to the selection of safety factors for the design of lattices in a biomechanical application.

Chapter 1 introduced a general framework of the orthopedic implants and a common postoperative problem that may occur, namely the stress shielding. Lattice structures were proposed as the way to lower the apparent elastic modulus of the implants and thus, to reduce the stress shielding phenomenon. The fundamental aspects regarding the design and the mechanical properties of the strut-based and TPMS-based lattices were detailed. Finally, additive manufacturing technology and particularly the SLM technique were proposed as a suitable and promising way to fabricate such complex and custom-made structures.

Chapter 2 described all the steps of the proposed numerical design chain of the unit cells, emphasizing mostly on the complex numerical way to design the TPMS-based topologies. Eight TPMS-based and two strut-based unit cells were studied in terms of various mechanical properties and local stress distribution. The design parameter was also related to the mechanical properties of the lattices. The results were acquired after the application of a periodic homogenization method since all the unit cells were periodic. A plethora of charts was exhibited to help the classification and selection of the appropriate topologies according to particular mechanical requirements.

Chapter 3 proposed a second set of numerical boundary conditions, namely the compressive boundary conditions imposed on the lattices during experimental testing. The predicted apparent elastic modulus of the unit cells was compared with the relevant elastic modulus obtained from the application of the PBC. Lattices were fabricated and tested experimentally under uniaxial monotonic compressive loading and the elastic modulus was measured. The numerical results that are the most representative of the experimental ones were determined. Therefore, PBC were selected as the most appropriate boundary conditions to predict the apparent elastic modulus of the unit cells. The macroscopic deformation mechanisms and fracture of the compressed lattices were also investigated experimentally to classify the topologies according to their suitability for a biomechanical application in a destructive case. The fracture occurred in the same direction for all lattices but the deformation mechanisms were topology-dependent.

Chapter 4 was dedicated to a partial replacement of a real femur bone subjected to real boundary conditions by a digital-implant. The latter consisted of a TPMS-based unit cell. Four different unit cell topologies were studied and compared in terms of average stress value, local stress distribution, and volume fraction when the elasticity requirement was satisfied. A weight function was finally proposed for the selection of the most suitable topology according to various requirements.

The previously described methodology combining numerical and experimental results are discussed to present topics for further investigations. These topics are associated with the design process that can be enriched, further experimental and numerical tests that can be carried out, and the use of lattices in biomechanical and other applications.

It is recalled that in this study only cubic unit cells and lattice structures were presented. The computational design could be improved to generate surfaces and then lattices and unit cells with various bounding shapes, such as spheres, pyramids, cones. Therefore, it would be easier to adapt the generated lattices to the macroscopic structures where they should be placed, for instance, the internal part of an orthopedic implant or any mechanical structure.

In this study, a comparison between experimental and numerical results has been carried out only for compression loading. Therefore, it would be interesting to design and fabricate appropriate specimens and then to carry out torsion testing in order to compare the mechanical response of the numerical and experimental tests. The results would be useful for any biomechanical and industrial application.

Furthermore, it would be interesting to generate composite structures associated with the TPMS-based lattices. The void of the lattices could be replaced by another material, namely a metal alloy or any material, and the generated structure would own exceptional mechanical properties.

Since the human bone presents a heterogeneous macroscopic structure where the density and the elastic properties are position-dependent, the design of adapted lattices could lead to highly tailored implants. The gradient in the wall thickness of the unit cells would lead to the generation of macro-porosity gradient lattices and thus, the volume and density of the implants could be adjusted to the volume and density of a real bone. Furthermore, the combination of several topologies would generate multi-morphology lattices. It would be interesting to select the most suitable topologies for various areas of an implant according to the proposed methodology in this study. Then, they could be combined with a smooth transition between every two topologies in order to create a highly tailored lattice structure that satisfies varying mechanical requirements [117].

Finally, the weight function, W, presented in chapter 4 (equation 24) could be used to optimize the selection of an appropriate TPMS-based lattice and the relevant volume fraction. For instance, the input design parameter t and the topology itself could be modified in order to adapt the output of the W to particular mechanical requirements.

Appendices

A. Complete numerical chain for the design of TPMS-based unit cells

In section 2.2.2., the complete methodology to design numerically TPMS-based unit cells and lattices is described. In this appendix, extra technical details are given. Figure Appendix.1. presents a complete example of the numerical design of Gyroid unit cells.

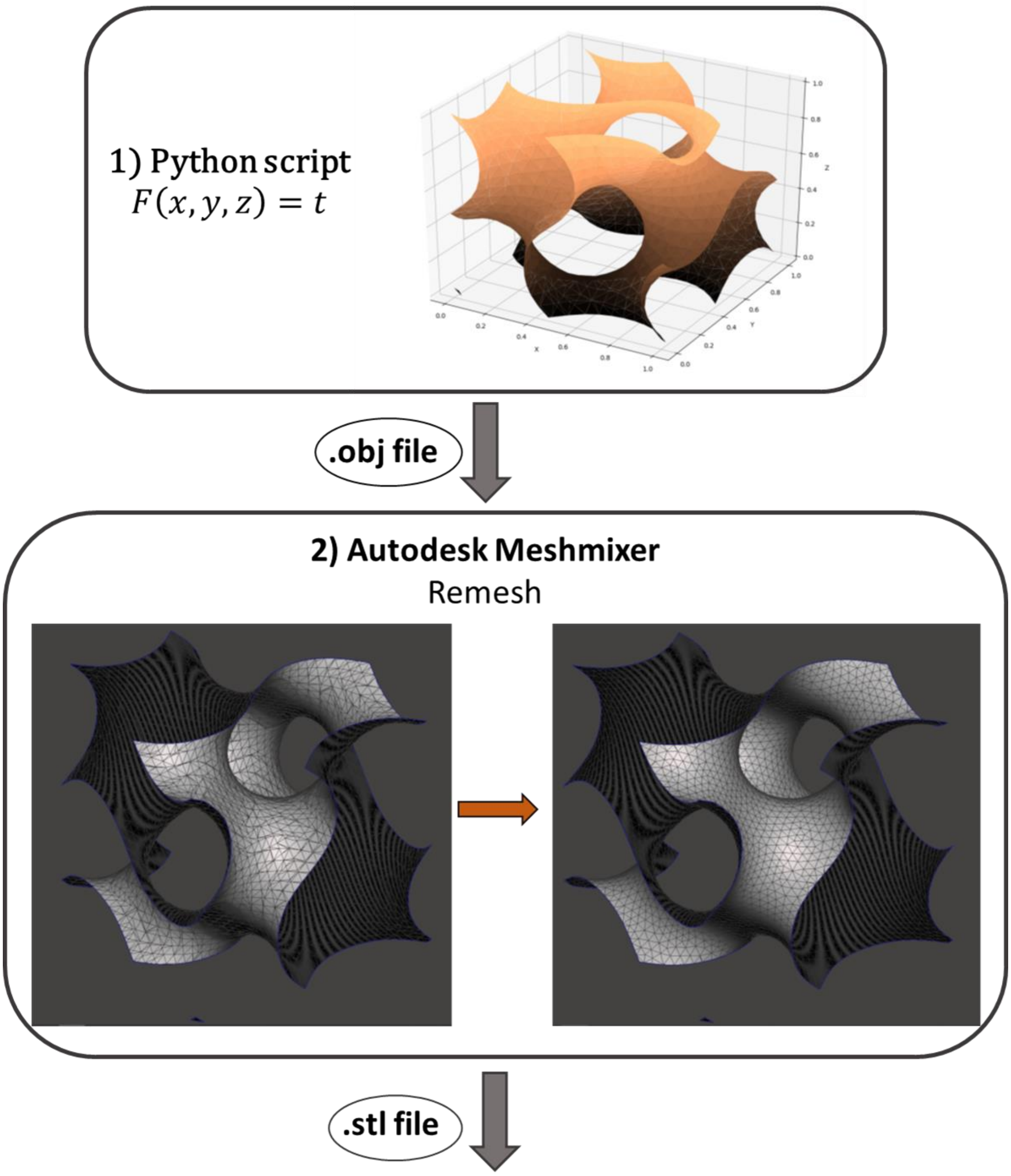

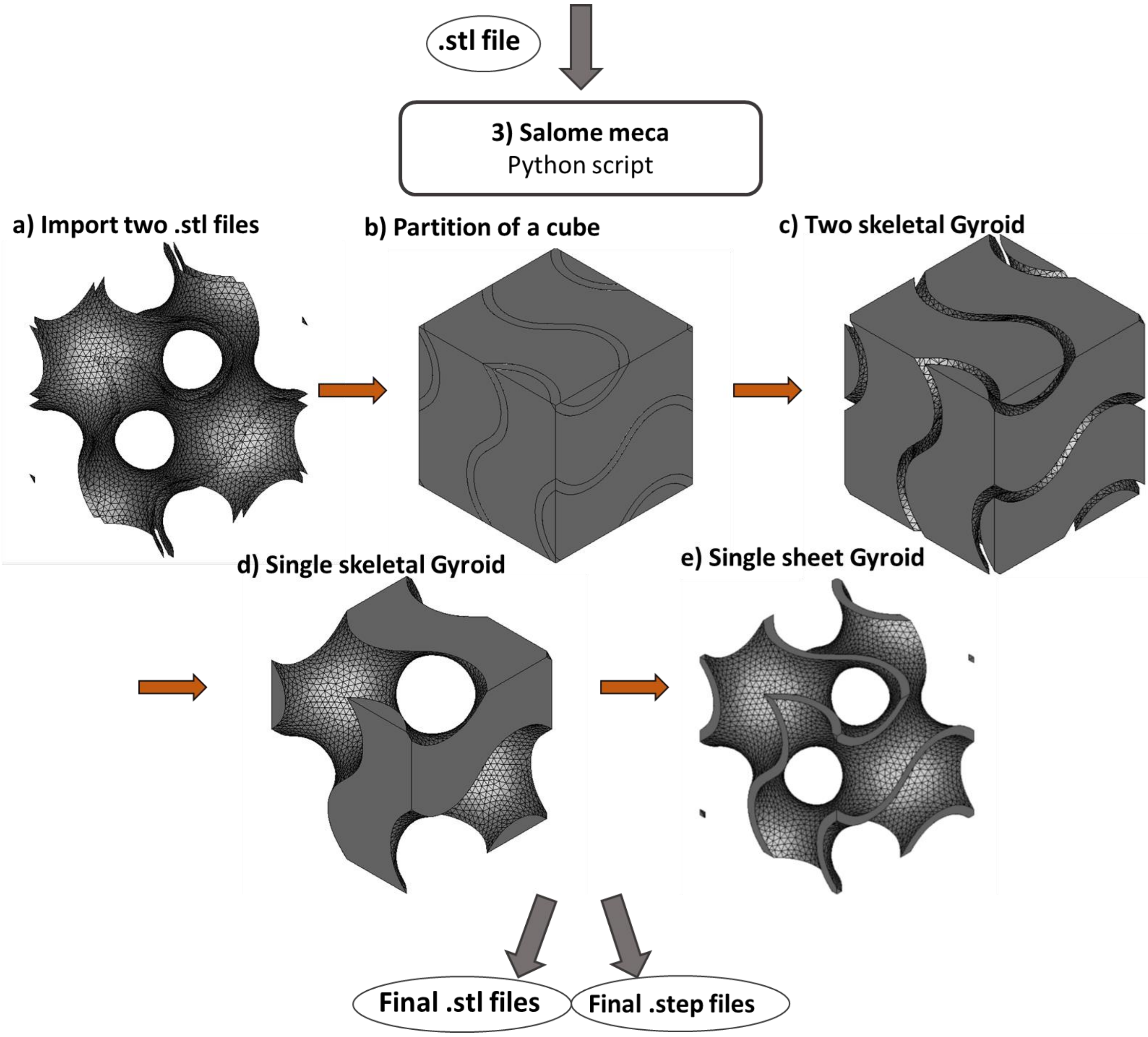

Figure Appendix.1. Complete numerical chain regarding the design of Gyroid unit cells.

1) Plot the TPMS according to the equation $f(x, y, z) = t$ and using the marching cubes lewiner algorithm. Save the vertices, the faces, and the normals of the faces. All these create the .OBJ file. Everything is carried out with the aid of a single script in Python.

2) Import the .OBJ in Autodesk Meshmixer software. First step is to remesh each surface to improve and homogenize the shape and size of all the triangles. Then, the file is saved with an .STL extension. Everything is performed manually.

3) Import two surfaces with an .STL extension in Salome meca software and design a bounding box. Make a partition of the cube based on the surfaces, and then 'explode' all the components to get each separate unit cell. Everything is carried out with the aid of s single script in Python.

B. Design of TPMS-based unit cells according to the fundamental-patch design approach

As have been mentioned in sections 1.4.2., 1.4.3., and 2.2.2., TPMS lattices are based on periodic unit cells that are repeated in one or more directions. The initial TPMS are designed in the range $0 - 2 * \pi$ according to the level set equations $(1) - (6)$ and then, they are repeated in multiple directions. This is the mathematical approach.

Another design approach that could be applied is called the fundamental-patch approach [118], [119]. Particularly, each TPMS unit cell consists of eight similar fundamental patches in various orientations. Therefore, it is necessary to design just one fundamental patch. Then, the latter is translated and mirrored inside a cubic bounding box and the complete TPMS unit cell is generated. The unit cell is repeated in multiple directions and a complete lattice can be generated. In Figure Appendix.2. the fundamental patches and the complete TPMS unit cells for two topologies, i.e. Gyroid and Schwartz Primitive, are presented.

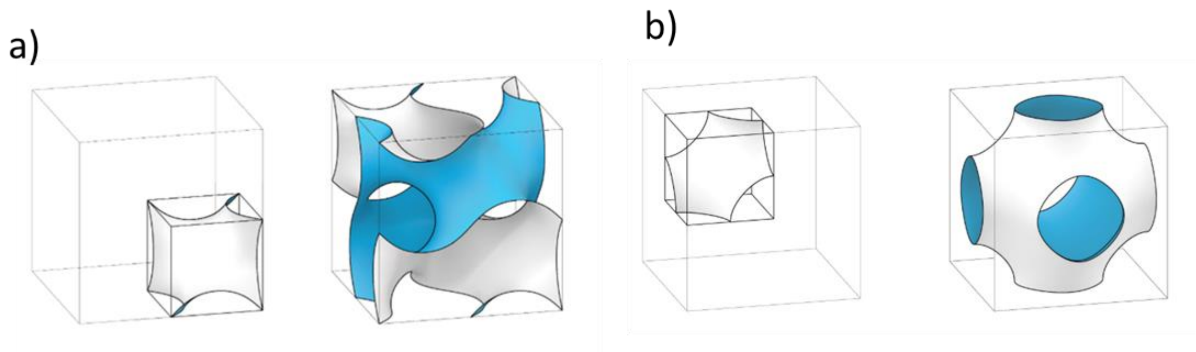

Figure Appendix.2. a) Gyroid fundamental patch and TPMS unit cell, and b) Schwartz Primitive fundamental patch and TPMS unit cell.

In our case, the free and open-source 3D software Blender is used for the generation of TPMS-based unit cells. A script in python is developed to generate the fundamental patch of various unit cell topologies and then, to translate it and orient it in an appropriate way for the TPMS unit cell generation. The fundamental patch is actually an approximation, i.e. the surface is designed according to a triangular surface mesh. Once the TPMS-based unit cell is ready, a suitable thickness is applied in the direction of the normal of every triangle. The next step is to smooth the surface of the unit cell to get a better surface quality by using subdivision surface algorithms [120]. The final unit cell is exported as file with either an .OBJ or an .STL extension. All the above-mentioned steps for the design of unit cells in Blender software according to the fundamental-patch approach are illustrated in Figure Appendix.3.

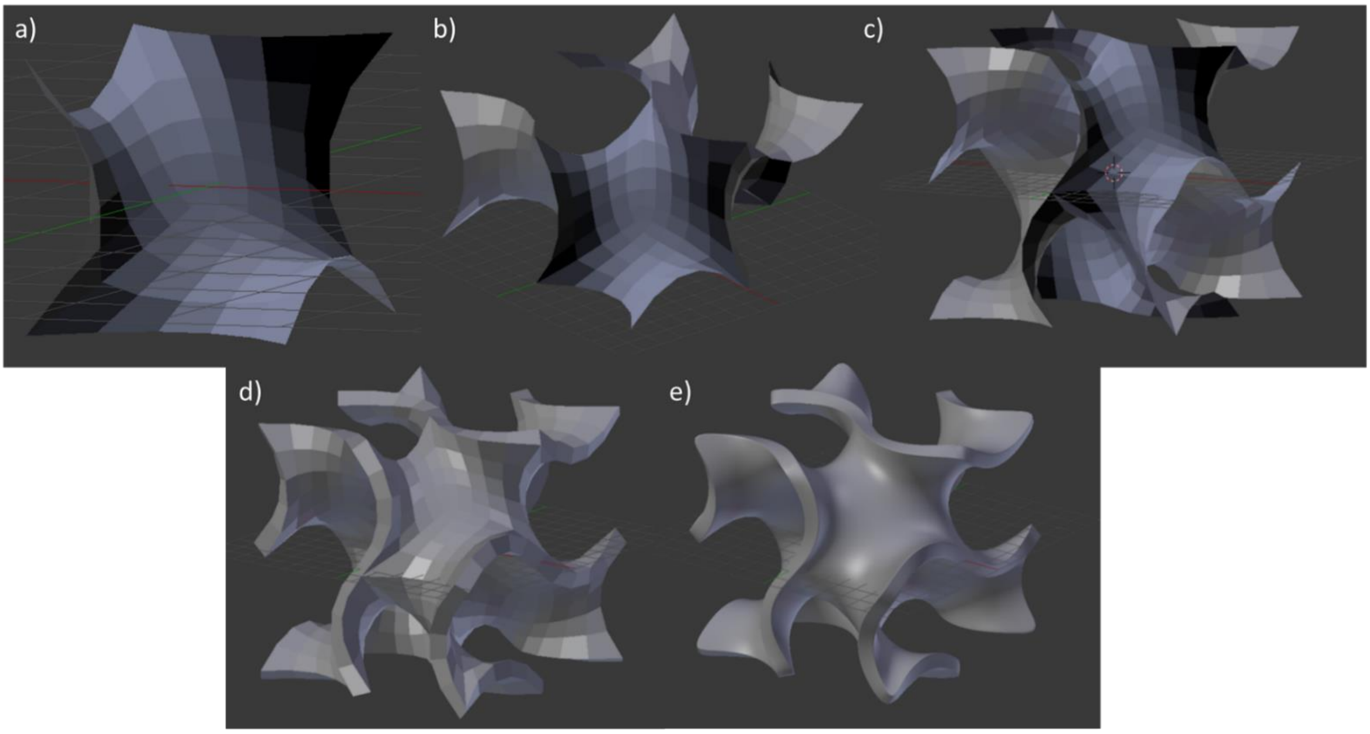

Figure Appendix.3. a) Fundamental patch of Gyroid topology, b) assembly of 4 patches, c) assembly of all 8 patches which create the complete TPMS-based unit cell, d) unit cell after the application of a suitable thickness and d) the final smoothed unit cell.

The above mentioned methodology presents some limitations that make its use a bit challenging. First, as .STL files are not suitable for a FE analysis, a conversion of the latter into .STEP files is necessary. However, this conversion is difficult to achieve due to the high complexity of the structure. Especially, when the number of the unit cell repetitions increases, the conversion gets even more difficult and most of times impossible to complete. Second, the above-mentioned method allows only the generation of sheet-type unit cells as thickness is applied to a surface. Therefore, the number of the designed TPMS-based unit cells is limited.

On the other hand, the above method is very fast and useful when it comes to the design of unit cells and lattices for fabrication with additive manufacturing technology. Once the script is ready, the thickness parameter is the only one that varies which can be done really easily. Also, the smoothness can be applied directly on the final unit cell until a suitable level is reached. .STL files are also suitable for AM technology and no further conversion is necessary. Therefore, this method can be used for relevant applications.

C. Constitutive law of the Ti-6Al-4V alloys applied in Abaqus

Compressive tests have been carried out previously in LEM3 laboratory in order to acquire the stress-strain curve for as-fabricated Ti-6Al-4V bulk specimens by an SLM machine.

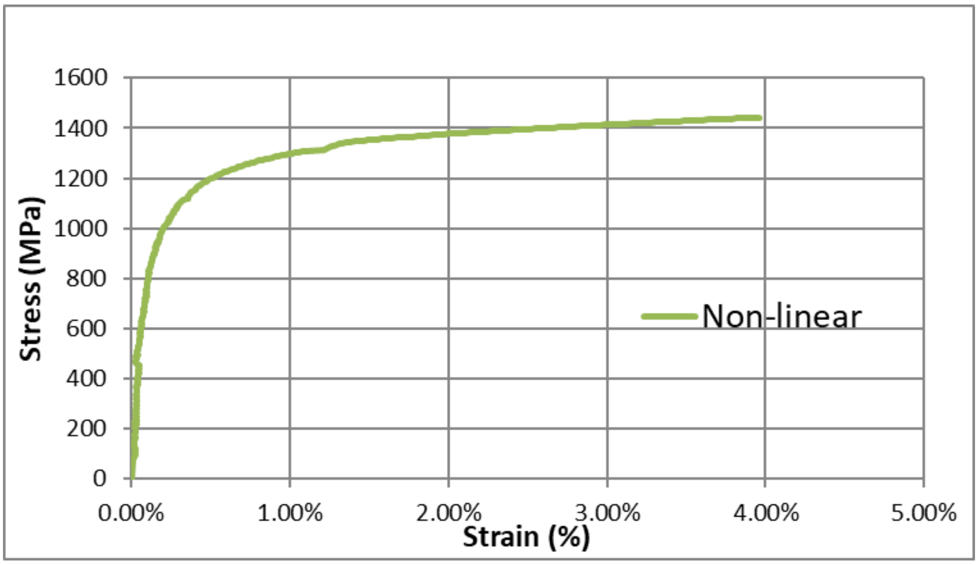

Figure Appendix.4. Stress-Strain curve obtained after post-processing of experimental results. Particularly, SLM-fabricated specimens with Ti-6Al-4V alloy have been tested under uniaxial compression load.

Engineering Stress [MPa]	**Engineering Strain**
801.791	0
820.657	0.0107%
872.736	0.028%
896.17	0.0332%
919.363	0.0521%
947.044	0.0648
970.085	0.075
992.928	0.096
1019.94	0.1236
1046.54	0.147
1077.23	0.1775
1107.26	0.2138
1143.03	0.27
1179.48	0.34
1209.61	0.43
1240.96	0.55
1269.77	0.7
1296.14	0.88
1336.37	1.205
1366.45	1.667
1387.89	2.173
1409.03	2.764
1442.86	3.8564
1500	20

Table Appendix.1. Tabular non-linear constitutive law of the Ti-6Al-4V material applied in Abaqus for numerical simulations. This law has been obtained by previously performed uniaxial compression loading tests in LEM3 laboratory.

D. Post-processing and data reduction steps for the as-acquired experimental curves

This appendix completes the post-processing of the acquired force-displacement curves after the compression (loading-unloading) of the lattice structures described in section 3.2.2.2. The post-processing of the force-displacement curves is necessary to allow the graphical comparison of the experimental linear and non-linear responses with the numerical ones although this step is not included in the ISO standard [80].

The slope of the second loading corresponds to the apparent elastic modulus of the lattices. The post-processing steps are detailed in section 3.2.2.2. Figure Appendix.5. presents the steps of the post-processing in a graphical way.

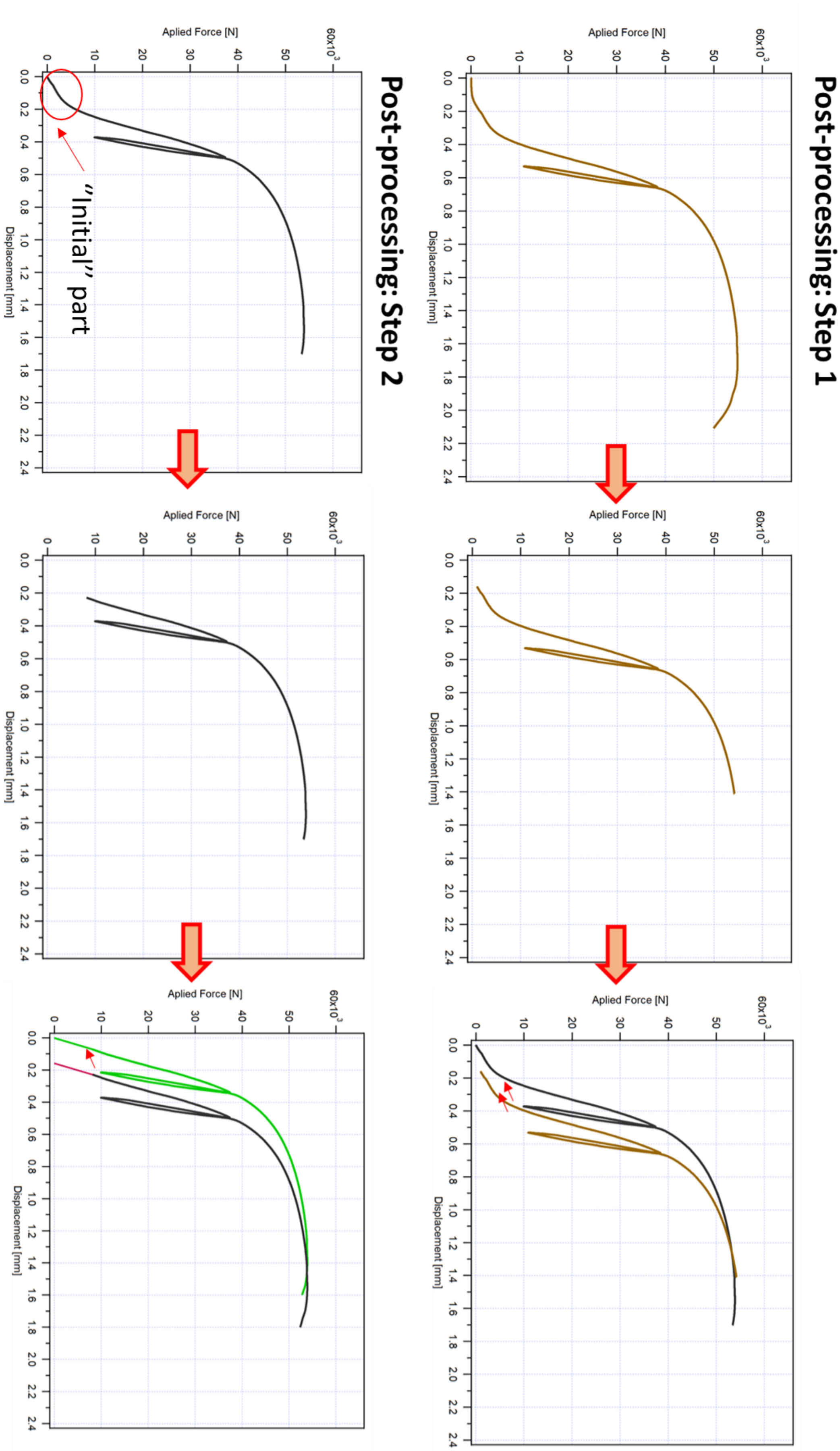

Post-processing: Step 1
Post-processing: Step 2
"Initial" part
Aplied Force [N]
Displacement [mm]
60x10³

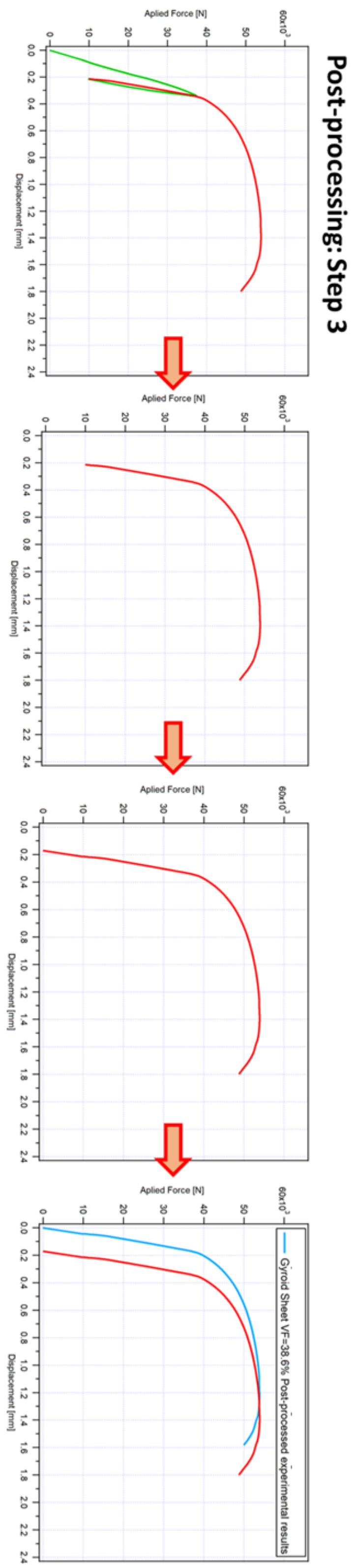

Figure Appendix.5. The steps of the post-processing of the experimental force-displacement curves after the compression (loading-unloading) of the lattice structures in a graphical way.

E. Compressive Boundary Conditions (CBC) applied to single unit cell and lattices with multiple unit cell repetitions

As can be seen in Table 3.4. the difference between the elastic modulus of the unit cells after the application of the CBC and the experimentally-measured elastic modulus is significant. This difference may be caused by the impact of the boundary effects and the lack of the geometric resemblance between the 3D model and the real lattice, as has been mentioned previously. Therefore, lattices with multiple unit cell repetitions are designed to investigate if the numerical apparent elastic modulus gets closer to the experimental one and $\boldsymbol{E_{PBC}}$ when the number of the unit cell repetitions increases and gets closer to the number of the unit cells of the real specimen. Lattices with only up to $3 * 3 * 3$ unit cells repetitions are designed because the size of the CAD files is very large. In Figure Appendix.6. Gyroid sheet lattices are presented with $2 * 2 * 2$ and $3 * 3 * 3$ unit cells repetitions. Apart from the elastic modulus of the lattices, the non-linear response is investigated as well when the number of the unit cell repetitions varies.

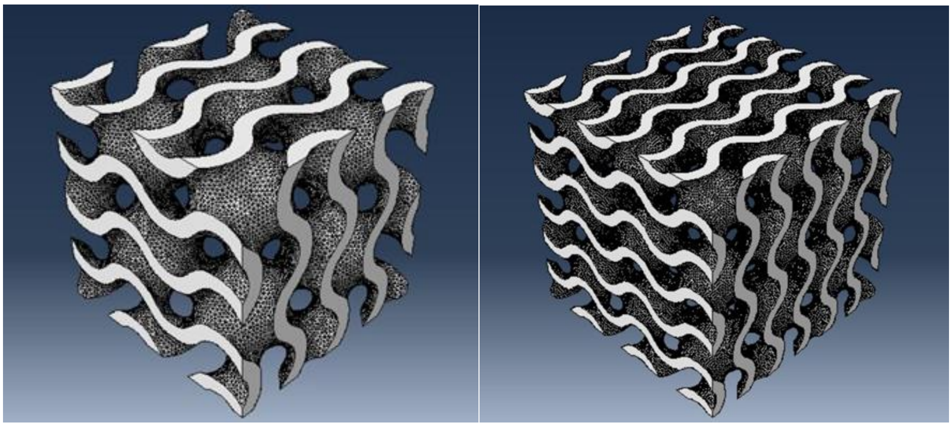

Figure Appendix.6. Gyroid sheet lattices with $2 * 2 * 2$ (left) and $3 * 3 * 3$ (right) unit cells repetitions.

For the complete numerical model, the non-linear constitutive law applied in Abaqus has been obtained by previously performed experimental tests in LEM3 laboratory. The tabular law is presented in Appendix C. To complete the material properties in Abaqus, the elastic modulus for the bulk material is set at $E = 85000\ MPa$ and Poisson's ratio is equal to 0.3.

It should be noted that the computation time is very high when the number of the unit cell repetitions increases and thus, representative numerical tests have been carried out only for few topologies, namely Gyroid sheet, IWP skeletal internal, and Gyroid skeletal (VF=0.386). Table Appendix.2. shows all the numerical results per topology, $\boldsymbol{E_{EXP}}$ is the experimentally measured elastic modulus, $\boldsymbol{E_{PBC}}$ is the numerically computed elastic modulus after the application of the PBC which is set as the reference elastic modulus in this appendix, $\boldsymbol{E_{CBC}}$ $(\mathbf{1})$ is the numerically computed elastic modulus for a single unit cell after the application of the CBC, $\boldsymbol{E_{CBC}}$ $(\mathbf{2})$ and $\boldsymbol{E_{CBC}}$ $(\mathbf{3})$ are the numerically computed elastic modulus for lattices with $2 * 2 * 2$ and $3 * 3 * 3$ unit cells repetitions after the application of the CBC, respectively.

Topology	VF_{CAD}	VF_{EXP}	E_{EXP} **[MPa]**	E_{PBC} **[MPa]**	E_{CBC} (1) **[MPa]**	E_{CBC} (2) **[MPa]**	E_{CBC} (3) **[MPa]**
Gyroid sheet	0.386	0.39	14565.85	14280.2	10533	12264	12966
Gyroid skeletal	0.452	0.46	15687.4	14310.8	14104	14199	14252
Gyroid skeletal	0.29	0.29	5932.6	5586.8	5133.7	-	-
IWP skeletal int	0.328	0.34	5658.9	5602.5	4803.2	5096	5464
Diagonal	0.4	0.41	6243.2	5603.1	4462	-	-

Table Appendix.2. The numerical elastic moduli per topology after the application of both PBC and CBC boundary conditions, and the experimentally measured elastic modulus.

As can be seen in Table Appendix.2., the elastic modulus of the investigated topologies increases and tends to converge to the elastic modulus computed after the PBC application when the number of the unit cells increases as well. It is shown that the Gyroid skeletal lattice is less sensitive to the boundary effects as it is the only topology that almost reaches the reference elastic modulus with $3 * 3 * 3$ unit cells repetitions. The elastic modulus after the CBC application convergence to the reference elastic modulus is illustrated graphically in Figure Appendix.7.

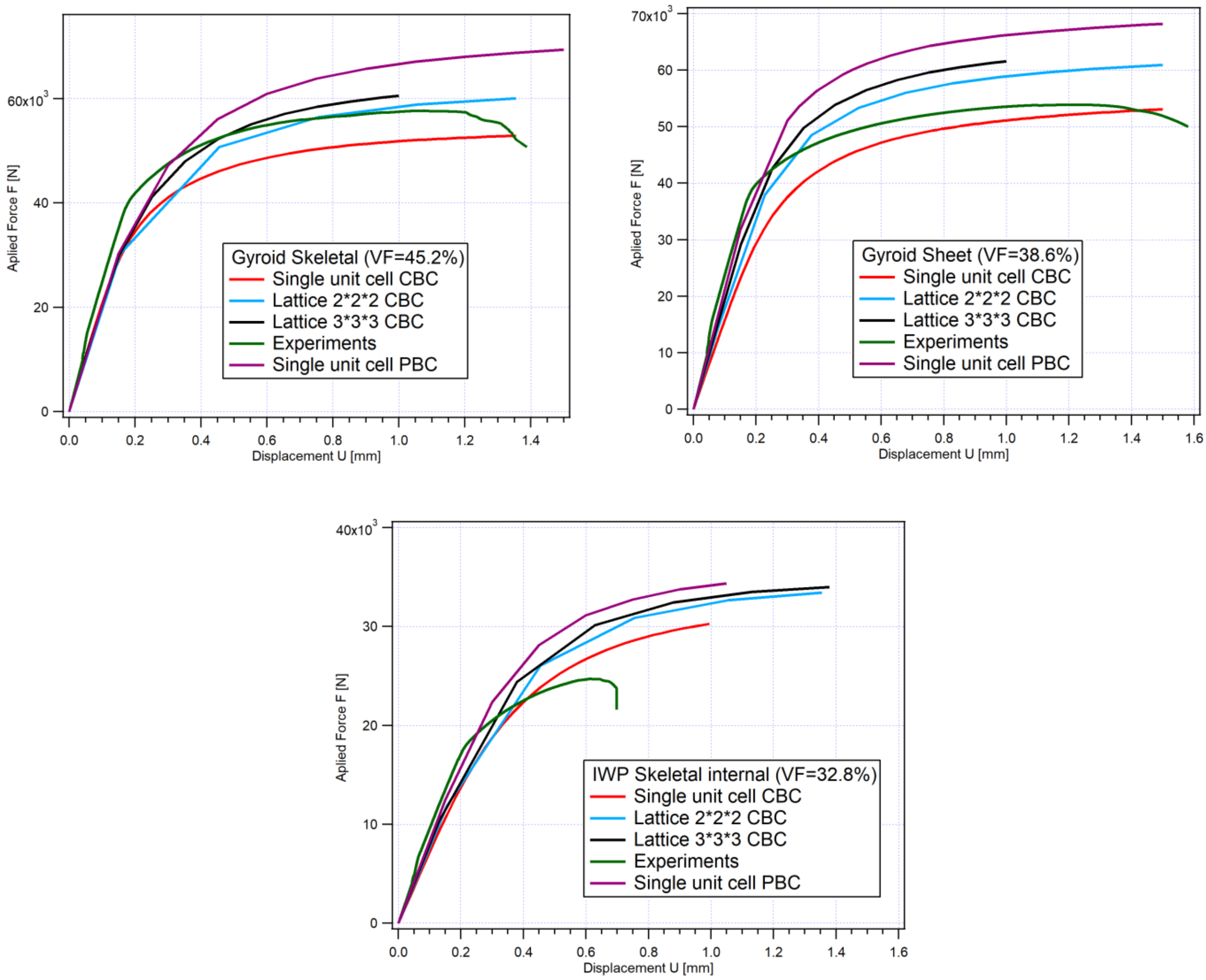

Figure Appendix.7. Graphical presentation of the linear and non-linear response of the topologies after the experimental and both the numerical tests for single unit cells and lattices with multiple unit cell repetitions.

In a numerical point of view, the non-linearity in Figure Appendix.7. always exhibits the same tendency, no matter the number of the unit cells. The apparent σ_{yield} and the maximum force also converge to the σ_{yield} after the PBC application and to a standard maximum force level when the number of unit cell repetitions increases. However, the computation time increases too. Therefore, for the sake of computation time, it is not necessary to analyze lattices with more than 3 unit cell repetitions per direction in the case of CBC application.

Bibliography

[1] C. Stewart, B. Akhavan, S. G. Wise, and M. M. M. Bilek, ‘A review of biomimetic surface functionalization for bone-integrating orthopedic implants: Mechanisms, current approaches, and future directions’, *Progress in Materials Science*, vol. 106, p. 100588, Dec. 2019, doi: 10.1016/j.pmatsci.2019.100588.

[2] L. Yuan, S. Ding, and C. Wen, ‘Additive manufacturing technology for porous metal implant applications and triple minimal surface structures: A review’, *Bioactive Materials*, vol. 4, pp. 56–70, Dec. 2019, doi: 10.1016/j.bioactmat.2018.12.003.

[3] I. Levadnyi, J. Awrejcewicz, J. E. Gubaua, and J. T. Pereira, ‘Numerical evaluation of bone remodelling and adaptation considering different hip prosthesis designs’, *Clinical Biomechanics*, vol. 50, pp. 122–129, Dec. 2017, doi: 10.1016/j.clinbiomech.2017.10.015.

[4] G. Osterhoff, E. F. Morgan, S. J. Shefelbine, L. Karim, L. M. McNamara, and P. Augat, ‘Bone mechanical properties and changes with osteoporosis’, *Injury*, vol. 47, pp. S11–S20, Jun. 2016, doi: 10.1016/S0020-1383(16)47003-8.

[5] N. M. B. K. Willems, G. E. J. Langenbach, V. Everts, and A. Zentner, ‘The microstructural and biomechanical development of the condylar bone: a review’, *The European Journal of Orthodontics*, vol. 36, no. 4, pp. 479–485, Aug. 2014, doi: 10.1093/ejo/cjt093.

[6] M. Fischer, ‘Élaboration in situ d’alliages de titane et de structures architecturées par fabrication additive : application aux dispositifs médicaux implantables’. 2017.

[7] J. Wolff, *The Law of Bone Remodelling*. Berlin, Heidelberg: Springer Berlin Heidelberg, 1986. doi: 10.1007/978-3-642-71031-5.

[8] R. Huiskes, H. Weinans, and B. van Rietbergen, ‘The relationship between stress shielding and bone resorption around total hip stems and the effects of flexible materials’, *Clin. Orthop. Relat. Res.*, no. 274, pp. 124–134, Jan. 1992.

[9] X. Wang *et al.*, ‘Topological design and additive manufacturing of porous metals for bone scaffolds and orthopaedic implants: A review’, *Biomaterials*, vol. 83, pp. 127–141, Mar. 2016, doi: 10.1016/j.biomaterials.2016.01.012.

[10] H. A. Almeida and P. J. da Silva Bártolo, ‘Mathematical Modeling of 3D Tissue Engineering Constructs’, in *3D Printing and Biofabrication*, A. Ovsianikov, J. Yoo, and V. Mironov, Eds. Cham: Springer International Publishing, 2018, pp. 223–252. doi: 10.1007/978-3-319-45444-3_5.

[11] ‘https://www.coastlineortho.com/joint-replacement-surgery-coastline-orthopaedic-associates.html’.

[12] I. D. Learmonth, C. Young, and C. Rorabeck, ‘The operation of the century: total hip replacement’, *The Lancet*, vol. 370, no. 9597, pp. 1508–1519, Oct. 2007, doi: 10.1016/S0140-6736(07)60457-7.

[13] G. Yamako *et al.*, ‘Improving stress shielding following total hip arthroplasty by using a femoral stem made of β type Ti-33.6Nb-4Sn with a Young’s modulus gradation’, *Journal of Biomechanics*, vol. 63, pp. 135–143, Oct. 2017, doi: 10.1016/j.jbiomech.2017.08.017.

[14] J. V. Bono, J. C. McCarthy, T. S. Thornhill, B. E. Bierbaum, and R. H. Turner, Eds., *Revision Total Hip Arthroplasty*. New York, NY: Springer New York, 1999. doi: 10.1007/978-1-4612-1406-9.

[15] M. Niinomi and M. Nakai, 'Titanium-Based Biomaterials for Preventing Stress Shielding between Implant Devices and Bone', *International Journal of Biomaterials*, vol. 2011, pp. 1–10, 2011, doi: 10.1155/2011/836587.
[16] A. A. Al-Tamimi, C. Peach, P. R. Fernandes, A. Cseke, and P. J. D. S. Bartolo, 'Topology Optimization to Reduce the Stress Shielding Effect for Orthopedic Applications', *Procedia CIRP*, vol. 65, pp. 202–206, 2017, doi: 10.1016/j.procir.2017.04.032.
[17] A. Schuh, J. Bigoney, W. Hönle, G. Zeiler, U. Holzwarth, and R. Forst, 'Second generation (low modulus) titanium alloys in total hip arthroplasty', *Mat.-wiss. u. Werkstofftech.*, vol. 38, no. 12, pp. 1003–1007, Dec. 2007, doi: 10.1002/mawe.200700230.
[18] S. Raghavendra *et al.*, 'Tensile and compression properties of variously arranged porous Ti-6Al-4V additively manufactured structures via SLM', *Procedia Structural Integrity*, vol. 13, pp. 149–154, 2018, doi: 10.1016/j.prostr.2018.12.025.
[19] P. Didier, B. Piotrowski, M. Fischer, and P. Laheurte, 'Mechanical stability of custom-made implants: Numerical study of anatomical device and low elastic Young's modulus alloy', *Materials Science and Engineering: C*, vol. 74, pp. 399–409, May 2017, doi: 10.1016/j.msec.2016.12.031.
[20] C. Yan, L. Hao, A. Hussein, and P. Young, 'Ti–6Al–4V triply periodic minimal surface structures for bone implants fabricated via selective laser melting', *Journal of the Mechanical Behavior of Biomedical Materials*, vol. 51, pp. 61–73, Nov. 2015, doi: 10.1016/j.jmbbm.2015.06.024.
[21] M. Niinomi, 'Mechanical properties of biomedical titanium alloys', *Materials Science and Engineering: A*, vol. 243, no. 1–2, pp. 231–236, Mar. 1998, doi: 10.1016/S0921-5093(97)00806-X.
[22] P. Laheurte, F. Prima, A. Eberhardt, T. Gloriant, M. Wary, and E. Patoor, 'Mechanical properties of low modulus ββ titanium alloys designed from the electronic approach', *Journal of the Mechanical Behavior of Biomedical Materials*, vol. 3, no. 8, pp. 565–573, Nov. 2010, doi: 10.1016/j.jmbbm.2010.07.001.
[23] W. Elmay *et al.*, 'Optimisation of mechanical properties of Ti–Nb binary alloys for biomedical applications', *Computer Methods in Biomechanics and Biomedical Engineering*, vol. 14, no. sup1, pp. 119–120, Aug. 2011, doi: 10.1080/10255842.2011.593760.
[24] D. Mahmoud and M. Elbestawi, 'Lattice Structures and Functionally Graded Materials Applications in Additive Manufacturing of Orthopedic Implants: A Review', *JMMP*, vol. 1, no. 2, p. 13, Oct. 2017, doi: 10.3390/jmmp1020013.
[25] T. A. Enab, N. Fouda, and I. Eldesouky, 'Comparison of Functionally Graded Hip Stem Implants with Various Second-Generation Titanium Alloys', *J. Appl. Comput. Mech.*, no. Online First, Apr. 2020, doi: 10.22055/jacm.2020.32964.2115.
[26] B. Piotrowski, A. A. Baptista, E. Patoor, P. Bravetti, A. Eberhardt, and P. Laheurte, 'Interaction of bone–dental implant with new ultra low modulus alloy using a numerical approach', *Materials Science and Engineering: C*, vol. 38, pp. 151–160, May 2014, doi: 10.1016/j.msec.2014.01.048.
[27] A. Ataee, Y. Li, M. Brandt, and C. Wen, 'Ultrahigh-strength titanium gyroid scaffolds manufactured by selective laser melting (SLM) for bone implant applications', *Acta Materialia*, vol. 158, pp. 354–368, Oct. 2018, doi: 10.1016/j.actamat.2018.08.005.
[28] E. Alabort, D. Barba, and R. C. Reed, 'Design of metallic bone by additive manufacturing', *Scripta Materialia*, vol. 164, pp. 110–114, Apr. 2019, doi: 10.1016/j.scriptamat.2019.01.022.

[29] D. Barba, E. Alabort, and R. C. Reed, 'Synthetic bone: Design by additive manufacturing', *Acta Biomaterialia*, vol. 97, pp. 637–656, Oct. 2019, doi: 10.1016/j.actbio.2019.07.049.
[30] M. F. Ashby, 'The properties of foams and lattices', *Phil. Trans. R. Soc. A.*, vol. 364, no. 1838, pp. 15–30, Jan. 2006, doi: 10.1098/rsta.2005.1678.
[31] X. P. Tan, Y. J. Tan, C. S. L. Chow, S. B. Tor, and W. Y. Yeong, 'Metallic powder-bed based 3D printing of cellular scaffolds for orthopaedic implants: A state-of-the-art review on manufacturing, topological design, mechanical properties and biocompatibility', *Materials Science and Engineering: C*, vol. 76, pp. 1328–1343, Jul. 2017, doi: 10.1016/j.msec.2017.02.094.
[32] I. Maskery *et al.*, 'Insights into the mechanical properties of several triply periodic minimal surface lattice structures made by polymer additive manufacturing', *Polymer*, vol. 152, pp. 62–71, Sep. 2018, doi: 10.1016/j.polymer.2017.11.049.
[33] K. Colic and A. Sedmak, 'The current approach to research and design of the artificial hip prosthesis: a review', *Rheumatol Orthop Med*, vol. 1, no. 1, 2016, doi: 10.15761/ROM.1000106.
[34] Y. He, D. Burkhalter, D. Durocher, and J. M. Gilbert, 'Solid-Lattice Hip Prosthesis Design: Applying Topology and Lattice Optimization to Reduce Stress Shielding From Hip Implants', in *2018 Design of Medical Devices Conference*, Minneapolis, Minnesota, USA, Apr. 2018, p. V001T03A001. doi: 10.1115/DMD2018-6804.
[35] S. Xu, J. Shen, S. Zhou, X. Huang, and Y. M. Xie, 'Design of lattice structures with controlled anisotropy', *Materials & Design*, vol. 93, pp. 443–447, Mar. 2016, doi: 10.1016/j.matdes.2016.01.007.
[36] O. Al-Ketan, D.-W. Lee, R. Rowshan, and R. K. Abu Al-Rub, 'Functionally graded and multi-morphology sheet TPMS lattices: Design, manufacturing, and mechanical properties', *Journal of the Mechanical Behavior of Biomedical Materials*, vol. 102, p. 103520, Feb. 2020, doi: 10.1016/j.jmbbm.2019.103520.
[37] P. Lohmuller, J. Favre, B. Piotrowski, S. Kenzari, and P. Laheurte, 'Stress Concentration and Mechanical Strength of Cubic Lattice Architectures', *Materials*, vol. 11, no. 7, p. 1146, Jul. 2018, doi: 10.3390/ma11071146.
[38] M. Leary, 'Design of titanium implants for additive manufacturing', in *Titanium in Medical and Dental Applications*, Elsevier, 2018, pp. 203–224. doi: 10.1016/B978-0-12-812456-7.00009-3.
[39] N. Soro, N. Saintier, J. Merzeau, M. Veidt, and M. S. Dargusch, 'Quasi-static and fatigue properties of graded Ti-6Al-4V lattices produced by Laser Powder Bed Fusion (LPBF)', *Additive Manufacturing*, p. 101653, Oct. 2020, doi: 10.1016/j.addma.2020.101653.
[40] O. Al-Ketan, R. Rowshan, and R. K. Abu Al-Rub, 'Topology-mechanical property relationship of 3D printed strut, skeletal, and sheet based periodic metallic cellular materials', *Additive Manufacturing*, vol. 19, pp. 167–183, Jan. 2018, doi: 10.1016/j.addma.2017.12.006.
[41] V. S. Deshpande, N. A. Fleck, and M. F. Ashby, 'Effective properties of the octet-truss lattice material', *Journal of the Mechanics and Physics of Solids*, vol. 49, no. 8, pp. 1747–1769, Aug. 2001, doi: 10.1016/S0022-5096(01)00010-2.
[42] I. Maskery *et al.*, 'An investigation into reinforced and functionally graded lattice structures', *Journal of Cellular Plastics*, vol. 53, no. 2, pp. 151–165, Mar. 2017, doi: 10.1177/0021955X16639035.
[43] J. Favre, P. Lohmuller, B. Piotrowski, S. Kenzari, P. Laheurte, and F. Meraghni, 'A continuous crystallographic approach to generate cubic lattices and its effect on relative stiffness of architectured materials', *Additive Manufacturing*, vol. 21, pp. 359–368, May 2018, doi: 10.1016/j.addma.2018.02.020.

[44] A. H. Schoen, ‘Infinite periodic minimal surfaces without self-intersections’, 1970.
[45] M. Pelanconi and A. Ortona, ‘Nature-Inspired, Ultra-Lightweight Structures with Gyroid Cores Produced by Additive Manufacturing and Reinforced by Unidirectional Carbon Fiber Ribs’, *Materials*, vol. 12, no. 24, p. 4134, Dec. 2019, doi: 10.3390/ma12244134.
[46] P. J. F. Gandy and J. Klinowski, ‘Exact computation of the triply periodic Schwarz P minimal surface’, *Chemical Physics Letters*, vol. 322, no. 6, pp. 579–586, Jun. 2000, doi: 10.1016/S0009-2614(00)00453-X.
[47] P. J. F. Gandy and J. Klinowski, ‘Exact computation of the triply periodic G (`Gyroid’) minimal surface’, *Chemical Physics Letters*, vol. 321, no. 5–6, pp. 363–371, May 2000, doi: 10.1016/S0009-2614(00)00373-0.
[48] D. Li, W. Liao, N. Dai, and Y. M. Xie, ‘Comparison of Mechanical Properties and Energy Absorption of Sheet-Based and Strut-Based Gyroid Cellular Structures with Graded Densities’, *Materials*, vol. 12, no. 13, p. 2183, Jul. 2019, doi: 10.3390/ma12132183.
[49] I. Maskery, A. O. Aremu, L. Parry, R. D. Wildman, C. J. Tuck, and I. A. Ashcroft, ‘Effective design and simulation of surface-based lattice structures featuring volume fraction and cell type grading’, *Materials & Design*, vol. 155, pp. 220–232, Oct. 2018, doi: 10.1016/j.matdes.2018.05.058.
[50] P. Lohmuller, J. Favre, S. Kenzari, B. Piotrowski, L. Peltier, and P. Laheurte, ‘Architectural effect on 3D elastic properties and anisotropy of cubic lattice structures’, *Materials & Design*, vol. 182, p. 108059, Nov. 2019, doi: 10.1016/j.matdes.2019.108059.
[51] R. K. Abu Al-Rub, D.-W. Lee, K. A. Khan, and A. N. Palazotto, ‘Effective Anisotropic Elastic and Plastic Yield Properties of Periodic Foams Derived from Triply Periodic Schoen’s I-WP Minimal Surface’, *J. Eng. Mech.*, vol. 146, no. 5, p. 04020030, May 2020, doi: 10.1061/(ASCE)EM.1943-7889.0001759.
[52] L. J. Gibson and M. F. Ashby, *Cellular Solids: Structure and Properties*, 2nd ed. Cambridge University Press, 1997. doi: 10.1017/CBO9781139878326.
[53] M. Helou and S. Kara, ‘Design, analysis and manufacturing of lattice structures: an overview’, *International Journal of Computer Integrated Manufacturing*, vol. 31, no. 3, pp. 243–261, Mar. 2018, doi: 10.1080/0951192X.2017.1407456.
[54] L.-Y. Zhu, L. Li, J.-P. Shi, Z.-A. Li, and J.-Q. Yang, ‘Mechanical characterization of 3D printed multi-morphology porous Ti6Al4V scaffolds based on triply periodic minimal surface architectures’, *Am J Transl Res*, vol. 10, no. 11, pp. 3443–3454, 2018.
[55] M. Afshar, A. Pourkamali Anaraki, and H. Montazerian, ‘Compressive characteristics of radially graded porosity scaffolds architectured with minimal surfaces’, *Materials Science and Engineering: C*, vol. 92, pp. 254–267, Nov. 2018, doi: 10.1016/j.msec.2018.06.051.
[56] N. Yang, Z. Quan, D. Zhang, and Y. Tian, ‘Multi-morphology transition hybridization CAD design of minimal surface porous structures for use in tissue engineering’, *Computer-Aided Design*, vol. 56, pp. 11–21, Nov. 2014, doi: 10.1016/j.cad.2014.06.006.
[57] P. Thanigaiarasu, ‘Biomimetics in the design of medical devices’, in *Trends in Development of Medical Devices*, Elsevier, 2020, pp. 35–41. doi: 10.1016/B978-0-12-820960-8.00003-4.
[58] S. Van Bael *et al.*, ‘The effect of pore geometry on the in vitro biological behavior of human periosteum-derived cells seeded on selective laser-melted Ti6Al4V bone scaffolds’, *Acta Biomaterialia*, vol. 8, no. 7, pp. 2824–2834, Jul. 2012, doi: 10.1016/j.actbio.2012.04.001.
[59] K. V. Wong and A. Hernandez, ‘A Review of Additive Manufacturing’, *ISRN Mechanical Engineering*, vol. 2012, pp. 1–10, Aug. 2012, doi: 10.5402/2012/208760.

[60] F. P. W. Melchels, M. A. N. Domingos, T. J. Klein, J. Malda, P. J. Bartolo, and D. W. Hutmacher, ‘Additive manufacturing of tissues and organs’, *Progress in Polymer Science*, vol. 37, no. 8, pp. 1079–1104, Aug. 2012, doi: 10.1016/j.progpolymsci.2011.11.007.

[61] F. Calignano *et al.*, ‘Overview on Additive Manufacturing Technologies’, *Proc. IEEE*, vol. 105, no. 4, pp. 593–612, Apr. 2017, doi: 10.1109/JPROC.2016.2625098.

[62] L.-C. Zhang, J. Wang, Y. Liu, Z. Jia, and S.-X. Liang, ‘Additive Manufacturing of Titanium Alloys’, in *Reference Module in Materials Science and Materials Engineering*, Elsevier, 2020, p. B9780128197264001000. doi: 10.1016/B978-0-12-819726-4.00002-8.

[63] K. Munir, A. Biesiekierski, C. Wen, and Y. Li, ‘Selective laser melting in biomedical manufacturing’, in *Metallic Biomaterials Processing and Medical Device Manufacturing*, Elsevier, 2020, pp. 235–269. doi: 10.1016/B978-0-08-102965-7.00007-2.

[64] LOHMULLER, PAUL, ‘Matériaux mésostructurés et Infiltration Métallique avec Optimisation du Squelette Architecturé’, 2019.

[65] K. A. Mumtaz, P. Erasenthiran, and N. Hopkinson, ‘High density selective laser melting of Waspaloy®’, *Journal of Materials Processing Technology*, vol. 195, no. 1–3, pp. 77–87, Jan. 2008, doi: 10.1016/j.jmatprotec.2007.04.117.

[66] A. Bandyopadhyay and S. Bose, Eds., *Additive manufacturing, second edition*, 2nd ed. Boca Raton: CRC Press, 2019.

[67] P. K. Gokuldoss, S. Kolla, and J. Eckert, ‘Additive Manufacturing Processes: Selective Laser Melting, Electron Beam Melting and Binder Jetting—Selection Guidelines’, *Materials*, vol. 10, no. 6, p. 672, Jun. 2017, doi: 10.3390/ma10060672.

[68] J. Chen, W. Hou, X. Wang, S. Chu, and Z. Yang, ‘Microstructure, porosity and mechanical properties of selective laser melted AlSi10Mg’, *Chinese Journal of Aeronautics*, vol. 33, no. 7, pp. 2043–2054, Jul. 2020, doi: 10.1016/j.cja.2019.08.017.

[69] C. Yan, L. Hao, A. Hussein, and D. Raymont, ‘Evaluations of cellular lattice structures manufactured using selective laser melting’, *International Journal of Machine Tools and Manufacture*, vol. 62, pp. 32–38, Nov. 2012, doi: 10.1016/j.ijmachtools.2012.06.002.

[70] I. Buj-Corral, A. Tejo-Otero, and F. Fenollosa-Artés, ‘Development of AM Technologies for Metals in the Sector of Medical Implants’, *Metals*, vol. 10, no. 5, p. 686, May 2020, doi: 10.3390/met10050686.

[71] M. I. Mohammed, A. P. Fitzpatrick, and I. Gibson, ‘Customised design of a patient specific 3D printed whole mandible implant’, *KEG*, vol. 2, no. 2, p. 104, Feb. 2017, doi: 10.18502/keg.v2i2.602.

[72] K. McHenry and P. Bajcsy, ‘An Overview of 3D Data Content, File Formats and Viewers’, National Center for Supercomputing Applications University of Illinois at Urbana-Champaign, Urbana, IL, Oct. 2008. [Online]. Available: http://isda.ncsa.illinois.edu/peter/publications/techreports/2008/NCSA-ISDA-2008-002.pdf

[73] D. Wang, O. Hassan, K. Morgan, and N. Weatherill, ‘Enhanced remeshing from STL files with applications to surface grid generation’, *Commun. Numer. Meth. Engng.*, vol. 23, no. 3, pp. 227–239, Sep. 2006, doi: 10.1002/cnm.894.

[74] Suquet, P. M, ‘Elements of homogenization for inelastic solid mechanics.’, *In Lecture Notes in Physics, Springer, Berlin*, vol. 272, pp. 193–278, 1987.

[75] F. Praud, G. Chatzigeorgiou, and F. Meraghni, ‘Fully integrated multi-scale modelling of damage and time-dependency in thermoplastic-based woven composites’, *International Journal of Damage Mechanics*, p. 105678952094498, Sep. 2020, doi: 10.1177/1056789520944986.

[76] F. Praud, ‘Multi-scale modelling of thermoplastic-based woven composites, cyclic and timedependent behaviour.’, Ecole nationale supérieure d’arts et métiers - ENSAM, 2018.

[77] J. Feng, B. Liu, Z. Lin, and J. Fu, 'Isotropic porous structure design methods based on triply periodic minimal surfaces', *Materials & Design*, vol. 210, p. 110050, Nov. 2021, doi: 10.1016/j.matdes.2021.110050.

[78] Z. Chen, Y. M. Xie, X. Wu, Z. Wang, Q. Li, and S. Zhou, 'On hybrid cellular materials based on triply periodic minimal surfaces with extreme mechanical properties', *Materials & Design*, vol. 183, p. 108109, Dec. 2019, doi: 10.1016/j.matdes.2019.108109.

[79] Q. Grimal and P. Laugier, 'Quantitative Ultrasound Assessment of Cortical Bone Properties Beyond Bone Mineral Density', *IRBM*, vol. 40, no. 1, pp. 16–24, Feb. 2019, doi: 10.1016/j.irbm.2018.10.006.

[80] 'INTERNATIONAL STANDARD, ISO 13314, First edition 2011-12-15, Mechanical testing of metals, Ductility testing, Compression test for porous and cellular metals'. Dec. 15, 2011.

[81] H. Zaharin *et al.*, 'Effect of Unit Cell Type and Pore Size on Porosity and Mechanical Behavior of Additively Manufactured Ti6Al4V Scaffolds', *Materials*, vol. 11, no. 12, p. 2402, Nov. 2018, doi: 10.3390/ma11122402.

[82] J. Kadkhodapour, H. Montazerian, A. Ch. Darabi, A. Zargarian, and S. Schmauder, 'The relationships between deformation mechanisms and mechanical properties of additively manufactured porous biomaterials', *Journal of the Mechanical Behavior of Biomedical Materials*, vol. 70, pp. 28–42, Jun. 2017, doi: 10.1016/j.jmbbm.2016.09.018.

[83] F. Liu, H. Zhou, and D. Li, 'Repair of STL errors', *International Journal of Production Research*, vol. 47, no. 1, pp. 105–118, Jan. 2009, doi: 10.1080/00207540701424539.

[84] H. Jee, 'Preparation of "Ready-Made STL (RMS)" for build assurance in additive metal manufacturing (AMM): A review', *J Mech Sci Technol*, vol. 33, no. 12, pp. 5643–5652, Dec. 2019, doi: 10.1007/s12206-019-1106-3.

[85] L. Yang, C. Yan, C. Han, P. Chen, S. Yang, and Y. Shi, 'Mechanical response of a triply periodic minimal surface cellular structures manufactured by selective laser melting', *International Journal of Mechanical Sciences*, vol. 148, pp. 149–157, Nov. 2018, doi: 10.1016/j.ijmecsci.2018.08.039.

[86] Q. C. Liu, J. Elambasseril, S. J. Sun, M. Leary, M. Brandt, and P. K. Sharp, 'The Effect of Manufacturing Defects on the Fatigue Behaviour of Ti-6Al-4V Specimens Fabricated Using Selective Laser Melting', *AMR*, vol. 891–892, pp. 1519–1524, Mar. 2014, doi: 10.4028/www.scientific.net/AMR.891-892.1519.

[87] P. Didier, 'Solutions matériaux et géométriques pour la réalisation de dispositifs médicaux implantables sur-mesure en alliages de titane : application aux implants endo-osseux et supra-osseux obtenus par fabrication additive. Mécanique des matériaux [physics.class-ph]. Université de Lorraine, 2019. Français. ffNNT : 2019LORR0262ff. fftel-02558288f'.

[88] L. Zhang *et al.*, 'Energy absorption characteristics of metallic triply periodic minimal surface sheet structures under compressive loading', *Additive Manufacturing*, vol. 23, pp. 505–515, Oct. 2018, doi: 10.1016/j.addma.2018.08.007.

[89] H. Mehboob *et al.*, 'A novel design, analysis and 3D printing of Ti-6Al-4V alloy bio-inspired porous femoral stem', *J Mater Sci: Mater Med*, vol. 31, no. 9, p. 78, Sep. 2020, doi: 10.1007/s10856-020-06420-7.

[90] J. Zacher and A. Gursche, '"Hip" pain', *Best Practice & Research Clinical Rheumatology*, vol. 17, no. 1, pp. 71–85, Feb. 2003, doi: 10.1016/S1521-6942(02)00108-0.

[91] P. Lang, H. K. Genant, H. E. Jergesen, and W. R. Murray, 'Imaging of the hip joint. Computed tomography versus magnetic resonance imaging', *Clin Orthop Relat Res*, no. 274, pp. 135–153, Jan. 1992.

[92] T. D. Roth, N. A. Maertz, J. A. Parr, K. A. Buckwalter, and R. H. Choplin, ‘CT of the Hip Prosthesis: Appearance of Components, Fixation, and Complications’, *RadioGraphics*, vol. 32, no. 4, pp. 1089–1107, Jul. 2012, doi: 10.1148/rg.324115183.

[93] J. Fritz, B. Lurie, T. T. Miller, and H. G. Potter, ‘MR Imaging of Hip Arthroplasty Implants’, *RadioGraphics*, vol. 34, no. 4, pp. E106–E132, Jul. 2014, doi: 10.1148/rg.344140010.

[94] R. Havaldar, S. Pilli, and B. Putti, ‘Insights into the effects of tensile and compressive loadings on human femur bone’, *Adv Biomed Res*, vol. 3, no. 1, p. 101, 2014, doi: 10.4103/2277-9175.129375.

[95] W. Solórzano, C. Ojeda, and A. Diaz Lantada, ‘Biomechanical Study of Proximal Femur for Designing Stems for Total Hip Replacement’, *Applied Sciences*, vol. 10, no. 12, p. 4208, Jun. 2020, doi: 10.3390/app10124208.

[96] Y. Jun and K. Choi, ‘Design of patient-specific hip implants based on the 3D geometry of the human femur’, *Advances in Engineering Software*, vol. 41, no. 4, pp. 537–547, Apr. 2010, doi: 10.1016/j.advengsoft.2009.10.016.

[97] J. M. Haglin, A. E. M. Eltorai, J. A. Gil, S. E. Marcaccio, J. Botero-Hincapie, and A. H. Daniels, ‘Patient-Specific Orthopaedic Implants: Orthopaedic Implants’, *Orthop Surg*, vol. 8, no. 4, pp. 417–424, Nov. 2016, doi: 10.1111/os.12282.

[98] K. C. Wong, ‘3D-printed patient-specific applications in orthopedics’, *ORR*, vol. Volume 8, pp. 57–66, Oct. 2016, doi: 10.2147/ORR.S99614.

[99] M. Mustra, K. Delac, and M. Grgic, ‘Overview of the DICOM standard’. 50th International Symposium ELMAR, 2008, pp. 39-44, 2008.

[100] ‘https://www.dicomstandard.org/’.

[101] D. R. Varma, ‘Managing DICOM images: Tips and tricks for the radiologist’, *Indian Journal of Radiology and Imaging*, vol. 22, no. 01, pp. 4–13, Jan. 2012, doi: 10.4103/0971-3026.95396.

[102] R. N. J. Graham, R. W. Perriss, and A. F. Scarsbrook, ‘DICOM demystified: A review of digital file formats and their use in radiological practice’, *Clinical Radiology*, vol. 60, no. 11, pp. 1133–1140, Nov. 2005, doi: 10.1016/j.crad.2005.07.003.

[103] T. D. DenOtter and J. Schubert, ‘Hounsfield Unit’, in *StatPearls*, Treasure Island (FL): StatPearls Publishing, 2021. Accessed: Nov. 23, 2021. [Online]. Available: http://www.ncbi.nlm.nih.gov/books/NBK547721/

[104] N. Okkalidis, C. Chatzigeorgiou, and D. Okkalides, ‘Assessment of 11 Available Materials With Custom Three-Dimensional-Printing Patterns for the Simulation of Muscle, Fat, and Lung Hounsfield Units in Patient-Specific Phantoms’, *Journal of Engineering and Science in Medical Diagnostics and Therapy*, vol. 1, no. 1, p. 011003, Feb. 2018, doi: 10.1115/1.4038228.

[105] S. N. Khan, R. M. Warkhedkar, and A. K. Shyam, ‘Analysis of Hounsfield Unit of Human Bones for Strength Evaluation’, *Procedia Materials Science*, vol. 6, pp. 512–519, 2014, doi: 10.1016/j.mspro.2014.07.065.

[106] ‘http://balticimplants.eu/patient-specific-medical-devices/hip-joint-implants/’.

[107] J. Y. Rho, M. C. Hobatho, and R. B. Ashman, ‘Relations of mechanical properties to density and CT numbers in human bone’, *Medical Engineering & Physics*, vol. 17, no. 5, pp. 347–355, Jul. 1995, doi: 10.1016/1350-4533(95)97314-F.

[108] V. N. Chougule, A. V. Mulay, and B. B. Ahuja, ‘Clinical Case Study: Spine Modeling for Minimum Invasive Spine Surgeries (MISS) using Rapid Prototyping’, presented at the Proceedings of 10th International Conference on Precision, Meso, Micro and Nano Engineering (COPEN 10) December 07-09, 2017, Indian Institute of Technology Madras, Chennai-600 036 INDIA, Feb. 2018.

[109] M. J. Ciarelli, S. A. Goldstein, J. L. Kuhn, D. D. Cody, and M. B. Brown, 'Evaluation of orthogonal mechanical properties and density of human trabecular bone from the major metaphyseal regions with materials testing and computed tomography', *J. Orthop. Res.*, vol. 9, no. 5, pp. 674–682, Sep. 1991, doi: 10.1002/jor.1100090507.

[110] 'https://my-ms.org/mri_planes.htm'.

[111] D. T. Reilly and A. H. Burstein, 'The elastic and ultimate properties of compact bone tissue', *Journal of Biomechanics*, vol. 8, no. 6, pp. 393–405, Jan. 1975, doi: 10.1016/0021-9290(75)90075-5.

[112] E. F. Morgan, G. U. Unnikrisnan, and A. I. Hussein, 'Bone Mechanical Properties in Healthy and Diseased States', *Annu. Rev. Biomed. Eng.*, vol. 20, no. 1, pp. 119–143, Jun. 2018, doi: 10.1146/annurev-bioeng-062117-121139.

[113] M. O. Heller *et al.*, 'Musculo-skeletal loading conditions at the hip during walking and stair climbing', *Journal of Biomechanics*, vol. 34, no. 7, pp. 883–893, Jul. 2001, doi: 10.1016/S0021-9290(01)00039-2.

[114] G. Bergmann, A. Bender, J. Dymke, G. Duda, and P. Damm, 'Standardized Loads Acting in Hip Implants', *PLoS ONE*, vol. 11, no. 5, p. e0155612, May 2016, doi: 10.1371/journal.pone.0155612.

[115] 'https://www.nlm.nih.gov/'.

[116] 'https://www.azom.com/article.aspx?ArticleID=9299'.

[117] N. Yang, Y. Song, J. Huang, Y. Chen, and I. Maskery, 'Combinational design of heterogeneous lattices with hybrid region stiffness tuning for additive manufacturing', *Materials & Design*, vol. 209, p. 109955, Nov. 2021, doi: 10.1016/j.matdes.2021.109955.

[118] Eric A. Lord, and Alan L. Macka, 'Periodic minimal surfaces of cubic symmetry'. Aug. 10, 2003. [Online]. Available: https://eprints.bbk.ac.uk/id/eprint/282/1/mackay1.pdf

[119] S. and A. M. International Conference on Computational Modeling, *Three Approaches to the Gyroid Structure Modelling as a Base of Lightweight Component Produced by Additive Technology*. 2nd International Conference on Computational Modeling, Simulation and Applied Mathematics (CMSAM 2017) October 22-23, 2017, Beijing, China., 2017. Accessed: Oct. 04, 2021. [Online]. Available: http://dpi-proceedings.com/index.php/dtcse/issue/view/179

[120] G. Savio, R. Meneghello, and G. Concheri, 'Design of variable thickness triply periodic surfaces for additive manufacturing', *Prog Addit Manuf*, vol. 4, no. 3, pp. 281–290, Sep. 2019, doi: 10.1007/s40964-019-00073-x.

Second Part :

Extended summary in French

Introduction

Les implants orthopédiques constituent un traitement efficace pour les maladies osseuses graves, telles que l'arthrose et les fractures osseuses. Par exemple, le remplacement de la hanche est l'une des opérations les plus courantes utilisant des implants orthopédiques. Bien que ces derniers permettent aux patients de retrouver leurs activités quotidiennes, plusieurs complications biomécaniques postopératoires peuvent survenir quelques années après la chirurgie et induire des sensations douloureuses, et nécessiter une reprise chirurgicale. D'un point de vue mécanique, un problème habituel qui se produit et appelé déviation des contraintes, (Stress-shielding), en raison de la forte inadéquation de rigidité entre un implant et l'os. Un résultat négatif de la déviation des contraintes est la diminution de densité de l'os environnant. Une solution pour résoudre le problème déviation des contraintes consiste à réduire la rigidité de l'implant pour mimer la réponse mécanique de l'os. Pour atteindre cet objectif, deux voies sont généralement explorées. La première est l'utilisation de matériaux dont le module d'élasticité est proche du niveau de l'os, tels que les alliages de titane de type Beta. Ces derniers présentent un module d'élasticité très faible pouvant atteindre jusqu'à 55 GPa, soit environ deux fois inférieur par rapport à l'alliage Ti-6Al-4V couramment utilisé pour les implants (E=110 GPa). La seconde est d'utiliser des implants avec une géométrie adaptée à l'échelle de leur mesostructure, c'est-à-dire des matériaux architecturés pour influer sur le module d'élasticité et le réduire en dessous de 55 GPa. Cette étude est indépendante des matériaux et la voie étudiée pour réduire la rigidité des matériaux est basée sur la génération de structures en treillis et leur optimisation topologique vers des applications biomécaniques.

Les treillis qui sont une sous-classe des matériaux architecturés présentent une géométrie définie qui permet le contrôle et l'optimisation des propriétés élastiques et mécaniques globales des implants. De plus, ils pourraient être utiles à d'autres applications d'ingénierie tissulaire. Ces « structures lattices » consistent en plusieurs répétitions de cellules unitaires dans toutes les directions, et périodiques. La réponse mécanique de ces structures dépend de la topologie et même si certaines structures peuvent avoir la même fraction volumique, les propriétés mécaniques peuvent différer de manière significative. Par conséquent, la sélection d'une topologie appropriée pour la génération d'implants est cruciale.

Les structures en treillis sont divisées en deux catégories ; treillis à base poutre et à structures basées sur des surfaces. Le comportement mécanique des premières a été largement étudié ces dernières années. Cependant, les connexions nettes entre les poutres sont considérées comme un inconvénient car elles peuvent devenir des zones de fortes concentrations de contraintes. Afin de surmonter cette limitation, les structures basées sur des surfaces ont été récemment étudiées et seules quelques études peuvent être trouvées dans la littérature. En particulier pour assurer la périodicité des cellules dans l'espace 3D, les structures basées sur des surfaces sont générées à partir des surfaces minimales triplement périodiques (TPMS). En ce qui concerne les structures TPMS, l'absence d'arêtes vives peut conduire à de meilleurs résultats concernant la concentration de contraintes par rapport aux topologies à base de poutres. Les réseaux à base de TPMS ont récemment attiré l'attention de nombreux chercheurs, non seulement en raison de la possibilité qu'ils offrent d'optimiser les propriétés mécaniques globales, mais aussi parce que des structures similaires peuvent être trouvées dans la nature. Par conséquent, les structures TPMS sont considérées comme des solutions inspirées de la nature et des structures prometteuses pour une utilisation dans des applications biomécaniques.

La fabrication de structures architecturées a été un défi pour les chercheurs en raison de leur géométrie complexe. Cependant, grâce aux améliorations des technologies de fabrication additive (FA), la fabrication de géométries et de formes complexes est réalisable. Il existe différentes technologies AM parmi lesquelles la plus appropriée peut-être sélectionnée en fonction de l'application des treillis et du matériau utilisé correspondant. La technologie de fusion laser sélective (SLM) peut être utilisée pour la fabrication de structures en treillis métallique et d'implants avec une grande variété d'alliages. Les structures construites par cette technologie présentent une grande précision car la technique SLM suit le concept de forme quasi nette et généralement un seul post-traitement limité est requis. Par conséquent, des structures architecturées et des implants sur mesure répondant aux exigences élastiques réelles peuvent être fabriqués avec succès.

Le principal défi de cette étude est la sélection de la topologie la plus appropriée répondant aux critères requis pour une application biomécanique spécifique, qui est la génération de formes d’implants pour le remplacement osseux. La conception des structures TPMS est basée sur une approche mathématique complexe qui se compose de plusieurs étapes. Le processus de conception développé permet le développement de toutes les structures TPMS possibles et la création des cellules unitaires et des réseaux pertinents qui conviennent à la fois aux analyses par éléments finis et à la fabrication avec les technologies de FA.

La compréhension de l'état de contrainte locale des structures architecturées est importante pour étudier leur durabilité. Étant donné que les structures du réseau sont périodiques, une méthode numérique d'homogénéisation périodique est mise en œuvre pour la prédiction de l'état de contrainte et des propriétés mécaniques équivalentes via la méthode des éléments finis. Afin de comparer différentes topologies. La relation entre les propriétés mécaniques et un paramètre de conception est analysée pour mettre en évidence les dépendances à la topologie et à la fraction volumique.

Avant d'appliquer les résultats susmentionnés à une étude de cas, il faut fabriquer et tester expérimentalement quelques structures pour obtenir la réponse globale et vérifier les prédictions numériques. Le premier objectif de la campagne expérimentale est la validation des résultats numériques concernant le module d'élasticité des réseaux dans un cas de chargement considéré comme standard. Le deuxième objectif est la comparaison des mécanismes de déformation et de rupture finale des structures testées dans un cas considéré comme destructif. Les deux cibles permettent la sélection d'une topologie appropriée dans l'étude du meilleur et du pire cas.

Ce travail porte principalement sur la conception de structures architecturées complexes à base de TPMS et à base de poutres, l'étude numérique de leurs propriétés mécaniques en considérant une méthode d'homogénéisation périodique, et la présentation d'outils statistiques pour la sélection d'une topologie appropriée en fonction de contraintes spécifiques. La classification des topologies est basée sur les propriétés mécaniques prédites numériquement et mesurées expérimentalement, en mettant l'accent principalement sur le module d'élasticité apparent qui permet la réduction de la déviation des contraintes. Ce document est structuré de la manière suivante :

Le premier chapitre présente une description du problème de déviation des contraintes qui se produit pour les implants orthopédiques et propose les structures architecturées comme une solution prometteuse. Ensuite, les aspects fondamentaux des réseaux à base de poutres et de TPMS, leur conception complexe et leurs propriétés mécaniques sont décrites. Enfin, la technologie de fabrication additive est détaillée et proposée comme procédé de fabrication approprié pour les structures en treillis.

Le deuxième chapitre se concentre sur l'analyse numérique des cellules unitaires, à savoir huit topologies de cellules unitaires basées sur TPMS et deux basées sur des poutres. Les étapes de conception des structures sont détaillées et les propriétés mécaniques de toutes les mailles unitaires sont calculées et comparées après la mise en œuvre d'une méthode d'homogénéisation périodique. La distribution locale des contraintes des cellules unitaires est également examinée et une application est présentée en tenant compte de tous les résultats susmentionnés.

Le troisième chapitre propose un deuxième ensemble de conditions aux limites qui est comparé aux conditions aux limites périodiques en termes de calcul de module élastique. Les résultats numériques sont comparés aux résultats expérimentaux pour évaluer l'approche de modélisation et sélectionner les conditions aux limites les plus représentatives. La rupture macroscopique sous chargement compressif et la limite d'élasticité apparente des structures sont également étudiées expérimentalement.

Le quatrième chapitre propose une application biomécanique dans laquelle une petite partie d'un véritable os fémoral est remplacée par une cellule unitaire appropriée à base de TPMS, appelée implant numérique. La charge appliquée sur le fémur correspond à un cas de chargement réel, ici le cas de la marche a été retenu. Quatre cellules unitaires différentes sont comparées en termes d'état de contrainte et de fraction volumique lorsque l'exigence d'élasticité est satisfaite.

1. Le problématique de la déviation des contraintes et les structures architecturées basées sur une description des surfaces

Les implants médicaux sont un traitement courant des blessures graves et le besoin d'implants orthopédiques a augmenté ces dernières années. Il est crucial de résoudre tous les problèmes biomécaniques postopératoires qui surviennent, tels que le problème lié aux déviation des contraintes (décrit par la loi de Wolff). Ce dernier est causé par la grande inadéquation de la rigidité entre un os humain et le matériau de l’implant. Elle entraîne alors une diminution de la densité osseuse qui se traduit par une instabilité de l'implant et des sensations douloureuses.
Une voie possible pour résoudre le problème précité est l'utilisation d'implants architecturés dont la partie interne est constituée d'une structure en treillis. Les treillis et particulièrement les structures à base de surface offrent une voie intéressante pour contrôler les propriétés mécaniques des implants. La conception et la fabrication des structures architecturées à base de surfaces est un défi, mais grâce aux technologies de fabrication additive, la fabrication de ces structures est possible et avec une précision suffisante.

Figure 1.5. Deux exemples d'implant de hanche fabriqués avec une structure interne différente. Une prothèse de hanche compacte (à gauche) et une prothèse de hanche architecturée (à droite).

La première étape dans la conception d'une structure en treillis est l'accent particulier mis sur l'aspect topologique de son architecture. La topologie particulière d'un réseau impacte fortement ses propriétés mécaniques apparentes. De plus, la densité relative des réseaux, ou la fraction dite volumique, joue un rôle important dans le contrôle de leurs propriétés mécaniques apparentes.

Il est à noter que la topologie elle-même des treillis induit des concentrations de contraintes locales dans différentes zones par rapport aux structures compactes, dans lesquelles la répartition des contraintes est uniforme. Par conséquent, la solution à ce nouveau problème, qui est la minimisation des concentrations de contraintes locales, est d'une grande importance afin d'améliorer la réponse à la fatigue des structures architecturées et d'éviter une défaillance locale imprévue due à la plasticité et/ou à l'accumulation d'endommagement.

Ces structures basées sur des surfaces minimales triplement périodiques (TPMS) et les topologies générées présentent des connexions lisses. Ils sont biomimétiques car des topologies similaires peuvent être trouvées dans la nature. Par exemple, certaines topologies TPMS sont le Gyroid de Schoen, le Primitive de Schwartz, le Neovius et l'IWP de Schoen. En particulier, les TPMS sont des surfaces périodiques dans les trois directions, comme leur nom l'indique. Elles peuvent être définies et conçues par des équations mathématiques qui offrent une approximation assez précise. Les équations de level-set sinusoïdales ont la forme générale suivante :

$$f\,(x, y, z) = t \qquad (1)$$

où t est une iso-valeur constante.

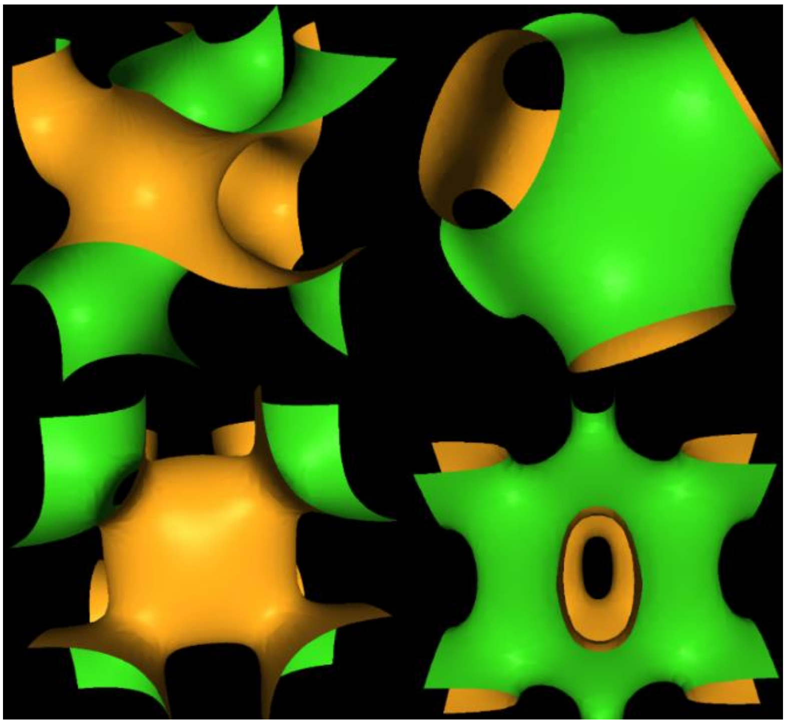

Figure 1.8. Quatre exemples de TPMS : a) Gyroid de Schoen (en haut à gauche), b) Primitive de Schwartz (en haut à droite), c) IWP de Schoen (en bas à gauche) et d) Neovius (en bas à droite).

En remplissant de matière un sous-espace partitionné par TPMS, on obtient un modèle 3D de réseau basé sur la surface dont la fraction volumique dépend de l'isovaleur t. Le processus de conception s'adapte à la manière dont les équations sinusoïdales sont utilisées et ainsi, deux types distincts de réseaux peuvent être générés, la « sheet » et la surface « skeletal » générées par l'équation (1).

Les réseaux peuvent présenter soit un gradient de macro-porosité, soit un gradient structurel dans une ou plusieurs directions. De plus, les réseaux peuvent présenter un gradient radial de macro-porosité. Ce type de réseaux offre une excellente opportunité aux chercheurs d'adapter la réponse mécanique de divers matériaux architecturés.

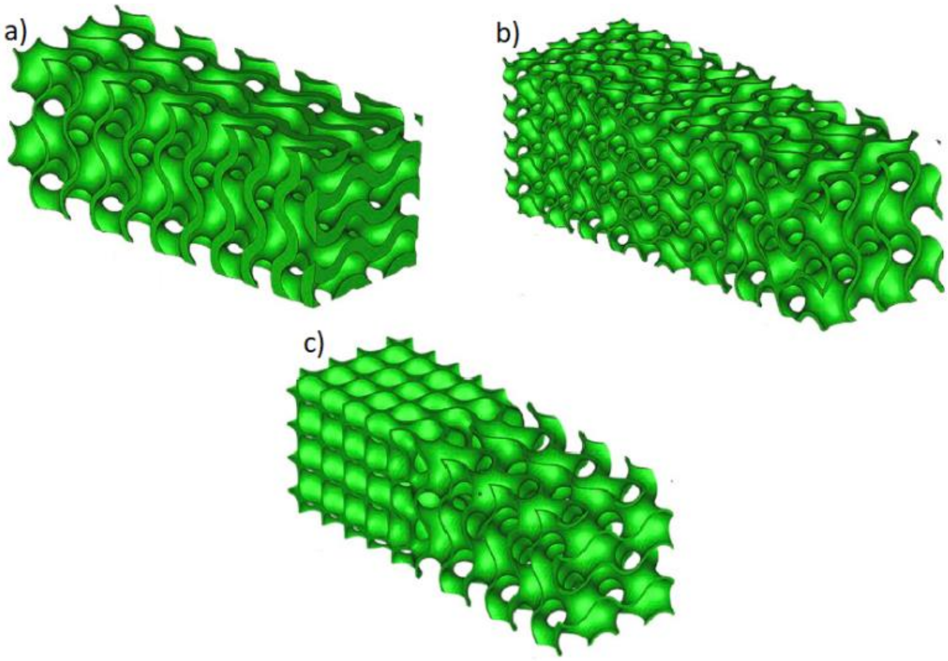

Figure 1.11. a) Gradient de macro-porosité pour une structure gyroid sheet, b) gradient de taille de cellule unitaire pour une structure gyroid sheet, et c) gradient de multi-morphologie pour une structure gyroid sheet Schwartz Diamond - sheet.

Il est évident que les structures en treillis présentent une géométrie assez complexe qui ne peut être fabriquée en utilisant les procédés de fabrication soustractifs conventionnels, tels que l'usinage, en raison de leurs capacités limitées. Cependant, grâce à l'avènement et aux améliorations récentes des technologies de fabrication additive (FA), la fabrication de formes complexes, telles que des structures en treillis, est aujourd'hui facilement réalisable. En particulier, les implants 3D et les dispositifs médicaux sont fabriqués par une machine SLM.

2. Conception, propriétés élastiques effectives et répartition locale des contraintes des structures à base de TPMS

La conception numérique des structures architecturées est l'étape initiale. Les réseaux sont des structures strictement définies qui consistent en plusieurs répétitions d'une cellule unitaire périodique. Une cellule unitaire contient tous les détails morphologiques et peut être basée sur des poutres ou sur des TPMS tandis que le processus de conception est adapté en conséquence. Dans cette étude, deux cellules unitaires basées sur des poutres et huit cellules unitaires basées sur TPMS ont été conçues et étudiées en ce qui concerne les propriétés mécaniques effectives et la distribution des contraintes locales. Les structures architecturées elles-mêmes induisent une concentration de contraintes locales sur différentes zones de chaque structure. La génération d'une chaîne numérique complète pour concevoir et étudier numériquement les propriétés élastiques et la distribution des contraintes locales est le premier défi de cette étude. Il est présenté graphiquement à la Figure 2.1.

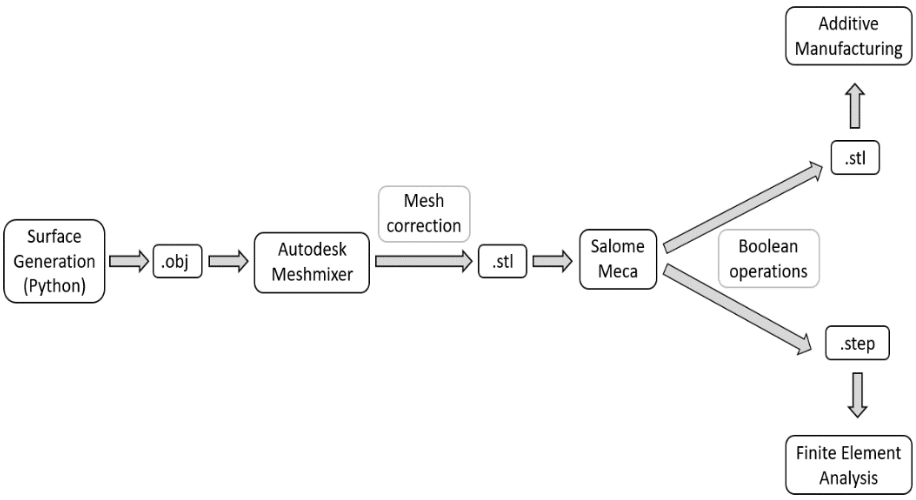

Figure 2.1. Chaîne numérique complète pour le processus de conception suivi dans cette étude.

En ce qui concerne la conception des cellules unitaires basées sur TPMS, deux surfaces opposées sont conçues à l'aide d'un script Python personnalisé et des équations suivantes $f(x, y, z) = t$ et $f(x, y, z) = -t$, où t est une isovaleur constante qui contrôle le décalage des surfaces. Chaque iso-surface est enregistrée séparément et le maillage de la surface est corrigé. Un modèle 3D d'un cube est partitionné par les deux surfaces en effectuant des opérations booléennes et ainsi, des cellules unitaires de types différents sont générées, c'est-à-dire une sheet et deux cellules unitaires skeletal (Figure 2.4.). La fraction volumique des cellules unitaires varie en fonction de la conception mathématique des surfaces initiales.

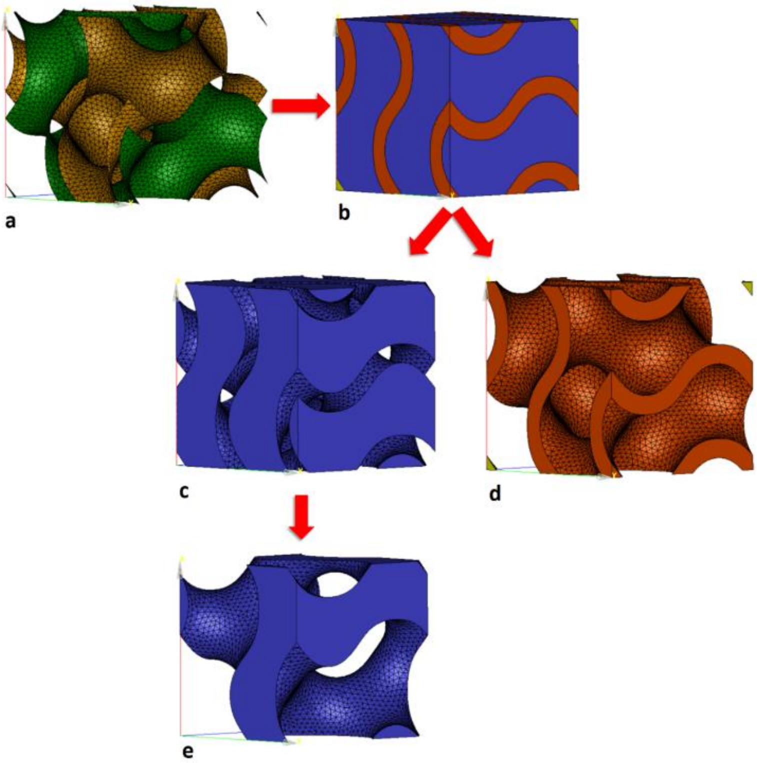

Figure 2.4. a) Deux surfaces de cellules unitaires gyroid avec un décalage opposé, b) un cube divisé par deux surfaces opposées, c) deux cellules unitaires skeletal générées, d) une cellule unitaire sheet (avec deux petites parties sur les coins pour assurer la périodicité), et e) une seule cellule unitaire skeletal.

Une méthode d'homogénéisation périodique compatible à la méthode des éléments finis est mise en œuvre sur les structures architecturées pour estimer avec précision leurs propriétés mécaniques effectives. Pour l'application correcte des conditions aux limites périodiques (PBC), le maillage du VER (Volume Elémentaire Représentatif) doit être périodique. Une méthode de perturbation linéaire et six cas de chargement contrôlés par déformation sont implémentés pour chaque VER. Pour chaque cas de charge, une colonne de la matrice de rigidité complète est obtenue. La forme générale de la matrice de rigidité cubique pour toutes les mailles unitaires est indiquée dans l'équation (15).

$$C_{ij} = \begin{bmatrix} C_{11} & C_{12} & C_{12} & 0 & 0 & 0 \\ C_{12} & C_{11} & C_{12} & 0 & 0 & 0 \\ C_{12} & C_{12} & C_{11} & 0 & 0 & 0 \\ 0 & 0 & 0 & C_{44} & 0 & 0 \\ 0 & 0 & 0 & 0 & C_{44} & 0 \\ 0 & 0 & 0 & 0 & 0 & C_{44} \end{bmatrix} \tag{15}$$

La combinaison des paramètres indépendants permet le calcul des propriétés mécaniques effectives des cellules unitaires, telles que le module d'élasticité, le module de cisaillement, le coefficient de Poisson et le coefficient de Zener. Plusieurs graphiques ont été générés reliant les propriétés mécaniques effectives à la fraction volumique et au paramètre de conception des cellules unitaires basées sur le TPMS. Un exemple est décrit en Figure 2.9.

a)

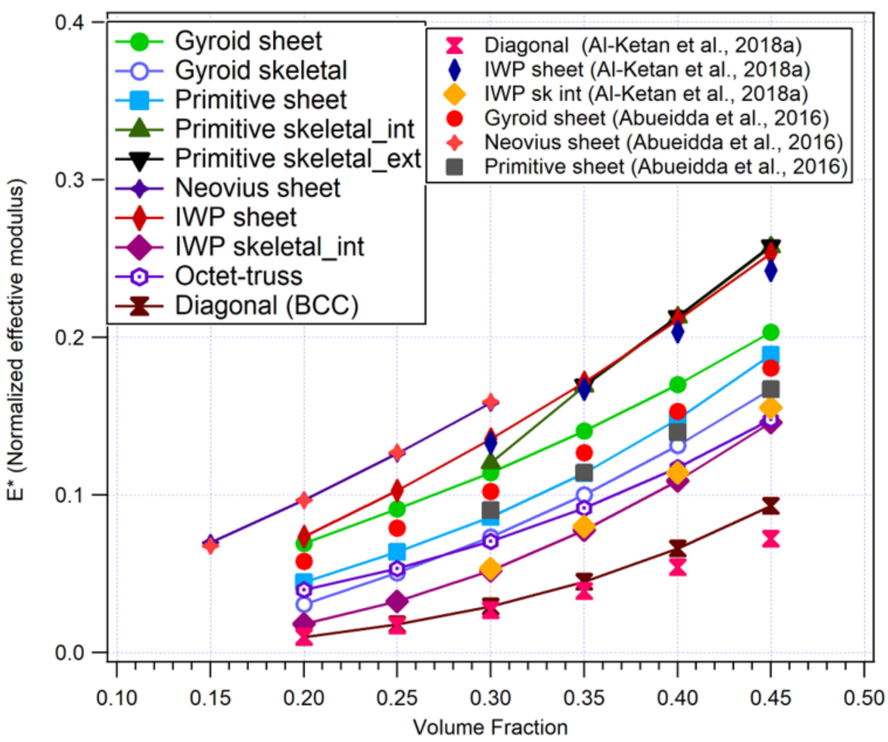

Figure 2.9. Evolution du module de Young normalisé effectif en fonction de la fraction volumique des cellules unitaires, présenté pour les topologies unitaires étudiées à base de TPMS et à base poutres indiquées dans la légende.

Une analyse de sensibilité du maillage est également effectuée et la distribution locale des contraintes des cellules unitaires est étudiée de manière quantitative dans des cas de fraction iso-volumique et d'iso-élasticité. Ce dernier est représenté sur la figure suivante. Enfin, les topologies sont comparées statistiquement pour la sélection de la plus appropriée dans une application spécifique.

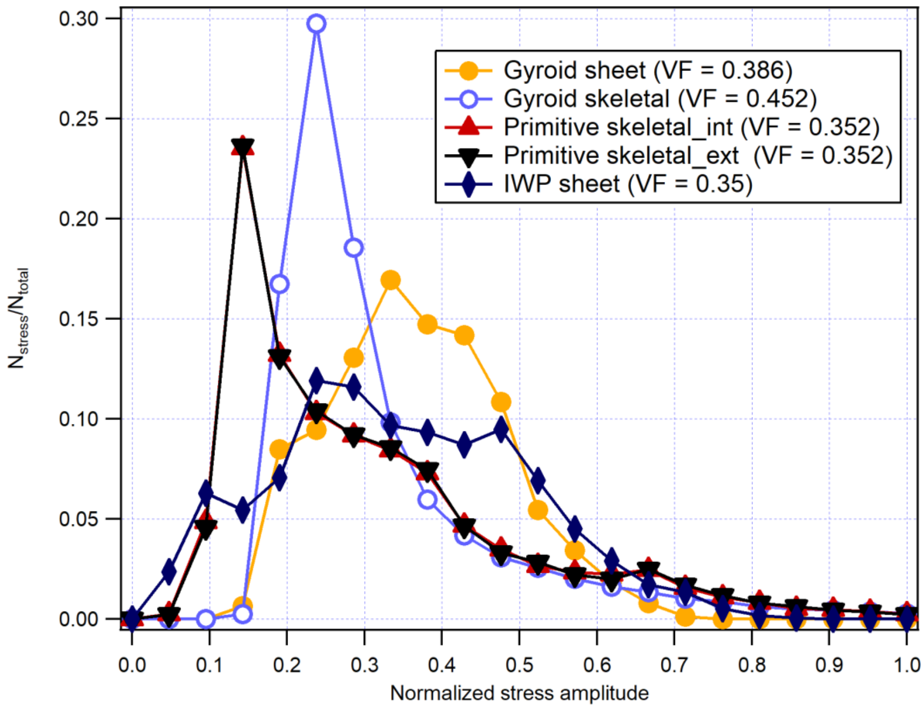

Figure 2.20. Distributions de contraintes locales normalisées du gyroid sheet, du gyroid skeletal, du primitive skeletal, du primitive skeletal externe et du IWP sheet sur la plage 0-1 au même module de Young apparent, $E' = 18500\ MPa$. (Comparaison des modules élastiques iso-efficaces).

3. Fabrication additive de structures en treillis : caractérisation multi-échelle et comparaison avec les prédictions numériques

Deux cas de chargement sont considérés dans ce chapitre pour la sélection d'une structure appropriée, à savoir les cas standard et destructif. Le cas standard traite de la sélection des conditions aux limites représentatives pour un réseau dont les propriétés élastiques imitent les propriétés de l'os réel. Le cas destructif traite de la sélection d'un réseau après la déformation plastique complète et la rupture sous une charge de compression. Bien que la rupture complète d'un implant soit un résultat non souhaitable, l'investigation de ce cas est importante afin d'identifier les limites du pire cas par topologie.

Concernant le cas standard, l'application de deux conditions aux limites différentes, à savoir les conditions aux limites compressives (CBC) et les PBC sur les topologies précitées est réalisée. Ensuite, les propriétés élastiques finales sont comparées pour sélectionner les conditions aux limites numériques les plus représentatives. L'objectif est simuler et prédire au plus proche la réponse à une charge de compression uniaxiale réelle. Ensuite, la validation expérimentale des résultats numériques est décrite. Après la comparaison de deux conditions aux limites numériques différentes et les tests expérimentaux, la sélection de la structure la plus appropriée est effectuée.

En ce qui concerne le cas destructif, des tests numériques et expérimentaux ont été effectués pour étudier la réponse non linéaire des cellules unitaires soumises à un chargement en compression. Par ailleurs, l'investigation expérimentale des structures telles que construites se poursuit jusqu'au niveau de la fracture.

Concernant les essais expérimentaux, la caractérisation mécanique est réalisée via des essais expérimentaux adaptés selon la norme internationale ISO 13314. Elle est utilisée pour la conception des réseaux métalliques et des matériaux généralement poreux, la procédure d'essai de compression et la caractérisation des réseaux. Les structures étudiées sont présentées à la figure 3.2.

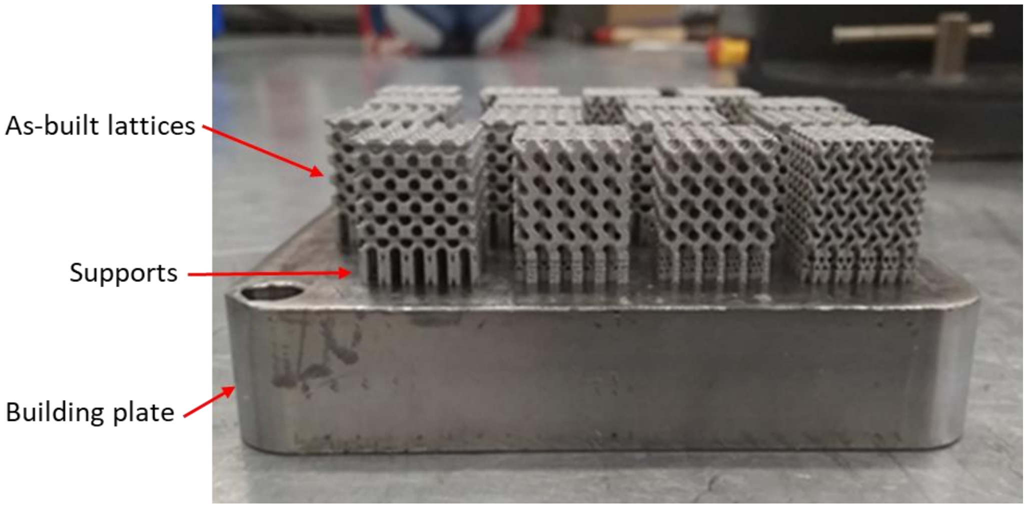

Figure 3.2. Une plaque de construction avec plusieurs structures architecturées et des éléments de construction en tant que supports sur le dessus, directement après la fin d'une production en SLM.

La comparaison du module élastique apparent après l'application des deux conditions aux limites numériques au module élastique mesuré expérimental conduit à la sélection des PBC comme les conditions limites numériques les plus représentatives. Les résultats sont présentés dans le tableau suivant.

Topology	E_{EXP} **[MPa]**	E_{PBC} **[MPa]**	E_{CBC} **[MPa]**
Gyroid sheet	14565	14280	10533
Gyroid skeletal	15687	14310	14104
Gyroid skeletal	5932	5586	5133
IWP skeletal int	5658	5602	4803
Diagonal	6243	5603	4462

Tableau. Les modules élastiques apparents calculés numériquement pour cinq topologies de cellules unitaires après l'application de PBC et CBC et celui correspondant mesuré expérimentalement.

Concernant le cas destructif, différentes structures ont été comprimées jusqu'à la fracture macroscopique finale sous une charge de compression uniaxiale afin d'étudier l'endommagement fonctionnel. Certains résultats expérimentaux sont présentés à la figure 3.10. Les structures fracturées présentées indiquent que généralement, la fracture se produit à 45^o pour toutes les topologies, mais le type de fracture, c'est-à-dire fracture « fragile » ou « ductile », dépend de la topologie.

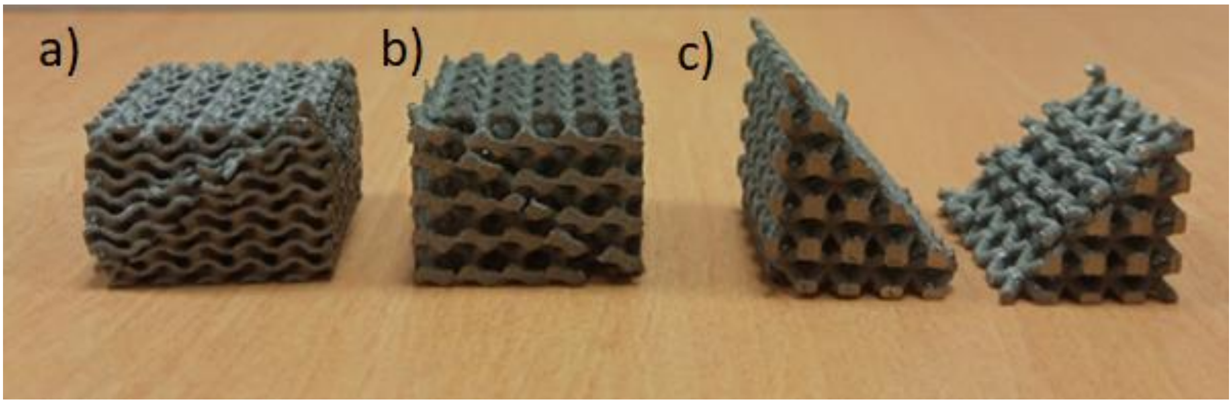

Figure 3.10. Fracture macroscopique à 45^o pour trois topologies de réseau, c'est-à-dire a) gyroid sheet, b) gyroid skeletal et c) Diagonal.

4. Remplacement partiel de l’os fémoral à l’aide de structures à base de TPMS, modélisation et analyse des contraintes

Les structures architecturées peuvent remplacer certaines pièces ou tout un dispositif biomédical et permettre la construction d'implants sur mesure et spécifiques au patient. Ce dernier peut mimer avec succès les propriétés matérielles de l'os humain réel. En réalisant ce processus, les problèmes mécaniques postopératoires qui surviennent, tels que la déviation des contraintes, sont minimisés comme cela a été mentionné précédemment.

Diverses techniques d'imagerie médicale, telles que l'imagerie par résonance magnétique (IRM) et la tomodensitométrie (CT scan) sont utilisées par les médecins et les chirurgiens pour le diagnostic des maladies de la hanche. De plus, les techniques médicales susmentionnées sont des outils de diagnostic utiles pour surveiller tout problème survenant sur les implants après un remplacement de la hanche. De plus, les techniques d'imagerie médicale sont très utiles lorsqu'il s'agit de collecter des données médicales personnelles et des informations orthopédiques auprès des patients afin de créer des implants spécifiques au patient. La taille et la forme de l'os fémoral et de l'articulation de la hanche diffèrent selon l'âge, le sexe, la taille, etc.

Il faut ajouter que le module d'élasticité d'un os n’a pas une valeur constante. Elle varie dans la gamme globale 0,02-30 GPa selon la structure osseuse, c'est-à-dire spongieuse ou corticale, et selon la direction, c'est-à-dire longitudinale ou transversale. Par conséquent, les implants spécifiques au patient peuvent être utilisés lorsque les implants commerciaux ne conviennent pas aux patients en raison d'une divergence de géométrie anatomique. Les implants sur mesure et spécifiques au patient offrent une option prometteuse pour traiter les maladies de la hanche de manière plus personnalisée, minimiser le temps chirurgical et les coûts de procédure globaux, et améliorer les résultats pour les patients.

Le stockage des données médicales est réalisé avec des images DICOM (Digital Imaging and Communication in Medicine). Ce sont des images en niveaux de gris selon les Unités Hounsfield (HU) qui permettent la mesure de la radio-densité de manière quantitative. En effet, la densité des tissus dans le corps humain est proportionnelle à l'absorption des faisceaux de rayons X. Les images DICOM sont un outil très utile non seulement pour les radiologues et les chirurgiens, mais aussi pour les ingénieurs. Après l'acquisition des images et le post-traitement approprié, le volume 3D peut être reconstruit pour une enquête plus approfondie, telle que la FEA ou la fabrication avec des techniques de fabrication additive et des tests expérimentaux. Ce processus est connu sous le nom de rétro-ingénierie et pourrait contribuer à l'amélioration du traitement en créant des implants spécifiques au patient et en optimisant typologiquement les dispositifs médicaux finaux.

L'objectif de ce chapitre est d'étudier le remplacement d'une partie spécifique (Area of Interest – AoI, zone d'intérêt) d'un os fémoral (modèle global) construit par des images DICOM par des structures basées sur TPMS (modèle local) de manière numérique. Les cellules unitaires sont générées pour avoir le même module d'élasticité que la partie fémorale et les conditions aux limites qui sont soumises pour simuler la charge physiologique. La comparaison de l'état de contrainte entre la partie fémorale et les cellules unitaires conduit à la sélection de la topologie la plus appropriée pour le remplacement dans une étude de cas particulière.

La géométrie et l'assignement des matériaux du modèle global sont basés sur des images DICOM. Dans la Figure 4.2., les images DICOM d'un patient et le modèle 3D d'un os fémoral dans le logiciel Materialise Mimics sont présentés. L'attribution du matériau, c'est-à-dire le module d'élasticité, a été effectuée à l'aide de l'unité HU et d'équations tirées de la littérature.

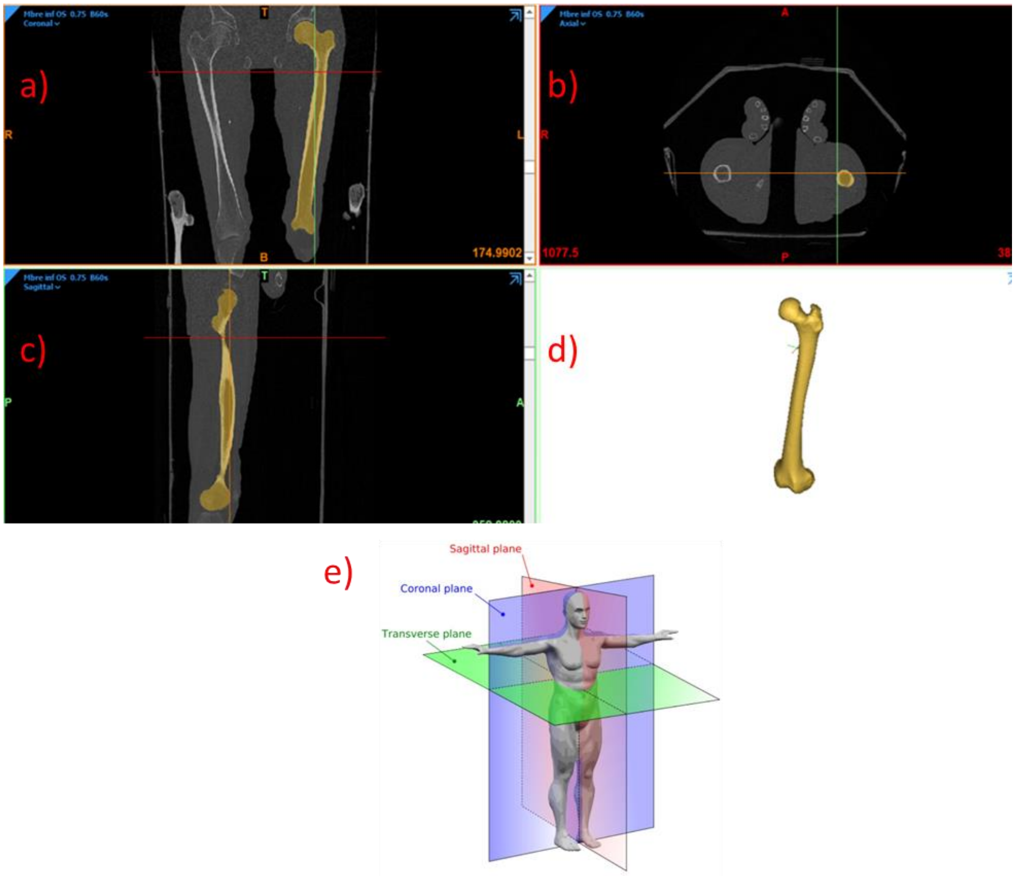

Figure 4.2. Trois vues d'images DICOM du bassin et de l'os fémoral d'un patient dans le logiciel Materialise Mimics : a) coronale, b) axiale et c) vues sagittales, d) le modèle 3D reconstruit d'un fémur et e) les plans anatomiques.

Un cas de charge réel, c'est-à-dire un cas de marche, est sélectionné et les valeurs de force correspondantes sont prises par une base de données en ligne en libre accès avec des données médicales (https://orthoload.com). Une zone d'intérêt (AoI) (Figure 4.9) est sélectionnée pour le remplacement partiel avec un implant numérique basé sur TPMS. Quatre topologies TPMS différentes (Figure 4.10.) sont comparées statistiquement et enfin, une fonction de pondération est proposée pour la sélection de la plus appropriée en fonction des exigences mécaniques et biologiques spécifiques, qui seront définies à la fois par les ingénieurs et les chirurgiens orthopédistes.

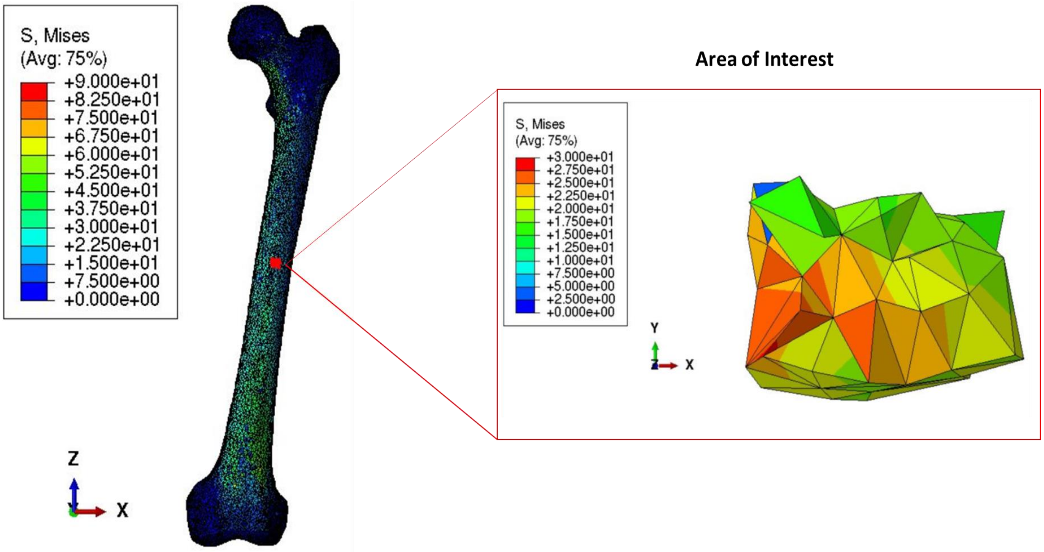

Figure 4.9. Distribution de la contrainte de Von Mises de l'ensemble du fémur et de l'AoI.

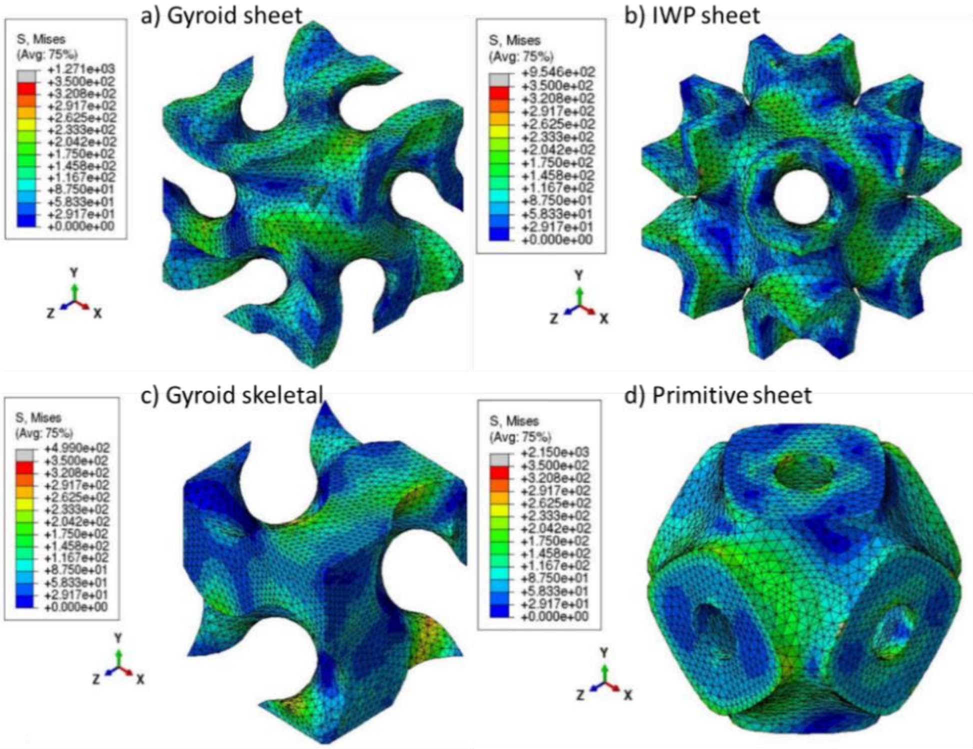

Figure 4.10. Distribution de la contrainte de Von Mises pour a) la gyroid sheet, b) la IWP sheet, c) la gyroid skeletal et d) la primitive sheet dans la plage de contraintes 0-350 MPa.

General Conclusions and Perspectives

Les travaux de cette thèse ont contribué à la résolution d'un problème mécanique concernant les implants orthopédiques constitués de matériaux architecturés. Les résultats numériques et les résultats expérimentaux obtenus à partir de la méthodologie proposée visaient la conception et la sélection d'une structure appropriée qui répond aux critères requis, tels qu'un faible module élastique et la minimisation des concentrations de contraintes. La méthodologie proposée combine à la fois la simulation numérique et les investigations expérimentales.

Le premier défi était le développement d'une chaîne numérique complète pour concevoir avec succès des cellules unitaires et des structures basées sur TPMS appropriés à la fois pour l'analyse par éléments finis et la fabrication additive. Visant la prédiction des propriétés mécaniques apparentes et l'étude des distributions locales des contraintes dans les mailles unitaires, une méthode d'homogénéisation périodique a été mise en place et appliquée. Cette méthode a été applicable aux structures à base de TPMS en raison de leur microstructure périodique. Afin d'assurer la capacité de réaliser les structures étudiées avec la fabrication additive, elles ont été fabriquées par la technique SLM. Ensuite, des tests de chargement de compression uniaxiale ont été effectués et comparés aux propriétés élastiques numériques prédites ainsi qu'à la réponse globale. L'objectif était de prendre en compte tous les résultats obtenus à partir de la méthodologie décrite ci-dessus pour remplacer partiellement un os réel soumis à une charge réelle par une cellule unitaire à base de TPMS.

En particulier, tout au long de cette thèse, une investigation numérique et expérimentale a été proposée pour décrire les propriétés mécaniques de dix topologies de cellules unitaires en mettant l'accent sur le contrôle du module d'élasticité apparent. Un faible module d'élasticité visait à réduire le phénomène de déviation des contraintes. La méthodologie proposée ici a commencé par la conception numérique des cellules unitaires à l'aide d'une formulation mathématique décrivant les surfaces. Tous les détails de la conception complexe de huit topologies à base de TPMS et de deux à base de poutres ont été expliqués. Deux types de conditions aux limites ont été appliqués numériquement aux mailles unitaires pour calculer les propriétés mécaniques apparentes. Tous les résultats ont finalement été comparés aux résultats expérimentaux pertinents pour déterminer quelles conditions aux limites ont permis de prédire le module d'élasticité le plus représentatif. De plus, l'analyse de la distribution locale des contraintes a permis la comparaison de l'état de contrainte des cellules unitaires. Il était également très intéressant de comparer les mécanismes macroscopiques de déformation et de rupture des structures architecturées qui conduisent à la sélection des facteurs de sécurité pour la conception des treillis dans une application biomécanique.

Le chapitre 1 a introduit un cadre général des implants orthopédiques et un problème postopératoire courant qui peut survenir, à savoir la déviation des contraintes. Des structures architecturées ont été proposées comme moyen d'abaisser le module d'élasticité apparent des implants et ainsi de réduire le phénomène de déviation des contraintes. Les aspects fondamentaux concernant la conception et les propriétés mécaniques des structures architecturées à base de poutres et à base de TPMS ont été détaillés. Enfin, la technologie de fabrication additive et en particulier la technique SLM a été proposée comme une voie appropriée et prometteuse pour la réalisation de telles structures complexes et sur mesure.

Le chapitre 2 décrit toutes les étapes de la chaîne de conception numérique proposée des cellules unitaires, en insistant principalement sur la manière numérique complexe de concevoir les topologies basées sur TPMS. Huit cellules unitaires à base de TPMS et deux à base de poutres ont été étudiées en termes de diverses propriétés mécaniques et de distribution de contraintes locales. L'influence des paramètres géométriques de conception sur les propriétés mécaniques des structures architecturées a également été étudié. Les résultats ont été acquis après l'application d'une méthode d'homogénéisation périodique puisque toutes les mailles unitaires étaient périodiques. Une pléthore de tableaux a été exposée pour aider à la classification et à la sélection des topologies appropriées en fonction des exigences mécaniques particulières.

Le chapitre 3 a proposé un deuxième ensemble de conditions aux limites numériques, à savoir les conditions aux limites de compression imposées aux structures lors des essais expérimentaux. Le module d'élasticité apparent prédit des cellules unitaires a été comparé au module d'élasticité pertinent obtenu à partir de l'application du PBC. Les structures architecturées ont été fabriquées et testées expérimentalement sous une charge de compression monotone uniaxiale, et le module d'élasticité a été mesuré. Les résultats numériques prédisant au mieux les résultats expérimentaux ont été déterminés. Par conséquent, les PBC ont été sélectionnés comme les conditions aux limites les plus appropriées pour prédire le module d'élasticité apparent des cellules unitaires. Les mécanismes macroscopiques de déformation et de rupture des réseaux comprimés ont également été étudiés expérimentalement afin de classer les topologies selon leur aptitude à une application biomécanique dans un cas destructif. La fracture s'est produite dans la même direction pour tous les réseaux, mais les mécanismes de déformation étaient dépendants de la topologie.

Le chapitre 4 était consacré au remplacement partiel d'un vrai fémur soumis à des conditions aux limites réelles par un digital-implant. Ce dernier consistait en une cellule unitaire basée sur le TPMS. Quatre topologies de cellules unitaires différentes ont été étudiées et comparées en termes de valeur de contrainte moyenne, de distribution de contrainte locale et de fraction volumique lorsque l'objectif sur la valeur d'élasticité était satisfait. Une fonction de pondération a finalement été proposée pour la sélection de la topologie la plus appropriée en fonction de diverses exigences.

La méthodologie décrite précédemment combinant des résultats numériques et expérimentaux est discutée pour présenter des sujets pour des investigations ultérieures. Ces sujets sont associés au processus de conception qui peut être enrichi, à d'autres tests expérimentaux et numériques qui peuvent être effectués, et à l'utilisation des treillis dans des applications biomécaniques et autres.

Il est rappelé que dans cette étude seules les cellules unitaires cubiques et les structures en treillis ont été présentées. La conception informatique pourrait être améliorée pour générer des surfaces, puis des réseaux et des cellules unitaires avec diverses formes de délimitation, telles que des sphères, des pyramides, des cônes. Par conséquent, il serait plus facile d'adapter les structures générées aux structures macroscopiques où elles devraient être placées, par exemple, la partie interne d'un implant orthopédique ou toute structure mécanique.

Dans cette étude, une comparaison entre les résultats expérimentaux et numériques a été effectuée uniquement pour le chargement en compression. Il serait donc intéressant de concevoir et de fabriquer des éprouvettes appropriées puis de réaliser des essais de torsion afin de comparer la réponse mécanique des essais numériques et expérimentaux. Les résultats seraient utiles pour toute application biomécanique et industrielle.

De plus, il serait intéressant de générer des structures composites associées aux structures à base de TPMS. Le vide des treillis pourrait être remplacé par un autre matériau, à savoir un alliage métallique ou tout autre matériau, et la structure générée posséderait des propriétés mécaniques exceptionnelles.

Étant donné que l'os humain présente une structure macroscopique hétérogène où la densité et les propriétés élastiques dépendent de la position, la conception de réseaux adaptés pourrait conduire à des implants hautement personnalisés. Le gradient d'épaisseur de paroi des cellules unitaires conduirait à la génération de réseaux de gradient de macroporosité et ainsi, le volume et la densité des implants pourraient être ajustés au volume et à la densité d'un os réel. De plus, la combinaison de plusieurs topologies générerait des réseaux multi-morphologies. Il serait intéressant de sélectionner les topologies les plus adaptées aux différentes zones d'un implant selon la méthodologie proposée dans cette étude. Ensuite, ils pourraient être combinés avec une transition en douceur entre toutes les deux topologies afin de créer une structure en treillis hautement adaptée qui répondrait à diverses exigences mécaniques.

Enfin, la fonction de poids, W, présentée au chapitre 4 pourrait être utilisée pour optimiser la sélection d'une structure basée sur des TPMS appropriées et la fraction volumique pertinente. Par exemple, le paramètre de conception d'entrée t et la topologie elle-même pourraient être modifiés afin d'adapter la sortie du W à des exigences mécaniques particulières.

Chrysoula CHATZIGEORGIOU

Optimisation topologique de structures lattices à base de surface minimale triplement périodique en Ti-6Al-4V pour implants osseux humains obtenus par fabrication additive

Résumé

Les structures lattices offrent des solutions performantes pour remplacer des structures tout en contrôlant leurs propriétés mécaniques. Ceci est particulièrement le cas pour réduire le phénomène de stress-shielding qui peut survenir dans l'os péri-implantaire suite à la pose d'implants. Outre les structures lattices à base de poutre largement étudiées, le concept de surfaces minimales triplement périodiques (TPMS) a été introduit pour créer des structures présentant des propriétés originales. Huit topologies de cellules unitaires basées sur TPMS et deux basées sur des poutres ont été étudiées numériquement pour calculer leurs propriétés élastiques effectives et la distribution des contraintes locales, en utilisant une méthode d'homogénéisation périodique. La dépendance de la topologie sur la distribution des contraintes locales est mise en évidence par une analyse statistique des cellules unitaires. La validation des résultats numériques a été effectuée par des résultats obtenus expérimentalement suite à la fabrication par une machine SLM de plusieurs structures et à des tests de compression. Deux types de sollicitation ont été étudiés : un cas fonctionnel mettant l'accent sur le module d'Young effectif des structures, et un cas destructif se concentrant sur la rupture de ces dernières. Sur la base de ces résultats, une étude numérique considérant le remplacement partiel d'un os par une structure lattice à base de TPMS, soumis à des conditions aux limites réelles, est développée. Un critère permettant de choisir une structure optimisée sur la base de contraintes mécaniques est proposé.

Mots clefs: structures lattices à base TPMS, déviation des contraintes, homogénéisation périodique, MEF, fabrication additive, prothèse de hanche

Résumé en anglais

Lattice structures offer the opportunity to control the mechanical properties of the structures they replace. The use of lattices in orthopedic implants is then a promising solution to the stress shielding problem that may occur postoperatively. Apart from the widely known strut-based lattices, the Triply Periodic Minimal Surfaces (TPMS) concept has been introduced to create surface-based lattices with tailored mechanical properties. Eight TPMS-based and two strut-based unit cell topologies have been numerically investigated to compute their apparent elastic properties and local stress distribution, considering a periodic homogenization method. The topology-dependence of the local stress distribution is highlighted by a statistical analysis of the unit cells. The validation of the numerical results has been performed by experimentally-obtained results following the fabrication of several lattices by an SLM machine and compression testing. Two solicitation types were investigated: a functional case emphasizes on the apparent Young modulus of lattices, and a destructive case focusing on fracture mechanism. According to all previous results, a numerical partial replacement of a real bone subjected to real boundary conditions by a TPMS-based unit cell is proposed according to various mechanical requirements.

Keywords : TPMS-based lattices, stress shielding, periodic homogenization method, FEA, additive manufacturing, SLM, hip implant